EAST EUROPEAN JOURNAL OF PHYSICS. **2.** 445-460 (2026)
DOI:10.26565/2312-4334-2026-2-50 ISSN 2312-4334

AMBIPOLAR DIFFUSION AND ELECTRIC FIELD REVERSAL IN ELECTRONEGATIVE PLASMA WITH CHARGED NANOPARTICLES

V. Lisovskiy*, S. Dudin, S. Bogatyrenko, S. Rezunenko, V. Yegorenkov
V.N. Karazin Kharkiv National University, 4 Svobody Sq., Kharkiv, 61022, Ukraine
**Corresponding Author email: lisovskiy@karazin.ua*

Received February 25, 2026; revised April 18, 2026; accepted May 20, 2026

An analytical model of ambipolar diffusion in plasma consisting of electrons, positive ions, negative ions, and negatively charged nanoparticles is proposed. Analytical expressions are derived for the ambipolar diffusion coefficients of all charged species, as well as for the ambipolar electric field strength. In plasma containing only electrons, positive ions, and negative ions, high concentrations of negative ions lead to a transition from ambipolar to free diffusion, where the ambipolar diffusion coefficients approach the corresponding free diffusion coefficients. In plasma consisting of electrons, positive ions, and negatively charged nanoparticles, high nanoparticle concentrations result in qualitatively different behavior: the ambipolar diffusion coefficient of electrons approaches twice the free electron diffusion coefficient, while the ambipolar diffusion coefficient of positive ions approaches twice the free diffusion coefficient of nanoparticles. For the general four-component plasma, the ambipolar diffusion regime is governed by the dominant electron-loss mechanism, namely, electron attachment to either electronegative gas molecules or nanoparticles. If electron attachment to gas molecules dominates, the ambipolar diffusion coefficients of electrons, negative ions, and nanoparticles remain close to their free diffusion coefficients. In contrast, when electron attachment to nanoparticles dominates, these coefficients approach twice the corresponding free diffusion coefficients. The ambipolar diffusion coefficient of positive ions was found to depend strongly on the dominant negatively charged species in plasma. Under intensive negative-ion formation, it approaches the free diffusion coefficient of negative ions, whereas in plasma dominated by electron attachment to nanoparticles it asymptotically approaches twice the free diffusion coefficient of nanoparticles. It is shown that sufficiently high concentrations of negative ions and/or charged nanoparticles substantially reduce the ambipolar electric field strength and may even reverse its sign. A weakly negative ambipolar electric field can remove excess negative ions and nanoparticles from plasma, thereby stabilizing the discharge. Experiments with acetylene plasma demonstrated intense transport of small nanoparticles toward the tube walls, which may serve as indirect evidence of an ambipolar electric-field reversal.

Keywords: *Ambipolar diffusion; Analytic model; Ambipolar electric field; Nanoparticles; Negative ions*
PACS: 52.80.Pi, 52.50.Qt, 52.65.Kj

INTRODUCTION

Gas-discharge plasma has found extremely broad application in modern technology and everyday life. At present, its use is no longer limited to hardening of metal surfaces and fabrication of microelectronic devices, as was the case several decades ago. A vast number of products and materials currently in use are either manufactured or modified using gas-discharge plasma. In addition, new research directions have emerged, including "plasma medicine" [1,2] and "plasma agriculture" [2–6]. Consequently, investigations of the processes governing the maintenance and transport properties of gas-discharge plasmas under various conditions remain highly relevant.

Quasineutral plasma is typically composed of electrons and positive ions with approximately equal concentrations, $n_e = n_+$, moving in a neutral gas background. Diffusion tends to smooth concentration gradients of charged particles. When the charged-particle density is sufficiently low, for example $n_e < 10^6$ cm^{-3}, electrons and positive ions diffuse almost independently and do not significantly affect each other's motion. Such diffusion is referred to as free diffusion, and the corresponding diffusion coefficients of electrons and positive ions are denoted by D_e and D_+, respectively.

The situation changes when the charged-particle density increases to $n_e > 10^8$ cm^{-3}, at which point free diffusion transitions to ambipolar diffusion. Because electrons possess a mobility μ_e much higher than the mobility of positive ions μ_+, their diffusion coefficient is also significantly larger, i.e., $D_e >> D_+$. As a result, the more mobile electrons, particularly those with higher energies, tend to escape from the plasma volume. In a gas-discharge chamber, these electrons are absorbed by the tube walls, charging them negatively. Consequently, the plasma acquires a positive space charge, and charge separation gives rise to the so-called ambipolar electric field. This field attracts positive ions toward the negatively charged wall and repels low-energy electrons away from it. Therefore, the fluxes of positive ions and electrons arriving at the wall become nearly equal. A positive ion reaching the wall recombines with one of the electrons accumulated there, while another energetic electron subsequently arrives, restoring the negative wall charge.

The first expressions for the ambipolar diffusion coefficient D_a and the corresponding ambipolar electric field were derived by Walter Schottky [7,8], who developed the theory of the positive column in electropositive quasineutral plasma, where $n_e = n_+$. In this case, both electrons and positive ions diffuse with the same ambipolar diffusion coefficient D_a.

Cite as: V. Lisovskiy, S. Dudin, S. Bogatyrenko, S. Rezunenko, V. Yegorenkov, East Eur. J. Phys. 2, 445 (2026), https://doi.org/10.26565/2312-4334-2026-2-50

However, many plasma technologies employ so-called electronegative gases, whose molecules capture free electrons and form molecular negative ions (e.g., SF_6^-, O_2^-, or produce atomic negative ions (F^-, H^-, O^-) through dissociative attachment processes [9–13]. Such negative ions may be directly accelerated, for example, for plasma heating purposes [14–19], and they also participate in various plasma-chemical processes [20–24]. Therefore, electronegative plasmas have attracted considerable attention from researchers [25–37].

The formation of negative ions represents a loss mechanism for free electrons, since negative ions in gas-discharge plasma generally cannot acquire sufficient energy to ionize gas molecules and, due to their low mobility, carry only a negligible electric current. In addition, negative ions are repelled by the negatively charged walls and may accumulate inside the plasma volume. Under certain conditions, the concentration of negative ions n_n can become comparable to or even significantly exceed the free-electron concentration [9,10,38–41]. This substantially affects the transport of electrons and positive ions toward the walls, thereby reducing the ambipolar electric field strength. William B. Thompson [42] was the first to investigate ambipolar diffusion in electronegative plasma consisting of electrons, positive ions, and negative ions. He demonstrated that, in contrast to electropositive plasma, the ambipolar diffusion coefficients become different for each charged species. Further studies of ambipolar diffusion in electronegative plasmas were reported, for example, in Refs. [43–47]. These works showed that the accumulation of negative ions may not only substantially reduce the ambipolar electric field strength, but may even cause a transition from ambipolar diffusion back to free diffusion, since the ambipolar diffusion coefficients of the charged species approach their corresponding free-diffusion coefficients [47].

Nanoparticles introduced into plasma from an external reservoir or formed in situ due to electrode sputtering [48–53] or plasma-chemical processes [54–60] also capture free electrons and may therefore be regarded as very heavy negative ions. Ambipolar diffusion in plasma consisting of electrons, positive ions, and negatively charged nanoparticles has been investigated numerically in Refs. [61–63], while an analytical model was developed in Ref. [64]. In contrast to the numerical studies [61–63], which provided results only for specific plasma conditions, Ref. [64] derived convenient analytical expressions for the ambipolar diffusion coefficients of each charged species and for the ambipolar electric field strength. It was shown that a high nanoparticle concentration, and consequently strong electron losses due to electron attachment to nanoparticle surfaces, may reduce the ambipolar electric field strength to zero.

It should also be noted that technological gases in which nanoparticles are formed through volumetric plasma polymerization are often simultaneously electronegative. For example, in acetylene plasma, H^-, C_2H^- and heavier negative ions can be generated [25–27]. The C_2H^- ions may cluster with acetylene molecules during collisions, eventually leading to nanoparticle formation [65]. Therefore, acetylene plasma simultaneously contains not only electrons and positive ions, but also negative ions and nanoparticles.

The aim of the present work is to develop an analytical model for such a complex plasma system, determine the conditions under which the ambipolar electric field reverses direction, and experimentally verify this phenomenon.

1. DESCRIPTION OF THE ANALYTICAL MODEL

For a four-component plasma consisting of one species of positive ions, electrons, negative ions, and negatively charged nanoparticles, the particle flux equations can be written in the following form:

$$\Gamma_+ = -D_+ \cdot \nabla n_+ + \mu_+ n_+ E\,, \tag{1}$$

$$\Gamma_e = -D_e \cdot \nabla n_e - \mu_e n_e E\,, \tag{2}$$

$$\Gamma_n = -D_n \cdot \nabla n_n - \mu_n n_n E\,, \tag{3}$$

$$\Gamma_p = -D_p \cdot \nabla n_p - \mu_p n_p E\,, \tag{4}$$

where D denotes the free diffusion coefficients, μ the mobilities, and n the concentrations of the charged species listed above. The subscripts "*e*", "+", "*n*", and "*p*" correspond to electrons, positive ions, negative ions, and negatively charged nanoparticles, respectively. Owing to the formation of a space charge, an ambipolar electric field arises, whose strength is denoted by E.

In quasineutral plasma, the total concentration of positive charges must equal the total concentration of negatively charged species:

$$n_+ = n_e + n_n + n_p \cdot Z_p\,, \tag{5}$$

Here it is taken into account that a nanoparticle may collect not only one but several electrons. The number of electrons attached to a single nanoparticle is denoted by Z_p. Consequently, the product $n_p \cdot Z_p$ represents the total number of electrons attached to nanoparticles within a unit volume of 1 cm^{-3}.

Furthermore, to maintain plasma quasineutrality, the flux of positive ions must balance the total flux of negatively charged species:

$$\Gamma_+ = \Gamma_e + \Gamma_n + \Gamma_p \cdot Z_p\,. \tag{6}$$

Let us introduce the dimensionless parameters = np/ne and = nn/ne, which represent the relative concentrations of nanoparticles and negative ions, respectively, normalized to the electron concentration. We also define $\gamma = T_e/T_+ = T_e/T_n$ and $\tau = T_e/T_p$, where T_e is the electron temperature, $T_+ = T_n$ are the temperatures of positive and negative ions (assumed equal), and T_p is the nanoparticle temperature.

Substituting the flux expressions (1)–(4) into Eq. (6), and taking into account the quasineutrality condition (5), the ambipolar electric field E can be eliminated, yielding:

$$\Gamma_+ = -D_{a+} \cdot \nabla n_+ , \tag{7}$$

$$\Gamma_e = -D_{ae} \cdot \nabla n_e , \tag{8}$$

$$\Gamma_n = -D_{an} \cdot \nabla n_n , \tag{9}$$

$$\Gamma_p = -D_{ap} \cdot \nabla n_p . \tag{10}$$

These equations contain the ambipolar diffusion coefficients for each charged species:

$$D_{a+} = D_+ \cdot \frac{\gamma + 2\alpha\gamma + \gamma\cdot\delta\cdot Z_p + 1 + \delta\cdot\tau\cdot Z_p}{1 + \alpha\gamma + \delta\cdot\tau\cdot Z_p} \cdot \frac{1 + \alpha\cdot(\mu_n/\mu_e) + \delta\cdot Z_p\cdot(\mu_p/\mu_e)}{(1+\alpha+\delta\cdot Z_p)\cdot(\mu_+/\mu_e) + \alpha\cdot(\mu_n/\mu_e) + \delta\cdot Z_p\cdot(\mu_p/\mu_e) + 1}, \tag{11}$$

$$D_{ae} = D_+ \cdot \frac{\gamma + 2\alpha\gamma + \gamma\cdot\delta\cdot Z_p + 1 + \delta\cdot\tau\cdot Z_p}{(1+\alpha+\delta\cdot Z_p)\cdot(\mu_+/\mu_e) + \alpha\cdot(\mu_n/\mu_e) + \delta\cdot Z_p\cdot(\mu_p/\mu_e) + 1} . \tag{12}$$

$$D_{an} = D_+ \cdot \frac{\mu_n}{\mu_e} \cdot \frac{\gamma + 2\alpha\gamma + \gamma\cdot\delta\cdot Z_p + 1 + \delta\cdot\tau\cdot Z_p}{(1+\alpha+\delta\cdot Z_p)\cdot(\mu_+/\mu_e) + \alpha\cdot(\mu_n/\mu_e) + \delta\cdot Z_p\cdot(\mu_p/\mu_e) + 1} . \tag{13}$$

$$D_{ap} = D_+ \cdot \frac{1}{\tau} \cdot \frac{\mu_p}{\mu_e} \frac{\gamma + 2\alpha\gamma + \gamma\cdot\delta\cdot Z_p + 1 + \delta\cdot\tau\cdot Z_p}{(1+\alpha+\delta\cdot Z_p)\cdot(\mu_+/\mu_e) + \alpha\cdot(\mu_n/\mu_e) + \delta\cdot Z_p\cdot(\mu_p/\mu_e) + 1} \tag{14}$$

By equating the expressions for the positive-ion fluxes in Eqs. (1) and (7) (or similarly Eqs. (2) and (8), etc.), and using the Einstein relation $D_+/\mu_+ = k\cdot T_+/e$ where k is the Boltzmann constant and e is the elementary charge, the following expression for the ambipolar electric field strength can be derived:

$$E_{Amb.Nano} = \frac{D_+ - D_{a+}}{\mu_+ n_+} \cdot \nabla n_+ = \frac{D_+}{\mu_+} \cdot \left(1 - \frac{D_{a+}}{D_+}\right) \cdot \frac{\nabla n_+}{n_+} = T_+ \cdot \left(1 - \frac{D_{a+}}{D_+}\right) \cdot \frac{\nabla n_+}{n_+} . \tag{15}$$

Taking Eq. (11) into account, Eq. (15) can be rewritten as

$$E_{Amb.Nano} = \frac{kT_+}{e} \cdot \frac{(1+\alpha+\delta\cdot Z_p)\cdot\left[(1+\alpha\cdot\gamma+\delta\cdot\tau\cdot Z_p)\cdot(\mu_+/\mu_e) - \alpha\cdot\gamma\cdot(\mu_n/\mu_e) - \delta\cdot Z_p\cdot\gamma\cdot(\mu_p/\mu_e) - \gamma\right]}{(1+\alpha\cdot\gamma+\delta\cdot\tau\cdot Z_p)\cdot\left[(1+\alpha+\delta\cdot Z_p)\cdot(\mu_+/\mu_e) + \alpha\cdot\gamma\cdot(\mu_n/\mu_e) + \delta\cdot Z_p\cdot(\mu_p/\mu_e) + 1\right]} \cdot \frac{\nabla n_+}{n_+} \tag{16}$$

For electropositive plasma consisting only of electrons and positive ions, Eq. (16) reduces to the well-known expression for the ambipolar electric field [66–68]:

$$E_{Amb} = \frac{D_+ - D_e}{\mu_+ + \mu_e} \cdot \frac{\nabla n}{n} . \tag{17}$$

Next, let us determine the floating potential φ_s acquired by a nanoparticle of radius a immersed in plasma and collecting electrons, positive ions, and negative ions with masses m_e, M_+ та M_n, respectively. This will allow us to determine the nanoparticle charge $Q = e\cdot Z_p$ and subsequently evaluate the ambipolar electric field strength using Eq. (16).

The currents of charged particles to the nanoparticle surface can be written as [69]:

$$I_+ = 4\pi a^2 e \cdot \frac{n_+}{4} \cdot \left(\frac{8kT_+}{\pi M_+}\right)^{1/2} \cdot \left(1 - \frac{e\varphi_s}{kT_+}\right), \tag{18}$$

$$I_e = 4\pi a^2 e \cdot \frac{n_e}{4} \cdot \left(\frac{8kT_e}{\pi m_e}\right)^{1/2} \cdot \exp\left(\frac{e\varphi_s}{kT_e}\right), \tag{19}$$

$$I_n = 4\pi a^2 e \cdot \frac{n_n}{4} \cdot \left(\frac{8kT_n}{\pi M_n}\right)^{1/2} \cdot \exp\left(\frac{e\varphi_s}{kT_n}\right). \tag{20}$$

Since nanoparticles are electrically isolated, they acquire a floating potential such that the total current to their surface is zero:

$$I_+ = I_e + I_n. \tag{21}$$

Using Eqs. (18)–(21) together with the quasineutrality condition (5), we obtain the following equation for the floating potential:

$$\left(1+\alpha+\delta\cdot Z_p\right)\cdot\left(\frac{T_+}{T_e}\cdot\frac{m_e}{M_+}\right)^{1/2}\cdot\left(1-\frac{e\varphi_s}{kT_+}\right)-\exp\left(\frac{e\varphi_s}{kT_e}\right)-\alpha\cdot\left(\frac{T_n}{T_e}\cdot\frac{m_e}{M_n}\right)^{1/2}\cdot\exp\left(\frac{e\varphi_s}{kT_n}\right)=0. \tag{22}$$

Usually, the nanoparticle floating potential relative to the plasma is determined only from the balance between positive-ion and electron currents to the particle surface. However, at sufficiently high negative-ion concentrations (large α), the free-electron concentration may become very low, leading to a substantial reduction in the electron current to the nanoparticle surface. Therefore, in Eqs. (21) and (22), the contribution of the negative-ion current to the nanoparticle surface has also been taken into account. Moreover, the depletion of free electrons due to their attachment to nanoparticles significantly affects plasma quasineutrality, which is reflected in the first term of Eq. (22).

As noted above, each nanoparticle collects Z_p electrons. If a nanoparticle is placed in plasma characterized by a Debye length λ_D, its charge Q is given by [69–77]:

$$Q = 4\cdot\pi\cdot\varepsilon_0\cdot a\cdot\left(1+\frac{a}{\lambda_D}\right)\cdot\varphi_s, \tag{23}$$

where $\varepsilon_0 = 8.85\cdot10^{-12}$ F/m is the vacuum permittivity.

The Debye length can be estimated as [66]

$$\lambda_D = 742\cdot\left(\frac{T_e\,[eV]}{n_e\,[cm^{-3}]}\right)^{1/2}[\mathrm{cm}] \tag{24}$$

For example, for an electron temperature of 1 eV and an electron concentration of 10^{10} cm^{-3}, one obtains $\lambda_D = 74$ µm. Since nanoparticles in plasma typically have sizes of several tens to hundreds of nanometers, Eq. (23) can be simplified to

$$Q = 4\cdot\pi\cdot\varepsilon_0\cdot a\cdot\varphi_s. \tag{25}$$

Taking into account that $Q = e\cdot Z_p$, substituting Eq. (25) into Eq. (22) yields the final equation for the nanoparticle potential:

$$\left(1+\alpha+\delta\cdot\frac{4\cdot\pi\cdot\varepsilon_0\cdot a\cdot\varphi_s}{e}\right)\cdot\left(\frac{T_+}{T_e}\cdot\frac{m_e}{M_+}\right)^{\frac{1}{2}}\left(1-\frac{e\varphi_s}{kT_+}\right)-\exp\left(\frac{e\varphi_s}{kT_e}\right)-\alpha\left(\frac{T_n}{T_e}\cdot\frac{m_e}{M_n}\right)^{1/2}\exp\left(\frac{e\varphi_s}{kT_n}\right)=0. \tag{26}$$

The nanoparticle potential φ_s, obtained for fixed values of α, δ, and charged-particle temperatures using Eq. (26), is substituted into Eq. (25) to determine the nanoparticle charge Z_p. Examples of the calculated nanoparticle potentials and charges are presented in Fig. 1 and Fig. 2, respectively.

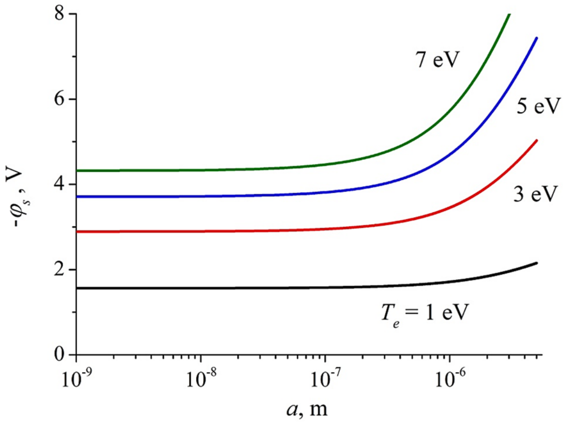

Figure 1. Dependence of the negative floating potential acquired by a nanoparticle in plasma on the nanoparticle radius a, for different electron temperatures T_e, in the absence of negative ions ($\alpha = 0$)

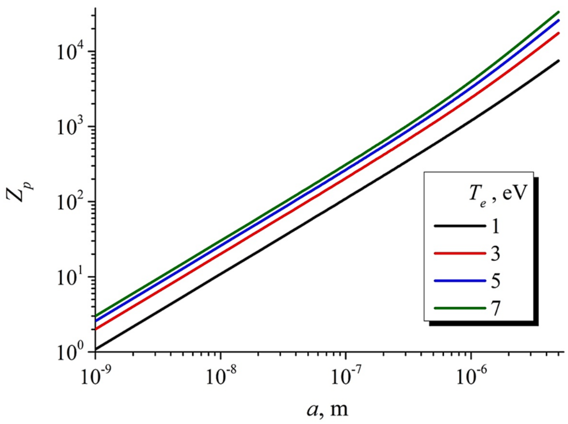

Figure 2. Dependence of the number of electrons attached to a nanoparticle in plasma on the nanoparticle radius a, for different electron temperatures T_e, in the absence of negative ions ($\alpha = 0$)

Figures 1 and 2 show that both the nanoparticle potential and charge increase with increasing electron temperature due to enhanced losses of free electrons to nanoparticle surfaces. Nanoparticle size also plays an important role. For radii $a < 100$ nm, the floating potential increases relatively slowly with increasing a, while the number of electrons attached to a nanoparticle is approximately proportional to its radius. However, for larger nanoparticles $a > 100$ nm, the rates of increase of both the potential and the charge become substantially higher.

Next, Eq. (16) is used to determine the ambipolar electric field strength. Here, our interest is focused on the average ambipolar electric field over the tube radius R, rather than on its radial distribution. An expression for the average ambipolar field in a two-component plasma (electrons and positive ions) is given, for example, in the Raizer's book [66]. Equation (16), as well as its simplified form (17), contains the factor $\nabla n_+/n_+$, which depends on the radial distribution of the positive-ion density.

To estimate this factor, Raizer assumed that the actual radial distribution of positive ions could be approximated by a straight line decreasing from its maximum value at the discharge center to zero at the tube wall of radius R. In this approximation, $\nabla n_+/n_+ \approx -1/R$.

A more realistic description of the plasma density profile often employs the zeroth-order Bessel function $n_+(r) = n_+(0)\cdot J_0(2.405\cdot r/R)$, where J_0 equals unity at the discharge axis ($r = 0$) and reaches its first root at the tube wall ($r = R$). In this case, the factor $\nabla n_+/n_+$ changes relatively weakly over most of the discharge radius, varying from zero at the axis to approximately -2 at $r = 0.8\cdot R$, and diverging rapidly to $-\infty$ only very close to the wall. Therefore, $\nabla n_+/n_+$ generally remains negative and is not directly responsible for a possible reversal of the ambipolar electric field.

However, in Eq. (16), the factor $\nabla n_+/n_+$ is multiplied by another term whose numerator may change sign depending on the parameters α, δ, γ, Z_p, and the mobility ratios of the charged species. This issue will be analyzed in more detail below. At this stage, it is sufficient to conclude that the conditions for ambipolar field reversal can be investigated using the average ambipolar field approximation with $\nabla n_+/n_+ \approx -1/R$. The average ambipolar electric field strength and the ambipolar diffusion coefficients of the charged species are important, for example, for the development of global plasma models and one-dimensional models of the positive column in dc glow discharges.

It should be noted that the calculations were performed for an acetylene plasma generated in a discharge tube with an inner radius of $R = 2.8$ cm.

The mobilities of positive and negative ions in acetylene were obtained from the analysis of experimental data reported in Ref. [78]: $\mu_+ = 1.414\cdot 10^3$ cm^2/(V·sec), $\mu_n = 1.179\cdot 10^3$ cm^2/(V·sec). The electron mobility μ_e was estimated from measured electron drift velocities in acetylene reported in Ref. [79]: $\mu_e = 2\cdot 10^5$ cm^2/(V·sec).

Let us now determine the mobility of charged nanoparticles. It can be evaluated using the expression

$$\mu_p = \frac{e\cdot Z_p}{M_p\cdot \nu_{pm}}. \tag{27}$$

As noted above, the product $e\cdot Z_p$ corresponds to the charge carried by the electrons attached to the nanoparticle. The nanoparticle collision cross section is assumed to be $\sigma = \pi\cdot a^2$ while the collision frequency between gas molecules and nanoparticles is

$$\nu_{pm} = N_{C2H2}\cdot \bar{V}_p\cdot \sigma, \tag{28}$$

where N_{C2H2} is the concentration of acetylene molecules in the discharge plasma,

$$\bar{V}_p = \left(\frac{8\cdot k\cdot T_p}{\pi\cdot M_p}\right)^{1/2}. \tag{29}$$

The nanoparticle mass can be estimated as

$$M_p = \frac{4}{3}\pi\cdot a^3\cdot \rho. \tag{30}$$

The nanoparticle material density ρ is also required. We assume that plasma polymerization processes occurring both on the chamber walls and within the plasma volume produce polymer materials (films and nanoparticles, respectively) of approximately the same density. The authors of Ref. [80] deposited polymer films from acetylene plasma and reported a density of 0.4 g/cm^{-3}, whereas Ref. [81] obtained a value of 0.6 g/cm^{-3}. Therefore, an average value of $\rho = 0.5$ g/cm^{-3} was used in the present calculations.

Substituting Eqs. (28)–(30) into Eq. (27) yields

$$\mu_p = \frac{3}{4\pi}\cdot\frac{e\cdot Z_p}{N_{C2H2}}\cdot\frac{\left(6kT_p\right)^{-1/2}}{a^{7/2}\cdot\rho^{1/2}}. \tag{31}$$

The calculated mobilities of nanoparticles of different sizes are presented in Fig. 3. Since the nanoparticle mobility μ_p is inversely proportional to $a^{7/2}$, a rapid decrease in μ_p is observed with increasing nanoparticle size.

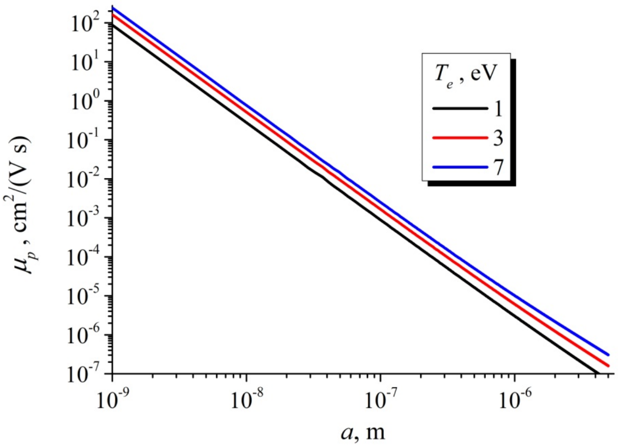

Figure 3. Dependence of nanoparticle mobility on nanoparticle radius for different electron temperatures

2. ANALYSIS OF THE AMBIPOLAR DIFFUSION COEFFICIENTS

Equations (12)–(14) for the ambipolar diffusion coefficients can be rewritten in a form more convenient for analysis:

$$D_{ae} = \frac{D_e}{\gamma}\frac{\mu_+}{\mu_e}\cdot\frac{\gamma+2\alpha\gamma+\gamma\cdot\delta\cdot Z_p+1+\delta\cdot\tau\cdot Z_p}{\left(1+\alpha+\delta\cdot Z_p\right)\cdot\left(\mu_+/\mu_e\right)+\alpha\cdot\left(\mu_n/\mu_e\right)+\delta\cdot Z_p\cdot\left(\mu_p/\mu_e\right)+1}, \tag{32}$$

$$D_{an} = \frac{D_n}{\gamma}\frac{\mu_+}{\mu_e}\cdot\frac{\gamma+2\alpha\gamma+\gamma\cdot\delta\cdot Z_p+1+\delta\cdot\tau\cdot Z_p}{\left(1+\alpha+\delta\cdot Z_p\right)\cdot\left(\mu_+/\mu_e\right)+\alpha\cdot\left(\mu_n/\mu_e\right)+\delta\cdot Z_p\cdot\left(\mu_p/\mu_e\right)+1}, \tag{33}$$

$$D_{ap} = \frac{D_p}{\gamma}\frac{\mu_+}{\mu_e}\cdot\frac{\gamma+2\alpha\gamma+\gamma\cdot\delta\cdot Z_p+1+\delta\cdot\tau\cdot Z_p}{\left(1+\alpha+\delta\cdot Z_p\right)\cdot\left(\mu_+/\mu_e\right)+\alpha\cdot\left(\mu_n/\mu_e\right)+\delta\cdot Z_p\cdot\left(\mu_p/\mu_e\right)+1}. \tag{34}$$

In Eqs. (11)–(14), all coefficients were expressed through the free diffusion coefficient of positive ions D_+. In contrast, Eqs. (32)–(34) express the ambipolar diffusion coefficients of each charged species through their own free diffusion coefficients. This representation makes it possible to analyze their behavior over a wide range of the parameters α, δ, and charged-particle temperatures.

First, let us consider a plasma containing electrons, positive ions, and negative ions, but without nanoparticles ($\delta = 0$). Using Eqs. (11), (32), and (33), the ambipolar diffusion coefficients for the charged species were calculated over a wide range of the relative negative-ion concentration α. The results are presented in Fig. 4.

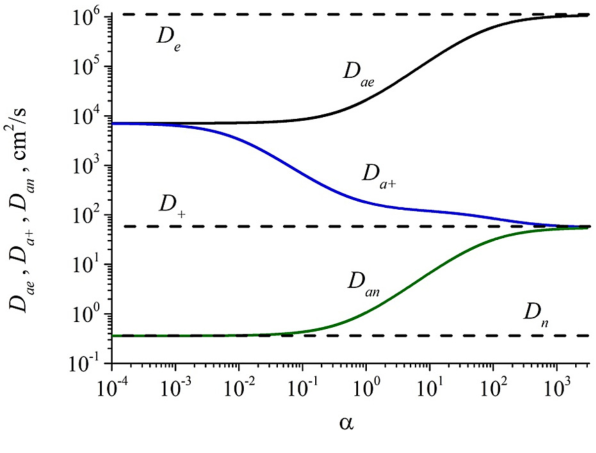

Figure 4. Dependence of the ambipolar diffusion coefficients of electrons D_{ae}, positive ions D_{a+}, and negative ions D_{an} on the relative concentration of negative ions α in the absence of nanoparticles ($\delta = 0$). Electron temperature $T_e = 5$ eV

Figure 4 shows that at very low relative concentrations of negative ions, $\alpha < 10^{-3}$, the ambipolar diffusion coefficients of electrons and positive ions coincide, $D_{ae} = D_{a+}$. In this case, the plasma effectively behaves as a two-component plasma consisting only of electrons and positive ions. For $\alpha = 0$, Eqs. (11) and (12) reduce to the classical ambipolar diffusion coefficient D_a [66–68]:

$$D_{ae} = D_{a+} \approx D_+ \frac{\gamma+1}{\left(\mu_+/\mu_e\right)+1} = \frac{D_+ \cdot \mu_e + D_e \cdot \mu_+}{\mu_e + \mu_+} = D_a \tag{35}$$

Furthermore, for small α and large $\gamma >> 1$, Eq. (33) yields $D_{an} \approx D_n \cdot (\mu_+/\mu_e) << D_n$. Thus, a small amount of negative ions added to an electron–ion plasma has almost no effect on the ambipolar diffusion process itself, while the negative ions remain effectively confined within the plasma due to their extremely small ambipolar diffusion coefficient.

However, the situation changes rapidly as the relative concentration of negative ions increases. The ambipolar diffusion coefficients of electrons D_{ae} and negative ions D_{an} increase, whereas the coefficient for positive ions D_{a+} decreases. At $\alpha > 100$, diffusion ceases to be ambipolar because $D_{ae} \to D_e$, $D_{a+} \to D_+$, $D_{an} \to D_n$. This means that charged particles of different species no longer significantly affect each other's transport. The loss of a small number of electrons from the plasma volume does not noticeably violate plasma quasineutrality; therefore, charge separation and the ambipolar electric field do not develop. Such a conclusion for strongly electronegative plasma at large α was previously reported in Ref. [47]. The present results demonstrate that the derived expressions for the ambipolar diffusion coefficients in four-component plasma, Eqs. (11) and (32)–(34), are fully consistent with previously established results for simpler plasma compositions.

Let us now consider a plasma containing electrons, positive ions, a small amount of negative ions with relative concentration $\alpha = 10^{-4}$, and charged nanoparticles. The calculated dependences of the ambipolar diffusion coefficients on the relative nanoparticle concentration δ are shown in Fig. 5a. Since the quantity of greater physical interest is not the nanoparticle concentration itself, but rather the losses of free electrons due to attachment to nanoparticles, the diffusion coefficients are also presented as functions of the product $\delta \cdot Z_p$ in Fig. 5b. For these calculations, it was determined beforehand that for an electron temperature of 5 eV and nanoparticle radius 100 nm, each nanoparticle acquires approximately $Z_p \approx 265$ electrons.

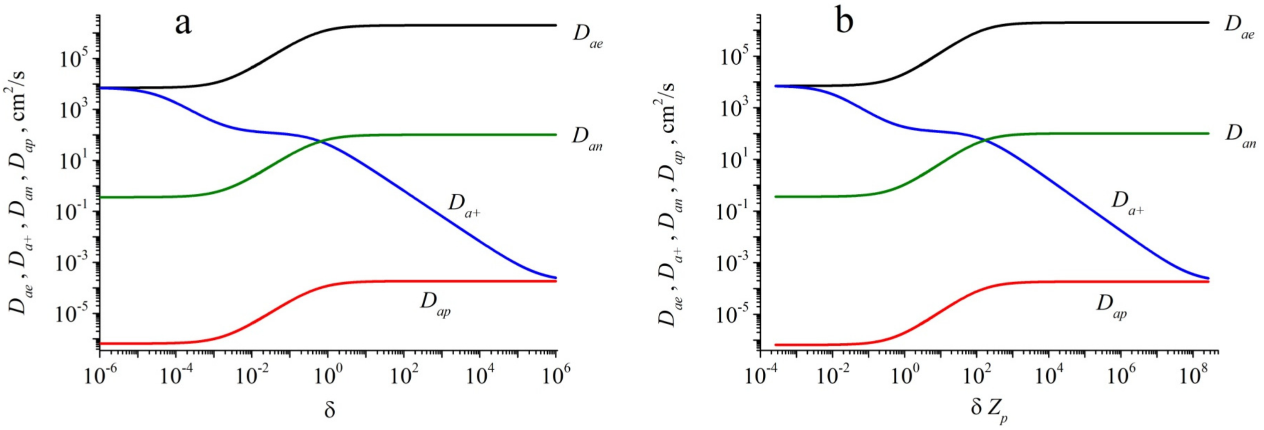

Figure 5. Dependence of the ambipolar diffusion coefficients of electrons D_{ae}, positive ions D_{a+}, negative ions D_{an}, and nanoparticles D_{ap} on the relative nanoparticle concentration δ (a) and on the product $\delta \cdot Z_p$ (b) at low relative concentration of negative ions ($\alpha = 10^{-4}$). Nanoparticle radius $a = 100$ nm, electron temperature $T_e = 5$ eV

Figure 5 indicates that the diffusion process remains essentially ambipolar, similarly to a two-component electron–ion plasma, only at very low nanoparticle concentrations, $\delta < 10^{-5}$. Under these conditions, the ambipolar diffusion coefficient of nanoparticles is extremely small, $D_{ap} \approx D_p \cdot (\mu_+/\mu_e) << D_p$. Thus, negatively charged nanoparticles, similarly to negative ions introduced in small concentration, are efficiently confined within the plasma volume by the strong ambipolar electric field.

However, with increasing δ, the ambipolar diffusion coefficients of nanoparticles, electrons, and negative ions increase rapidly and eventually approach saturation values. For $\alpha << 1$ and $\delta >> 1$, one obtains $D_{ap} \approx 2 \cdot D_p$, $D_{ae} \approx 2 \cdot D_e$, $D_{an} \approx 2 \cdot D_n$. It should be emphasized that these coefficients at $\delta >> 1$ ($\delta \cdot Z_p >> 1$) are twice as large as the corresponding free diffusion coefficients, unlike the case without nanoparticles at large $\alpha >> 1$, where the ambipolar coefficients simply approach the free-diffusion values.

In realistic discharge plasma, however, both negative ions and nanoparticles may be present simultaneously in significant concentrations. Therefore, for the limiting case $\alpha >> 1$ and $\delta \cdot Z_p >> 1$, Eqs. (32)–(34) reduce to:

$$D_{ae} = D_e \cdot \left(1 + \frac{\delta \cdot Z_p}{2\alpha + \delta \cdot Z_p}\right), \tag{36}$$

$$D_{an} = D_n \cdot \frac{2 \cdot \left(\alpha + \delta \cdot Z_p\right)}{2\alpha + \delta \cdot Z_p}, \tag{37}$$

$$D_{ap} = D_p \cdot \frac{2 \cdot (\alpha + \delta \cdot Z_p)}{2\alpha + \delta \cdot Z_p}. \tag{38}$$

From Eq. (36), it follows that for $\delta \cdot Z_p >> \alpha$, we have $D_{ae} \approx 2 \cdot D_e$, whereas for the opposite condition $\delta \cdot Z_p << \alpha$, $D_{ae} \approx D_e$. Similarly, Eqs. (37) and (38) yield $D_{an} \approx 2 \cdot D_n$ and $D_{ap} \approx 2 \cdot D_p$, for $\delta \cdot Z_p >> \alpha$, while $D_{an} \approx D_n$ та $D_{ap} \approx D_p$ for $\delta \cdot Z_p << \alpha$.

The situation is more complicated for positive ions. Figure 5 shows that with increasing nanoparticle concentration δ, the ambipolar diffusion coefficient of positive ions initially decreases and tends to approach the coefficient for negative ions, $D_{a+} \rightarrow D_{an}$ similarly to the behavior observed in Fig. 4 for plasma without nanoparticles ($\delta = 0$). However, with further increase in δ and $\delta \cdot Z_p$, the coefficient D_{a+} decreases again and eventually approaches $D_{a+} \rightarrow D_{ap}$.

Of course, the regime $D_{a+} \approx D_{ap}$ corresponds to extremely low free-electron concentrations, when the plasma effectively consists only of positive ions and negatively charged nanoparticles. Such a situation may arise, for example, in corona discharges with low discharge current and low electron density in aerosol media ("foggy plasmas"), where fine droplets capture nearly all free electrons.

Analysis of Eq. (11) under the simultaneous conditions $\alpha >> 1$ and $\delta \cdot Z_p >> 1$ gives:

$$D_{a+} = 2D_+ \cdot \frac{\alpha + \delta \cdot Z_p \cdot (\mu_p / \mu_+)}{2\alpha + \delta \cdot Z_p}, \tag{39}$$

This expression shows that for $\delta \cdot Z_p << \alpha$ one obtains $D_{a+} \approx D_+ \approx D_n$, whereas for $\delta \cdot Z_p \cdot (\mu_p/\mu_+) >> \alpha$ the limiting relation becomes $D_{a+} \approx 2 \cdot D_p$. Thus, *the ambipolar diffusion coefficient of positive ions strongly depends on which negatively charged species dominate in the plasma.* If negative ions dominate, then at sufficiently high concentrations of electronegative species (large electron losses due to attachment to gas molecules), we have $D_{a+} \rightarrow D_n$. In plasma where electron losses due to attachment to nanoparticles dominate, the asymptotic behavior becomes $D_{a+} \rightarrow 2 \cdot D_p = D_{ap}$.

This unusual behavior of positive ions can be understood rather straightforwardly. In a two-component plasma consisting only of electrons and positive ions, both species leave the plasma region (for example, toward the discharge-tube walls) with approximately equal fluxes: $\Gamma_+ \approx \Gamma_e$. If a substantial fraction of electrons attaches to molecules and forms negative ions with $\alpha >> 1$, then the loss of a small number of free electrons is no longer critical for sustaining the discharge, and the balance condition becomes $\Gamma_+ \approx \Gamma_n$. Finally, if almost all electrons attach to nanoparticles, while the concentrations of free electrons and negative ions remain relatively small, then the positive-ion flux from the plasma must compensate the extremely small flux of heavy nanoparticles: $\Gamma_+ \approx \Gamma_p$.

The calculated dependences of the ambipolar diffusion coefficients on the product $\delta \cdot Z_p$ for a high relative concentration of negative ions, $\alpha = 100$, are shown in Fig. 6. The initially high concentration of negative ions results in relatively large ambipolar diffusion coefficients for electrons, nanoparticles, and negative ions even at low nanoparticle concentrations; these coefficients are already close to their free-diffusion values. With increasing electron losses to nanoparticles $\delta \cdot Z_p$, these coefficients increase further and approach twice their free-diffusion values. In contrast, the ambipolar diffusion coefficient of positive ions is initially close to twice its free-diffusion value, but decreases rapidly with increasing $\delta \cdot Z_p$, eventually approaching the nanoparticle ambipolar diffusion coefficient.

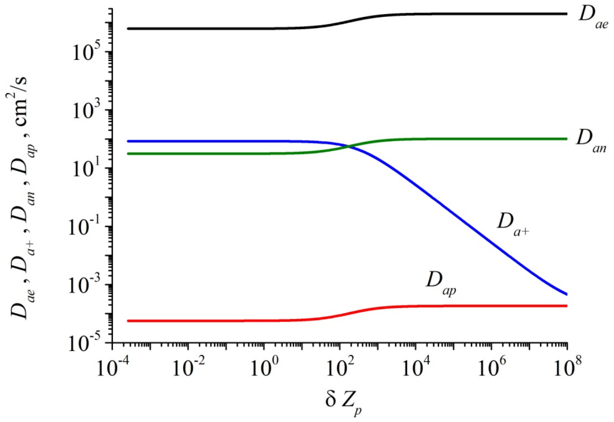

Figure 6. Dependence of the ambipolar diffusion coefficients of electrons, positive and negative ions, and nanoparticles on the product $\delta \cdot Z_p$ at relative concentration of negative ions $\alpha = 100$. Nanoparticle radius $a = 100$ nm, electron temperature $T_e = 5$ eV

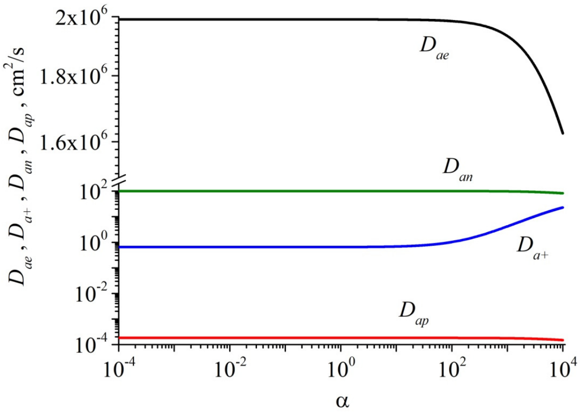

Figure 7. Dependence of the ambipolar diffusion coefficients of electrons, positive and negative ions, and nanoparticles on the relative concentration of negative ions α at $\delta = 100$. Nanoparticle radius $a = 100$ nm, electron temperature $T_e = 5$ eV

Finally, let us consider the case of plasma with a high relative concentration of nanoparticles ($\delta = 100$). The corresponding results are presented in Fig.7. At low negative-ion concentrations, the electron ambipolar diffusion coefficient D_{ae} is approximately equal to twice the free electron diffusion coefficient. However, at $\alpha > 100$, D_{ae}

decreases and approaches the free electron diffusion coefficient. The ambipolar diffusion coefficients of nanoparticles and negative ions behave similarly, decreasing from twice their free-diffusion values toward the corresponding free-diffusion coefficients. The behavior of the positive-ion ambipolar diffusion coefficient again appears unusual: initially small, it increases at $\alpha > 100$ and eventually approaches the free diffusion coefficient at very large α.

Therefore, the ambipolar diffusion process in four-component plasma is highly complex and strongly depends on the relative importance of free-electron losses due to attachment either to nanoparticles or to electronegative gas molecules forming stable negative ions. The dominant electron-loss mechanism ultimately determines the ambipolar diffusion coefficients of all charged species present in the plasma.

3. AMBIPOLAR ELECTRIC FIELD

As noted above, we are primarily interested in the average value of the ambipolar electric field strength over the discharge-tube radius. It is this field that controls the confinement of negatively charged ions and nanoparticles within the plasma volume. Therefore, we calculated its magnitude for different plasma conditions and nanoparticle sizes.

The calculated results will be compared with those for a conventional two-component plasma consisting only of electrons and positive ions. The corresponding ambipolar electric field strength E_{Amb} obtained from Eq. (17) will hereafter be referred to as the “classical” ambipolar field. For an electron temperature of 5 eV, its value is shown in Fig. 8 and is approximately equal to 1.77 V/cm. Naturally, this field does not depend on the nanoparticle radius, since Eq. (17) does not account for the possible presence of nanoparticles in plasma.

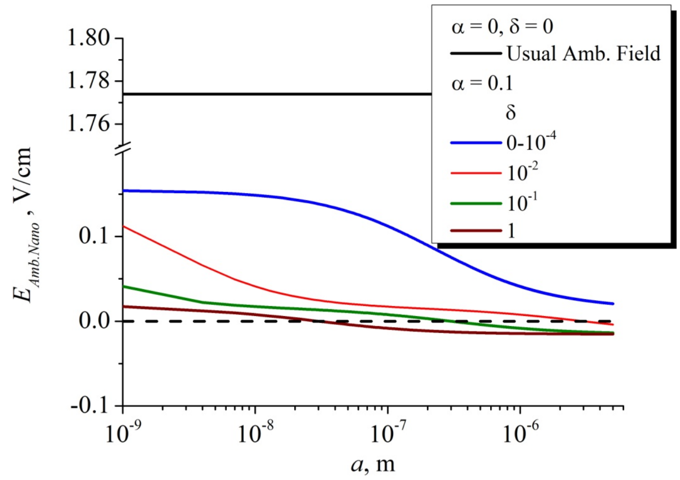

Figure 8. Dependence of the average ambipolar electric field on nanoparticle radius at $\alpha = 0.1$ for different values of the relative nanoparticle concentration δ. Electron temperature $T_e = 5$ eB

Let us now consider plasma additionally containing negative ions with a relatively low concentration $\alpha = 0.1$. This means that approximately 10% of the electrons have attached to gas molecules and formed negative ions. However, even such comparatively moderate electron losses lead to a substantial, nearly tenfold reduction in the ambipolar electric field strength (the blue curve in Fig. 8 at small nanoparticle radii). If nanoparticles are additionally introduced into the plasma and their size increases, the ambipolar electric field strength rapidly decreases and approaches zero.

Let us further increase the nanoparticle concentration in plasma. As the relative nanoparticle concentration δ increases, volumetric polymerization processes also lead to an increase in nanoparticle radius. Figure 8 shows that at sufficiently high nanoparticle concentration and sufficiently large nanoparticle size, the ambipolar electric field reaches zero and may even reverse its sign. The larger the relative nanoparticle concentration δ, the smaller the nanoparticle radius at which this sign reversal occurs.

Let us examine the behavior of the ambipolar electric field under different conditions. Figure 9 presents its dependence on the relative concentration α for different values of δ. If nanoparticles are absent from plasma ($\delta = 0$) and negative ions are present only in very small amounts ($\alpha \leq 10^{-4}$), the ambipolar field strength remains close to its “classical” value given by Eq. (17). Increasing α results in a gradual decrease in the ambipolar field strength, and at $\alpha \approx 850$ the field reaches zero and subsequently reverses its sign as the negative-ion concentration increases further.

In the presence of nanoparticles (the curves in Fig. 9 corresponding to $\delta = 10^{-4}$, 10^{-2} and 1), increasing their concentration substantially reduces the ambipolar electric field strength. In fact, negative ions and charged nanoparticles jointly affect the field magnitude. The ambipolar field again reaches zero at sufficiently high α and then changes sign. Moreover, the higher the relative nanoparticle concentration δ, the smaller the value of α at which this occurs. For example, at $\delta = 10^{-2}$ and $\delta = 1$, the sign reversal of the ambipolar field occurs at $\alpha = 826$ and $\alpha = 796$, respectively. If the nanoparticle concentration becomes very high, for example $\delta = 100$, the ambipolar electric field remains negative over the entire α range, and the corresponding curve in Fig. 9 lies entirely below zero.

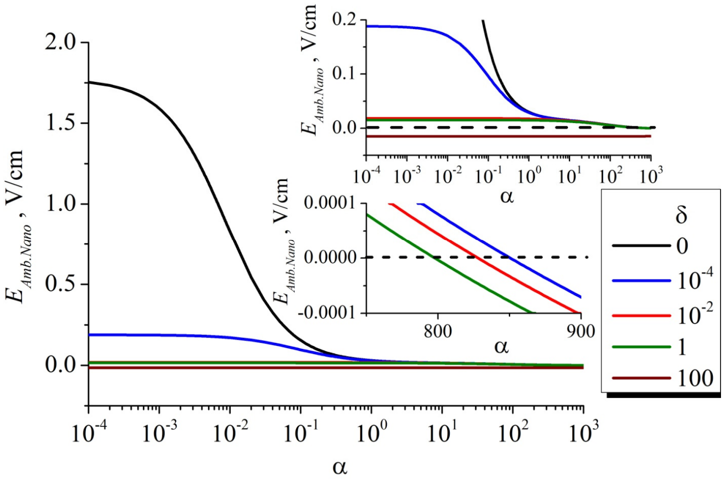

Figure 9. Dependence of the average ambipolar electric field on α for different values of the relative nanoparticle concentration δ and nanoparticle radius a = 100 nm, T_e = 5 eV

It is also instructive to consider the dependence of the average ambipolar electric field strength on the product $\delta{\cdot}Z_p$ rather than only on the relative nanoparticle concentration δ (see Fig. 10). Since for nanoparticle radius a = 100 nm and electron temperature 5 eV, one has $Z_p \approx 265$, replacing δ with $\delta{\cdot}Z_p$ shifts the corresponding ambipolar-field curves toward larger values along the horizontal axis.

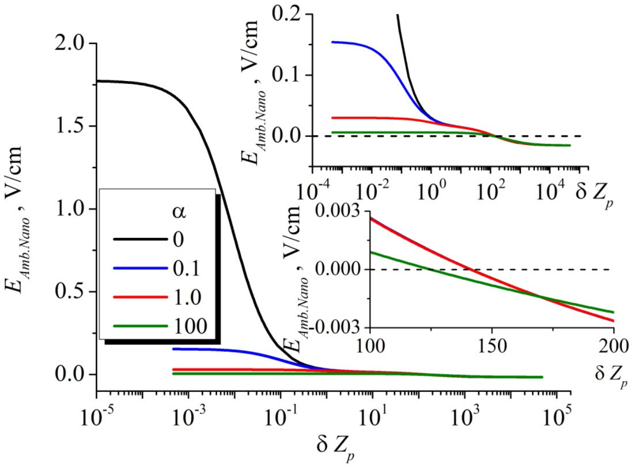

Figure 10. Dependence of the average ambipolar electric field on the product $\delta{\cdot}Z_p$ for different values of the relative negative-ion concentration α and nanoparticle radius a = 100 nm, T_e = 5 eV

Similarly to the previous case, the ambipolar electric field decreases with increasing both the relative concentration of negative ions α and the normalized number of electrons attached to nanoparticles $\delta{\cdot}Z_p$. At $\alpha \leq 1$, the curves corresponding to different α practically coincide for $\delta{\cdot}Z_p \geq 10$, and the ambipolar field reaches zero at approximately the same value, $\delta{\cdot}Z_p \approx 141$. However, at higher α the sign reversal occurs earlier. For example, at $\alpha = 100$ the ambipolar field changes sign already at $\delta{\cdot}Z_p \approx 123$.

The reversal of the ambipolar electric field at sufficiently high concentrations of nanoparticles and negative ions indicates the appearance of conditions for the removal of their excess from plasma. In real gas-discharge plasma, the ambipolar electric field strength will likely remain close to zero or slightly negative. If an excessive number of nanoparticles and negative ions is produced, the ambipolar field will drive their excess toward the discharge-tube walls, after which the field will again approach zero. The stationary state corresponds to a zero ambipolar electric field, while the nanoparticle concentration reaches saturation.

Thus, if a sufficiently dense nanoparticle cloud is present in plasma, the ambipolar electric field inside this cloud may become nearly zero. As shown above, at high nanoparticle concentrations the ambipolar diffusion coefficients of electrons, negatively charged ions, and nanoparticles approach twice their free-diffusion values. In three-component plasma (electrons, positive ions, and negative ions), ambipolar diffusion effectively transformed into free diffusion for all charged species. However, after introducing nanoparticles into plasma, the diffusion losses of negatively charged species become additionally enhanced by a factor of two owing to their removal from the plasma volume by the electric field after it reverses its sign.

To determine the conditions for ambipolar-field sign reversal in more detail, let us analyze Eq. (16). Its denominator is a combination of positive quantities. However, the numerator contains a factor in square brackets that may become zero under the condition given by Eq. (40).

$$\left(1+\alpha\cdot\gamma+\delta\cdot\gamma\cdot Z_p\right)\cdot\left(\mu_+/\mu_e\right)-\alpha\cdot\gamma\cdot\left(\mu_n/\mu_e\right)-\delta\cdot Z_p\cdot\gamma\cdot\left(\mu_p/\mu_e\right)-\gamma=0\,. \tag{40}$$

Equation (40) can be rewritten in the following form:

$$\delta\cdot Z_p=\frac{\mu_e}{\mu_+-\mu_p}\cdot\left[1-\frac{1}{\gamma}\cdot\frac{\mu_+}{\mu_e}+\alpha\cdot\left(\frac{\mu_n}{\mu_e}-\frac{\mu_+}{\mu_e}\right)\right]. \tag{41}$$

From Eq. (41), it follows that the value of $\delta\cdot Z_p$ at which the ambipolar electric field changes sign depends only weakly on the electron temperature. Since $\gamma = T_e/T_+ >> 1$ and simultaneously $\mu_+/\mu_e << 1$, the second term inside the square brackets in Eq. (41) may be neglected. Calculations show (see Fig. 11) that the dependences of $\delta\cdot Z_p$ on α for different electron temperatures (from 1 eV to 10 eV) practically coincide for nanoparticle radius $a = 100$ nm. Since the calculations were performed for acetylene plasma, where the mobility of negative ions is lower than that of positive ions ($\mu_+ = 1414$ cm^2/(V·s), $\mu_n = 1179$ cm^2/(V·s)), the dependence in Fig. 11 decreases approximately linearly with increasing α.

However, some dependence on electron temperature appears for very small nanoparticles. Figure 11 shows that the curves corresponding to nanoparticle radius $a = 1$ nm and electron temperatures 1 eV and 5 eV differ substantially from each other. In Fig.3, we presented the calculated nanoparticle mobility μ_p, which decreases rapidly with increasing nanoparticle size. At the same time, increasing electron temperature leads to an increase in μ_p. The mobility of small nanoparticles with radii of the order of several nanometers may reach 100–200 cm^2/(V·s), corresponding to 10–20% of the positive-ion mobility. Therefore, the denominator of the factor preceding the square brackets in Eq. (41) may vary significantly in this case.

Therefore, in Fig.12 the values of $\delta\cdot Z_p$ corresponding to ambipolar-field sign reversal remain nearly constant over a wide range of nanoparticle radii at fixed α, but increase noticeably for radii $a < 5$ nm. Figure 12 also demonstrates that $\delta\cdot Z_p$ decreases with increasing relative concentration of negative ions α, as already discussed above.

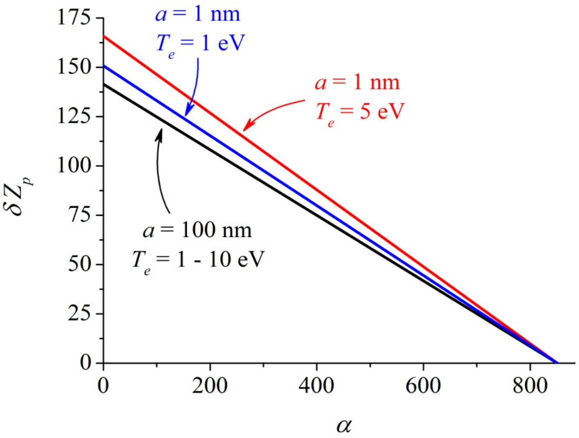

Figure 11. Dependence of the product $\delta\cdot Z_p$, at which the ambipolar electric field reaches zero, on the relative concentration of negative ions α for nanoparticle radii $a = 1$ nm and $a = 100$ nm at different electron temperatures

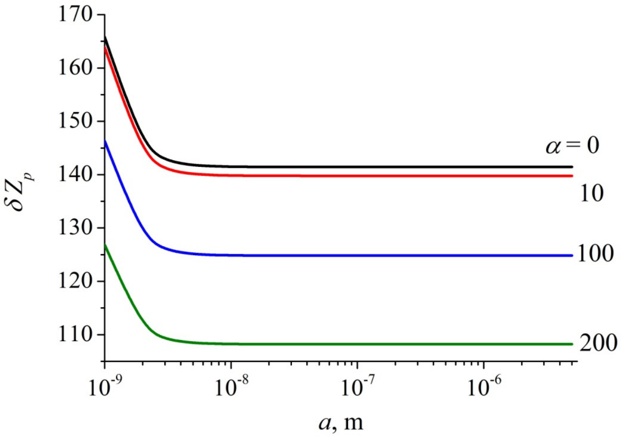

Figure 12. Dependence of the values of $\delta\cdot Z_p$ corresponding to zero ambipolar electric field on nanoparticle radius for different values of the relative negative-ion concentration α at electron temperature 5 eV

If the relative concentration of negative ions is fixed at $\alpha = 100$, then for nanoparticles with radii $a > 10$ nm the calculated values of $\delta\cdot Z_p$ corresponding to different electron temperatures coincide with each other. However, for smaller nanoparticles with radii $a < 10$ nm, the curves corresponding to different electron temperatures diverge strongly. This means that in plasma containing very small nanoparticles with radii $a \approx 1$ nm and hot electrons, a larger relative nanoparticle concentration δ is required for ambipolar-field sign reversal than in plasma containing larger nanoparticles.

Calculations show that nanoparticles with radius 1 nm collect $Z_p = 1$ and $Z_p = 3$ electrons at electron temperatures of 1 eV and 7 eV, respectively. As follows from Fig. 13, sign reversal of the ambipolar field for such 1 nm particles requires $\delta = 133$ at $T_e = 1$ eV and $\delta = 150/3 = 50$ at $T_e = 7$ eV. For large nanoparticles, for example with $a = 100$ nm, one has $Z_p \approx 265$ and $\delta\cdot Z_p \approx 125$. Therefore, the corresponding relative concentration of such large nanoparticles is much smaller, $\delta = 125/265 \approx 0{,}47$. This means that approximately one nanoparticle with $a = 100$ nm is required per two free electrons for the ambipolar electric field strength to reach zero and potentially reverse its sign.

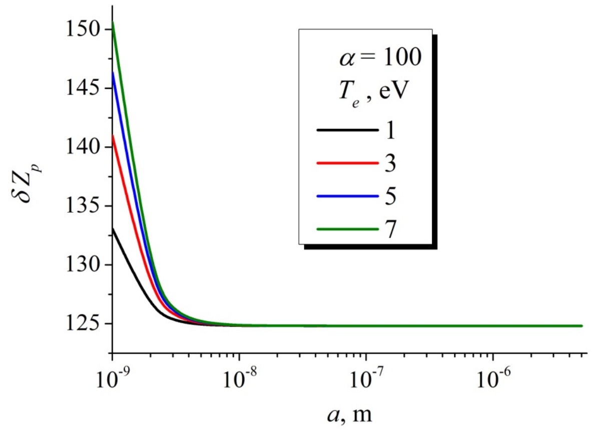

Figure 13. Dependence of the values of δZ_p corresponding to zero ambipolar electric field on nanoparticle radius at relative concentration of negative ions $\alpha = 100$ for different electron temperatures

IV. Experimental Verification

Direct experimental measurements of the radial ambipolar electric field strength in acetylene plasma using Langmuir probes and wall probes are difficult because their surfaces are rapidly covered by dielectric polymer films. In addition, the gas pressure and plasma parameters also vary with time [58,64].

However, there exists a pronounced phenomenon confirming the possibility of ambipolar-field sign reversal. Let us consider the conditions of our experiments.

The experiments were performed in a quartz discharge tube with an inner diameter of 80 mm, in the acetylene pressure range of 0.05–1 Torr, while the maximum acetylene flow rate reached 5 sccm. The distance between the flat steel electrodes was 76.2 mm. The electrodes were positioned vertically inside the tube, whereas the discharge tube itself was oriented horizontally. A DC or 20 kHz AC voltage was applied to the powered electrode (cathode).

When the electrodes are arranged horizontally inside a discharge tube or chamber, nanoparticles introduced into plasma from an external source or formed in the discharge due to volumetric polymerization are trapped near the boundary of the cathode sheath or electrode sheath by the strong electric field in these discharge regions. In contrast, the vertical arrangement of the electrodes made it possible to reveal the influence of the ambipolar electric field on nanoparticle confinement.

Here, we will not focus on the specific discharge regions where the nanoparticle cloud is formed or on the methods used for its detection. For the present discussion, it is sufficient to note the experimental observation that during discharge operation the tube walls become coated with a certain substance of particular interest. This substance appears after several tens of seconds of discharge operation in acetylene. Such behavior was observed both in dc discharges and in pulsed and high-frequency capacitive discharges. Photographs of the discharge tube with this deposited coating are shown in Figs. 14 and 15. During the discharge operation, the cathode was on the left and the anode on the right.

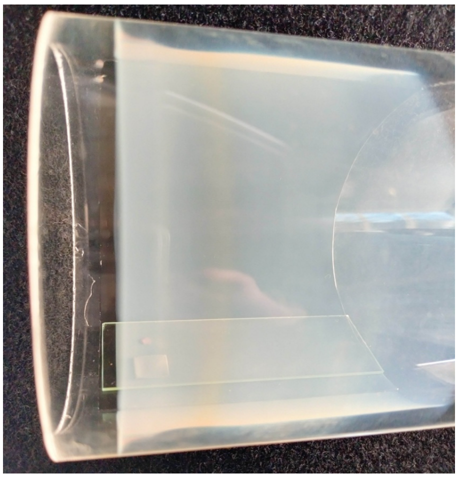

Figure 14. Photograph of the discharge tube with a deposited layer of polymer film containing nanoparticles. DC discharge. Acetylene pressure 0.5 Torr. Voltage between electrodes 1000 V, discharge current 14 mA. Film deposition time 1 min

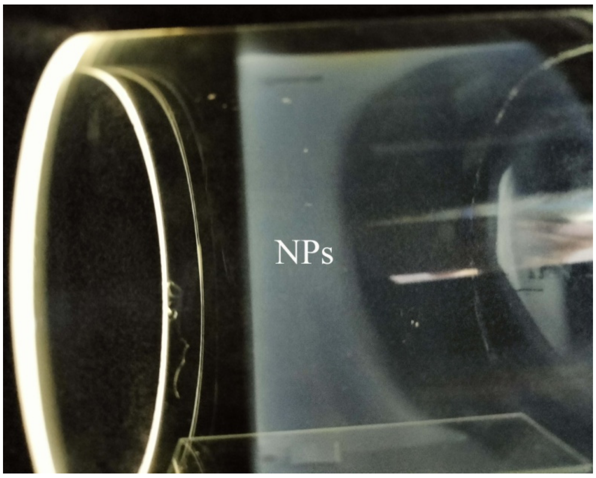

Figure 15. Photograph of the discharge tube with a deposited layer of polymer film containing nanoparticles (NPs). Bipolar pulsed discharge with frequency 20 kHz and duty cycle 50%. Acetylene pressure 0.14 Torr. Peak-to-peak voltage between electrodes 1419 V. Film deposition time 1 min

Near the cathode or powered electrode of the pulsed discharge, the cathode sheath or electrode sheath is formed, and the large voltage drop across this region expels negatively charged nanoparticles into the plasma volume. Therefore, only a thin polymer film can be deposited there. In the negative glow region, by contrast, the inner surface of the tube becomes covered with a layer of material that becomes opaque as its thickness increases.

Samples of this material were deposited onto grids for transmission electron microscopy (TEM) in a Selmi REM-125 K. The grids were positioned both at the bottom of the tube and in its upper part. Figure 16 shows a TEM image of the surface of a grid placed in the upper part of the discharge tube, recorded at a magnification of 25,000×. It can be seen that a polymer film containing a large number of embedded nanoparticles with diameters of 10–20 nm was deposited on the grid.

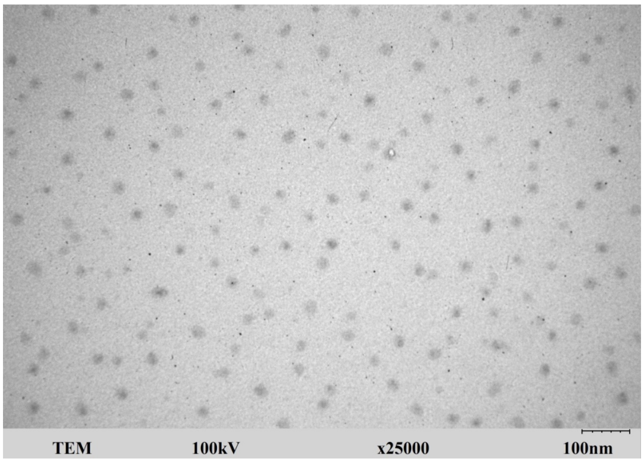

Figure 16. TEM image of the polymer film and embedded nanoparticles deposited onto the upper part of the tube from a dc discharge at acetylene pressure 0.15 Torr and deposition time 30 s. Voltage between electrodes 471 V, discharge current 1 mA

These nanoparticles were formed not on the surface itself, but inside the plasma volume. Free electrons attach to them, charging them negatively. Under ordinary conditions, the ambipolar electric field arises when a fraction of energetic free electrons escapes from plasma to the tube wall, charging it negatively. The resulting field subsequently attracts positive ions toward the wall and repels colder electrons and negatively charged nanoparticles back into the plasma volume. The Coulomb force prevents such nanoparticles from settling onto the bottom of the tube and acts against gravity. For the upper part of the tube, the same Coulomb force, together with gravity, should instead drive negatively charged nanoparticles back toward the plasma volume. Nevertheless, small nanoparticles were found embedded inside the polymer film deposited on the upper part of the tube, meaning that they must have moved against both gravitational and Coulomb forces.

However, the analytical calculations presented above demonstrated that nanoparticle accumulation in plasma leads to a substantial reduction of the ambipolar electric field strength. When the nanoparticle concentration reaches a critical value (more precisely, when the number of electrons attached to nanoparticles per unit plasma volume becomes sufficiently high), the ambipolar field reaches zero and may reverse its sign. In this case, the field begins to confine positive ions within the plasma while expelling excess negatively charged nanoparticles and negative ions from it. This mechanism is responsible for the radial ejection of nanoparticles from the plasma in all directions, including upward. It should be noted that the ion drag force, which is commonly taken into account when analyzing nanoparticle transport in plasma, is not expected to play a significant role in the present case, because the radial ambipolar electric field approaches zero and therefore does not provide substantial acceleration of positive ions.

CONCLUSIONS

In this work, the process of ambipolar diffusion in a four-component plasma consisting of electrons, positive ions, negative ions, and negatively charged nanoparticles has been investigated. An analytical model was developed based on the conditions of plasma quasineutrality and zero total current of all charged species to the discharge-tube wall. As a result, simple analytical expressions were obtained for the ambipolar diffusion coefficients of each charged species, as well as for the ambipolar electric field strength.

The derived expressions were analyzed over wide ranges of the relative concentrations of negative ions α, nanoparticles δ, the normalized concentration of electrons attached to nanoparticles $\delta \cdot Z_p$, and electron temperature. It was shown that in plasma consisting of electrons, positive ions, and negative ions, the ambipolar diffusion regime gradually transforms into free diffusion at high relative concentrations of negative ions α. In this limit, the ambipolar diffusion coefficient of electrons approaches the free electron diffusion coefficient, while the ambipolar diffusion coefficients of positive and negative ions approach their corresponding free diffusion coefficients, which are close to each other.

In plasma containing electrons, positive ions, and negatively charged nanoparticles, high nanoparticle concentrations lead to qualitatively different behavior. In this case, the ambipolar diffusion coefficient of electrons approaches twice the free electron diffusion coefficient, whereas the diffusion flux of positive ions compensates mainly the ambipolar losses of nanoparticles. For the general four-component plasma, the behavior of the ambipolar diffusion coefficients is governed by the dominant electron-loss mechanism, namely electron attachment either to electronegative gas molecules or to nanoparticles. If electron attachment to gas molecules dominates, the ambipolar diffusion coefficients of electrons, negative ions, and nanoparticles remain close to their free diffusion coefficients. In contrast, when electron losses to nanoparticles dominate, these coefficients approach twice the corresponding free diffusion coefficients.

The behavior of the ambipolar diffusion coefficient for positive ions was found to be particularly unusual and strongly dependent on the dominant negatively charged species in the plasma. It approaches the free diffusion coefficient of negative ions under conditions of intensive negative-ion formation, whereas in a plasma dominated by electron attachment to nanoparticles, it approaches twice the free diffusion coefficient of nanoparticles.

It was further demonstrated that the accumulation of negative ions and/or negatively charged nanoparticles substantially reduces the ambipolar electric field strength. Under critical conditions, the ambipolar electric field may reach zero and even reverse its sign. A stationary plasma state corresponds to a nearly zero or slightly negative ambipolar field, which can remove excess negative ions and nanoparticles from the plasma volume.

Experimental observations performed in acetylene plasma demonstrated intensive radial removal of small nanoparticles from the plasma volume, including toward the upper part of the discharge tube against gravity. This behavior may serve as indirect evidence of ambipolar electric field reversal caused by high concentrations of negative ions and charged nanoparticles.

ORCID

V. Lisovskiy, https://orcid.org/0000-0002-6339-4516; **S. Dudin,** https://orcid.org/0000-0001-9161-4654;
S. Bogatyrenko, https://orcid.org/0000-0002-6044-6886; **S. Rezunenko,** https://orcid.org/0009-0001-5871-495X
V. Yegorenkov, https://orcid.org/0000-0002-7252-3711

REFERENCES

[1] A. Fridman, and G. Friedman, *Plasma Medicine*, (John Wiley, Chichester. 2013).
[2] M. Domonkos, P. Tichá, J. Trejbal, and P. Demo, Appl. Sci. **11**, 4809 (2021). https://doi.org/10.3390/app11114809
[3] C. E. Luchian, C. Lungoci, M.-A. Ciolan, C.-M. Rimbu, L. D. Miron, and I. Motrescu, Appl. Sci. **15**, 10366 (2025). https://doi.org/10.3390/app151910366
[4] P. Attri, K. Ishikawa, T. Okumura, K. Koga, and M. Shiratani, Processes **8**, 1002 (2020). https://doi.org/10.3390/pr8081002
[5] N. Puač, M. Gherardi, and M. Shiratani, Plasma Processes and Polymers, **15**, 1700174 (2018). https://doi.org/10.1002/ppap.201700174
[6] N.N. Misra, Oliver Schlüter, and P.J. Cullen, editors, *Cold Plasma in Food and Agriculture: Fundamentals and Applications*, (Academic Press, London, 2016). https://doi.org/10.1016/C2014-0-00009-3
[7] W. Schottky, Physikalische Zeitschrift **25**, 342 (1924).
[8] W. Schottky, and J. Issendorff, Zeitschrift für Physik **31**, 163 (1925). https://doi.org/10.1007/BF02980570
[9] V. Lisovskiy, S. Dudin, and V. Yegorenkov, Phys. Scr. **98**, 106101 (2023). https://doi.org/10.1088/1402-4896/acf89c
[10] V. Lisovskiy, J.-P. Booth, J. Jolly, S. Martins, K. Landry, D. Douai, V. Cassagne, and V. Yegorenkov, J. Phys. D: Appl. Phys. **40**, 6989 (2007). https://doi.org/10.1088/0022-3727/40/22/020
[11] N. R. Behera, A. K. Kanakati, S. Barik, S. Dutta, and G. Aravind, J. Chem. Phys. **163**, 024322 (2025). https://doi.org/10.1063/5.0278243
[12] B. Naik, Sh. Sharma, R. Narayanan, D. Sahu, M. Bandyopadhyay, A. Chakraborty, M. Singh, R. D. Tarey, and A. Ganguli, J. Instrumentation, **20**, C09003 (2025). https://doi.org/10.1088/1748-0221/20/09/C09003
[13] Z. E. Ankouri, M. El Bojaddaini, M. E. Kaouini, A. Missaoui, and H. Chatei, Contributions to Plasma Physics, **65**, e70058 (2025). https://doi.org/10.1002/ctpp.70058
[14] A. Paul, S. Melanson, T. Junginger, and M. Dehnel, J. Phys. Confer. Series, **2743**, 012083 (2024). https://doi.org/10.1088/1742-6596/2743/1/012083
[15] A. Paul, S. Melanson, T. Junginger, and M. Dehnel, J. Instrumentation, **19**, C05053 (2024). https://doi.org/10.1088/1748-0221/19/05/C05053
[16] I. Sereda, Y. Hrechko, M. Azarenkov, and K. Sereda, Intern. J. Hydrogen Energy, **109**, 1321 (2025). https://doi.org/10.1016/j.ijhydene.2025.02.222
[17] I. Sereda, Y. Hrechko, and M. Azarenkov, Phys. Plasmas, **31**, 053516 (2024). https://doi.org/10.1063/5.0202579
[18] I. Sereda, Y. Hrechko, I. Babenko, and M. Azarenkov, Vacuum, **200**, 111006 (2022). https://doi.org/10.1016/j.vacuum.2022.111006
[19] C. Poggi, A. Pimazzoni, E. Sartori, and G. Serianni, Nuclear Fusion, **65**, 026064 (2025). https://doi.org/10.1088/1741-4326/adabf9
[20] M. Bacal, editor, *Physics and Applications of Hydrogen Negative Ion Sources* (Springer, Cham, Switzerland, 2023). https://doi.org/10.1007/978-3-031-21476-9
[21] V. Dudnikov, *Development and Applications of Negative Ion Sources*, (Springer, Cham, Switzerland, 2023). https://doi.org/10.1007/978-3-031-28408-3
[22] V. Lisovskiy, S. Dudin, A. Shakhnazarian, P. Platonov, and V. Yegorenkov, East European Journal of Physics, (3), 172 (2024). https://doi.org/10.26565/2312-4334-2024-3-17
[23] S. V. Dudin, S. D. Yakovin, and A. V. Zykov, East European Journal of Physics **3**, 606 (2023). https://doi.org/10.26565/2312-4334-2023-3-72
[24] V. O. Litvinov, I. I. Okseniuk, D. I. Shevchenko, and V. V. Bobkov, East European Journal of Physics **3**, 10 (2023). https://doi.org/10.26565/2312-4334-2023-3-01

[25] M. Jiménez-Redondo, I. Tanarro, and V.J. Herrero, Plasma Sources Sci. Technol. **31**, 065003 (2022). https://doi.org/10.1088/1361-6595/ac70f8
[26] T. Wang, Sh. Rauf, N. Friedrichs, I. Korolov, J. Kenney, and J. Schulze, Phys. Plasmas, **33**, 023501 (2026). https://doi.org/10.1063/5.0300388
[27] I. Tanarro, R. J. Peláez, and V. J. Herrero, Plasma Physics and Controlled Fusion, **67**, 035014 (2025). https://doi.org/10.1088/1361-6587/adb17b
[28] K. Kalita, R. Moulick, and B. Saikia, Phys. Plasmas, **32**, 62105 (2025). https://doi.org/10.1063/5.0267438
[29] V. Lisovskiy, J.-P. Booth, K. Landry, D. Douai, V. Cassagne, and V. Yegorenkov, J. Phys. D: Appl. Phys. **40**, 6631 (2007). https://doi.org/10.1088/0022-3727/40/21/023
[30] V. Lisovskiy, J.-P. Booth, K. Landry, D. Douai, V. Cassagne, and V. Yegorenkov, Plasma Sources Sci. Technol. **17**, 025002 (2008). https://doi.org/10.1088/0963-0252/17/2/025002
[31] E. Baratte, L. Kuijpers, T. Silva, V. Guerra, M. C. M. van de Sanden, J.-P. Booth, and O. Guaitella, Plasma Sources Sci. Technol. **35**, 015009 (2026). https://doi.org/10.1088/1361-6595/ae24a9
[32] P. Viegas, B. Berdugo, and V. Guerra. Plasma Chemistry and Plasma Processing, **46**, 22 (2026). https://doi.org/10.1007/s11090-025-10607-7
[33] R. Masheyeva, M. Vass, M. Myrzaly, Ch.-B. Tian, K. Dzhumagulova, J. Schulze, Z. Donkó, and P. Hartmann, Plasma Sources Sci. Technol. **34**, 045017 (2025). https://doi.org/10.1088/1361-6595/adcb6b
[34] V.A. Lisovskiy, and V.D. Yegorenkov, Vacuum, **80**, 458 (2006). https://doi.org/10.1016/j.vacuum.2005.07.038
[35] Bh. Ramkorun, G. Chandrasekhar, V. Rangari, S. C. Thakur, R. B Comes, and E. Thomas, Plasma Sources Sci. Technol. **33,** 115004 (2024). https://doi.org/10.1088/1361-6595/ad8ae8
[36] J. Niemann, V. Schneider, and H. Kersten, Phys. Plasmas, **32**, 013510 (2025). https://doi.org/10.1063/5.0243765
[37] L. Vogelhuber, I. Korolov, M. Vass, K. Nösges, T. Bolles, K. Köhn, M. Klich, R. P. Brinkmann, and T. Mussenbrock, Plasma Sources Sci. Technol. **34**, 125012 (2025). https://doi.org/10.1088/1361-6595/ae253e
[38] D. Yang, X. Wang, Zh. Zhou, H. Li, W. Zhang, Y. Liu, J. Schulze, P. Hartmann, Z. Donkó, and Y. Fu, Appl. Phys. Letters, **127**, 124101 (2025). https://doi.org/10.1063/5.0281351
[39] B. Mahdavipour and J. T. Gudmundsson, Plasma Sources Sci. Technol. **34**, 045005 (2025). https://doi.org/10.1088/1361-6595/adc503
[40] R. Masheyeva, M. Vass, X.-K. Wang, Y.-X. Liu, A. Derzsi, P. Hartmann, J. Schulze, and Z. Donkó, Plasma Sources Sci. Technol. **33**, 045019 (2024). https://doi.org/10.1088/1361-6595/ad3c69
[41] X.-K. Wang, I. Korolov, S. Wilczek, R. Masheyeva, Y.-X. Liu, Y.-H. Song, P. Hartmann, Z. Donkó, and J. Schulze, Plasma Sources Sci. Technol. **33**, 085001 (2024). https://doi.org/10.1088/1361-6595/ad5eb9
[42] J. B. Thompson, Proc. Phys. Soc. **73**, 818 (1959). https://doi.org/10.1088/0370-1328/73/5/416
[43] A. J. Lichtenberg, V. Vahedi, M. A. Lieberman, and T. Rognlien, J. Appl. Phys. **75**, 2339 (1994). http://dx.doi.org/10.1063/1.356252
[44] E. Stoffels, W. W. Stoffels, D. Vender, M. Haverlag, G. M. W. Kroesen, F de Hoog, J. Contrib. Plasma Phys. **35**, 331 (1995). https://doi.org/10.1002/ctpp.2150350404
[45] Y. T. Lee, M. A. Lieberman, A. J. Lichtenberg, F. Bose, H. Baltes, R. Patrick, J. Vac. Sci. Technol. A, **15**, 113 (1997). https://doi.org/10.1116/1.580452
[46] S. Kim, M. A. Lieberman, A. J. Lichtenberg, and J. T. Gudmundsson, J. Vac. Sci. Technol. A **24**, 2025 (2006). http://dx.doi.org/10.1116/1.2345645
[47] V. Lisovskiy, and V. Yegorenkov, Europhysics Letters, **99**, 35002 (2012). https://doi.org/10.1209/0295-5075/99/35002
[48] C. Dominique, and C. Arnas, J. Appl. Phys. **101**, 123304 (2007). https://doi.org/10.1063/1.2748365
[49] C. Arnas, A. Mouberi, K. Hassouni, A. Michau, G. Lombardi, X. Bonnin, F. Bénédic, and B. Pégourié, J. Nuclear Materials, **390-391**, 140 (2009). https://doi.org/10.1016/j.jnucmat.2009.01.148
[50] K.K. Kumar, L. Couëdel, and C. Arnas, Phys. Plasmas, **20**, 043707 (2013). https://doi.org/10.1063/1.4802809
[51] L. Couëdel, K. Kishor Kumar, and C. Arnas, Phys. Plasmas, **21**, 123703 (2014). https://doi.org/10.1063/1.4903465
[52] S. Barbosa, F. R. A. Onofri, L. Couëdel, M. Wozniak, C. Montet, C. Pelcé, C. Arnas, L. Boufendi, E. Kovacevic, J. Berndt, and C. Grisolia, J. Plasma Phys. **82**, 615820403 (2016). https://doi.org/10.1017/S0022377816000714
[53] C. Arnas, A. Michau, G. Lombardi, L. Couëdel, and K. Kishor Kumar, Phys. Plasmas **20**, 013705 (2013). https://doi.org/10.1063/1.4776681
[54] L. Worner, E. Kovacevic, J. Berndt, H. M. Thomas, M. H. Thoma, L. Boufendi, and G. E. Morfill, New Journal of Physics, **14**, 023024 (2012). https://doi.org/10.1088/1367-2630/14/2/023024
[55] J. Beckers, J. Berndt, D. Block, M. Bonitz, P. J. Bruggeman, L. Couëdel, G. L. Delzanno, *et al.* Phys. Plasmas, **30**, 120601 (2023). https://doi.org/10.1063/5.0168088
[56] E. Kovacevic, J. Berndt, Th. Strunskus, and L. Boufendi, J. Appl. Phys. **112**, 013303 (2012). https://doi.org/10.1063/1.4731751
[57] E. Kovačević, J. Berndt, I. Stefanović, H.-W. Becker, C. Godde, Th. Strunskus, J. Winter, and L. Boufendi, J. Appl. Phys. **105**, 104910 (2009). http://dx.doi.org/10.1063/1.3129318
[58] V. A. Lisovskiy, S. V. Dudin, P. P. Platonov, S. I. Bogatyrenko, and A. A. Minenkov, Probl. At. Sci. Technol. **4**, 135 (2019), https://vant.kipt.kharkov.ua/ARTICLE/VANT_2019_4/article_2019_4_135.pdf
[59] M. Mikikian, L. Couedel, M. Cavarroc, Y. Tessier, and L. Boufendi, Eur. Phys. J. Appl. Phys. **49**, 13106 (2010). https://doi.org/10.1051/epjap/2009191
[60] M. Mikikian, S. Labidi, E. von Wahl, J. F. Lagrange, T. Lecas, V. Massereau-Guilbaud, I. Géraud-Grenier, *et al.*, Plasma Phys. Control. Fusion, **59**, 014034 (2017). https://doi.org/10.1088/0741-3335/59/1/014034
[61] Sh. Amiranashvilia, and M.Y. Yu, Phys. Plasmas, **9**, 4825 (2002). https://doi.org/10.1063/1.1517049
[62] J.X. Ma, M.Y. Yu, X.P. Liang, J. Zheng, W.D. Liu, and C.X. Yu, Phys. Plasmas, **9**, 1584 (2002). https://doi.org/10.1063/1.1468234

[63] L.Z. Hadid, O. Shebanits, J.-E. Wahlund, M.W. Morooka, A.F. Nagy, and W.L. Tseng, J. Plasma Physics, **88**, 555880201 (2022). https://doi.org/10.1017/S0022377822000186
[64] V. Lisovskiy, A. Minenkov, S. Dudin, S. Bogatyrenko, P. Platonov, and V. Yegorenkov, ACS Omega, **7**, 47941 (2022). https://doi.org/10.1021/acsomega.2c05846
[65] M. Mao, J. Benedikt, A. Consoli, and A. Bogaerts, J. Phys. D: Appl. Phys. **41**, 225201 (2008). https://doi.org/10.1088/0022-3727/41/22/225201
[66] Yu.P. Raizer, *Gas Discharge Physics*, (Springer, Berlin, 1991).
[67] M. A. Lieberman, and A. J. Lichtenberg, *Principles of plasma discharges and materials processing*, (Wiley, New York, 2005).
[68] M. Keidar, and I. I. Beilis, *Plasma engineering*, (Academic Press, London, 2018).
[69] J. Berndt, E. Kovačević, I. Stefanović, O. Stepanovic, S. H. Hong, L. Boufendi, and J. Winter, Contrib. Plasma Phys. **49**, 107 (2009). http://dx.doi.org/10.1063/1.3224874
[70] D. U. B. Aussems, S. A. Khrapak, I. Dogan, M. C. M. van de Sanden, and T. W. Morgan, Phys. Plasmas, **24**, 113702 (2017). https://doi.org/10.1063/1.5001576
[71] D. Winske, and M. E. Jones, IEEE Trans. Plasma Sci. **22**, 454 (1994). https://doi.org/10.1109/27.310655
[72] S. J. Choi, and M. J. Kushner, IEEE Trans. Plasma Sci. **22**, 138 (1994). https://doi.org/10.1109/27.279017
[73] H. H. Hwang, and M. J. Kushner, J. Appl. Phys. **82**, 2106 (1997). https://doi.org/10.1063/1.366020
[74] W. Xu, N. D'Angelo, and R. L. Merlino, J. Geophys. Res. **98**, 7843 (1993). https://doi.org/10.1029/93JA00309
[75] J. Goree, and T. E. Sheridan, J. Vac. Sci. Technol. A **10**, 3540 (1992). https://doi.org/10.1116/1.577781
[76] T. E. Sheridan, J. Goree, Y. T. Chiu, R. L. Rairden, and J. A. Kiessling, J. Geophys. Res. **97**, 2935 (1992). https://doi.org/10.1029/91JA02801
[77] G. Lapenta, Phys. Plasmas, **6**, 1442 (1999). https://doi.org/10.1063/1.873395
[78] H. A. Erikson, Phys. Rev. **28**, 372 (1926). https://doi.org/10.1103/PhysRev.28.372
[79] V.A. Lisovskiy, S.V. Dudin, P. P. Platonov, and V.D. Yegorenkov, Phys. Scr. **98**, 025601 (2023). https://doi.org/10.1088/1402-4896/acae48
[80] J.C.W. Chien, *Polyacetylene: Chemistry, Physics, and Material*, (Academic Press, New York, 1984).
[81] A. M. Saxman, R. Liepins, and M. Aldissi, Prog. Polym. Sci. **11**, 57 (1985). https://doi.org/10.1016/0079-6700(85)90008-5

АМБІПОЛЯРНА ДИФУЗІЯ ТА РЕВЕРСІЯ ЗНАКУ ЕЛЕКТРИЧНОГО ПОЛЯ В ЕЛЕКТРОНЕГАТИВНІЙ ПЛАЗМІ ІЗ ЗАРЯДЖЕНИМИ НАНОЧАСТИНКАМИ

В. Лісовський, С. Дудін, С. Богатиренко, С. Резуненко, В. Єгоренков
Харківський національний університет імені В.Н. Каразіна, майдан Свободи 4, Харків, 61022, Україна

У цій роботі запропоновано аналітичну модель амбіполярної дифузії в плазмі, яка складається з електронів, позитивних і негативних іонів та негативно заряджених наночастинок. Отримані формули для коефіцієнтів амбіполярної дифузії як для кожного із сортів заряджених частинок, так і для напруженості амбіполярного електричного поля. У плазмі, що містить лише електрони та позитивні й негативні іони, за високих концентрацій негативних іонів коефіцієнти амбіполярної дифузії кожного виду заряджених частинок наближаються до коефіцієнтів їхньої вільної дифузії, тобто амбіполярна дифузія стає вільною. В плазмі з негативно заряджених наночастинок, електронів та позитивних іонів при високих концентраціях наночастинок коефіцієнт амбіполярної дифузії електронів дорівнює подвійному коефіцієнту їх вільної дифузії, а коефіцієнт амбіполярної дифузії позитивних іонів наближається до подвійного коефіцієнта вільної дифузії наночастинок. В плазмі, що складається з електронів, позитивних та негативних іонів, а також наночастинок, важливим є те, як саме втрачаються вільні електрони, тобто, будуть вони переважно утворювати негативні іони або прилипати до поверхні наночастинок. Якщо домінує прилипання електронів до молекул газу й накопичення негативних іонів, то коефіцієнти амбіполярної дифузії електронів, негативних іонів та наночастинок близькі до їхніх коефіцієнтів вільної дифузії. Якщо вільні електрони переважно зникають внаслідок їх прилипання до наночастинок, то коефіцієнти амбіполярної дифузії електронів, негативних іонів та наночастинок дорівнюють їх подвійним коефіцієнтам вільної дифузії. Виявлено, що коефіцієнт амбіполярної дифузії позитивних іонів залежить від того, як саме вільні електрони втрачаються з плазми. Якщо інтенсивно утворюються негативні іони, то він наближається до коефіцієнта вільної дифузії негативних іонів, а при інтенсивних втратах електронів на поверхні наночастинок він асимптотично зближується з подвійним значенням коефіцієнта вільної дифузії наночастинок. За наявності в плазмі достатньо високих концентрацій негативних іонів та/або заряджених наночастинок напруженість амбіполярного електричного поля суттєво зменшується й навіть може досягти нуля та змінити знак. З плазми зі слабко негативним амбіполярним полем може видалятися надлишок негативних іонів та наночастинок, які накопичуються, що стабілізує горіння розряду. Під час експериментів з ацетиленовою плазмою спостерігався потік дрібних наночастинок на стінку трубки, що може свідчити про зміну знака амбіполярного електричного поля.

Ключові слова: *амбіполярна дифузія; аналітична модель; амбіполярне електричне поле; наночастинки; негативні іони*

East European Journal of Physics. **2.** 461-469 (2026)
DOI:10.26565/2312-4334-2026-2-51 ISSN 2312-4334

STRUCTURAL, MORPHOLOGICAL AND ELECTROCHEMICAL PROPERTIES OF $NaFeO_2$ SYNTHESIZED BY SOLAR MELTING

M.S. Payzullakhanov[1,2], F.A. Giyasova[3], M.A. Yuldoshev[4]*, B.B. Gulyamov[5], F.A. Giyasov[3], A.E. Otarbaev[6], S.M. Kasimov[6], U.A. Nasritdinova[7], G.B. Rizamuxamedova[8], N.B. Xolboyeva[9], A.A. Abduvakhobov[3], A.A. Mamadaliyev[3]
[1]Institute of Materials Science, Academy of Sciences of the Republic of Uzbekistan. Tashkent, Uzbekistan
[2]Fergana State Technical University, Uzbekistan
[3]Kimyo International University in Tashkent, Uzbekistan
[4]Turan International University, Namangan, Uzbekistan
[5]Center of Advanced Technologies, Tashkent, Uzbekistan
[6]Nukus State Pedagogical Institute Named After Ajiniyaz, Nukus, Uzbekistan
[7]Tashkent Institute of Irrigation and Agricultural Mechanization Engineers, National Research University, Uzbekistan
[8]Namangan State Technical University, Namangan, Uzbekistan
[9]Namangan State University, Namangan, Uzbekistan
**Corresponding Author e-mail: murod.yuldoshev1993@gmail.com*

Received March 4, 2026; revised April 30, 2026; accepted May 2, 2026

This paper presents the synthesis of tetragonal sodium ferroxide ($NaFeO_2$) via a solar-furnace melting method. The resulting material is characterized by a quasi-spherical morphology, an average particle size of ~1.2 µm, high crystallinity (~ 92%), and a polydisperse distribution, which ensures efficient transport pathways and uniform electrolyte penetration. SEM analysis revealed the formation of porous aggregates of nanogranular particles (200-500 nm) with a developed specific surface area (5-10 m^2/g). DTA/TGA demonstrates multistage thermal transformations of the Na_2CO_3+Fe_2O_3 system with the formation of $NaFeO_2$ at 800-850 °C, confirming the thermal stability of the material. X-ray diffraction analysis confirmed the high crystallinity of the tetragonal phase with parameters $a = 4.47$ Å, $c = 14.4$ Å, and a coherent scattering region size of ~ 28 nm. The obtained data indicate the high structural stability and electrochemical activity of $NaFeO_2$, making it promising for use in sodium-ion batteries.

Keywords: *$NaFeO_2$; Solar furnace; Melt synthesis; Crystallinity; Microstructure; Porous aggregates; Scanning electron microscopy (SEM); X-ray diffraction (XRD); Thermal analysis (DTA/TGA); Solid-state reactions*
PACS: 68.37.Hk, 78.70.Ck, 77.84.-s

INTRODUCTION

The development of sodium-ion batteries (SIB) is one of the priority areas of modern electrochemical energy, due to the high abundance of sodium in the earth's crust, low cost of source materials and a comparatively lower environmental impact compared to lithium-ion systems [1-3]. Despite their lower theoretical energy density and less favorable ion-transport kinetics, SIBs are considered a promising alternative for stationary and large-scale energy storage systems, where safety, service life, and cost-effectiveness are key requirements [4]. The higher standard oxidation-reduction potential of the Na^+/Na pair (≈-2.71 V relative to the standard hydrogen electrode) compared to Li^+/Li leads to a decrease in the maximum cell voltage, but a rational choice of the structure and chemical composition of electrode materials can partially compensate for this disadvantage [5]. The cathode material largely determines the specific energy, operating voltage and cyclic stability of SIBs. Among the various classes of cathode compounds, $NaFeO_2$ oxide is of particular interest, combining the availability of raw materials, the environmental safety of its components, and structural compatibility with sodium ions. The theoretical specific capacity of sodium ferroxide ($NaFeO_2$) with complete extraction of Na^+ from the crystal lattice is approximately 242 $mA\cdot h\cdot g^{-1}$, which corresponds to one electron transfer per formula unit and can be estimated based on Faraday's law, taking into account the molar mass of the compound [6]. However, experimental studies [7, 8], primarily for the layered α-modification of $NaFeO_2$, demonstrate significantly lower values of reversible capacity, typically in the range of 80-120 $mA\cdot h\cdot g^{-1}$ at an average working potential of approximately 3.3 V relative to Na^+/Na. These characteristics indicate the possibility of reversible sodium intercalation and deintercalation without catastrophic structural failure at moderate charge depths, but also highlight a significant gap between the material's theoretical and practical potential. Limiting factors include low electron conductivity, limited contact area with the electrolyte, and structural transformations that occur during deep Na^+ extraction. One of the key mechanisms of $NaFeO_2$ degradation is the migration of iron ions. When charging to potentials above 3.4-3.5 V, partial release of the sodium layers occurs, accompanied by the transition of Fe cations from octahedral positions to interlayer regions. This leads to blocking of diffusion channels for Na^+, an increase in internal resistance, and a rapid loss of capacity [9, 10]. This effect significantly limits the reversible charge depth and the cathode's cyclic stability.

Cite as: M.S. Payzullakhanov, F.A. Giyasova, M.A. Yuldoshev, B.B. Gulyamov, F.A. Giyasov, A.E. Otarbaev, S.M. Kasimov, U.A. Nasritdinova, G.B. Rizamuxamedova, N.B. Xolboyeva, AA. Abduvakhobov, A.A. Mamadaliyev, East Eur. J. Phys. 2, 461 (2026), https://doi.org/10.26565/2312-4334-2026-2-51

The ionic conductivity of $NaFeO_2$ is an important parameter that determines the material's kinetic characteristics. For α-$NaFeO_2$, the activation energy for Na^+ transfer is approximately 0.31 eV in the temperature range of 306-498 K, which corresponds to the migration mechanism between octahedral sites through adjacent tetrahedral spaces, typical of layered oxides. This value indicates the possible but relatively limited transfer of sodium ions within the crystalline matrix [11].

The phase composition, morphology, and particle size are considered key factors that determine the electrochemical activity of $NaFeO_2$, according to several studies [12, 13]. In particular, for the β-modification, characterized by a tetragonal prismatic structure, specific capacity values of up to 590 $mA\cdot h\cdot g^{-1}$ were recorded after mechanical grinding and extended cycling, which is associated with increased specific surface area and improved contact between the active material and the electrolyte. These data emphasize that morphological control and optimization of Na^+ ion diffusion pathways are priority factors for improving the capacitive characteristics of cathode materials [14].

An additional effective approach to improving the electrochemical characteristics of $NaFeO_2$ is cation doping, in which the partial replacement of Fe with Mn, Ni, or Mg suppresses iron migration and stabilizes the crystal lattice, thereby increasing cyclic stability [15]. A similar effect is observed when protective coatings such as Al_2O_3 or carbon are applied, which reduce the intensity of side reactions at the electrode-electrolyte interface [16]. Electrochemical studies of the Na><$NaFeO_2$><Al system using metallic sodium Na+/Na as a reference electrode revealed a redox peak at a potential of about 0.8 V, accompanied by a specific capacity of about 110 $mA\cdot h\cdot g^{-1}$. The observed behavior is due to the sequential process of leaching and insertion of Na^+ ions followed by the Fe^{2+}/Fe^{3+} redox transition, which determines the electrochemical activity of the material [17, 18]. With increasing interest in developing cost-effective and environmentally friendly cathode materials for sodium-ion batteries, the use of compounds based on readily available elements is a relevant area of research. The tetragonal modification of $NaFeO_2$ has attracted attention due to the use of iron and the possibility of implementing reversible redox processes, but remains insufficiently studied, especially when produced by alternative high-temperature synthesis methods [19]. In this context, using a solar furnace (SF) as a source of thermal energy is a promising, energy-efficient approach.

The objective of this study is to synthesize the tetragonal modification of $NaFeO_2$ by melting in a superconducting furnace and to investigate its structural, morphological, and electrochemical properties to assess the potential of this material as a cathode for sodium-ion batteries.

This study aims to establish the temperature-dependent formation of the $NaFeO_2$ phase, determine the crystal structure and degree of crystallinity of the resulting material, analyze the morphology and particle size distribution, and investigate the electrochemical activity associated with Na^+ ion intercalation/deintercalation processes and Fe^{2+}/Fe^{3+} redox transitions.

EXPERIMENTAL SAMPLES AND MEASUREMENT METHODS

The synthesis of $NaFeO_2$ material was carried out by melting a stoichiometric mixture of $Na_2CO_3 + Fe_2O_3$ in a stream of concentrated solar radiation on a solar panel with a vertical optical axis [20, 21]. The density of the concentrated radiation flux was calculated based on the Stefan-Boltzmann equation, which describes the radiation of heated bodies:

$$Q = \varepsilon\sigma T^4 \tag{1}$$

where ε is the emissivity of the material, $\sigma=5.67\times10^{-8}$ W/m^2K^4 is the Stefan–Boltzmann constant, T is the body temperature (K).

With the emissivity of rocks being $\varepsilon = 0.85$, the required flux density for melting AMMP metallurgical waste (T=1750 K) was Q=50 W/cm^2. The melt was cooled by pouring it into water at a high cooling rate (~10^3°C/s). After quenching, the melt was ground to a particle size of about 60 μm and molded into cylindrical samples with a diameter of 8 mm and a height of 2 mm. The resulting cylinders were sintered at various temperatures [22-25].

X-ray diffraction (XRD) analysis of the samples was performed on a PANalytical Empyrean diffractometer with Kα radiation in Bragg-Brentano geometry (λ = 1.5418 Å) at a 2θ range of 20–60°. The slit system was selected such that the X-ray beam completely covered the sample surface over the entire 2θ range.

Surface morphology was examined using scanning electron microscopy (JEOL JSM 6510 and HITACHI FLEXSEM 100), and chemical functional groups were determined using FT-IR (SHIMADZU 8210PK). Electrical conductivity of the samples was measured by impedance using an LCR meter (frequency range 20 Hz - 500 kHz).

The relative density of the samples was calculated using the formula:

$$\rho_r = \rho_m/\rho_{dw}, \tag{2}$$

where, ρ_m is the density of the sample material, $\rho_{d.w}$= 0.98 g/cm^3 is the density of distilled water under normal conditions. For $NaFeO_2$, the relative density was ρ_r=4.07 g/cm^3.

Thermophysical properties were studied using a synchronous thermal analyzer STA PT 1600/LT (Linseis), performing simultaneously thermogravimetric analysis (TGA), differential thermal analysis (DTA), and differential scanning calorimetry (DSC). The morphology of the samples was additionally investigated using an SEM EVO MA 10 (Carl Zeiss, Germany) [26-28].

Particle size distribution was determined using a Laser Particle Size Analyzer Winner 2005. Measurements were performed using laser diffraction, which is based on recording the intensity of light scattered by particles at different angles. The diffraction pattern was processed using Mie theory [29] to determine the volume distribution of particles in the size range from 10 nm to several millimeters.

RESULTS AND DISCUSSION

To determine the phase transformation temperatures of the studied material ($NaFeO_2$), comprehensive measurements were conducted using DTA, TGA, and calorimetry. These experiments were performed on a Na_2CO_3+Fe_2O_3 mixture in the temperature range from 27 °C to 1000 °C, and the results are presented in Fig 2.

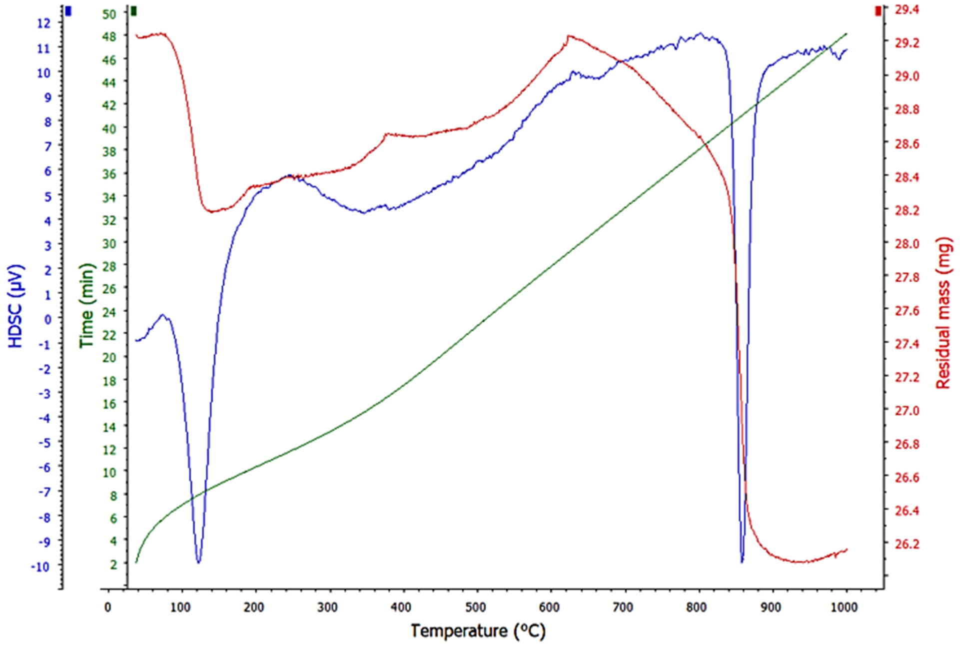

Figure 1. TG-DTA/DSC curves of a sample of the Na_2CO_3 + Fe_2O_3 mixture

In the low-temperature range of 27-150 °C, the thermogravimetric curve shows a small mass loss, while in the range of 80-120 °C, the DTA registers a distinct endothermic minimum. This thermal effect is due to the absorption of energy during the desorption of physically bound moisture, the removal of low-molecular volatile impurities from the pore space and the surface of the sample, and the dehydration of hygroscopic sodium carbonate [30, 31]:

$$Na_2CO_3 \cdot nH_2O \rightarrow Na_2CO_3 + nH_2O\uparrow \quad (3)$$

In this temperature range, the initial mass loss of the sample is $\Delta m_1 \approx 2.8\%$ of the initial mass m_0. The mass loss is expressed through the ratio:

$$\Delta m_1 = \frac{m_0 - m_{150}}{m_0} \times 100\ \% \quad (4)$$

where, m_{150} is the mass of the sample after heating to 150°C.

The DSC curve shows a pronounced endothermic effect (minimum heat flow) [32] associated with heat absorption. The enthalpy of the thermal effect was determined using the formula [33]:

$$\Delta H = \frac{1}{\beta} \int_{T_1}^{T_2} \Phi\,(T)\,dT \quad (5)$$

The enthalpy of this process, ΔH_1, was estimated from the area of the endothermic peak on the DTA curve and is $\Delta H \approx 20$-50 J/g, which corresponds to the typical range for moisture evaporation processes. The presence of the endothermic peak confirms heat absorption during desorption and removal of volatile components.

In the medium temperature range (150-500 °C), a more gradual change in sample mass occurs – 3.5 %, and the total mass loss by 500 °C is 6.3%. The TG curve indicates a gradual decrease in mass, which may be associated with the thermal decomposition of organic components, dehydroxylation, or the removal of chemically bound water. In the range of 200–500 °C, smoothed deviations in heat flow are observed, corresponding to overlapping endo- and exothermic processes [34, 35]. The enthalpies of these effects are estimated as moderate, not exceeding 100 J/g.

With a further increase in temperature in the range of 500-800 °C, the DTA curve shows an increase in thermal effects, which is associated with the rearrangement of the material structure, phase transformations, and the onset of crystallization. The change in mass in this range does not exceed 1.7 %, remains moderate, and indicates the relative thermal stability of the main inorganic matrix of the sample. The observed exothermic effect is due to the onset of solid-phase interaction between Na_2CO_3 and DTA with the formation of sodium-iron oxide phases, in particular $NaFeO_2$ [36]:

$$Na_2CO_3 + Fe_2O_3 \rightarrow 2NaFeO_2 + CO_2\uparrow \tag{6}$$

The exothermic effect indicates the release of heat during the formation of a new crystalline structure; the magnitude of the thermal effect is 50-100 J/g.

In the region of intense transformations, at temperatures of 800-850 °C, a sharp exothermic peak is recorded on the DTA curve, accompanied by a sudden decrease in residual mass of approximately 4.6 %. This effect is associated with the intense decomposition of Na_2CO_3 and the active reaction with Fe_2O_3, releasing carbon dioxide:

$$Na_2CO_3 \rightarrow Na_2O + CO_2\uparrow \tag{7}$$

A large peak area indicates the occurrence of an intense phase or structural transformation, and a semi-quantitative estimate of the process enthalpy is 100–300 J/g, corresponding to high-energy phase and chemical transformations [37].

Upon further heating to 1000 °C, the sample mass stabilizes, and the thermal effects become less pronounced. Reaching a residual mass of 88-90 % of the initial mass is associated with the completion of decarbonization processes and the formation of thermodynamically stable sodium-iron oxide phases. DTA and TGA data for the initial Na_2CO_3+Fe_2O_3 mixture revealed the removal of adsorbed moisture and volatile components in the range of 27-330 °C, as well as a pronounced exothermic effect at 850 °C, corresponding to the completion of the $NaFeO_2$ phase formation [38].

Next, to determine the phase state and structure of the material, X-ray phase analysis was performed (Fig. 2).

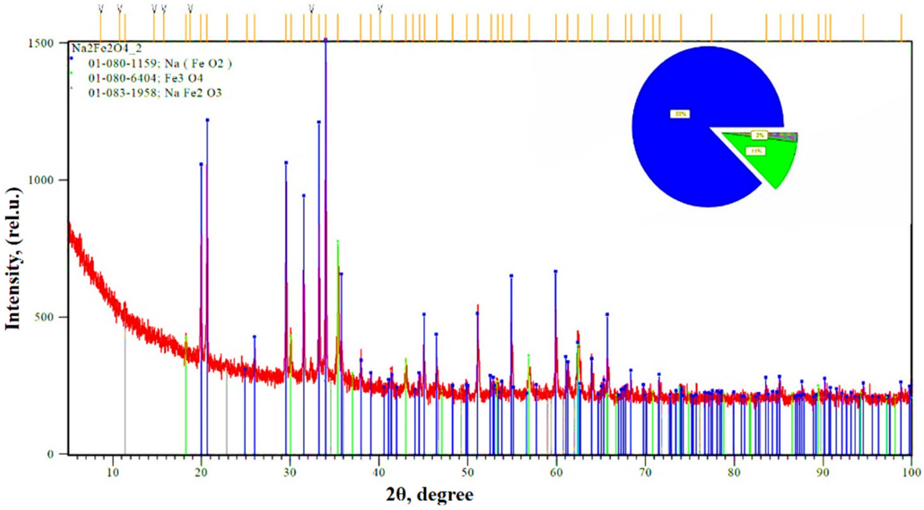

Figure 2. XRD pattern of $NaFeO_2$ synthesized by the melting method in SP

Figure 3 shows the X-ray diffraction pattern of a $NaFeO_2$ sample obtained from a melt in a solar synthesis facility. X-ray phase analysis of the pattern indicates the formation of a highly crystalline material, as evidenced by the presence of intense and narrow diffraction reflections. The set of main diffraction maxima is correctly indexed within the tetragonal crystal structure of $NaFeO_2$, indicating the successful formation of the target phase under high-temperature solar synthesis conditions. Based on the experimental positions of the diffraction peaks, the interplanar distances were calculated and the reflections were indexed. The interplanar distances d were determined using Bragg's law [39]:

$$n\lambda=2d\sin\theta, \tag{8}$$

where, λ is the X-ray wavelength, θ is the diffraction angle, and n=1 is the reflection order. For the tetragonal crystal system, the lattice parameters were calculated using the corresponding relationships between interplanar spacings and Miller indices. The calculation results are presented in Table 1.

Table 1. X-ray structural parameters of $NaFeO_2$ synthesized from the melt

Peak no.	2θ, degree	Interplanar distance (d), Å	Miller indices (hkl)	Half-width at half maximum (β), degree	Relative intensity, %
1	18.5	4.79	(003)	0.28	100.0
2	32.0	2.80	(104)	0.30	96,7
3	37.2	2.41	(110)	0.32	80.0
4	43.4	2.08	(113)	0.34	53.3
5	57.4	1.60	(116)	0.36	33.3

The most intense diffraction maxima were recorded at angles of 2θ ≈ 18.5° and 32.0°, which corresponded to the (003) and (104) crystallographic planes. The interplanar distances calculated using Bragg's law were approximately 4.79 Å and 2.80 Å, respectively. Using the (003) reflection, we determined the lattice parameter c=14.4 Å, while a joint analysis of the (003) and (104) reflections yielded a parameter value of a=4.47 Å [40, 41]. Comparison of the obtained unit cell parameters with the literature data [42] for tetragonal $NaFeO_2$ confirms the preservation of structural order during synthesis from the melt. The unit cell volume is V=144 Å³, and the degree of crystallinity of the material reaches 92 %. The half-width at half maximum (β) of the peak for the most intense reflection (104) is about 0.30°, indicating a high degree of crystallinity of the material and a relatively low level of microdeformations of the crystal lattice. Based on the β values, the average size of the coherent scattering regions, estimated using the Scherrer formula [43]:

$$D=K\lambda/\beta\cos\theta, \tag{9}$$

where K is the shape factor (0.9) and is 28 nm, which is typical for materials obtained under conditions of rapid cooling of the melt.

Analysis of the diffraction peaks indicates minor distortions in the $NaFeO_2$ crystal lattice relative to the ideal tetragonal structure. The absence of pronounced splitting of the diffraction maxima and the small β value reflect a weak monoclinic distortion of the structure. Low-intensity additional reflections were detected in the diffraction pattern, presumably corresponding to iron oxides Fe_2O_3 and Fe_3O_4, the appearance of which is likely associated with partial non-stoichiometry and local oxidation of iron under high-temperature solar synthesis conditions [44, 45]. However, the low intensity of these reflections relative to the main peaks of $NaFeO_2$ allows us to consider the material obtained as predominantly single-phase.

Based on these data, a generalized analysis of thermal transformations in the $Na_2CO_3+Fe_2O_3$ system was also carried out using DTA/TGA methods in the temperature range from room temperature to above 850 °C (Table 2).

Table 2. Characterization of thermal transformations in the $Na_2CO_3+Fe_2O_3$ system based on DTA/TGA and XRD data

Temperature range, °C	Δm, %	Thermal effect (DTA/DSC)	Enthalpy of the process, ΔH, J/g	The main process	Phase state (XRD)
27-150	2.8	Endothermic	20-50	Desorption of adsorbed water, removal of volatile components	$Na_2CO_3+Fe_2O_3$
150-500	3.5	Weak endo/exothermic	≤ 100	Dehydroxylation, removal of chemically bound water, surface activation	$Na_2CO_3+Fe_2O_3$
500-800	1.7	Exothermic	50-100	The beginning of the solid-phase reaction, structural rearrangement, the formation of $NaFeO_2$	$Na_2CO_3+Fe_2O_3+NaFeO_2$
800-850	4.6	Intense exothermic	100-300	Decarbonization, active formation of $NaFeO_2$, phase transition	$NaFeO_2+Fe_2O_3$
> 850	≈ 0	Absent	-	Formation of a thermodynamically stable phase of $NaFeO_2$	$NaFeO_2$ (main)

The table presents mass loss values, the nature of thermal effects, the predominant processes, and the phase composition determined by XRD. The results obtained allow for a comprehensive characterization of the thermal stability of the system's components and the sequence of phase transformations upon heating.

The microstructural features of $NaFeO_2$, studied by scanning electron microscopy, are shown in Figure 4 at a magnification of ×1000.

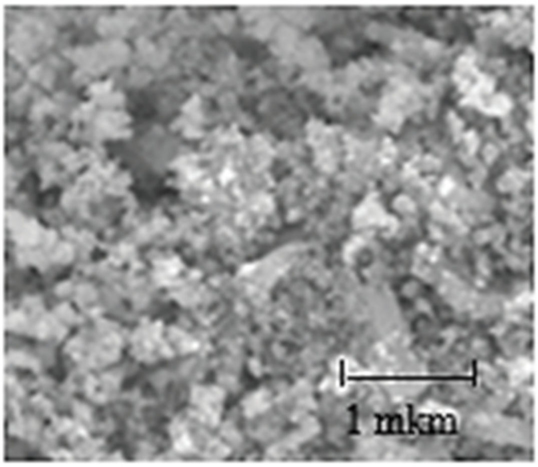

Figure 4. SEM micrograph of the surface of a sample of $NaFeO_2$ material

The image scale corresponds to 1 μm, enabling detailed assessment of the particles' morphological features. As can be seen in Fig 4, the particles have a quasi-spherical shape and exhibit a high degree of agglomeration, with their sizes varying from 0.5 to 10 μm, with a maximum particle number of approximately 1.2 μm. The surface microstructure is characterized by a coarse-grained and porous texture with the formation of aggregates of small crystalline grains approximately 200-500 nm in size, indicating material growth through crystallization from the melt with subsequent aggregation of crystals into larger aggregates. The high degree of surface roughness provides a specific surface area of approximately 5-10 m²/g, which increases the contact area with the electrolyte and facilitates the diffusion of Na^+. Moreover, the particle distribution is relatively uniform, without pronounced defects or cracks, reflecting the high crystalline integrity of the material [46-48].

To evaluate the particle size and distribution of the synthesized $NaFeO_2$, laser transmission spectroscopy (LPSA/LD) was used, as shown in Fig 5.

The obtained data showed an asymmetric particle volume distribution with a distinct main peak at approximately 1.5 μm. Analysis of the particle volume fraction revealed that approximately 70 % of the powder consisted of particles up to 5 μm in diameter, indicating the predominance of the finely dispersed component. The median particle size (d_{50}) was 1.5 μm, which corresponded to the position of the main distribution peak. The particle spread from d_{10}=0.5 μm to d_{90}=7 μm corresponds to a wide polydisperse spectrum (PDI ≈ 4.3). This distribution is characterized by the presence of both small and relatively large particles [49, 50]. Finely dispersed particles provide a significant reactive surface, which can contribute to higher reaction rates in thermal and electrochemical processes. Large particles, including agglomerates up to 20 μm in size, are relatively rare, which minimizes potential problems with material homogeneity and deterioration of properties during pressing or forming electrodes [51, 52].

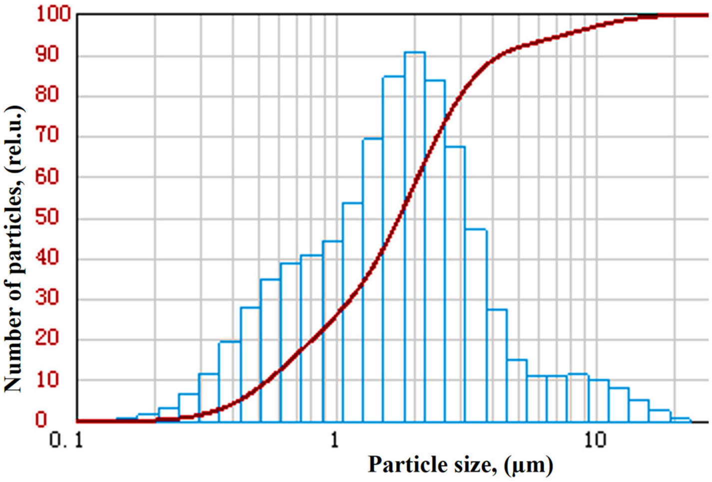

Figure 5. Particle distribution spectrum of $NaFeO_2$ by LPSA/LD method

CONCLUSIONS

Sodium ferroxide ($NaFeO_2$) was synthesized via solar melting, yielding quasi-spherical particles with an average size of 1.2 μm and a crystallinity of 92%. These characteristics facilitate uniform electrolyte penetration and the formation of efficient Na^+ transport pathways. The synthesis method significantly influences the structural and morphological properties of $NaFeO_2$. High-temperature processes, including melt synthesis, enable the formation of a material with a high degree of crystallinity and minimal secondary-phase content.

The resulting $NaFeO_2$ powder exhibits a polydisperse particle distribution, with a predominance of small and medium-sized particles, thereby ensuring a combination of high reactivity and structural stability. The variety of particle sizes also affects powder packing and the density of pressed samples, both of which are important to consider when developing electrochemical cells. SEM data confirm that the synthesized $NaFeO_2$ forms a microstructure with porous aggregates of nanogranular particles (200-500 nm) and a developed specific surface area (5-10 m²/g), which positively impacts its functional properties.

Thermal studies of the Na_2CO_3+Fe_2O_3 system have shown that the formation of tetragonal $NaFeO_2$ occurs at high temperatures (500-850°C) through successive stages of moisture desorption, dehydration, and solid-phase reactions. Low-temperature effects ($\Delta H \approx 20$-50 J/g) are due to the removal of adsorbed and chemically bound water, medium-temperature effects ($\Delta H \approx 50$-100 J/g) are due to gradual structural rearrangement and dehydroxylation, and at 800-850 °C intense exothermic processes are observed with the decomposition of Na_2CO_3 and the formation of $NaFeO_2$ ($\Delta H \approx 100$-300 J/g). DTA/TGA analysis revealed that thermal transformations occur in several stages, with a total mass loss of approximately 10-12 %, primarily due to dehydration and CO_2 evolution. The highest activity of solid-phase interactions and the formation of the target phase are observed at 800-850°C, confirming the material's thermal stability and enabling us to determine the optimal synthesis conditions for its functional application.

X-ray diffraction (XRD) analysis revealed that $NaFeO_2$ synthesized by solar melting forms a highly crystalline tetragonal material with unit cell parameters a=4.47 Å, c=14.4 Å, and a volume V=144 Å³. The presence of the main diffraction peaks (003) and (104), their width (0.30°), and the calculated size of the coherent scattering regions (28 nm) confirm the high crystallinity of the material and low microstrain. Trace additional reflections of Fe_2O_3 and Fe_3O_4 do not disrupt the single-phase nature of the sample.

These comprehensive data confirm that solar melting enables the synthesis of stable tetragonal $NaFeO_2$ with high electrochemical activity and cycling stability, creating favorable conditions for its application in sodium-ion batteries.

ORCID

F.A. Giyasova, https://orcid.org/0000-0003-0746-4986; **M.A. Yuldoshev,** https://orcid.org/0000-0002-9722-9439
B.B. Gulyamov, https://orcid.org/0009-0008-8838-4278; **F.A. Giyasov,** https://orcid.org/0009-0003-9882-0655
S.M. Kasimov, https://orcid.org/0009-0009-5445-372X; **A.E. Otarbaev,** https://orcid.org/0009-0009-7942-9398
N.B. Xolboyeva, https://orcid.org/0009-0007-7480-5572

REFERENCES

[1] A.F. Salam, X. Zheng, Z. Chen, Y. Liao, D.K. Kim, S.S. Mofarah, P. Koshy, *et al.*, "Sodium-ion battery development since 2020 with future perspectives," Journal of Materials Chemistry A, **14**, 9115-9137 (2026). https://doi.org/10.1039/D5TA07726E

[2] Y. Li, "Review of sodium-ion battery research," Advances in Engineering Innovation, **16**(3), 31-37 (2025). https://doi.org/10.54254/2977-3903/2025.21919

[3] S.F. Samadov, N.V.M. Trung, A.A. Sidorin, S.I. Ibragimova, S.H. Jabarov, M.A. Yuldoshev, O.S. Orlov, Y.I. Aliyev, Micro and Nanostructures, **209**, 208451 (2026). https://doi.org/10.1016/j.micrna.2025.208451

[4] P. Phogat, S. Dey, and M. Wan, "Comprehensive review of Sodium-Ion Batteries: Principles, Materials, Performance, Challenges, and future Perspectives," Materials Science and Engineering: B, **312**, 117870 (2025). https://doi.org/10.1016/j.mseb.2024.117870

[5] L. Zhao, T. Zhang, W. Li, T. Li, L. Zhang, X. Zhang, and Zh. Wang, "Engineering of Sodium-ion Batteries: Opportunities and Challenges," Engineering, **24**(5), (2023). https://doi.org/10.1016/j.eng.2021.08.032

[6] J.Y. Hwang, S.T. Myung and Y.K. Sun, "Sodium-ion batteries: present and future," Chem. Soc. Rev. **46**, 3529-3614 (2017). https://doi.org/10.1039/C6CS00776G

[7] J.-Y. Hwang, S.-T. Myung, and Y.-K. Sun, "Sodium-ion batteries: present and future," Chem. Soc. Rev. **46**, 3529-3614 (2017). https://doi.org/10.1039/C6CS00776G

[8] J. Jayachitra, J.R. Joshua, A. Balamurugan, N. Sivakumar, V. Sharmila, S. Shanavas, M.A. Haija, *et al.*, "High electrode performance of hydrothermally developed activated C coated O$_3$-NaFeO$_2$ electrode for Na-ion batteries applications," Ceramics International, **49**(1), 48-56 (2023). https://doi.org/10.1016/j.ceramint.2022.07.110

[9] Y. Li, Y. Gao, X. Wang, Xi Shen, Q. Kong, R. Yu, G. Lu, *et al.*, "Iron migration and oxygen oxidation during sodium extraction from NaFeO$_2$," Nano Energy, **47**, 519-526 (2018). https://doi.org/10.1016/j.nanoen.2018.03.007

[10] Zh.Ch. Jian, J.X. Guo, Y. Liu, Y. Zhu, J. Wang, and Y. Xiao, "Cation migration in layered oxide cathodes for sodium-ion batteries: fundamental failure mechanisms and practical modulation strategies," Chem. Sci, **15**, 19698-19728 (2024). https://doi.org/10.1039/D4SC05206D

[11] M.C. Blesa, E. Moran, C. León, J. Santamaria, J.D. Tornero, and N. Menéndez, "α-NaFeO$_2$: ionic conductivity and sodium extraction," Solid State Ionics, **126**(1-2), 81-87 (1999). https://doi.org/10.1016/S0167-2738(99)00145-9

[12] R.D. McAuliffe, G.E. Kamm, M.J. McDermott, R.P. Hermann, N.V. Garcia, R.L. Sacci, K.A. Persson, *et al.*, "Direct Mechanochemical Synthesis, Phase Stability, and Electrochemical Performance of α NaFeO$_2$," Inorganic Chemistry, **62**(8), 3358-3367 (2023). https://doi.org/10.1021/acs.inorgchem.2c03286

[13] M.A. Rusho, T.A. Ahmed, L.H. Saleh, S.W. Ghori, E. Muniyandy, S. Usanov, M. Latipova, *et al.*, "Design and synthesis of decorated palladium nanoparticles on chitosan-tannic acid modified magnetic nanoparticles and evaluation of its catalytic application in the Heck coupling reactions," Journal of Organometallic Chemistry, **1039**, 123773 (2025). https://doi.org/10.1016/j.jorganchem.2025.123773

[14] H. Watanabe, H. Usui, Y. Domi, T. Nishida, K. Uetake, T. Tanaka, H. Kurokawa, *et al.*, "NaFeO$_2$: Possible Materials for Anode and Cathode of Na-Ion Batteries," ACS Electrochemistry, **1**(1), 73-81 (2025). https://doi.org/10.1021/acselectrochem.4c00024

[15] V. Shipitsyn, *et al.*, "Advancing Sodium-Ion Battery Cathodes: A Low-Cost, Eco-Friendly Mechanofusion Route from TiO$_2$ Coating to Ti^{4+} Doping," Chem. Mater. **37**, 6059-6068 (2025). https://doi.org/10.1021/acs.chemmater.5c01485

[16] X. Zhao, Qi Liu, W. He, D. Mu, L. Li, R. Chen, and F. Wu, "Uniform Al$_2$O$_3$ coating for improved cycling stability of O$_3$-type sodium-ion batteries cathode: Mechanisms and performance insights," Journal of Energy Storage, **131**, Part A, 117548 (2025). https://doi.org/10.1016/j.est.2025.117548

[17] J. Zhao, L. Zhao, N. Dimov, Sh. Okada, and T. Nishida, "Electrochemical and thermal properties of α-NaFeO$_2$ cathode for Na-ion batteries," Journal of the Electrochemical Society, **160**(5), A3077-A3081 (2013). https://doi.org/10.1149/2.007305jes

[18] N. Yabuuchi, K. Kubota, M. Dahbi, and Sh. Komaba, "Research Development on Sodium-Ion Batteries," Chem. Rev. **114**(23), 11636-11682 (2014). https://doi.org/10.1021/cr500192f

[19] M.G.D. Guaita, O.J. Oliveira, P.R. Silva, L.H. Antonia, and A. Urbano, "New NaFeO$_2$ synthesis route for green sodium-ion batteries," Green Materials, **11**(3), 115-124 (2022). https://doi.org/10.1680/jgrma.21.00050

[20] M.S. Paizullakhanov, F.A. Giyasova, Kh.N. Bakhronov, M.A. Yuldoshev, A.A. Mamadaliev, F.A. Giyasov, F.T. Akbarova, *et al.*, "Investigation of the Processes Involved in the Formation of Pyroxene Materials during Solar Melting in a Large Solar Furnace," Journal of Ovonic Research, **22**(1), (2026). https://doi.org/10.15251/JOR.2026.221.51

[21] M.S. Payzullakhanov, F.A. Giyasova, M.A. Yuldoshev, Ch.X. Toshpulatov, R.U. Ernazarov, F.A. Giyasov, A. Urishev, *et al.*, East Eur. J. Phys. (1), 233 (2026). https://doi.org/10.26565/2312-4334-2026-1-25

[22] M.S. Paizullakhanov, O.R. Parpiev, F.N. Ernazarov, *et al.*, "Features of Barium–Strontium Cobaltite as a Catalyst for Hydrogen Generation," Glass Phys. Chem. **50**, 55–60 (2024). https://doi.org/10.1134/S1087659623601181

[23] M.S. Paizullakhanov, N.K. Karshieva, F.N. Ernazarov, *et al.*, "Studying the Possibility of Applying Barium-Strontium Cobaltite in Hydrogen Energy," Therm. Eng. **71**, 280–284 (2024). https://doi.org/10.1134/S0040601524030054

[24] N.Yu. Sharibaev, A.Q. Ergashov, S.B. Fazliddinov, R.G. Ikramov, M.A. Yuldoshev, and A.A. Abdulxayev, "Photoelectric characteristics of TiO2-based on thin-film solar elements with ruthenium (II) compounds," Journal of Ovonic Research, **21**(6), (2025). https://doi.org/10.15251/JOR.2025.216.859

[25] Sh. I. Klychev, S. A. Bakhramov, O. R. Parpiev, M. S. Paizullakhanov, L. S. Suvonova, D. E. Kadyrgulov, E. K. Matjanov, *et al.*, "Optical-Energy Characteristics and Heating Temperatures in Small Single-Mirror Solar Furnaces," Applied Solar Energy, **60**(5), 703-707 (2025). https://doi.org/10.3103/S0003701X24602394

[26] Sh.B. Utamuradova, F.A. Giyasova, K.N. Bakhronov, M.A. Yuldoshev, M.R. Bekchanova, and B. Ismatov, "Current Transfer Mechanism in A Thin-Based Heterosystem Based on A^2B^6 Compounds," East Eur. J. Phys. (3), 325 (2025). https://doi.org/10.26565/2312-4334-2025-3-31

[27] M.A. Yuldoshev, Z.T. Azamatov, A.B. Bakhromov, and M.R. Bekchanova, East Eur. J. Phys. (4), 250 (2024), https://doi.org/10.26565/2312-4334-2024-4-25

[28] F.A. Giyasova, A.Z. Rakhmatov, Kh.N. Bakhronov, M.A. Yuldoshev, F.A. Giyasov, A.N. Olimov, and N.A. Sattarov, East Eur. J. Phys. (4), 397 (2025). https://doi.org/10.26565/2312-4334-2025-4-38

[29] A. Mudroch, J.M. Azcue, and P. Mudroch, *Manual of Physico-Chemical Analysis of Aquatic Sediments*, (CRC Press, 1996).

[30] N. Đorđević, S. Mihajlović, G. Jovanović, and B. Marković, "DTA/TG analysis of mechanochemically activated sodium carbonate," Podzemni Radovi, (38), 47-55 (2021). https://doi.org/10.5937/podrad2138047Q

[31] J. Matrasulov, J.R. Yusupov, and A.A. Saidov, "Fast forward evolution in heat equation: Tunable heat transport in adiabatic regime," Phys. Chem. Math, **14**(4), 421-427 (2023). https://doi.org/10.17586/2220-8054-2023-14-4-421-427

[32] A.J. Müller, and R.M. Michell, "Differential Scanning Calorimetry of Polymers" in: *Polymer Morphology*, (2016), pp.72-99, https://doi.org/10.1002/9781118892756

[33] P. Kaur, M. Singh, and P. Birwal, "Differential Scanning Calorimetry (DSC) for the Measurement of Food Thermal Characteristics and Its Relation to Composition and Structure," in: *Techniques to Measure Food Safety and Quality*, edited by M.S. Khan, and M.Sh. Rahman, (Springer, 2021). https://doi.org/10.1007/978-3-030-68636-9_13

[34] M. Labus, M. Irena, and K. Ziemianin, "Thermal Decomposition Processes in Relation to the Type of Organic Matter, Mineral and Maceral Composition of Menilite Shales," Energies, **16**(11), 4500 (2023). https://doi.org/10.3390/en16114500

[35] F.A. Giyasova, Kh.N. Bakhronov, M.A. Yuldoshev, I.B. Sapaev, R.G. Ikramov, F.A. Giyasov, M.R. Bekchanova, *et al.*, "Study of The Influence of Temperature on the Transitions of the CdS/Si/CdTe Heterosystem," East Eur. J. Phys. (4), 461 (2025). https://doi.org/10.26565/2312-4334-2025-4-47

[36] G.P. Luo, Q. Sun, Y.B. Wang, and J.G. Zhu, "Influence of Na_2O Content on Lattice Structures of Iron Oxides during Reduction Process of Fe_2O_3 Briquetting," in: *4th Annual International Conference on Material Science and Engineering, (ICMSE 2016)*, pp. 0118-0126.

[37] H. Takasu, H. Hoshino, Y. Tamura, S.T. Kim, and Y. Kato, "Sodium Ferrite/Carbon Dioxide Reactivity for High Temperature Thermochemical Energy Storage," ISIJ International, **59**(4), 715-720 (2019). https://doi.org/10.2355/isijinternational.ISIJINT-2018-182

[38] J. Huang, T. Furukawa, and K. Aoto, "High temperature behavior of Na-Fe oxides in H_2O+CO_2 atmosphere," Journal of Physics and Chemistry of Solids, **66**(2-4), 388-391 (2005). https://doi.org/10.1016/j.jpcs.2004.06.084

[39] T. Arlt, R.J. Angel, R. Miletich, Th. Armbruster, and T. Peters, "High-pressure P21/c-C2/c phase transitions in clinopyroxenes; influence of cation size and electronic structure," American Mineralogist, **83**, 1176-1181 (1998). https://doi.org/10.2138/am-1998-11-1205

[40] N. Kuganathan, N. Kelaidis, and A. Chroneos, "Defect Chemistry, Sodium Diffusion and Doping Behaviour in $NaFeO_2$ Polymorphs as Cathode Materials for Na-Ion Batteries: A Computational Study," Materials, **12**(19), 3243 (2019). https://doi.org/10.3390/ma12193243

[41] G.M. Milibaeva, H.T. Yusupov, D.G. Berdiyorova, Y. Rakhimova, M. Yusupov, A. Chaves, and Kh. Rakhimov, "Wave packet propagation through square and triangular patterned circular potential scatterers in graphene," Physica Scripta, **100**(12), 125945 (2025). https://doi.org/10.1088/1402-4896/ae2a7d

[42] N. Yabuuchi, H. Yoshida, and S. Komaba, "Crystal structures and electrode performance of alpha-$NaFeO_2$ for rechargeable sodium batteries," Electrochemistry, **80**(10), 716-719 (2012). https://doi.org/10.5796/electrochemistry.80.716

[43] D. Balzar, "X-Ray Diffraction Line Broadening: Modeling and Applications to High-Tc Superconductors," J. Res. Natl. Inst. Stand. Technol. **98**(3), 321-353 (1993). https://doi.org/10.6028/jres.098.026

[44] O. Ergashev, Kh. Bakhronov, F. Giyasova, E. Nazirakhon, R. Yunusova, V. Gaffarova, O. Ochilova, *et al.*, "Energy Characteristics, Adsorption Kinetics, and Mechanism of Triethylamine Adsorption on CsZSM-5 Zeolite," J. Appl. Organomet. Chem, **6**(1), 43-52 (2026). https://doi.org/10.48309/JAOC.2026.546865.1334

[45] B. Silván, E. Gonzalo, L. Djuandhi, F. Fauth, N. Sharma, and D. Saurel, "On the dynamics of transition metal migration and its impact on the performance of layered oxides for sodium-ion batteries: $NaFeO_2$ as a case study," Journal of Materials Chemistry A, **6**(31) (2018). https://doi.org/10.1039/C8TA02473A

[46] Y. Zhao, Q. Lai, Y. Hao, H. Zeng, H. Chu, and Zh. Lin, "A porous spherical aggregation of $Li_4Mn_5O_{12}$ nanorods and its electrochemical performance," Journal of Power Sources, **195**(13), 4400-4405 (2010). https://doi.org/10.1016/j.jpowsour.2010.01.072

[47] M. Müller, L. Schneider, N. Bohn, J.R. Binder, and W. Baue, "Effect of Nanostructured and Open-Porous Particle Morphology on Electrode Processing and Electrochemical Performance of Li-Ion Batteries," ACS Appl. Energy Mater, **4**, 1993-2003 (2021). https://doi.org/10.1021/acsaem.0c03187

[48] Sh.I. Nabiyev, Kh.N. Bozorov, *et al.*, "Study of the Formation of Radiation Defects in Irradiated Silicon Samples, Doped with Chromium Atoms," East Eur. J. Phys. (1), 228 (2026). https://doi.org/10.26565/2312-4334-2026-1-24

[49] Zh. Sun, N. Ya, R.C. Adams, and F.S. Fang, "Particle size specifications for solid oral dosage forms: A regulatory perspective," American Pharmaceutical Review, **13**(4), 68-73 (2010).

[50] A.J.R. Rennie, V.L. Martins, R.M. Smith, and P.J. Hall, "Influence of Particle Size Distribution on the Performance of Ionic Liquid-based Electrochemical Double Layer Capacitors," Scientific Reports, **6**(1), 22062 (2016). https://doi.org/10.1038/srep22062

[51] H. Liu, X. Cheng, Y. Chong, Hong Yuan, and J. Huang, "Advanced electrode processing of lithium-ion batteries: A review of powder technology in battery fabrication," Particuology, **57**, 56-71 (2021). https://doi.org/10.1016/j.partic.2020.12.003

[52] M.S. Payzullakhanov, Sh.D. Payziyev, and S.Kh. Suleymanov, “Modeling of Processes of Heating and Cooling of Materials in a Solar Furnace,” Applied Solar Energy, **55**(6), 404-408 (2019). https://doi.org/10.3103/S0003701X19060082

СТРУКТУРНІ, МОРФОЛОГІЧНІ ТА ЕЛЕКТРОХІМІЧНІ ВЛАСТИВОСТІ $NaFeO_2$, СИНТЕЗОВАНОГО СОНЯЧНИМ ПЛАВЛЕННЯМ

М.С. Пайзуллаханов[1,2], Ф.А. Гіясова[3], М.А. Юлдошев[4], Б.Б. Гулямов[5], Ф.А. Гіясов[3], А.Е. Отарбаєв[6], С.М. Касімов[6], U.А. Насрітдінова[7], Г.Б. Різамухамедова[8], Н.Б. Холбоєва[9], А.А. Абдувахобов[3], А.А. Мамадалієв[3]
[1]Інститут матеріалознавства Академії наук Республіки Узбекистан. Ташкент, Узбекистан
[2]Ферганський державний технічний університет, Узбекистан
[3]Міжнародний університет Кімьо в Ташкенті, Узбекистан
[4]Міжнародний університет Туран, Наманган, Узбекистан
[5]Центр передових технологій, Ташкент, Узбекистан
[6]Нукусський державний педагогічний інститут імені Аджиніяза, Нукус, Узбекистан
[7]Ташкентський інститут інженерів іригації та механізації сільського господарства, Національний дослідницький університет, Узбекистан
[8]Наманганський державний технічний університет, Наманган, Узбекистан
[9]Наманганський державний університет, Наманган, Узбекистан

У цій статті представлено синтез тетрагонального фероксиду натрію ($NaFeO_2$) методом плавлення в сонячній печі. Отриманий матеріал характеризується квазісферичною морфологією, середнім розміром частинок ~1,2 мкм, високою кристалічністю (~ 92%) та полідисперсним розподілом, що забезпечує ефективні шляхи транспорту та рівномірне проникнення електроліту. SEM-аналіз виявив утворення пористих агрегатів ногранулярних частинок (200-500 нм) з розвиненою питомою поверхнею (5-10 м²/г). DTA/TGA демонструє багатоступеневі термічні перетворення системи $Na_2CO_3+Fe_2O_3$ з утворенням $NaFeO_2$ при 800–850 °C, що підтверджує термічну стабільність матеріалу. Рентгеноструктурний аналіз підтвердив високу кристалічність тетрагональної фази з параметрами a = 4,47 Å, c = 14,4 Å та розміром області когерентного розсіювання ~ 28 нм. Отримані дані свідчать про високу структурну стабільність та електрохімічну активність $NaFeO_2$, що робить його перспективним для використання в натрій-іонних акумуляторах.

Ключові слова: *$NaFeO_2$; сонячна піч; синтез розплаву; кристалічність; мікроструктура; пористі агрегати; скануюча електронна мікроскопія (SEM); рентгенівська дифракція (XRD); термічний аналіз (DTA/TGA); твердофазні реакції*

EAST EUROPEAN JOURNAL OF PHYSICS. 2. 470-475 (2026)
DOI:10.26565/2312-4334-2026-2-52 ISSN 2312-4334

FORMATION AND EXTRACTION OF H^- IONS FROM PENNING DISCHARGE WITH METAL HYDRIDE CATHODES IN LMF AND HMF MODES

Ihor Sereda[1]*, Yaroslav Hrechko[1], Kostyantyn Sereda[1], Oleh Vorobiov[2]
[1]V.N. Karazin Kharkiv National University, Kurchatov av. 31, 61108, Kharkiv, Ukraine
[2]Ivan Kozhedub Kharkiv National Air Force University, Kharkiv, Ukraine
**Corresponding author email: igorsereda@karazin.ua*

Received January 31, 2026; revised March 23, 2026; accepted May 20, 2026

The use of metal hydride cathodes in Penning discharges offers a promising approach to the efficient production of negative hydrogen ions under low- and ultralow-pressure conditions. In this work, we summarize and extend our experimental studies on the influence of metal hydride elements on the characteristics of Penning discharge with axial extraction of negative ions. At low residual pressure, the introduction of metal hydride cathodes enables plasma generation exclusively from hydrogen released by the cathode material, without any external gas injection. This feature opens the way to the development of compact, gas-feed-free ion sources with excellent gas utilization. The negative ions extraction mechanism is shown to depend strongly on the operating mode of the Penning discharge, determined by the magnetic field strength. In the low magnetic field mode, the expansion of the anode layer toward the discharge axis and the associated negative space charge suppresses efficient extraction, limiting it mainly to paraxial ions and those formed near the extraction aperture. In contrast, in the high magnetic field mode, the anode layer becomes thin, and the central plasma region is essentially field-free, enabling the extraction of negative ions from the entire discharge cross-section. Furthermore, the effect of increasing the anode diameter is investigated. Enlarging the anode diameter increases the plasma volume surrounding the metal hydride cathodes, leading to improved plasma uniformity, more homogeneous cathode heating, and a more uniform hydrogen release. These effects enhance the conditions for negative ions formation and result in a higher extracted current. The results demonstrate the feasibility and advantages of metal-hydride-based Penning ion sources for efficient production of negative ions under low-pressure operation.

Keywords: *Negative ions; Hydrogen; Penning discharge; Metal hydride; Volume source*
PACS: 29.25.Bx, 81.40.Wx

Recent progress in high-energy hydrogen neutral beam technology has intensified interest in negative-ion sources, since efficient neutralization at energies above ~60 keV per nucleon is only feasible for H^- beams [1]. Negative ions can be produced either in plasma volume via dissociative attachment to rovibrationally excited $H_2(v)$ molecules or on low-work-function cesiated surfaces [2]. Although cesium greatly enhances H^- yield, its leakage degrades high-voltage insulation and limits long-term reliability, motivating the search for cesium-free alternatives [3].

Efforts to reduce cesium consumption have included the development of specialized cartridges based on Cs_2CrO_4 alloy combined with an St101 getter [4]. Although this approach improves source stability and operational reliability, it does not resolve the fundamental issue of identifying alternative materials that can deliver negative-ion yields comparable to those of cesium-coated surfaces. Subsequent experimental studies have demonstrated that tantalum surfaces in hydrogen plasma can enhance H^- production through the formation of highly rovibrationally excited $H_2(v)$ molecules generated by recombinative desorption [5]. Alkali-metal-based surface coatings have also been shown to increase negative-ion emission; however, their practical application is limited by high chemical reactivity and rapid sputtering under plasma exposure [6]. As a result, current research has increasingly focused on inorganic compounds and metal alloys as more robust candidates. In particular, LaB_6 cathodes have exhibited promising performance in cesium-free Penning discharges, indicating that suitable alternative materials may ultimately replace cesium in negative ion sources [7].

Among the most promising candidates for volume negative ion sources are stable hydrides formed from ZrV getter alloys, similar to St707, which are well known for their extremely low equilibrium hydrogen pressures, fast sorption–desorption kinetics, and pronounced thermal effects [8]. Ion bombardment of such hydrides induces the controllable release of rovibrationally excited $H_2(v)$ molecules into the plasma providing a substantial enhancement of volume H^- production. This concept opens the possibility of developing a compact, gas-feed-free ion source that operates at very low pressure and achieves high gas efficiency. It has recently been demonstrated that ZrV-based metal hydrides offer a significant advantage for H^- ion production, since hydrogen molecules are released from the hydride surface in a vibrationally excited state [9].

The extraction of negative ions is typically performed perpendicular to the magnetic field through the anode slit [2], but using high discharge voltages significantly simplifies the source design by modifying the discharge behavior [10]. Particularly, a flux of negative particles (ions and electrons), together with positive ions, is yielding along the magnetic field [17]. Therefore, replacing the cathode with a metal-hydride cathode and reversing the extraction electrode polarity can convert a conventional positive-ion source into a gas-feed-free negative-ion source.

Cite as: I. Sereda, Y. Hrechko, K. Sereda, O. Vorobiov, East Eur. J. Phys. 2, 470 (2026), https://doi.org/10.26565/2312-4334-2026-2-52

In this paper, we summarize our previous results on the impact of metal hydrides on the properties of a Penning discharge with axial extraction of H^- ions, and extend the analysis to different anode diameters. This approach is used to demonstrate the possibility of increasing the negative-ion current by enlarging the plasma volume in which the metal-hydride cathodes are immersed.

EXPERIMENTAL SETUP

The experiments were performed in a Penning-type discharge cell comprising two opposing flat cathodes (1 and 5) and a tubular anode (4) placed in an external longitudinal magnetic field of up to 0.1 T (Fig. 1). Discharge operation was achieved by applying a positive potential to the anode. The cathode (1*)* could be electrically biased up to −400 V, while the opposite cathode (5) was maintained at ground potential.

To increase the plasma-filled volume, the anode of 37 mm in diameter and 12 mm in length could be replaced by an enlarged anode with a diameter of 56 mm and a length of 30 mm. In both configurations, the cathodes were disk-shaped electrodes 20 mm in diameter and 5 mm thick, mounted coaxially at a distance of 15 mm from the respective anode ends.

Two cathode configurations were used: single metal hydride cathode (1MH) with cathode (1) made of metal hydride and cathode (5) made of copper and double metal hydride cathodes (2MH), with both cathodes made of metal hydride.

The cathode material captures and retains a large amount of hydrogen due to its multiphase structure, which includes tetragonal ε-ZrH_2 and the C15-type ZrV_2H_x intermetallic Laves phase with the metal type of hydrogen bond [8]. This intermetallic phase absorbs hydrogen efficiently already at room temperature and pressures of about 0.1 MPa, with a sorption rate that is 2 – 3 orders of magnitude higher than that of pure zirconium. In contrast, the formation of zirconium hydride ZrH_2 in pure zirconium requires temperatures of about 500 K and high pressures of 7 – 10 MPa. The intermetallic phase promotes rapid hydrogen uptake and diffusion, so that even zirconium becomes effectively hydrogenated at room temperature. As a result, a mixture of hydrides is formed, where both phases are highly saturated with hydrogen. Additionally, zirconium hydride has an extremely low equilibrium dissociation pressure (about 1.5×10^{-9} Pa at 500 K), which ensures strong hydrogen retention within the lattice, enabling operation under high-vacuum conditions.

Since the process of the alloy uptake with hydrogen is accompanied by the crystal lattice destruction, the obtained hydride powder was mixed with a copper binder and then pressed into a disk 2 cm in diameter with a thickness of 0.5 cm. Each cathode absorbed approximately 870 cm^3 of hydrogen at atmospheric pressure and room temperature.

The main advantage of a metal hydride cathode is its ability to absorb hydrogen isotopes and release them into the plasma at low pressure via controlled thermal decomposition of the hydride phases. To avoid uncontrolled desorption and pressure spikes, the cathode temperature was monitored with thermocouples and maintained below 80 °C, well below the hydride decomposition threshold [8]. Under these conditions, hydrogen is released exclusively through ion-stimulated processes. Rovibrationally excited $H_2(v)$ molecules form by surface recombination of hydrogen atoms and are then converted to H^- via dissociative electron attachment, providing an energy-efficient, surface-driven pathway for enhanced negative-ion production.

The experiments were conducted at a residual pressure of 0.2 mPa in the vacuum chamber pumped by a diffusion pump, which went to approximately 0.6 mPa during discharge operation due to hydrogen release from the cathodes. Notably, no external gas injection was used under these conditions. The residual gas composition was not controlled in our experiment; however, it is assumed to be typical for such conditions, consisting mainly of N_2, CH-containing species, and water vapor. The partial pressures of molecular and atomic hydrogen under similar conditions of metal hydride application were measured in [9], and it was shown that the gases incapable of forming stable negative ions results in very low extracted negative currents, primarily composed of co-extracted electrons.

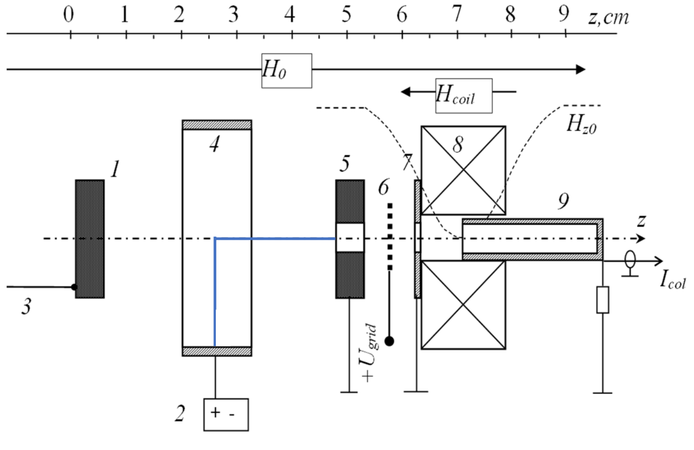

Figure 1. The scheme of the experiment.
1 – metal hydride cathode, 2 – power unit, 3 – thermocouple, 4 – anode, 5 – metal hydride/copper cathode with an aperture, 6 – reflecting grid $U_{grid} = +1.6$ kV, 7 – electrons collector, 8 – filter magnetic coil, 9 – H^- ion collector, H_0 – main axial Penning magnetic field ($H_0 = 0 - 0.1$ T), H_{coil} – reverse magnetic field of the filter.

During Penning discharge operation in high-voltage mode axial electrons oscillate between the cathode layers and could fall in the central region of the cathodes, which allows for the axial output of negatively charged particles including negative ions [10]. To suppress electrons and positive ions in the extracted axial beam, an electromagnetic filter was used. It was positioned behind the cathode (5) with the central aperture of 5 mm in diameter and consisted of a grid (6) for retarding positive ions, a magnetic coil (8) for deflecting electrons, an electron collector (7) for the diverted electrons, and a collector (9) for the extracted axial H^- ion beam. The required parameters for the filter operation were determined through numerical analysis of electron and H^- ion trajectories [11].

RESULTS AND DISCUSSION

The operation of volume sources of negative hydrogen ions relies on the interaction between low-energy (thermal) electrons and rovibrationally excited hydrogen molecules $H_2(v)$. In this process, an electron is temporarily captured, forming a short-lived resonant compound state H_2^-. The decay of this state can proceed through dissociative electron attachment, resulting in the production of a negative hydrogen ion (H^-) and a neutral hydrogen atom:

$$H_2(v) + e \rightarrow H_2^- \rightarrow H^- + H. \tag{1}$$

The intensity of resulted H^- ion beam is determined primarily by the concentration of rovibrationally excited $H_2(v)$ molecules, which generated in plasma by energetic electron impact with neutral hydrogen. In case of using a preliminary hydrogenated metal hydride, rovibrational excitation of hydrogen molecules are ensured by recombination of H-atoms at the metallic surface, which then can be converted to H^- ion by dissociative electron attachment. So, the challenge is to increase the concentration of rovibrationally excited $H_2(v)$ molecules keeping the working pressure below 0.3 Pa to eliminate the negative ion losses due to collisional destruction [16].

The concept of the source relies on a specific feature of Penning discharge operated at low pressure and high voltage. The electron current dominates in the central cathode region, enabling axial extraction of negatively charged particles, including negative ions. In contrast to the Ellers-type ion source operating in a high-current mode, H^- ions in this Penning discharge are generated in the central field-free plasma region via dissociative attachment of low-energy electrons (2 – 4 eV) to vibrationally excited hydrogen molecules $H_2(v)$, released from the metal hydride cathode. The produced negative ions then drift axially through the field-free plasma, confined by the anode layer, and can be easily extracted through a central aperture in the cathode [2, 10].

The characteristics of a Penning discharge are known to be strongly influenced by the experimental conditions. The discharge operating modes were identified as functions of the key physical parameters, namely the anode voltage, magnetic field strength, and working gas pressure [10]. Particularly under our experimental conditions (the pressure in the vacuum chamber of 0.6 mPa, the applied voltage of 5 kV and the discharge current of about 0.8 mA) the discharge burns between “low-magnetic field mode” (LMF -mode) at $H_0 = 0.06$ T and “high-magnetic field mode” (HMF-mode) at $H_0 = 0.1$ T. Graphically it can be described in Fig.2. In LMF-mode, the axial potential is distorted by a negative space charge distributed throughout the entire discharge volume resulting in the potential sag on the axis cell. In contrast, in the HMF-mode a field-free plasma region forms near the discharge axis, while the electron cloud is confined to a sheath adjacent to the anode. Due to the potential sag in LMF-mode, the energy spectrum of the emitted axial H_2^+ ions is strongly shifted to the low-energy region (Fig.3).

Since the transition from LMF-mode to HMF-mode is not abrupt because of its dependence on gas pressure, it is not possible to unambiguously define the point at which LMF-mode changes into HMF-mode. Instead, a regime of gradual transition exists in which effects characteristic of both LMF and HMF modes coexist and mutually influence each other.

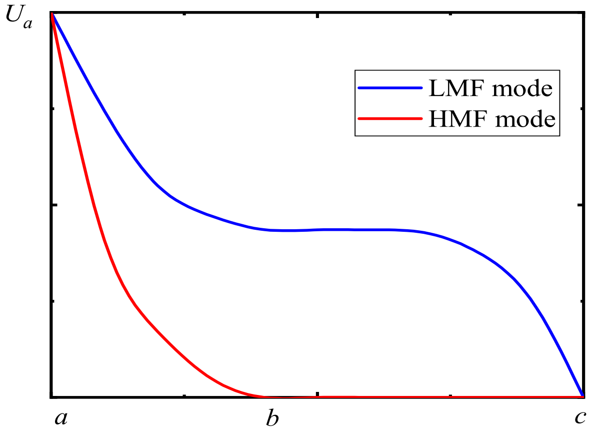

Figure 2. The schematic potential distribution curve inside the discharge cell when measuring the energy spectra of extracted ions. Dots a, b, c (see Fig. 1) designate: a – anode, b – cell center, c – cathode

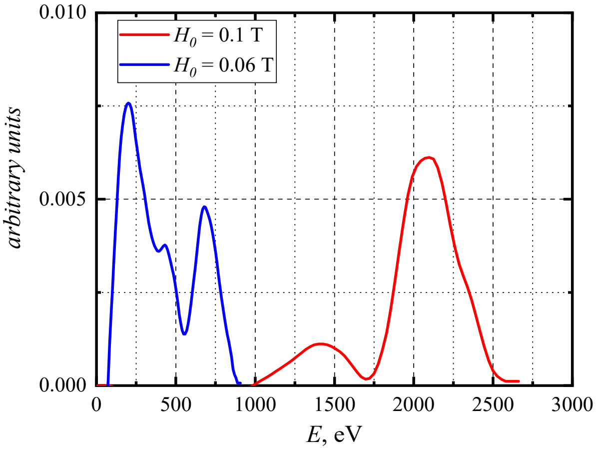

Figure 3. The H_2^+ ion energy distribution function axially emitted from Penning discharge with metal hydride cathode at $P = 0.6$ mPa and $U_d = 5$ kV

Using the relations between the magnitude of the potential sag and the discharge current for LMF-mode [10] one can obtain the following expressions for the discharge current:

$$I_d = 4\pi l \varepsilon_0 n_0 v_e \sigma_i (U_a - U_0) \tag{2}$$

Substituting the following parameters: anode length $l = 0.0015$ m, ionization cross section of the hydrogen molecule $\sigma_i \approx 10^{-20}$ m^2, electron velocity for ionization $v_e = 2.35 \times 10^6$ m/s, neutral particle density n_0 [m^{-3}] = $2.6 \times 10^{20} p$ [Pa], anode potential $U_a = 5$ kV, and assuming ($U_0 \sim E_{max}/e \approx 250$ V from Fig.3), Eq. (2) yields a local pressure in the cell of $p \approx 16$ mPa at $I_d = 0.8$ mA.

Thus, the release of hydrogen from metal-hydride leads to a local pressure increase from 0.6 mPa to 16 mPa near the cathode surface, and, when the rovibrational excitation of the released molecules is taken into account, results in a significant enhancement of negative ion formation according to Eq. (1).

The extraction mechanism of H⁻ ions depends on the mode of Penning discharge operation. In LMF-mode the anode layer expands toward the axis, and its negative space charge expels H⁻ ions from the plasma volume. In this case only ions formed near the extraction aperture in the cathode and paraxial ones could be efficiently extracted. In HMF-mode, the anode layer is thin, and the central plasma region is essentially field-free, enabling H⁻ ions to be extracted from the entire cross-section of the cell. It is demonstrated in Fig. 4 and Fig. 5.

Using single metal hydride cathode placed opposite the extraction region results in the poorest source performance, particularly for small anode radii. In LMF mode, the extraction of H⁻ ions generated near the metal hydride surface is hindered by a thick anode layer, which suppresses the extracted H⁻ current almost to zero. As the magnetic field increases, the anode layer contracts toward the anode, allowing paraxial negative ions to reach the extraction region and contribute to the extracted current, which rises to about 2.5 µA. Applying a negative bias to the metal-hydride cathode only weakly affects this behavior, increasing the extracted current to approximately 15 µA.

In HMF-mode, this effect becomes more pronounced. The anode layer is thin and only weakly affects the axial transport of H⁻ ions. As a result, the extracted H⁻ current increases by more than a factor of two due to the pushing effect of the negative potential applied to the metal hydride cathode, near which the main production of negative ions occurs.

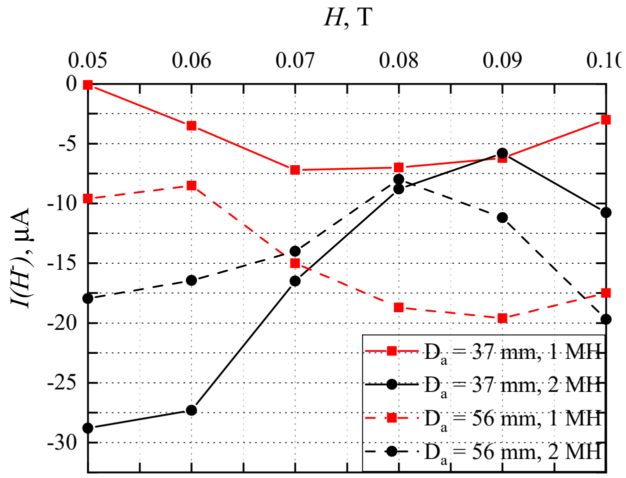

Figure 4. The current of extracted negative ions via magnetic fields at *P* = 0.6 mPa, U_d = 5 kV, I_d = 0.8 mA and grounded cathodes

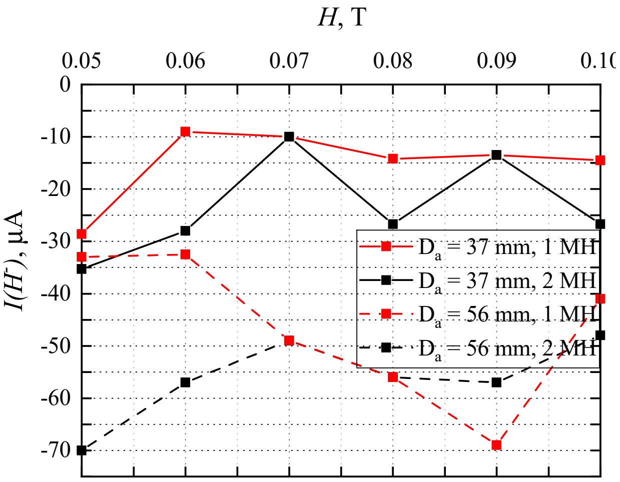

Figure 5. The current of extracted negative ions via magnetic fields at *P* = 0.6 mPa, U_d = 5 kV, I_d = 0.8 mA and electrically biased cathode (1) U_{bias} = -400 V in Fig.1.

The introduction of second metal-hydride cathode leads to much stronger increase in the extractable current. In this configuration, two spatially separated regions of efficient H⁻ ion production are formed, characterized by different extraction mechanisms. H⁻ ions generated near the cathode opposite the extraction region propagate along the discharge axis with thermal velocity when both cathodes are grounded, or are additionally accelerated toward the extraction region when a negative bias is applied. In contrast, H⁻ ions produced near the extraction region are directly extracted by the electromagnetic filter grid biased at a positive potential. The remaining ions, which are not affected by the grid potential, may be deflected toward the extraction grid by the negative space charge of the anode layer expanding toward the axis.

This effect is clearly pronounced in LMF mode, as shown in Fig. 4 and Fig. 5, both with and without the application of a negative bias. In the HMF mode, however, this difference becomes much less pronounced.

Increasing the anode diameter improves the utilization of the metal hydride cathode surface by enlarging the plasma volume in which the cathodes are immersed. The expansion of this region improves plasma uniformity and increases the effective plasma–cathode interaction area, resulting in more homogeneous cathode heating and a more uniform release of hydrogen from the metal hydride. Consequently, the conditions for negative-ion production are enhanced, leading to a higher extracted H⁻ current.

The transition from LMF to HMF mode is accompanied by the formation of a tenuous plasma region around the discharge axis, which can be distorted by potential sag [10]. This effect complicates the interpretation of the experimental results; nevertheless, the overall trends described above remain clearly observable.

CONCLUSIONS

The experimental results demonstrate the promising results of metal hydride elements using in plasma sources with efficient negative ion production. The key advantage of metal hydride lies in its ability to take up hydrogen isotopes in atomic form and release them into the plasma in a controlled manner under low-pressure conditions. Recombination of hydrogen atoms on the metal hydride surface directly produces rovibrationally excited hydrogen molecules. The feedback coupling between the discharge current and the hydrogen release rate provides efficient gas utilization, increases the density of rovibrationally excited molecules, and consequently enhances H^- ion production via dissociative electron attachment.

In a Penning discharge operated at low residual pressure, the introduction of metal-hydride cathodes enables plasma generation only on hydrogen released from the metal hydride, without any external gas injection. This opens the way to the development of a new type of compact, gas-feed-free ion source capable of operating at low and ultralow pressures with excellent gas utilization.

Formation of negative ions occurs via the dissociative mechanism of low-energy electron attachment near the surface of metal hydride cathodes, where the heightened density of rovibrationally excited hydrogen molecules is achieved. The extraction mechanism of negative ions depends on the operating mode of the Penning discharge. At low pressure, the determining factors are the electron drift within the anode layer and the presence of a practically field-free central zone, where axial electrons oscillate between the cathodes and may impinge on the central area, thereby opening the possibility of their extraction together with negative ions.

In the low magnetic field (LMF) mode, the anode layer expands toward the axis, and its negative space charge expels negative ions from the plasma volume. As a result, only ions formed near the extraction aperture in the cathode and paraxial ions can be efficiently extracted. In contrast, in the high magnetic field (HMF) mode the anode layer becomes thin, and the central plasma region is essentially field-free, allowing negative ions to be extracted from the entire cross-section of the discharge cell.

Increasing the anode diameter further enhances the efficiency of negative ions production by enlarging the plasma volume in which the metal hydride cathodes are immersed. The expansion of this region improves plasma uniformity and increases the effective plasma–cathode interaction area, leading to more homogeneous cathode heating and a more uniform release of hydrogen from the metal hydride. Consequently, the conditions for negative-ion formation are improved, resulting in a higher extracted negative-ion current.

ORCID

Ihor Sereda, https://orcid.org/0000-0002-9111-9853; **Yaroslav Hrechko**, https://orcid.org/0000-0001-9198-3660; **Kostyantyn Sereda,** https://orcid.org/0000-0001-6934-2752; **Oleh Vorobiov**, https://orcid.org/0000-0001-5966-4037

REFERENCES

[1] R.S. Hemsworth, D. Boilson, P. Blatchford, M. Dalla Palma, G. Chitarin, H.P.L. de Esch *et al.*, New J. Phys. **19**, 025005 (2017). https://doi.org/10.1088/1367-2630/19/2/025005

[2] M. Bacal, editor, *Physics and Applications of Hydrogen Negative Ion Sources*, Springer Series on Atomic, Optical, and Plasma Physics, (Springer, Cham, 2023). https://doi.org/10.1007/978-3-031-21476-9

[3] V. Dudnikov, *Development and Applications of Negative Ion Sources*, 2nd ed., Springer Series on Atomic, Optical, and Plasma Physics, (Springer, Cham, 2023). https://doi.org/10.1007/978-3-031-28408-3

[4] M.P. Stockli, B. Han, S.N. Murray, T.R. Pennisi, M. Santana, and R.F. Welton, Rev. Sci. Instrum. **81**, 02A729 (2010). https://doi.org/10.1063/1.3325085

[5] M. Bacal, K. Maeshiro, S. Masaki, and M. Wada, Plasma Sources Sci. Technol. **30**, 075014 (2021). https://doi.org/10.1088/1361-6595/abfbc8

[6] H. Kawano, Prog. Surf. Sci. **97**, 100583 (2022). https://doi.org/10.1016/j.progsurf.2022.100583

[7] R. Friedl, S. Cristofaro, and U. Fantz, AIP Conf. Proc. **2011**, 050009 (2018). https://doi.org/10.1063/1.5053307

[8] G. Sandrock, in: *Hydrogen Energy System: Production and Utilization of Hydrogen and Future Aspects*, edited by Y. Yürüm, NATO Science Series E, Vol. 295 (Kluwer Academic, Norwell, MA, 1995), pp. 135–166. https://doi.org/10.1007/978-94-011-0111-0

[9] I. Sereda, Y. Hrechko, M. Azarenkov, and K. Sereda, Int. J. Hydrogen Energy, **109**, 1321 (2025). https://doi.org/10.1016/j.ijhydene.2025.02.222

[10] W. Schuurman, Physica, **36**, 136–160 (1967). https://doi.org/10.1016/0031-8914(67)90086-9

[11] I. Sereda, A. Tseluyko, N. Azarenkov, D. Ryabchikov, and Y. Hrechko, Int. J. Hydrogen Energy, **42**, 21866 (2017). https://doi.org/10.1016/j.ijhydene.2017.07.129

УТВОРЕННЯ ТА ЕКСТРАКЦІЯ ІОНІВ H^- З РОЗРЯДУ ПЕННІНГА В LMF ТА HMF РЕЖИМАХ

Ігор Середа[1], Ярослав Гречко[1], Костянтин Середа[1], Олег Воробйов[2]
[1]Харківський національний університет імені В.Н. Каразіна, просп. Курчатова, 31, 61108, Харків, Україна
[2]Харківський національний університет Повітряних Сил імені Івана Кожедуба, Харків, Україна

Використання металгідридних катодів у розрядах Пеннінга пропонує перспективний підхід до ефективного утворення негативних іонів водню в умовах низького та наднизького тиску. У цій роботі ми підсумовуємо та розширюємо наші експериментальні дослідження впливу металогідридних елементів на характеристики розряду Пеннінга з аксіальною екстракцією негативних іонів. При низькому залишковому тиску введення металгідридних катодів дозволяє генерувати плазму виключно з водню, що виділяється матеріалом катода, без будь-якого зовнішнього напуску газу. Ця особливість відкриває шлях до розробки компактних джерел іонів без подачі газу, а також до ефективного використання газу. Показано, що механізм екстракції негативних іонів значною мірою залежить від режиму роботи розряду Пеннінга, який визначається напруженістю магнітного поля. У режимі низького магнітного поля розширення анодного шару до осі розряду та пов'язаний із ним негативний об'ємний заряд пригнічують ефективну екстракцію, обмежуючи її переважно параксіальними іонами та тими, що утворюються поблизу отвору екстракції. Навпаки, в режимі високого магнітного поля анодний шар стає тонким, а центральна область плазми практично вільна від поля, що дозволяє екстрагувати негативні іони з усього поперечного перерізу розряду. Крім того, досліджується вплив збільшення діаметра анода. Збільшення діаметра анода збільшує об'єм плазми, що оточує катоди з гідридів металу, що призводить до покращення однорідності плазми, більш однорідного нагрівання катода та більш рівномірного виділення водню. Ці ефекти покращують умови для утворення негативних іонів та призводять до вищого струму вилучення. Результати демонструють доцільність і переваги джерел іонів Пеннінга на основі гідридів металу для ефективної генерації негативних іонів за низького тиску.

Ключові слова: *негативні іони; водень; розряд Пеннінга; гідрид металу; об'ємне джерело*

East European Journal of Physics. 2. 476-481 (2026)
DOI:10.26565/2312-4334-2026-2-53 ISSN 2312-4334

STRUCTURAL, MORPHOLOGICAL, AND OPTICAL PROPERTIES OF ZnO THIN FILMS GROWN ON Si SUBSTRATES VIA ULTRASONIC SPRAY PYROLYSIS

Azim K. Soatov[1]*, **Abdumajit R. Turayev**[1], **Azamat O. Arslonov**[2]
[1]*Center for Development of Nanotechnologies, National University of Uzbekistan*
[2]*Department of Physics, National University of Uzbekistan, Tashkent 100174, Uzbekistan*
**Corresponding Author e-mail: soatovazim36@gmail.com*

Received March 1, 2026, revised April 10, 2026; accepted April 14, 2026

Based on scientific sources presenting modern semiconductor device fabrication technologies and growth methods, the influence of external factors on ZnO samples was evaluated through various approaches. In this work, ZnO thin films were grown on Si substrates using the ultrasonic spray pyrolysis (USP) method. The physical characteristics of the obtained samples, including the optical bandgap energy and in-situ laser Raman spectroscopy measurements, were investigated. The primary objective of this study was to synthesize ZnO thin films with precise nanometric thicknesses on silicon (Si) substrates and to investigate the influence of substrate temperature, precursor composition, and evaporation rate. Using Ellipsometry, XRD, and SEM, we characterized the film thickness, crystal lattice structure, and morphological evolution during growth.

Keywords: *Silicon; Zinc oxide; Crystal structure; Molar concentration; Bandgap*
PACS: 81.15.Rs

INTRODUCTION

Zinc oxide (ZnO) is a semiconductor characterized by a wide direct bandgap, with an energy of approximately 3.37 eV at room temperature. This value significantly exceeds the bandgap energies of conventional diamond-structured semiconductors such as Si, Ge, and GaAs. These unique properties enable the development of a new generation of nanomaterials. Consequently, ZnO is considered a promising material for optoelectronic devices, including ultraviolet (UV) photodetectors, light-emitting diodes (LEDs), transparent conducting oxides, pressure sensors, and next-generation memory elements [1]. The exciton binding energy of ZnO is approximately 60 meV, which is relatively high. This results in strong exciton emission even at room temperature, thereby enhancing the efficiency of its application in light-emitting devices [2,3].

Various methods have been developed to synthesize ZnO thin films with diverse morphological and structural properties. These include sol-gel spin-coating, hydrothermal growth, chemical vapor deposition (CVD), and spray pyrolysis [4]. Among these techniques, ultrasonic spray pyrolysis (USP) has gained particular attention for its simplicity, cost-effectiveness, and ability to control film thickness and composition over large areas [5]. This method allows for precise control over the precursor solution concentration, which significantly influences the crystal structure, defect density, and optical properties of the ZnO films [6]. It is well known that defects within the ZnO structure, specifically oxygen vacancies (V_O) and zinc interstitials (Zn_i), strongly affect its optical and electronic properties [7]. These defects create localized energy levels within the bandgap, resulting in defect-related emissions in the visible spectrum and altering the overall quality of the film. Previous studies have demonstrated that increasing the precursor concentration during deposition enhances crystalline quality, reduces defect density, and improves photoluminescence properties [8,9]. The aim of this research is to investigate how the molar concentration of the precursor affects the structural and optical properties of ZnO thin films deposited via the USP method. By analyzing the variations in crystallinity, morphology, and photoluminescence behavior across different molar concentrations, this study explores the potential to optimize ZnO thin films for advanced optoelectronic applications [10].

2. MATERIALS AND METHODS

2.1. Substrate Preparation

Zinc oxide (ZnO) thin films were deposited on Si (100) oriented silicon substrates using the ultrasonic spray pyrolysis (USP) technique. Prior to the deposition process, the silicon substrates underwent a rigorous cleaning procedure to eliminate contaminants and ensure optimal film-to-substrate adhesion. The cleaning process involved sequential immersion of the substrates in three different solutions for 10 minutes each: 1-Hydrofluoric acid (HF), 2-Acetone, 3-Ethanol. Hydrofluoric acid was employed to remove the native oxide layer (SiO_2) from the silicon surface, while acetone and ethanol were used to eliminate organic residues. Following the chemical cleaning steps, the substrates were thoroughly rinsed with deionized (D.I.) water to ensure the complete removal of any remaining impurities and organic solvents. This cleaning protocol is critical for achieving uniform, planar growth of ZnO thin films and for establishing strong adhesion to the substrate.

2.2. Solution Preparation

Zinc acetate dihydrate [$Zn(CH_3COO)_2{\cdot}2H_2O$] was employed as the zinc precursor during the deposition process. Precursor solutions were prepared at three distinct molar concentrations: 0.3 M, 0.4 M, 0.5 M [11]. Each solution was

---

Cite as: A.K. Soatov, A.R. Turayev, A.O. Arslonov, East Eur. J. Phys. 2, 476 (2026), https://doi.org/10.26565/2312-4334-2026-2-53

synthesized by dissolving the appropriate amount of zinc acetate in deionized water. The mixture was continuously stirred until a completely homogeneous solution was achieved. These specific molar concentrations were selected to systematically investigate the influence of precursor concentration on the structural and morphological properties of the resulting ZnO thin films [12,13].

2.3. Deposition Process

The deposition of ZnO thin films was carried out using an ultrasonic nebulizer operating at a frequency of 1.7 MHz. This device atomizes the precursor solution into fine aerosol droplets. The generated droplets were transported into the reaction chamber by a carrier gas flow of oxygen at a constant rate of 500 sccm (standard cubic centimeters per minute). Oxygen was chosen as the carrier gas to facilitate the oxidation of zinc acetate during the pyrolysis process, leading to the formation of the ZnO phase. Silicon substrates were placed on a heated substrate holder, and the temperature was maintained at a constant 400 °C throughout the deposition process. This specific temperature was selected to facilitate the thermal decomposition of the zinc acetate precursor, leading to the formation of high-quality ZnO thin films [14,15].

The thickness of the deposited films for all samples was approximately 80–100 nm. The thickness of both single-layer and multi-layer thin film structures was measured at various incidence angles. Additionally, the optical properties of the film structures, namely the refractive index and extinction coefficient, were determined across the ultraviolet (UV), visible, and infrared (IR) wavelength ranges (240–2500 nm). The thickness of the primary ZnO film layer is 86.64 nm, which is considered an optimal thickness for semiconductor optoelectronics. A surface roughness layer with a thickness of 40.18 nm was also identified, aligning perfectly with the granular structure observed in the SEM images. An interface layer of 6.21 nm and a native SiO_2 oxide layer of 10.50 nm were detected between the ZnO and the Si substrate. At a wavelength of 632.8 nm, the refractive index of the ZnO layer was found to be n = 1.8491. This value is close to the theoretical parameters of ZnO, indicating the high optical density of the synthesized film [16,17].

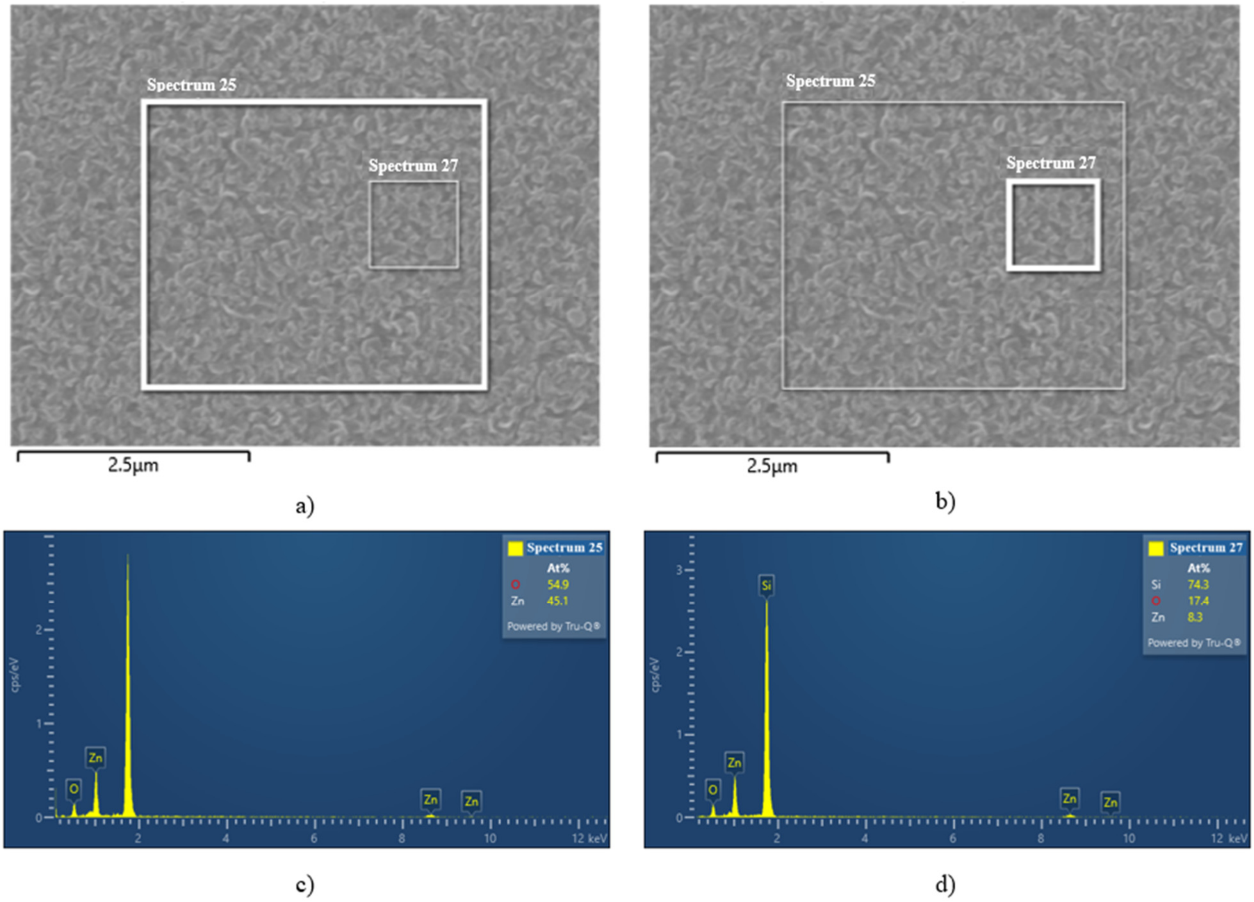

a) b)

c) d)

Figure 1. Morphological images and elemental analysis of ZnO thin films obtained using a JEOL JSM-IT510 Scanning Electron Microscope (SEM) (Japan) equipped with an Aztec Advanced (Oxford Instruments) EDX system: a-b) surface morphology of the thin film; c-d) quantitative elemental composition data (EDX spectra)

2.4. Characterization Methods

The morphology and structural properties of the grown ZnO thin films were analyzed using a Scanning Electron Microscope (SEM) to determine surface topography, uniformity, and grain size. Structural analysis was conducted using a Shimadzu X-ray diffractometer (XRD) with CuKα radiation. XRD measurements were performed over the 2θ range of 20° to 60°, enabling identification of crystallographic phases and determination of the film's preferred orientation.

3. RESULTS AND DISCUSSION

3.1. SEM Analysis of ZnO/Si Thin Films

As illustrated by the micrographs in Figure 1, the ZnO thin films synthesized via ultrasonic spray pyrolysis (USP) exhibit a nanostructured, polycrystalline morphology with well-defined grain boundaries. The film surface is composed of closely packed microcrystallites (grains) that are well-interconnected. The size of these grains varies from several tens to hundreds of nanometers, which is in good agreement with the crystallite size of 481 Å determined from the previous XRD analysis. The film surface appears dense and continuous across the entire substrate area. This is a critical physical indicator for ensuring stable electrical conductivity in semiconductor devices. When the growth mechanism and orientation are analyzed alongside the XRD results, several conclusions can be drawn. The shape and alignment of the grains suggest a preferential vertical growth orientation relative to the substrate, typically along the c-axis. This granular morphology, resulting from droplet evaporation followed by crystallization during the USP process, is reflective of the high surface energy inherent to ZnO. The SEM analysis shown in Figure 1(a, b) demonstrates that the ZnO films grown on the Si substrate are well-formed, low in defects, and nanostructured, consistent with established scientific literature. The strong correlation between the morphological (SEM), structural (XRD/Raman), and optical (UV-Vis) analysis results scientifically confirms the high quality and stability of the film's crystal lattice. Furthermore, while the SEM images highlight the dense packing of the grains, the EDX analysis confirms the stoichiometric purity of the elemental composition [18,19].

Elemental Analysis (EDX)

The energy-dispersive X-ray (EDX) spectra confirm the chemical purity and stoichiometry of the synthesized samples. As shown in the spectra of Figures 1(c, d), only peaks corresponding to Zn (zinc), O (oxygen), and Si (silicon) from the substrate were observed. The absence of foreign impurities demonstrates the high selectivity and cleanliness of the ultrasonic spray pyrolysis (USP) process. In Spectra 25, the atomic percentages (At.%) of Zn and O are close to a 1:1 ratio (e.g., 45.1% Zn and 54.9% O). The slight excess of oxygen can be attributed to atmospheric absorption or surface oxidation effects. Furthermore, the high intensity of the Si signal (74.3%) in Spectra 27 indicates either localized thinning of the film at these points or electron-beam penetration through the thin film to the underlying substrate [20].

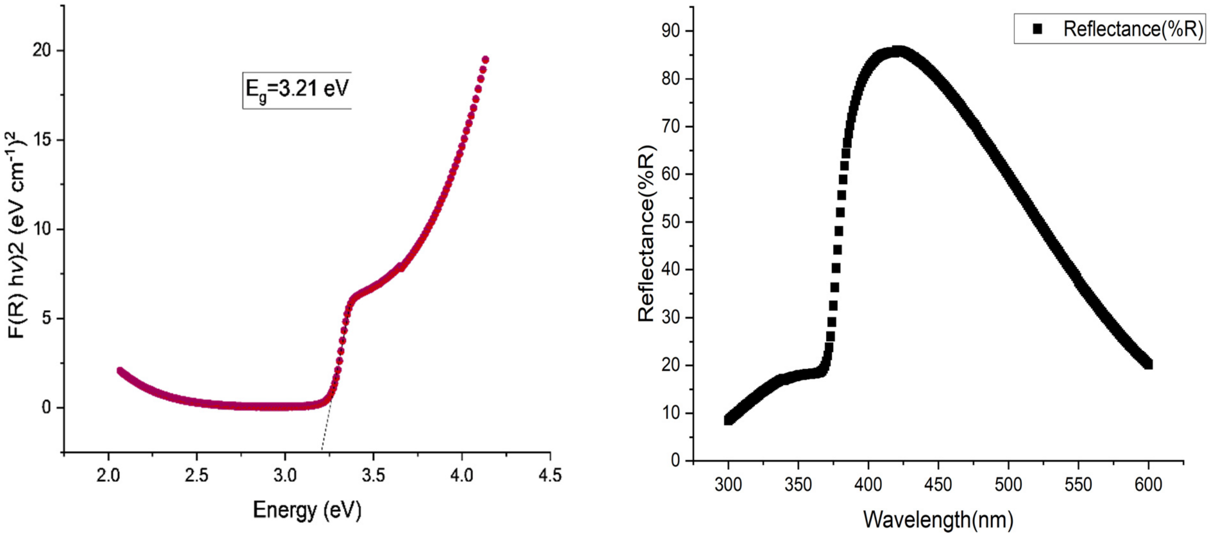

Figure 2. (a) Determination of the optical bandgap energy and (b) dependence of the reflectance coefficient on the wavelength, measured using a YOKE Focus on Lab M601S-X Spectrophotometer

3.2. Reflectance Spectrum and Optical Bandgap Analysis

Spectrophotometric measurements were employed to evaluate the optical characteristics of the synthesized ZnO thin films. Figure 2b illustrates the reflectance spectrum as a function of wavelength (λ), where a sharp increase in the reflectance index is observed near the absorption edge in the 370–380 nm range. This behavior corresponds to the fundamental absorption edge characteristic of ZnO. In the visible region (400–450 nm), the reflectance reaches a maximum value of approximately 85%, indicating high optical quality and excellent transparency (low absorption) for visible electromagnetic waves. The spectral characteristics in the 300–370 nm range confirm the material's strong absorption of ultraviolet (UV) radiation, which may be influenced by hydroxyl groups and intrinsic defects. To determine the optical bandgap energy, a Tauc plot of $[F(R)*h\nu]^2$ versus photon energy (hν) was constructed based on experimental data [21]. By extrapolating the linear portion of the curve to the energy axis in Figure 2a, the bandgap was calculated as $E_g = 3.21$ eV. While this value is close to the standard bulk ZnO bandgap of 3.37 eV, the observed redshift to 3.21 eV can be attributed to intrinsic defects, grain-size effects, or lattice strain associated with the Si substrate during the USP process. The linear nature of the plot confirms the presence of direct allowed electronic transitions in the synthesized ZnO films [22].

3.3. Structural Characterization and Crystallite Size Analysis of Zinc Oxide (ZnO)

The X-ray diffraction (XRD) pattern presented in Figure 3 fully corresponds to the hexagonal wurtzite structure of zinc oxide. The primary diffraction peaks observed at 2θ angles of 31.75°, 34.43°, and 36.25° are indexed to the (100), (002), and (101) crystallographic planes of the ZnO lattice, respectively. The structural properties of the ZnO thin films were characterized using a high-resolution X-ray diffractometer equipped with a Cu Kα radiation source (λ= 1.5406 Å). The measurements were performed in the Bragg-Brentano (BB) geometry using a D/teX Ultra 250 high-speed detector. To ensure high data quality, a K_β filter was utilized to eliminate secondary radiation. The diffraction patterns were recorded in the 2θ range of 20° to 60° with a step size of 0.01° and a scanning speed of 3.00 °/min. The X-ray diffraction (XRD) analysis confirms that the synthesized ZnO thin films possess a hexagonal wurtzite structure. The dominant diffraction peak, exhibiting the maximum intensity (100%), was observed at 2θ = 34.43°, corresponding to the (002) crystallographic plane. This finding indicates a strong preferred orientation (texture) along the c-axis, perpendicular to the substrate surface. The preferential growth along the (002) direction is a hallmark of high-quality ZnO thin films deposited on silicon substrates via ultrasonic spray pyrolysis (USP). Furthermore, the average crystallite size (D), estimated using the Scherrer formula, was found to be approximately 48 nm. This size suggests that the material is approaching the quantum-scale effect regime, which is beneficial for enhanced optoelectronic performance.

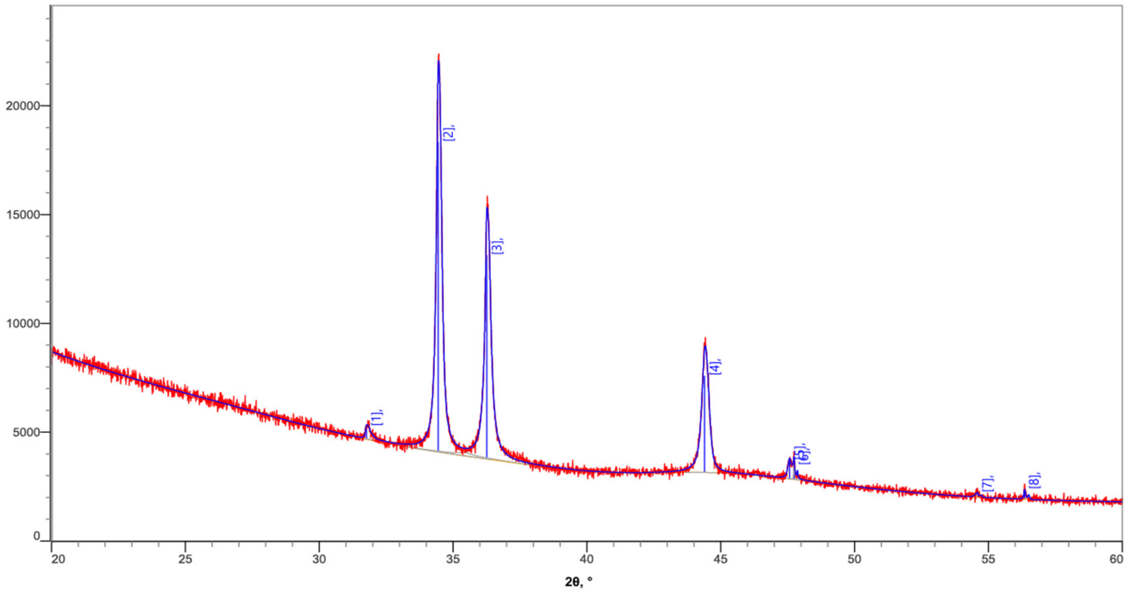

Figure 3. X-ray diffraction (XRD) patterns of the ZnO thin films grown on Si substrates

The high intensity and narrow full-width at half-maximum (FWHM) of the (002) peak (2θ = 34.43°) further demonstrate that the ZnO crystals grew in an ordered, vertical fashion on the Si substrate. The strong correlation between the X-ray structural data and the vibrational spectroscopy (Raman) results provides conclusive evidence of the high crystalline quality and structural integrity of the USP-grown ZnO thin films. The crystalline structure and phase purity of the ZnO thin films were characterized using X-ray diffraction (XRD). As shown in Figure 4, the diffraction patterns exhibit well-defined peaks that are in excellent agreement with the standard hexagonal wurtzite structure of ZnO (JCPDS card no. 36-1451). The most prominent diffraction peak is observed at 2θ = 34.43°, corresponding to the (002) plane. The high intensity of this peak relative to the (100) and (101) reflections indicates that the films possess a strong *c*-axis preferred orientation perpendicular to the substrate surface. This vertical alignment is crucial for enhancing the electrical and piezoelectric properties of the films. The average crystallite size (D) was estimated to be approximately 48 nm using the Scherrer formula:

$$D = \frac{0.9\lambda}{\beta cos\theta}$$

where λ is the X-ray wavelength (1.5406 Å), θ is the Bragg angle, and β is the full width at half maximum (FWHM) of the (002) peak. The relatively narrow FWHM values confirm the high crystalline quality and the successful growth of nanostructured ZnO via the ultrasonic spray pyrolysis method [23].

The crystalline quality of the synthesized ZnO thin films was further evaluated by analyzing the peak intensity and the full width at half maximum (FWHM) of the (002) diffraction plane. As shown in the XRD patterns, the (002) peak exhibited a remarkably high intensity of 14,230 counts per second (cps). The narrowness of the diffraction peaks, characterized by an FWHM of 0.18°, signifies a high degree of crystallinity and a low concentration of lattice defects or internal strain within the ZnO matrix. The average crystallite size (D) was calculated using the Scherrer formula, yielding values of approximately 481 Å (48 nm) and 474 Å (47 nm) for different sampling points. These dimensions confirm that the USP-grown ZnO films are characterized by a well-defined nanostructured morphology.

Table 1. Detailed XRD Structural Parameters for ZnO Thin Films

no.	**2θ (°)**	**d-spacing (Å)**	**Height (counts/s)**	**FWHM (°)**	**Int. Int. (counts/s)**	**Int. Width (W°)**	**Size (Å)**	**Norm. Int. (%)**
1	31.759(8)	2.8153(7)	580(18)	0.14(3)	141(13)	0.24(3)	630(116)	3.62
2	34.436(3)	2.60231(19)	14230(215)	0.180(3)	3906(18)	0.274(5)	481(8)	100.00
3	36.250(3)	2.47608(18)	9352(175)	0.184(5)	2885(17)	0.308(8)	474(13)	73.86
4	44.386(7)	2.0393(3)	4432(105)	0.257(6)	1594(17)	0.360(12)	348(8)	40.80
5	47.557(14)	1.9104(5)	844(31)	0.140(17)	179(31)	0.21(4)	646(79)	4.59
6	47.725(3)	1.90410(12)	636(22)	0.042(9)	34(23)	0.05(4)	2173(492)	0.87
7	54.575(13)	1.6802(4)	191(9)	0.12(4)	29(8)	0.15(5)	777(267)	0.75
8	56.327(12)	1.6320(3)	445(19)	0.071(15)	44(6)	0.099(19)	1321(279)	1.13

The correlation between high peak intensity and the nanometric crystallite size indicates that the ultrasonic spray pyrolysis process at 400°C successfully facilitates the formation of a stable, high-quality crystal lattice, suitable for high-performance optoelectronic applications. The quantitative structural data summarized in Table 1 provides a comprehensive insight into the crystalline quality of the USP-deposited ZnO thin films. The diffraction peak at 2θ = 34.436° is the most dominant, with a normalized intensity of 100.00%, which corresponds to the (002) reflection plane of the hexagonal wurtzite phase. The high crystalline integrity of the films is further evidenced by the high peak intensity (14,230 counts/s) and relatively small full width at half maximum (FWHM = 0.180°) for the (002) reflection. The average crystallite size for the major peaks – (002) and (101) – was calculated to be 481 Å and 474 Å, respectively. Interestingly, the diffraction peak at 2θ = 47.725° exhibits an exceptionally narrow FWHM (0.042°). This yields a significantly larger local crystallite size of 2173 Å, despite its relatively low normalized intensity of 0.87%. These structural parameters indicate that the films are highly ordered and nanostructured. The stability of the *d*-spacing values (e.g., $d = 2.602$ Å for the 002 plane) confirms the successful formation of the ZnO lattice on the Si substrate with minimal parasitic phases or impurities [24].

CONCLUSIONS

The analytical results demonstrate that the investigated samples are pure-phase, polycrystalline zinc oxide with hexagonal symmetry, predominantly textured along the (002) plane. Such a structural configuration is characteristic of high-quality thin films and nanopowders utilized in optoelectronics and sensor technologies. Based on the ZnO thin films grown on Si substrates via the ultrasonic spray pyrolysis (USP) method, X-ray diffraction (XRD) analysis confirmed a hexagonal wurtzite phase with a high degree of crystallinity. The preferred orientation along the (002) plane (2θ = 34.436°) signifies ordered growth along the c-axis of the crystal lattice. The average crystallite size, determined by the Scherrer formula, ranges between 34 nm and 64 nm. SEM and ellipsometric analyses revealed a continuous, granular morphology. The geometric thickness of the film was measured at 86.64 nm, with a surface roughness of 40.18 nm. A refractive index of $n = 1.8491$ (at $\lambda = 632.8$ nm) reflects the high optical density of the material. EDX analysis verified high chemical purity and stoichiometric stability (Zn≈45.1 At. %, O ≈54.9 At. %). The absence of secondary phases or impurities was further corroborated by the characteristic E_2(high) (437 cm^{-1}) Raman mode. Spectrophotometric analysis determined a direct optical bandgap of $E_g = 3.21$ eV. The samples exhibited high reflectance (~85%) and transparency in the visible region, with a sharp absorption edge in the ultraviolet (UV) spectrum.

In summary, the synthesized ZnO/Si thin films – characterized by their nanostructured nature, excellent crystalline quality, and optimal optical parameters – represent promising active layers for modern optoelectronic devices, particularly third-generation solar cells and high-sensitivity gas sensors.

ORCID

Azim K. Soatov, https://orcid.org/0009-0004-0375-2889; **Abdumajit R. Turayev,** https://orcid.org/0009-0006-7635-3162;
Azamat O. Arslonov, https://orcid.org/0009-0000-4817-8770

REFERENCES

[1] Y.A. Odedunmoye, I.T. Bello, O.K. Adedokun, M.O. Awodele, and A.A. Awodugba, "Morphological and optical characteristics of ZnO and F: ZnO thin films by a sol-gel spin coating technique," Asian Journal of Physics and Chemical Sciences, **6**(2), 1-11 (2018). https://doi.org/10.9734/AJOPACS/2018/42421

[2] Ü. Özgür, Ya.I. Alivov, C. Liu, A. Teke, M.A. Reshchikov, S. Doğan, V. Avrutin, *et al*. "A comprehensive review of ZnO materials and devices," Journal of Applied Physics, **98**(4), 041301 (2005). https://doi.org/10.1063/1.1992666

[3] C. Klingshirn, *Zinc Oxide: From Fundamental Properties Towards Novel Applications*, (Springer Science & Business Media, 2012). https://doi.org/10.1007/978-3-642-10577-7

[4] Z.L. Wang, "Zinc oxide nanostructures: Growth, properties and applications," Journal of Physics: Condensed Matter, **16**(25), R829-R858 (2004). https://doi.org/10.1088/0953-8984/16/25/R01

[5] A.V. Babalola, V. Oluwasusi, V.A. Owoeye, J.O. Emegha, D.A. Pelemo, A.Y. Fasasi, and S. Yusuf, "Effect of tin concentrations on the elemental and optical properties of zinc oxide thin films," Heliyon, **10**(1), e23190 (2024). https://doi.org/10.1016/j.heliyon.2023.e23190

[6] T.P. Rao, M.S. Kumar, S.A. Angayarkanni, and M. Ashok, "Effect of stress on optical band gap of ZnO thin films with substrate temperature by spray pyrolysis," J. Alloys Compd. **485**(1–2), 413–417 (2009). https://doi.org/10.1016/j.jallcom.2009.05.116

[7] M.R. Wagner, G. Callsen, J.S. Reparaz, J.-H. Schulze, R. Kirste, M. Cobet, I.A. Ostapenko, *et al*. "Bound excitons in ZnO: Structural defect complexes versus shallow impurity centers," Physical Review B, **84**, 035313 (2011). https://doi.org/10.1103/PhysRevB.84.035313

[8] N.L. Tarwal, A.V. Rajgure, A.I. Inamdar, R.S. Devan, I.Y. Kim, S.S. Suryavanshi, and P.S. Patil, "Growth of multifunctional ZnO thin films by spray pyrolysis technique," Sensor Actuator Phys. **199**, 67–73 (2013). https://doi.org/10.1016/j. sna.2013.05.003

[9] K.E. Knutsen, A. Galeckas, A. Zubiaga, F. Tuomisto, G.C. Farlow, B.G. Svensson, and A.Yu. Kuznetsov, "Zinc vacancy and oxygen interstitial in ZnO revealed by sequential annealing and electron irradiation," Physical Review B, **86**(12), 121203 (2012). https://doi.org/10.1103/PhysRevB.86.121203

[10] S.H. Ribut, C.A.C. Abdullah, and M.Z.M. Yusoff, "Investigations of structural and optical properties of zinc oxide thin films growth on various substrates," Results Phys. **13**, 102146 (2019). https://doi.org/10.1016/j.rinp.2019.02.082

[11] A. Arslanov, Sh. Yuldashev, N. Botirova, R. Nusretov, J. Murodov, and J. Xudoyqulov, "Impact of Precursor Molar Concentration on the Structural and Optical Properties of ZnO Thin Films Synthesized by Ultrasonic Spray Pyrolysis," Physical Science International Journal, **29**(1), 29-35 (2025). https://doi.org/10.9734/psij/2025/v29i1871

[12] D.C. Look, "Recent advances in ZnO materials and devices," Materials Science and Engineering: B, **80**(1-3), 383-387 (2001). https://doi.org/10.1016/s0921-5107(00)00604-8

[13] C. Jagadish, and S.J. Pearton, *Zinc Oxide Bulk, Thin Films and Nanostructures*, (Elsevier, 2006). https://doi.org/10.1016/B978-0-08-044722-3.X5000-3

[14] L. Znaidi, "Sol–gel deposition of ZnO thin films: A review," Materials Science and Engineering: B, **174**(1-3), 18-30 (2010). https://doi.org/10.1016/j.mseb.2010.07.001

[15] D.K. Schroder, *Semiconductor Material and Device Characterization*, (John Wiley & Sons, 2006). https://doi.org/10.1002/0471749095

[16] G.E. Jellison Jr, and L.A. Boatner, "Optical functions of ZnO determined by generalized ellipsometry," Physical Review B, **58**(7), 3581 (1998). https://doi.org/10.1103/physrevb.58.3586

[17] H. Fujiwara, *Spectroscopic Ellipsometry: Principles and Applications*. (John Wiley & Sons, 2007). https://doi.org/10.1002/9780470060193

[18] S. Roguai, and A. Djelloul, "Structural, microstructural, and optical properties of ZnO thin films prepared by spray pyrolysis," Algerian Journal of Renewable Energy and Sustainable Development, **4**(1), 94-100 (2022). https://doi.org/10.46657/ajresd.2022.4.1.9

[19] A.Q. Soatov, and A.R. Turaev, "Pressure-induced phase transitions and memristive behavior in Mn- and Co-doped ZnO oxide structures," Scientific Reports of Bukhara State University, **12**(129), 288-292 (2025).

[20] V.K. Devanarayanan, S. Deepa, J. Jassi, and Arshad Salim, "Spray-pyrolysed tin doped zinc oxide thin films-analysis based on microstructural, optical and morphological characterizations," Results in Surfaces and Interfaces, **20**, 100624 (2025). https://doi.org/10.1016/j.rsurfi.2025.100624

[21] T.P. Rao, and M.C. Santhoshkumar, "Effect of thickness on structural, optical and electrical properties of nanostructured ZnO thin films by spray pyrolysis," Appl. Surf. Sci. **255**(8), 4579–4584 (2009). https://doi.org/10.1016/j.apsusc.2008.11.079

[22] J.X. Murodov, Sh.U. Yuldashev, A.O. Arslanov, N.U. Botirova, R.Sh. Sharipova, and J.Sh. Khudoykulov, "NDR in Co:SnO_2 Memristors: Nanocluster Control for Enhanced Performance," Crystal Growth & Design, **26**(1), 317-321 (2026). https://pubs.acs.org/10.1021/acs.cgd.5c01258

[23] F. Zahedi, R.S. Dariani, and S.M. Rozati, "Structural, optical and electrical properties of ZnO thin films prepared by spray pyrolysis: effect of precursor concentration," Bull. Mater. Sci. **37**(3), 433–439 (2014). https://doi.org/10.1007/s12034- 014-0696-8

[24] J.X. Murodov, Sh.U. Yuldashev, A.O. Arslanov, N.U. Botirova, J.Sh. Xudoyqulov, R.Sh. Sharipova, R.A. Nusretov, *et al*., "Resistive Switching Behavior of SnO_2/ZnO Heterojunction Thin Films for Non-Volatile Memory Applications," East Eur. J. Phys. (3), 348−352 (2025). https://doi.org/10.26565/2312-4334-2025-3-34

СТРУКТУРНІ, МОРФОЛОГІЧНІ ТА ОПТИЧНІ ВЛАСТИВОСТІ ТОНКИХ ПЛІВОК ZnO, ВИРОЩЕНИХ НА ПІДКЛАДКАХ Si ЗА ДОПОМОГОЮ УЛЬТРАЗВУКОВОГО РОЗПИЛЮВАЛЬНОГО ПІРОЛІЗУ

Азім К. Соатов[1], Абдумаджит Р. Тураєв[1], Азамат О. Арслонов[2]
[1]Центр розвитку нанотехнологій, Національний університет Узбекистану
[2]Кафедра фізики, Національний університет Узбекистану, Ташкент 100174, Узбекистан

На основі наукових джерел, що представляють сучасні технології виготовлення напівпровідникових приладів та методи вирощування, а також вплив зовнішніх факторів на зразки ZnO було оцінено за допомогою різних підходів. У цій роботі тонкі плівки ZnO були вирощені на підкладках Si за допомогою методу ультразвукового розпилення (USP). Було досліджено фізичні характеристики отриманих зразків, зокрема енергію оптичної забороненої зони та лазерну раманівську спектроскопію *in situ*. Основною метою цього дослідження був синтез тонких плівок ZnO з точною нанометричною товщиною на кремнієвих (Si) підкладках, а також дослідження впливу температури підкладки, складу прекурсора та швидкості випаровування. Використовуючи еліпсометрію, рентгенівську дифракцію та скануючу електронну мікроскопію (СЕМ), ми охарактеризували товщину плівки, структуру кристалічної решітки та морфологічну еволюцію під час процесу росту.

Ключові слова: *кремній; оксид цинку; кристалічна структура; молярна концентрація; заборонена зона*

East European Journal of Physics. 2. 482-490 (2026)
DOI:10.26565/2312-4334-2026-2-54 ISSN 2312-4334

OPTIMIZATION OF MULTILAYER GRAPHENE-BASED ABSORBERS UNDER H-POLARIZATION VIA DIFFERENTIAL EVOLUTION IN A HYBRID COMPUTING ENVIRONMENT

Mstyslav E. Kaliberda[1,2]*, **Sergey A. Pogarsky**[1,2], **Vladyslav M. Nasonov**[1], **Viktoriia A. Lunova**[1]
[1] V. N. Karazin Kharkiv National University, 4, Svobody Sq., Kharkiv, Ukraine, 61022
[2] Institute of Radio Astronomy of NAS of Ukraine, 4, Mystetstv St. Kharkiv, Ukraine, 61002
**Corresponding Author e-mail: KaliberdaME@gmail.com*

Received February 20, 2026; revised March 29, 2026; accepted May 24, 2026

A computationally efficient framework for optimizing multilayer radar-absorbing structures based on periodic planar gratings of resistive strips embedded in a dielectric slab is presented for the *H*-polarization case. The electromagnetic response is modeled using a rigorous singular integral equation (SIE) formulation combined with an operator-based cascading technique, providing high numerical accuracy and stability with low computational cost. This ultra-fast forward solver is integrated into a parallel differential evolution (DE) optimization framework implemented in a client–server architecture, enabling efficient solution of high-dimensional inverse design problems. The optimization targets broadband absorption under normal incidence while preserving optical transparency, with graphene used as a representative resistive material. Numerical results demonstrate effective suppression of resonance-induced spectral holes and stable, wideband absorption in multilayer structures with 10 layers, showing robustness under fabrication-inspired constraints and oblique incidence.

Keywords: *Graphene; Wideband absorber; Differential evolution; Singular integral equations; Multilayer periodic structure; Global optimization*
PACS: 42.25.Bs, 02.60.Pn, 02.30.Rz, 07.05.Tp

INTRODUCTION

The ability to lower the radar visibility of various platforms is essential for their protection in modern high-threat environments. The mitigation of radar cross-section (RCS) directly determines the operational survivability of these assets [1]. This reduction in radar signatures can be achieved by optimizing sophisticated structural configurations, such as multi-layered systems, capable of broadband absorption. Beyond stealth applications, absorbing materials are essential for ensuring the electromagnetic compatibility of electronic equipment, protecting biological entities from electromagnetic radiation, and eliminating reflections in anechoic chambers [2]. However, many of the proposed absorber designs rely on complex geometries and fabrication techniques that are difficult to implement in practice, especially under constrained industrial or real-world field -deployment conditions. This motivates the development of structurally simple, scalable, and computationally efficient absorber designs. In recent years, graphene-based structures have attracted particular interest due to their unique surface conductivity, mechanical flexibility, and optical transparency, which open new possibilities for multifunctional devices. The present study focuses on the efficient optimization of the scattering and absorption characteristics of an infinite periodic multilayer grating of resistive strips, enabled by our home-made ultra-fast rigorous electrodynamic solver. The emphasis is not on proposing new exotic absorber geometry, but on demonstrating a computationally efficient optimization framework suitable for structurally simple and scalable designs.

Designing an efficient wideband device, be it an absorber, focuser, or radiator, is a non-trivial task that requires solving a complex multi-parameter optimization problem. The primary objective of this research is to achieve maximum absorption over a broad frequency band while maintaining the structure's optical transparency for H-polarization. From a computational perspective, this problem is a high-dimensional inverse design task, in which each additional layer introduces multiple strongly coupled geometric and material parameters. This requirement is dictated by the potential use of such absorbers as transparent shielding coatings for aircraft cockpit canopies or protective glass for optical sensors, where graphene interacts effectively with microwave radiation without obstructing visibility in the visible range. Although graphene is used as a representative resistive material, the proposed optimization framework and solver are applicable to a wide class of resistive or impedance-type surfaces. To ensure modeling accuracy, the dielectric medium hosting the multilayer grating is assumed to be lossless. The solution to this electrodynamic problem is implemented via a hybrid computational framework built on a client-server architecture. This approach separates the global search logic from the intensive numerical kernel, enabling efficient parallelization of the rigorous singular integral equation (SIE) method and the operator method [3], [4] across multiple computing nodes. This methodology significantly reduces the dimensionality of the resulting system of linear algebraic equations by decomposing the complex problem into stages, while the stochastic nature of the optimization algorithm enables the simultaneous analysis of high-dimensional search spaces. A key advantage of this approach is the explicit incorporation of the edge

---

Cite as: M.E. Kaliberda, S.A. Pogarsky, V.M. Nasonov, V.A. Lunova, East Eur. J. Phys. 2, 482 (2026), https://doi.org/10.26565/2312-4334-2026-2-54

condition, which accounts for the singular behavior of the electromagnetic field at the boundaries of the graphene strips. Unlike approximate approaches based on equivalent circuit models [5] or commercial codes based on finite-element method, this rigorous formulation ensures high numerical convergence and accuracy, which is essential for the precise modeling of multilayer graphene-based structures.

In such electrodynamic problems, classical optimization methods, such as gradient descent, often fail. Typically non-convex objective functions lead to stagnation in local minima. To overcome these topological challenges, the differential evolution (DE) algorithm is used [6].

While DE is a robust global search tool [6], its performance is often enhanced through specialized strategies. Recent advancements include perturbation estimation for complex Pareto fronts [7], self-adaptive mutation strategies to handle noisy functions [8], and multi-strategy approaches to prevent premature convergence [9]. The versatility of DE extends beyond electromagnetics, proving effective in training high-gain controllers [10] and optimizing magnetic sensor placement [11].

In applied electrodynamics, the current trend shifts toward hybridizing DE with surrogate modeling and machine learning to accelerate the design of ultra-wideband antennas [12], [13], slow-wave structures [14], and textile metasurfaces [15]. Neural networks are frequently employed to assist DE in learning variable patterns [16] or to replace computationally expensive simulations [17]. Despite the popularity of approximate transmission line models for absorbers [5], our approach prioritizes a rigorous SIE formulation. By leveraging an in-house developed, ultra-fast solver combined with a parallelized client-server framework, we bypass the need for surrogate models.

PROBLEM FORMULATION AND OPTIMIZATION GOALS

Consider a multilayer periodic structure consisting of N dielectric layers separated by infinite graphene strip gratings. The entire stack is situated in a Cartesian coordinate system (x, y, z), where the z-axis is directed along the infinite graphene strips, and the z-axis is normal to the layers (see Fig. 1). All gratings share a common period l along the y-axis, which allows the structure to be treated as a single periodic system. However, the geometric parameters of each layer are independent: the n-th layer, $n = 1, 2, ..., N$ is characterized by the strip width $2d_n$, and the chemical potential of the graphene μ_{cn}. The distance between the n-th and (n+1)-th gratings is Δ_n, the distance from the vacuum-dielectric interface to the first grating is h. The structure is illuminated by an H-polarized plane electromagnetic wave incident from the upper half-space ($z > 0$) at an angle θ relative to the normal. The structure is infinite along the x-axis. The magnetic field vector of the incident wave is directed along the strips (the x-axis):

$$H_x^i(y,z) = \exp(-ik_0(y\sin\theta + z\cos\theta)), \tag{1}$$

where $k_0 = 2\pi/\lambda$ is the wavenumber in free space, and the time dependence is assumed to be $\exp(-i\omega t)$.

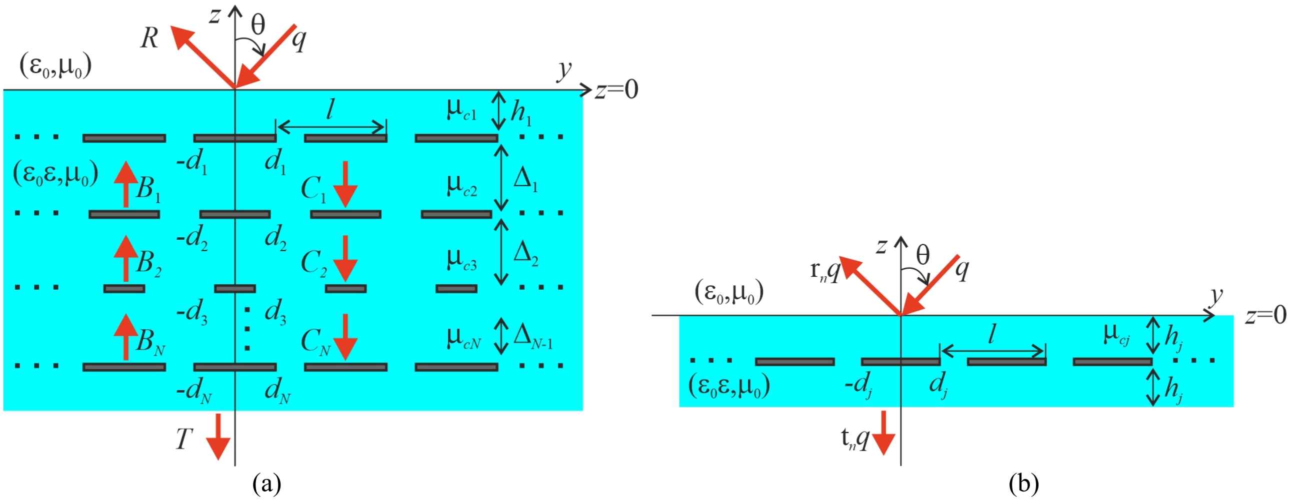

(a) (b)

Figure 1. Structure geometry. (a) Multilayer structure, (b) single layer.

Graphene is modeled as an infinitesimally thin conductive sheet with a surface conductivity $\sigma = (f, \mu_c, \tau, T)$, calculated using the Kubo formula, which includes both intraband and interband transitions [18], [19]. Here, f is the frequency, τ is relaxation time, and T is the temperature. In our model, graphene strips are treated as resistive boundaries imposing a discontinuity in the tangential magnetic field proportional to the surface current density and continuity of the tangential electric field component:

$$E_y^+ = E_y^-, \text{ in the plane of strips,} \tag{2}$$

$$H_x^+ - H_x^- = \sigma E_y^+, \text{ on graphene strips.} \tag{3}$$

Here, the superscripts "+" and "–" denote the field values on the upper and lower sides of the graphene strip, respectively.

The primary objective of the optimization is to design a structure that acts as a wideband absorber in the microwave range while maintaining optical transparency. Since optical transparency is inherent to the material choice (graphene and transparent dielectrics), the optimization routine focuses on maximizing the absorbance $A(f)$ in the target frequency band $[f_{\min}, f_{\max}]$ under normal incidence, $\theta = 0^{\circ}$. The absorbance is defined as $A = 1-R-T$, where R and T are the power reflection and transmission coefficients, respectively. Thus, the problem is reduced to finding the optimal vector of parameters $\mathbf{P} = (h, \Delta_1,..., \Delta_{N-1}, d_1,..., d_N, \mu_{c1},..., \mu_{cN})$ that minimizes the following cost function:

$$F(\mathbf{P}) = \int_{f_{\min}}^{f_{\max}} S(A(f,\mathbf{P}))df\,, \tag{4}$$

where $S(x)$ is local scoring or penalty function.

The search space is constrained by physical realizability and fabrication limits, such as minimum strip width and feasible doping levels.

NUMERICAL MODELING STRATEGY

The electromagnetic simulation of the proposed structure is performed using a hybrid scheme that combines a rigorous SIE method for individual layers and an operator-based cascading technique for multilayer systems.

Scattering Matrix of a Single Layer

First, let us consider an auxiliary problem of diffraction by the n-th individual periodic grating embedded in a dielectric slab of width h_n, characterized by a strip width of $2d_n$, a period l, and a graphene chemical potential μ_{cn}. Following the rigorous derivation presented in our previous work [3], the problem is reduced to finding the unknown function $F(\xi)$, which is related to the derivative of the surface current density on graphene strips. The enforcement of boundary conditions leads to SIE of the first kind with a Cauchy-type kernel:

$$\frac{1}{\pi} PV \int_{-\delta}^{\delta} \frac{F(\xi)}{\xi-\psi} d\xi + \frac{1}{\pi} \int_{-\delta}^{\delta} K(\psi,\xi) F(\xi) d\xi = -\frac{l}{2\pi} \frac{\partial}{\partial z} H^p, \ |\psi| < \delta, \tag{5}$$

where $\xi = 2\pi y/l$, $\delta = \pi d_n/l$ are dimensionless coordinate and half of the strip width, $K(\psi, \xi)$ is a regular kernel function, H^p is so-called primary field and it describes the excitation field.

We discretize (5) using the Nyström-type method [20], [21] with Gauss-Chebyshev quadrature rules, converting the integral equation into a compact system of linear algebraic equations. Solving this system yields the Fourier coefficients of the scattered field and allows one to construct the local reflection r_n and transmission t_n operators.

Coupling via Operator Equations

Once the scattering operators r_n and t_n are determined for all N layers, the electromagnetic response of the entire stack is determined using the operator method for multilayer structures [4]. Unlike standard transfer matrix methods, which may suffer from numerical instability due to exponentially growing terms, we employ a stable recursive system of matrix equations of the second kind.

Let $\mathbf{B}_m$ and $\mathbf{C}_m$ denote the vectors of Fourier amplitudes of the waves propagating upwards (away from the substrate) and downwards (towards the substrate) in the region between the m-th (m+1)-th gratings, respectively (see Fig. 1). The coupling between adjacent layers is governed by the following set of Fredholm second-order matrix equations:

$$\mathbf{B}_m = \mathrm{t}_{m+1}\mathrm{e}_m\mathbf{B}_{m+1} + \mathrm{r}_{m+1}\mathrm{e}_m\mathbf{C}_m, \tag{6}$$

$$\mathbf{C}_m = \mathrm{r}_m\mathrm{e}_m\mathbf{B}_m + \mathrm{t}_m\mathrm{e}_{m-1}\mathbf{C}_{m-1}, \tag{7}$$

where e_m is a diagonal matrix of phase shifts accounting for the propagation of spatial harmonics through the dielectric of thickness $\Delta_m = h_m + h_{m+1}$: $\mathrm{e}_m = \mathrm{diag}\{\exp(i\,\gamma_k\,\Delta_m)\}$, $k = -\infty...+\infty$.

For a finite stack of N layers, the structure is closed by the radiation conditions at the top and bottom interfaces. The total reflection, $\mathbf{R}$, and transmission, $\mathbf{T}$, amplitude vectors are expressed as:

$$\mathbf{R} = \mathrm{r}_1\mathrm{q} + \mathrm{t}_1\mathrm{e}_1\mathbf{B}_1, \tag{8}$$

$$\mathbf{T} = \mathrm{t}_N\,\mathrm{e}_N\mathbf{C}_N. \tag{9}$$

For numerical implementation, the operators are truncated by retaining Floquet harmonics with indices $k \in [-M_{tr}, M_{tr}]$, resulting in matrices of size $(2M_{tr} + 1)\times(2M_{tr} + 1)$. Due to the exponential decay of evanescent modes in dielectric spacers, values $M_{tr}\approx5–10$ provide sufficient accuracy. The computational cost scales linearly with the number of layers N.

The key advantage of the proposed formulation lies not only in numerical accuracy but also in its ability to serve as an efficient forward solver within large-scale optimization loops. By reducing the electromagnetic problem to a surface-based formulation, the number of unknowns scales with the number of interfaces rather than with the physical volume of the multilayer structure. This makes repeated forward evaluations feasible even for multilayer systems, which is generally impractical for volumetric methods such as the finite-element method (FEM) or the finite-difference time-domain (FDTD) method.

PARALLEL COMPUTATIONAL FRAMEWORK

To efficiently solve the inverse scattering (optimization) problem, which requires evaluating the objective function thousands of times, we developed a heterogeneous parallel computing framework. The system follows a master-slave architecture, leveraging Python's flexibility for the evolutionary algorithm and C++'s raw computational speed for the rigorous electrodynamic solver.

The framework consists of two distinct software components communicating over a TCP/IP network:

The server (Orchestrator) is written in Python. This component manages DE population, handles the genetic operations (mutation, crossover, selection), and dispatches computing jobs to available clients. It uses the asyncio library for non-blocking network communication and threading to separate the DE logic from the graphical user interface (GUI). The clients (solvers) represent the High-performance applications written in C++. Each client acts as a function evaluator. It receives a set of geometric and material parameters, constructs the corresponding scattering matrices, and computes the spectral response.

Both server and client applications have graphical user interfaces (GUI). On the server side, this enables real-time visualization of the convergence curve and dynamic adjustment of DE hyperparameters such as mutation factor, F, crossover rate, CR. On the client side, the GUI provides visual feedback on the current structure-layer profile and field distribution, which is essential for debugging and monitoring the physical validity of the solution.

The core optimization logic resides on the Python server. To maximize resource utilization, the server maintains a pool of connected C++ clients. The DE algorithm is parallelized at the generation level.

During population initialization, the server generates an initial population of NP vectors within the specified bounds. The initialization and subsequent evolution are confined within a hyper-rectangular search space defined by the lower and upper bounds for each parameter, e.g., graphene chemical potential $\mu_{cn} \in [0,\ 1]$ eV, layer spacing $\Delta_n = h_{1,n+1}+h_{2,n}$, where h_1, $h_2 \in [\varepsilon_{gap},\ h_{\max}]$. A specific geometric constraint is applied to the strip width $2d_n$ to ensure the physical realizability of the periodic structure. To prevent the graphene strips from overlapping with neighboring periods or touching the cell boundaries, the maximum strip width is strictly limited $2d_{\max} = l - \varepsilon_{gap}$, where ε_{gap} is a small safety margin, while the minimum strip width $2d_{\min} = \varepsilon_{gap}$. This constraint is enforced during the trial vector generation and DE execution.

At the job dispatching stage, for each generation G, the server generates trial vectors $\boldsymbol{U}_{i,G}$. These vectors are converted into "jobs" and placed in an asynchronous queue. The job_dispatcher coroutine continuously monitors the status of connected clients and assigns pending jobs to free workers.

A critical feature of our implementation is the strict elitist selection strategy. After all trial vectors in a generation are evaluated, the server compares the trial fitness $F(\mathbf{U}_{i,G})$ with the target fitness $F(\mathbf{X}_{i,G})$, where:

$$\mathbf{X}_{i,G+1} = \begin{cases} U_{i,G}, & \text{if } F(\mathbf{U}_{i,G}) \le F(\mathbf{X}_{i,G}), \\ \mathbf{X}_{i,G}, & \text{otherwise.} \end{cases} \tag{10}$$

Here, $\mathbf{X}_{i,G}$ denotes the parameter vector of the i-th individual in the current population (the target vector). This mechanism ensures that the best traits are preserved ("elitism"), and the global fitness of the population monotonically improves over time. The best individual of each generation is serialized to disk to prevent data loss and allow for result analysis.

The client software is implemented in C++ to ensure maximum execution speed for complex matrix operations. The application listens on a TCP socket for incoming commands. Upon receiving a request, the client performs the following steps. During the parameter loading step, it reads the specific layer configuration (thicknesses and permittivity) from shared storage. During the matrix construction step, it generates truncated scattering matrices of size $(2M_{tr} + 1)\times(2M_{tr} + 1)$. At the recursive solving step, it executes the recursive operator algorithm (7)-(10) to determine reflection and transmission coefficients, as well as absorbance. At the fitness calculation step, it compares the computed spectral characteristics with the required ones using the weighted objective function and returns the result to the server.

To minimize network overhead, we implemented a custom lightweight text-based protocol. Heavy data (such as full layer topology vectors) is exchanged via a shared network file system, while the TCP socket is used exclusively for control commands and synchronization. The communication cycle is defined as follows. Upon connection, the server assigns a unique ClientID to the worker. The server sends a job request in the ASCII format. It sends the specific configuration file location and the dynamic weights for the objective function components. The C++ client uses a buffered socket reader. It parses the tokenized string, loads the geometry from configuration file, and runs the solver. After computation, the client sends back a concise response.

This approach decouples the data structure complexity from the transmission protocol, allowing us to change the number of layers or parameters without rewriting the network code.

The numerical analysis is performed on a discrete frequency grid $f_k = f_{\min} + k\Delta f$, k=1, 2, ..., M, where M is the number of frequency points, the integral objective function (4) is replaced by a discrete summation of local penalties. The client calculates the total fitness F_1 as:

$$F_1(\mathbf{P}) = \sum_{k=1}^{M} S_1(A(f_k, \mathbf{P})) , \tag{11}$$

where $S_1(A)$ is a piecewise linear penalty function defined by a set of thresholds (t_1, ..., t_4) and value parameters (v_1, ..., v_4) received from the server. This function assigns a low penalty value v_1 if the absorbance A exceeds the high threshold t_1, and a maximum penalty v_4 if A falls below the critical threshold t_4. Intermediate values are determined via linear interpolation, allowing for a flexible definition of the optimization goal ("soft" vs "hard" constraints) by simply adjusting the weights in the server configuration,

$$S_1(x) = \begin{cases} v_1, & x \ge t_1, \\ v_2 + \dfrac{x - t_2}{t_1 - t_2}(v_1 - v_2), & t_2 \le x < t_1, \\ v_3 + \dfrac{x - t_3}{t_2 - t_3}(v_2 - v_3), & t_3 \le x < t_2, \\ v_4, & x < t_4. \end{cases} \tag{12}$$

NUMERICAL RESULTS AND DISCUSSION

The primary goal of the optimization is to maximize the absorbance $A(f)$ over the frequency band of interest, $f \in [f_{\min}, f_{\max}]$. Namely, our purpose is to maximize absorption, at least at the level $A > 0.8$, preferably $A > 0.95$. For wideband applications, absorption uniformity is as critical as its peak value. Sharp drops in absorbance (where $A \to 0$) due to the excitation of high-Q resonances render the device ineffective. Consequently, the objective function must strictly penalize such spectral holes. The structure under study can support multiple resonances. Resistive graphene strip acts a resonator for the plasmon modes in the terahertz and infrared frequency range. However, at GHz, they are not excited. Periodic structures support Rayleigh anomalies on vacuum or grating modes in a dielectric slab. Also, inter-layer Fabry-Perot modes and corresponding resonances can be excited.

Based on the discrete frequency model (11), we employ a piecewise-linear penalty function with the following empirically determined coefficients: thresholds t_1=1.00, t_2=0.95, t_3=0.80, t_4=0.20, and corresponding values v_1= –5.0, v_2= –0.5, v_3=0.0, v_4=50.0. This configuration creates a "soft" reward for high absorption ($A > 0.95$) and a severe "hard" penalty for any drop below 0.2, effectively guiding the evolutionary search away from solutions with deep reflection resonances.

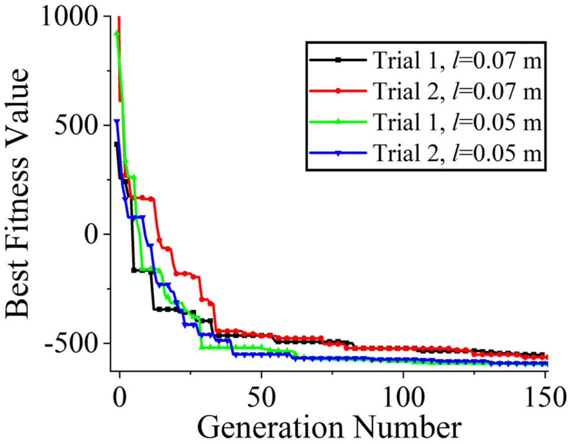

Figure 2. Convergence curves. The best fitness value vs. the generation number for different periods, l = 0.05 m and l = 0.07 m, and two trials, N=10, θ=0^0.

The population consisted of NP=50 individuals. Since DE is a stochastic process, multiple independent runs were performed to avoid stagnation in local optima. Fig. 2 shows convergence curves of the best fitness value versus the generation number. The convergence exhibits a characteristic step-like behavior and typical two distinct phases [10]. In the early stages, we observe large steps corresponding to the "exploration" phase, where the algorithm rapidly discards clearly non-optimal geometries. In the later stages, the curve shows long plateaus separated by small improvements ("exploitation" phase), as the algorithm fine-tunes the strip widths and chemical potentials to suppress residual resonances.

For the optimization, we take the number of frequency points $M = 250$, the frequency step is $\Delta f = 0.1$ GHz, the frequency band is $f_{\min} = 1$ GHz, $f_{\max} = 25.9$ GHz, and the number of layers $N = 10$. The relative permittivity of the medium is typical for fighter jet cockpit canopy (polycarbonate), $\varepsilon = 3$. The incidence angle is $\varphi_0 = 90^0$ (orthogonal incidence). The graphene parameters are $\tau = 1$ ps, T = 300 K. The geometric parameters are $h_{\max} = 0.7$ m, ε_{gap} is set to 0.01 m in the configuration.

Direct optimization of a 10-layer structure involves a high-dimensional search space (4 parameters × 10 layers = 40 variables), which can lead to slow convergence. To mitigate this, we employ a dimensionality reduction strategy based on cubic spline interpolation. The chromosome (trial vector) of each individual consists of only 16 reference parameters. These correspond to the four physical characteristics (d_n, h_{1n}, h_{2n}, μ_{cn},) defined at four specific "anchor" layers: indices $n = \{1, 4, 7, 10\}$. During the evaluation phase, the server expands this 16-element vector into the full set of 40 parameters for all 10 layers using cubic interpolation (scipy.interpolate.interp1d). This approach ensures a smooth gradient of properties across the stack, which is physically favorable for wideband matching. After the cubic interpolation, the constraints are applied preventing parameters for non- anchor layers to be out of ranges.

All computations are performed on a 12th-generation Intel Core i7 processor (featuring 8 performance and 4 efficiency cores). Electromagnetic simulation for a single individual takes approximately 80 seconds on a single computational thread. The order of the resulting linear algebraic system is 30 for a single layer. Additionally, 21 plane waves (both propagating and evanescent) are considered in the multilayer structure. During the optimization, the efficiency cores were deliberately excluded. The number of parallel threads is strictly limited to 10. Allocation of additional threads increases the computation time per task due to memory access overhead and cache contention among the performance cores. Consequently, evaluation of a single population of 50 individuals in parallel takes approximately 400 seconds. The time required for the differential evolution algorithm operations, task distribution, and data exchange is negligibly small compared to the rigorous electromagnetic simulation.

To visualize the effectiveness of the DE optimization, we compare the spectral response of the best individuals at different stages of the evolutionary process. Fig. 3 presents the power reflection, transmission and absorption coefficients vs. the frequency for the best candidate obtained at the 25th generation (early stage) versus the final solution at the 100th generation. As observed, the solution at the 25th generation already satisfies the basic requirement of $A > 0.8$ over a significant portion of the band. However, the dependencies exhibit highly oscillatory behavior, with several sharp minima where the absorbance drops significantly. These dips typically correspond to the excitation of high-Q resonances within the multilayer structure, which have not yet been fully compensated. Crucially, the final converged solution (100th generation) demonstrates that the algorithm successfully adjusted the geometric and physical parameters to significantly suppress these detrimental resonances. The optimization effectively flattened the spectral response, maximizing the area under the absorbance curve and eliminating the "holes" in the operational band. For a complete optimization run of 100 generations, the total number of objective function calls (forward solver evaluations) is 5000 per trial.

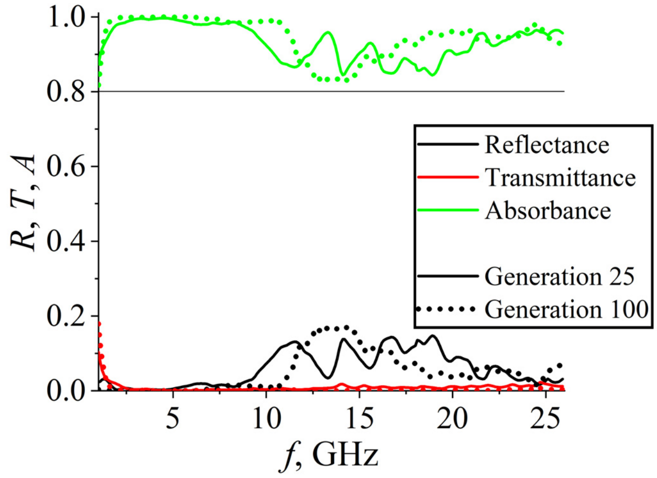

Figure 3. Power reflection, transmission, and absorption coefficients vs. the frequency for the best individuals from the 25th (dashed lines) and 100th (solid lines) generations, $l = 0.05$ m, N=10, θ=0^0

We further investigated the influence of the structure period l on the optimization results. Fig. 4 shows the dependence of the power reflection, transmission, and absorption coefficients on frequency. Two distinct cases are presented in Fig.4, for $l = 0.05$ m and $l = 0.07$ m. The results shown in Fig. 4 indicate that the interpolation-based optimization successfully finds high-absorption solutions in both cases. With a larger period, more resonances can be excited in the considered frequency band, creating a strong perturbation that the optimizer must counteract by precisely tuning the graphene chemical potential and strip widths. This increased complexity is clearly reflected in the convergence curves shown in Fig. 2. The fitness levels for the structure with the larger period remain consistently higher (indicating a larger penalty) throughout the optimization process. DE algorithm requires more generations to find a specific combination of parameters that can "cancel out" the additional grating-induced resonances. Essentially, each new resonance peak in the spectrum acts as an additional constraint in the parameter space, shifting the global minimum of fitness function $F(\mathbf{P})$ and making the optimization landscape more rugged. Despite this, the final absorbance profiles for both periods reach the target level.

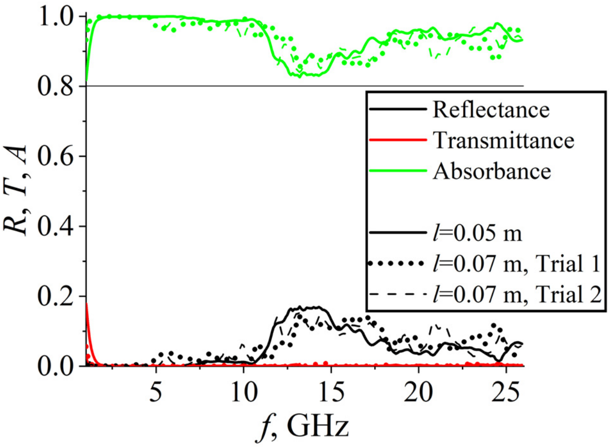

Figure 4. Power reflection, transmission, and absorption coefficients vs. the frequency for different periods $l = 0.05$ m and $l = 0.07$ m, N=10, θ=0^0

From a practical engineering perspective, supplying an individual DC bias voltage to each isolated graphene strip in a 10-layer stack presents a significant fabrication challenge. To address this, we performed a constrained optimization run simulating "unbiased" graphene. In this scenario, the chemical potential μ_{cn} was removed from the gene vector and fixed at μ_{cn}=0 eV, leaving only the geometric parameters (strip widths and layer spacings) available for optimization. The results are shown in Fig.5 for 100th generation. As shown, even without active tuning of the chemical potential, the algorithm successfully identifies a geometric configuration that yields substantial absorption.

Finally, we study the angular stability of the optimized 10-layer absorber. Although the structure was optimized for normal incidence ($\theta = 0°$), its performance was evaluated at oblique angles of $\theta = 30°$ and $\theta = 60°$. The results, presented in Fig. 6, demonstrate that the absorbance remains remarkably stable. Except for a narrow frequency range at the lower end of the spectrum, the absorption coefficient remains above the required level of 0.8 even at significant tilt angles. The results indicate that the proposed multilayer configuration possesses high angular tolerance, which is essential for effective electromagnetic shielding and radar-absorbing applications in real-world scenarios.

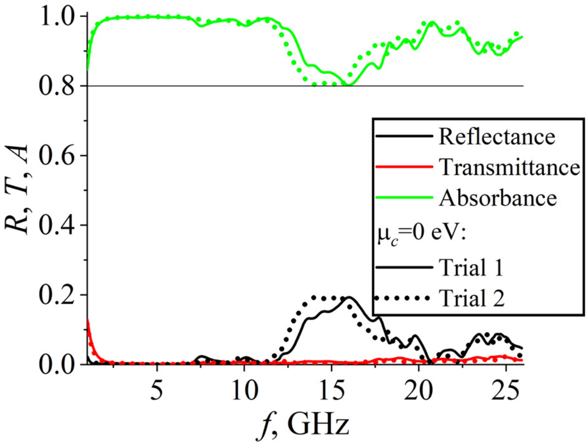

Figure 5. Power reflection, transmission, and absorption coefficients vs. the frequency for unbiased graphene structure, $l = 0.05$ m, $\mu_{cn} = 0$ eV, N=10, θ=0^0

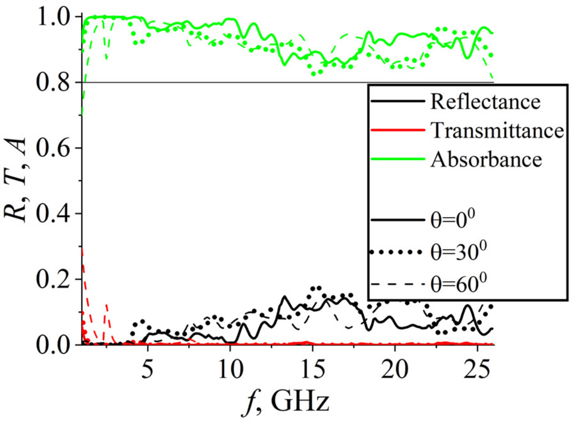

Figure 6. Power reflection, transmission, and absorption coefficients vs. the frequency for different incidence angles θ=0^0, θ=30^0, and θ=60^0, $l = 0.07$ m, N=10

The angular stability of the optimized structure under oblique incidence is primarily governed by the strips' resistive nature and the applied optimization strategy. The surface conductivity of graphene strips is independent of the angle of incidence. In the microwave range, the localized resonance effects on the isolated graphene strip are less pronounced than in the terahertz frequency range, where high-Q plasmon resonances can arise. Also, the DE optimization process finds a set of parameters that maximally suppresses the resonances connected with the periodicity, thereby preventing the formation of narrow dips in the frequency dependences. As a result, the absorption mechanism becomes less sensitive to phase variations introduced by oblique incidence, while the contribution of resistive losses remains dominant over a broad angular range.

CONCLUSIONS

The developed surface-based electromagnetic formulation enables efficient analysis of multilayer periodic absorbing structures with a large number of layers, avoiding volumetric discretization of the dielectric domain. By reducing the problem dimensionality to the grating interfaces, the computational cost scales with the number of layers rather than the physical thickness of the structure. As a result, the proposed forward solver is orders of magnitude more efficient than domain-discretization techniques such as FEM or FDTD, making it particularly suitable for repeated evaluations within iterative optimization loops.

Coupling this solver with a parallel differential evolution algorithm allows practical optimization of high-dimensional multilayer designs under broadband performance requirements and fabrication-inspired constraints. The numerical results demonstrate that the optimized ten-layer resistive grating structure provides stable broadband absorption, effectively suppresses resonance-induced spectral holes, and preserves optical transparency and robustness under oblique incidence.

The proposed approach provides a scalable, computationally efficient tool for designing advanced multilayer radar absorbers and can be readily extended to other classes of planar periodic electromagnetic structures and polarization scenarios.

ORCID

Mstyslav E. Kaliberda, https://orcid.org/0000-0002-8169-4360; **Sergey A. Pogarsky,** https://orcid.org/0000-0003-0833-1421

Acknowledgments

The work of S.A.P., V.A.L. was partially supported by the Ministry of Education and Science of Ukraine, grants number 0124U000670, 0126U000999, and that of M.E.K. by the National Research Foundation of Ukraine via project #2025.07/0094.

REFERENCES

[1] E.F. Knott, J.F. Shaeffer, and M.T. Tuley, *Radar Cross Section*, 2nd ed. (Scitech Publishing Inc., Raleigh, NC, USA, 2004).
[2] B.A. Munk, *Frequency Selective Surfaces: Theory and Design*, (John Wiley & Sons, Inc., New York, 2000), 410 p.
[3] M.E. Kaliberda, L.M. Lytvynenko, and S.A. Pogarsky, J. Opt. Soc. Amer. A. **36**(10), 1787 (2019). https://doi.org/10.1364/JOSAA.36.001787
[4] M.E. Kaliberda, L.M. Lytvynenko, and S.A. Pogarsky, Int. J. Microw. Wireless Technol. **12**(5), 380 (2020). https://doi.org/10.1017/S1759078719001430
[5] R.P.S. Bhadoriya, V. Bajaj, and R. Panwar, in: *2023 International Conference on Electrical, Electronics, Communication and Computers (ELEXCOM)*, edited by R. Roorkee, (IEEE, Roorkee, India, 2023), pp. 1-4.
[6] R. Storn, and K. Price, J. Glob. Optim. **11**(4), 341 (1997). https://doi.org/10.1023/A:1008202821328
[7] S. Wang, A. Zhou, and Y. Zhang, Chin. J. Electron. **34**(3), 871 (2025). https://doi.org/10.23919/cje.2023.00.322
[8] I. Farda, A. Thammano, and J. Morris, IEEE Access. **12**, 131809 (2024). https://doi.org/10.1109/ACCESS.2024.3460385
[9] Z. Cai, S. Gao, X. Yang, and M. Zhou, IEEE Trans. Syst. Man Cybern. Syst. **54**(12), 7318 (2024). https://doi.org/10.1109/TSMC.2024.3447051
[10] J. de Jesús Rubio, IEEE Trans. Neural Netw. Learn. Syst. **36**(8), 14201 (2025). https://doi.org/10.1109/TNNLS.2025.3526580
[11] D. Cai, *et al.*, IEEE Sens. J. 23(20), 25271 (2023), https://doi.org/10.1109/JSEN.2023.3311467
[12] P. Singh, and R.S. Hegde, IEEE Antennas Wirel. Propag. Lett. **24**(11), 3986 (2025). https://doi.org/10.1109/LAWP.2025.3598331
[13] K. Dutta, M.O. Akinsolu, P. Kumar Mishra, B. Liu, and D. Guha, IEEE Open J. Antennas Propag. **5**(3), 693 (2024). https://doi.org/10.1109/OJAP.2024.3385675
[14] F. Lan, *et al.*, IEEE Trans. Plasma Sci. 52(7), 2991 (2024). https://doi.org/10.1109/TPS.2024.3412995
[15] M. Zhai, *et al.*, IEEE Antennas Wirel. Propag. Lett. **23**(10), 3043 (2024). https://doi.org/10.1109/LAWP.2024.3421549
[16] F. Peng, X. Chen, and J. Xue, IEEE Trans. Antennas Propag. **73**(7), 4384 (2025). https://doi.org/10.1109/TAP.2025.3553761
[17] L. Zuo, Z. Liang, and Y. Long, IEEE Antennas Wirel. Propag. Lett. **24**(6), 1367 (2025). https://doi.org/10.1109/LAWP.2025.3537215
[18] G.W. Hanson, J. Appl. Phys. **103**, 064302 (2008). https://doi.org/10.1063/1.2891452
[19] G.W. Hanson, IEEE Trans. Antennas Propag. **56**, 747 (2008). https://doi.org/10.1109/TAP.2008.917005
[20] Yu.V. Gandel, and V.D. Dushkin, J. Math. Sci. **212**, 156 (2015). https://doi.org/10.1007/s10958-015-2656-2
[21] M.E. Kaliberda, S.A. Pogarsky, and A.A. Sierhieieva, Opt. Quantum Electron. **55**, 1050 (2023). https://doi.org/10.1007/s11082-023-05288-5

ОПТИМІЗАЦІЯ БАГАТОШАРОВОГО ПОГЛИНАЧА НА БАЗІ ГРАФЕНУ У ВИПАДКУ Н-ПОЛЯРИЗАЦІЇ З ВИКОРИСТАННЯМ ДИФЕРЕНЦІАЛЬНОЇ ЕВОЛЮЦІЇ В ГІБРИДНОМУ ОБЧИСЛЮВАЛЬНОМУ СЕРЕДОВИЩІ

Мстислав Є. Каліберда[1,2], Сергій О. Погарський[1,2], Владислав М. Насонов[1], Вікторія А. Луньова[1]
[1]Харківський національний університет імені В. Н. Каразіна, майдан Свободи, 4, Харків, Україна, 61022
[2]Радіоастрономічний інститут НАН України, вул. Мистецтв, 4, Харків, Україна, 61002

Представлено обчислювально ефективну методику оптимізації багатошарових радіопоглинаючих структур на основі періодичних плоских решіток з резистивних стрічок, розташованих у діелектричному шарі, для випадку *H*-поляризації. Електромагнітні характеристики моделюються з використанням строгого методу сингулярних інтегральних рівнянь у поєднанні з операторним методом, що забезпечує високу точність і числову стабільність за низьких обчислювальних витрат. Цей надшвидкий алгоритм розв’язання прямої задачі інтегровано в паралельну систему оптимізації на основі диференціальної еволюції, реалізовану в архітектурі клієнт–сервер, що дозволяє ефективно розв’язувати багатовимірні задачі зворотного проєктування. Оптимізація спрямована на досягнення широкосмугового поглинання за нормального падіння зі збереженням оптичної прозорості. Як репрезентативний резистивний матеріал використано графен. Числові результати демонструють ефективне придушення резонансних провалів у спектрі та стабільне широкосмугове поглинання для десятишарових структур, а також стійкість характеристик за умов похилого падіння та з урахуванням конструктивних обмежень.

Ключові слова: *графен; широкосмуговий поглинач; диференціальна еволюція; сингулярне інтегральне рівняння; багатошарова періодична структура; глобальна оптимізація*

EAST EUROPEAN JOURNAL OF PHYSICS. 2. 491-497 (2026)
DOI:10.26565/2312-4334-2026-2-55 ISSN 2312-4334

RADIATION EMBRITTLEMENT OF TANTALUM COATING OF THE NEUTRON SOURCE TARGETS

O.O. Parkhomenko[1,2]*, **V.V. Gann**[1], **B.W. Borts**[1], **A.Yu. Zelinsky**[1], **I.M. Karnaukhov**[1], **Yu.O. Marchenko**[1]
[1]*NSC "Kharkiv Institute of Physics and Technology", Kharkiv, Ukraine*
[2]*V.N. Karazin Kharkiv National University, Kharkiv, Ukraine*
Corresponding Author e-mail: parkhomenko@kipt.kharkov.ua

Received February 24, 2026; revised April 19, 2026, accepted May 7, 2026

The works in the field of radiation materials science of targets for neutron sources based on subcritical assemblies driven with linear accelerators of electrons or protons, the so-called ADS systems, are presented. Currently, electronuclear ADS systems are prototypes of safe 5th-generation nuclear reactors. In connection with the physical start-up of the neutron source installation of the NSC KIPT the target of which is made of tungsten coated with tantalum, the effect of radiation on mechanical properties is considered, and the resource of the tantalum coating of the target is estimated.

Keywords: *Neutron sources; Accelerators driven systems; Targets; Tantalum coating; Radiation hardening; Embrittlement; Dose dependences*
PACS: 41.75.Ht,25.20.-x

INTRODUCTION

The creation of safe nuclear facilities, designed for both electricity production and the transmutation of thermal reactor products, is one of the priorities of the world nuclear energy industry. Already in one of the first proposals for the development of such facilities, the so-called ADS systems, all the elements of the future reactors were described [1]. The basis of such facilities is a subcritical nuclear reactor using fast neutrons. It was planned to use a proton accelerator with an energy of up to 1 GeV and a current of up to 20 mA as the so-called driver of such a reactor.

Today, 30 years later, the basic structure of such systems is as follows. The accelerator of high-energy particles irradiates the material (target), as a result of which neutrons are formed, which fall on the fuel elements of the subcritical assembly (SCA), after which their multiplication occurs tens of times. The system starts working as a source of neutrons (NS).

Most ADS use neutron sources in which high-energy protons bombard targets made of heavy elements to produce so-called spallation neutrons. In 1947, the term spallation began to be used in nuclear terminology (Siborg, Serber). For nuclear fission to occur, the proton energy must be sufficiently high. Its criterion is the de Broglie wavelength λ. It should be smaller than the size of the nucleus, which will allow the proton to interact individually with the nucleons inside the nucleus. ($\lambda = h/p$, where p is the momentum of the proton), and split it.

Creating (development of) such nuclear accelerator systems, ADS, is a very difficult and challenging task. Electron accelerators can also be used to test the basic ideas of these systems. As shown in 2002 [2], to obtain flows of less than 1016 n/cm2 per second, electron accelerators require significantly lower costs for installation. This is explained by the fact that photonuclear (e, γ) processes in this sense have an advantage over reactions induced by protons.

One of the most important areas of experimental work in nuclear materials science is the study of radiation damage in materials used or intended for use in nuclear reactor and ADS components. Two types of neutron-producing targets are being considered for use in future accelerator-driven safe nuclear power systems (ADS): liquid and solid metal. Among the latter, tungsten, tantalum, and their alloys have attracted considerable attention from researchers.

The purpose of the work is the analysis of radiation damage and changes (degradation) of the mechanical properties of tantalum, after irradiation in the active zone of the subcritical assembly, as a structural material (coating) of the "tungsten" target of the neutron source of the NSC KIPT.

KHARKIV NEUTRON SOURCE DRIVEN WITH HIGH-ENERGY ELECTRON ACCELERATOR

In 2021, the physical start-up of just such a facility was carried out at the NSC KIPT together with the Argonne National Laboratory of the USA. Its main functions include developing work in nuclear materials science and medical research. The facility will conduct research in reactor physics and materials science [3,4]. The first target of this installation is a tungsten target with a tantalum coating.

The purpose of the development is to create in Ukraine a safe experimental base for neutron physics research using intense neutron flows (up to 3 10^{14} n/sec). The main components of the installation are a linear electron accelerator, a

Cite as: O.O. Parkhomenko, V.V. Gann, B.W. Borts, A.Yu. Zelinsky, I.M. Karnaukhov, Yu.O. Marchenko, East Eur. J. Phys. 2, 491 (2026), https://doi.org/10.26565/2312-4334-2026-2-55

system for transporting the electron beam from the linear accelerator to the target, a neutron generation target (NGT), a subcritical assembly, neutron channels, biological protection, and auxiliary systems.

Primary neutrons are born in photonuclear reactions with the help of hard γ-radiation, which is formed during the scattering of electrons on the nuclei of heavy elements. Two target variants are considered: tungsten and natural uranium. The initial energy of electrons is 100 MeV.

The target is simultaneously exposed to two sources of irradiation: high-energy electron irradiation (100 MeV) and irradiation from the surrounding environment, i.e., subcritical assembly neutrons (SCA).

The subcritical assembly is designed to obtain the maximum neutron flux with a criticality of 0.98. Thus, the possibility of a chain reaction in an installation of this type is excluded. The size of the neutron flux is regulated by the beam current, and the neutron field in the source disappears after the beam is switched off.

W-Ta neutron-generating targets of ADS systems

Due to its high melting point, density, thermal conductivity, strength, and neutron interaction cross-section, tungsten has been used as a target material in ADS systems such as LANCE, KENS, etc., for many years. [5,6]. However, tungsten corrodes in water, especially under irradiated conditions. This problem can be solved by coating the tungsten with a corrosion-resistant material. These include titanium, stainless steel, and tantalum.

Targets using bimetal tantalum-tungsten were used in the ISIS and KENS installations. A significant positive metallurgical factor is the good compatibility of these materials, due to their complete solubility in the solid state.

Why tantalum? Having unique physical and metallurgical properties, tantalum is one of the most suitable materials for targets. Among the refractory metals of groups 4-6, it has the highest melting point after tungsten (3140°C) and is characterized by exceptional plasticity and viscosity in the cast and recrystallized states, so it can be deformed at room temperature to 90-95% without intermediate annealing.

Pure tantalum (99.99%) retains high plasticity and viscosity at temperatures close to absolute zero [7]. However, as with other bcc metals, it becomes sharply pronounced as the content of interstitial impurities increases. For example, [8] showed that when the oxygen content increases to 1.3 at.%, tantalum becomes brittle at room temperature.

Among all low-value materials, it has the highest corrosion resistance, approaching that of platinum at temperatures up to 150°C. However, it has low resistance to oxidation in air and other oxidizing media at temperatures above 500°C.

The radiation properties of tantalum have not been sufficiently studied and are controversial. Thus, high plasticity of tantalum irradiated to a dose of 10 dpa (displacements per atom) was reported in [9]. However, complete embrittlement of technically pure tantalum was found in [10] even with irradiation doses of only 0.14 dpa. According to one of the authors, the cause of fragility may be the material's oxygen saturation even before the start of irradiation. Alloys of tantalum with tungsten also "do not save the situation": they exhibit a complete loss of plasticity at doses below 1 dpa [7].

The disadvantages of tantalum as a target material include its relatively large interaction cross section with neutrons (especially in the superthermal energy range), which leads to its high radioactivity after irradiation. An analysis of an ESS installation (5MW) showed that after a year of exposure, tantalum exhibited induced activity 10 times greater than that of tungsten or mercury [11]. That is why the two nuclear installations KENS and ISIS immediately replaced tantalum targets with tungsten ones.

One of the main requirements for this effective anti-corrosion tantalum coating is to maintain reliable contact with the tungsten throughout the target's lifetime. The presence of a gap in the tungsten coating dramatically reduces heat removal from the target by a water stream. In turn, the tantalum coating improves heat transfer from the target to the cooling water compared to tungsten.

Reliable Ta-W contact when creating multiple targets for megawatt spallation neutron sources is achieved using the HIP (hot isostatic pressing) method. The successful use of this method was first demonstrated at the ISIS facility (Rutherford Appleton Laboratory in Great Britain) [8], and then by Japanese scientists at the KENS facility [6].

For these purposes, a high-temperature vacuum rolling method, combined with gas-phase deposition of tantalum on the target's side surfaces, has been developed at the National Research Center of KIPT.

At the same time, tantalum with a thickness of 0.25...0.3 mm is used to cover the tungsten plates, as in the LANCE installation (USA). This value is determined by a compromise between ensuring, on the one hand, the reliability of tungsten protection against water corrosion in an active environment and, on the other hand, preventing a significant decrease in neutron yield.

Analysis of the results of mechanical studies of irradiated tantalum.

To achieve the purpose of the work, regarding the assessment of the degree of radiation embrittlement and the target's resource, it was necessary to do three things.

1. To determine the tantalum radiation dose, for example, for one year of operation of the neutron source.

2. To conduct an analysis of the results of mechanical tests of samples irradiated at temperatures corresponding to the conditions of irradiation of the KIPT neutron source.

3. To mark on the dose dependences of strength and plasticity, the tantalum irradiation dose of the KIPT neutron source, and determine the corresponding values of the strength and plasticity of the irradiated material that correspond to it. Based on this, it is necessary to make an estimate of the target coverage resource.

Determination of the radiation dose in tantalum

When the target is irradiated with a beam of electrons with energy of 100 MeV, radiation defects are formed in the target material. The main sources of the formation of such defects will be recoil nuclei, which arise during the scattering of electrons and neutrons on nuclei, as well as a results of nuclear reactions involving gamma- rays.

With the help of the MCNPX program [12], the rate of creation of displacements in the coating of the tungsten target of the neutron source of the NSC KIPT was calculated when irradiated with high-energy electrons with energy of 100 MeV [13]. It was established that the largest contribution to the rate of damage is made by the elastic interaction of high-energy electrons with nuclei. The maximum dose rate is about 0.45 dpa / year, and is reached at a depth of ~ 1 cm (Figure 1).

Figure 2 shows the radiation damage dose distribution in tantalum on the surface of the second tungsten plate.

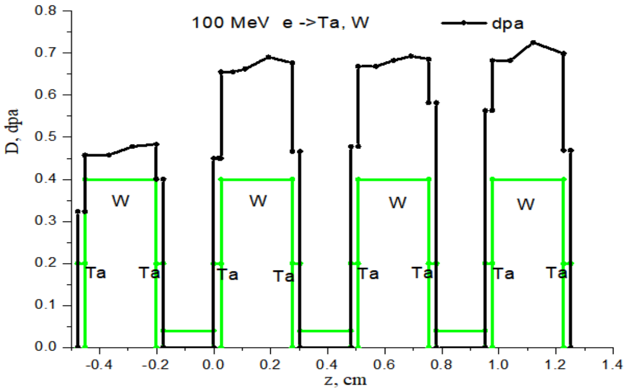

Figure 1. The doses in Ta and W accumulated during one year

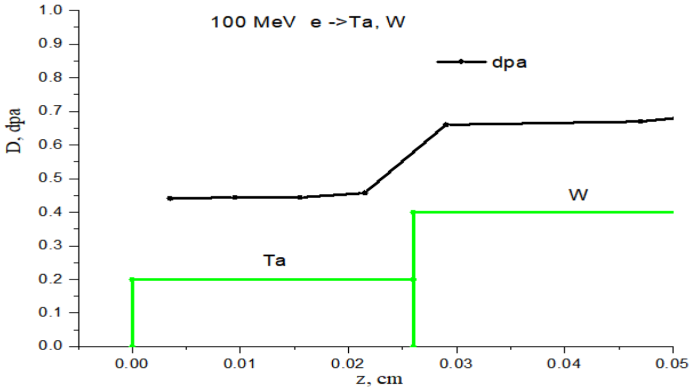

Figure 2. Distribution of radiation damage doses in Ta and tungsten that were accumulated during one year of exposure.

Consideration of damage by neutrons of a subcritical assembly. Let's not forget that the target is under the simultaneous action of two sources of radiation, high-energy electron (100 MeV) and radiation from subcritical assembly neutrons (SCA). It was shown in [13] that the contribution to the dose of irradiation of a tungsten plate from neutrons of a subcritical assembly is 0.15 dpa/year.

Tantalum nucleas differ little from tungsten, but the threshold displacement energies differ greatly. It is 70 eV for tungsten, and 90 eV for tantalum. Taking this into account, we obtain for tantalum the rate of damage by SCA neutrons equal to approximately 0.11 dpa / year. Thus, the total dose accumulation rate (electrons + SCA) in the coating of the second plate is 0.45 + 0.11 = 0.56 dpa/year. Let's pay attention to the fact that the contribution to damage from high-energy electrons is four times greater than from neutron damage to a subcritical assembly. Is it too much or not enough? What kind of radiation risk does such a dose of exposure indicate? Let's look at the results of mechanical tests of tantalum samples for tension.

Analysis of deformation curves of irradiated tantalum samples

Tantalum turned out to be very sensitive to radiation. As can be seen from Figure 3, the decrease in its plasticity begins already at very low doses - about 4 10^{-5} dpa. [10].

It is possible to distinguish 3 stages of the development of radiation embrittlement of tantalum:

1) At a dose of 4 10^{-5} dpa, there is already a reduction in elongation (the strain diagram is shortened), but strain hardening still remains (after the yield point, the flow stress increases slightly).

2) At this stage, starting from 4 10^{-4} to 4 10^{-2} dpa, strain hardening no longer takes place. After the formation of the so-called "yield tooth" on the diagram, the stress only decreases. Deformation softening occurs.

3) At a dose of 0.14 dpa, the strain hardening stage and uniform elongation are completely absent. Immediately after reaching the maximum stress, destruction occurs. There is no plastic deformation.

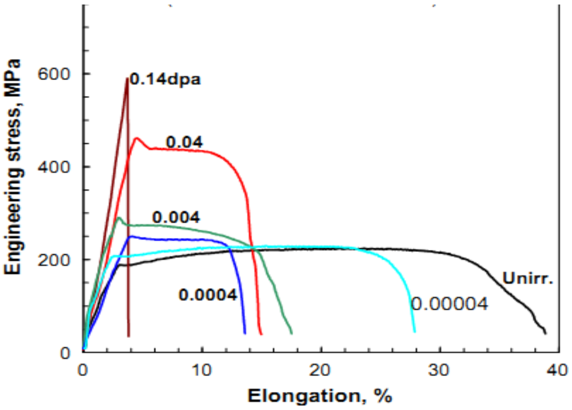

Figure 3. Deformation curves of tantalum irradiated under conditions close to the operating conditions of the neutron source of the NSC KIPT

Dose dependence of flow stress and fracture strength of irradiated tantalum

The main criteria for choosing construction materials are their strength characteristics. The material's ability to undergo uniform deformation is also of great importance. It is generally accepted that the higher these indicators are, the better the material withstands technological and operational loads. That is why, in this section, the dependencies of flow stress and uniform elongation of tantalum of different purities in the initial and irradiated states are presented.

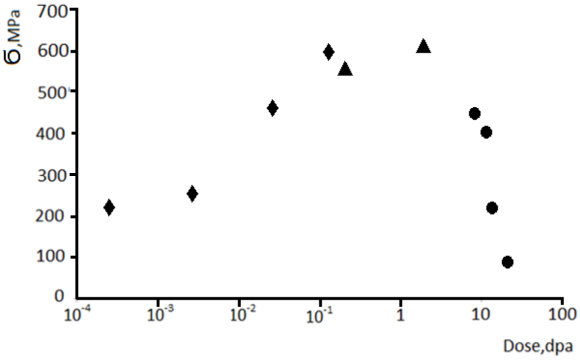

Figure 4. Dose dependence of the flow stress of irradiated tantalum. Rhombuses are work [10], balls are work [14]. triangles - work [15]

During the analysis, it should be remembered that the value of the yield strength of non-irradiated samples of tantalum in these works is (depending on the purity of the metal) from 180 to 220 MPa.

Taking into account the value of the working temperature of the KIPT target, when constructing the dependence, we tried to use the results of work on tantalum irradiation at temperatures not exceeding 100°C. Currently, the most number of works on tantalum were carried out at irradiation temperatures higher than 500°C, and were aimed at the operating conditions of future thermonuclear reactors [6].

Dependence (Figure 4) can be divided into two components. At the first stage of irradiation, there is a significant effect of radiation hardening. The yield strength increases almost three times - up to 600 MPa. After reaching a dose of 1 dpa, the flow stress begins to decrease, and for doses greater than 10 dpa, the stress decreases even below the values of the yield strength in the unirradiated state. This means that the process of brittle fracture occurs in the elastic region of stresses, without the contribution of plastic deformation. This is directly evidenced by the deformation curves of material irradiated to high doses [14].

Dose dependence of plasticity (uniform elongation) of irradiated tantalum

In order to predict the degree of fragility of the tantalum coating of the target, it is necessary to know to which purity category the original tantalum belongs to. As can be seen from Figure 5, there is a significant discrepancy between the behavior of tantalum with an oxygen purity of 50 appm and "dirty" tantalum (500 appm): the latter completely loses plasticity at doses slightly above 0.1 dpa. Chemical analysis of tantalum by KIPT on the ELVAX analyzer, showed that the purity of tantalum is 98.8% (category - "dirty").

Thus, the established annual dose of 0.56 dpa for tantalum with a high concentration of oxygen (which corresponds to the operating conditions of the target coating of the NSC KPTI) corresponds to the absolute loss of plasticity.

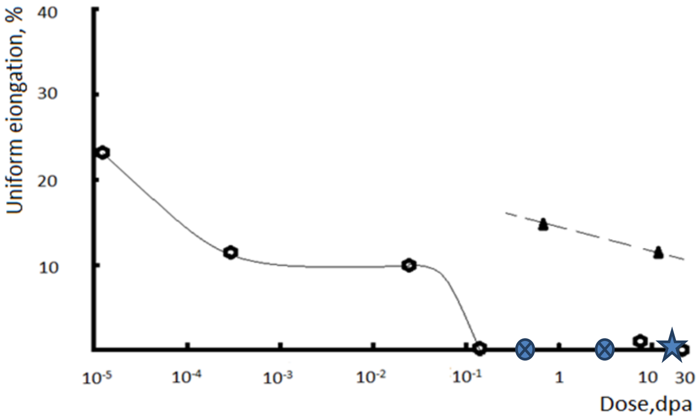

Figure 5. Dose dependence of uniform elongation of tantalum samples of different purity, irradiated at the LANCE (USA) (hexagons), SINQ (Switzerland) (circles and asterisk), triangles ISIS(UK). Triangles correspond to oxygen concentration of 50 appm (510^{-3} %), and hexagons to oxygen concentration of 500 appm (510^{-2} %). The size of the asterisk corresponds to the doses of Saito *et al.* [14], which are equal to 10…31 dpa (SINQ). Circles correspond to doses of 0.26 and 2.6 dpa [16], of irradiated “dirty” tantalum (LANCE)

The influence of the impurities and products of nuclear reactions on the development of radiation embrittlement in metals of the 5th group of the Periodic Table of Elements (tantalum). Mechanisms of embrittlement

Fleischer's theory explains the strengthening of bcc metals and alloys by the interaction of dislocations with tetragonal strain fields arising in the metal lattice in the presence of interstitial impurities [17]. Thus, the maximum interaction force of a screw dislocation with an obstacle is given by the expression $F = \mu\ \Delta\varepsilon\ b^2 / 3.86$, where μ is the shear modulus, Δε is the tetragonal strain (distortion) introduced into the metal lattice by a defect (1 for dislocation loops, either vacancy or interstitial in nature), and b is the Burgers vector.

Analysis showed that for Group 5 metals, interstitial oxygen atoms are one of the most strengthening factors at the neutron irradiation temperatures of interest, which are on the order of 100°C [18]. Specifically, the decoration of dislocations by interstitial atoms or clusters (loops) under irradiation, blocking dislocation generation by Frank-Read-type sources, causes so-called "source" strengthening (increase) of the yield strength—the formation of a "physical yield stress" As we can see from the curves shown in Figure 3, with further increase in strain, this leads to a virtually complete absence of strain hardening and the development of plastic instability.

At the mesostructural level, this is associated with the localization of plastic flow as so-called "dislocation channeling." This effect leads to the formation of defect-free regions—channels. In these channels, the first dislocations to escape from their sources, destroy defective clusters of radiation defects [19]. Dislocation channeling is responsible for the negative slope of the stress-strain curves at doses greater than 10^{-3} dpa (see Figure 3) [20]. The authors of [21] reached similar conclusions on bcc materials irradiated with high-energy protons (590 MeV) to doses ranging from 10^{-3} to 0.3 dpa, and deformed at room temperature. The first study to detect channeling in irradiated (2.510^{22} n/cm^2) tantalum deformed at room temperature may be [22].

How might all these mechanisms influence the initiation of crack formation and propagation in irradiated materials? The absence of dislocation generation leads to suppression of the dislocation mechanism for "healing" crack nuclei, and the crack propagates freely across the entire cross-section of the specimen [23].

Impact of products of nuclear reactions. At the same time, it was established that, in addition to radiation defects and oxygen, the brittleness of materials under high doses of irradiation in ADS-systems can be associated with the influence of high concentrations of nuclear reaction products, mainly helium and hydrogen, which are formed during irradiation [24-27].

According to the authors [26], the main contribution to the sharp (from 35 to 0.5%) decrease in uniform elongation of steel during tensile tests at room temperature is made by helium and hydrogen, the total concentration of which, even at a dose of 3 dpa (in ADS), is about 0.6 at.%. At the same time, it is not related to a change in the microstructure of steel (even the formation of pores), but is determined by a combination of radiation hardening followed by a sharp deformation softening, which is associated with the localization of plastic deformation processes (see explanation to Fig. 3).

CONCLUSIONS

- A brief review of the current state of development of ADS-systems, prototypes of future 5th generation reactors, and an analysis of the use of Ta coatings in neutron-generating targets of ADS-systems was conducted. It is established that W-Ta composites occupy a prominent place in the world, among the targets of the most powerful ADS.
- An analysis of the influence of tantalum irradiation in ADS systems and reactors on its main mechanical properties was carried out. Features of the dose dependence of the plasticity of tantalum (its three-stage nature) and the fact of the determining effect of oxygen on its radiation fragility are shown.

- The dose dependence of the flow and fracture stress of irradiated Ta was established. It is shown that there is a transition from radiation strengthening (at doses of the order of 1-2 dpa) to a significant loss of tantalum strength (radiation suftenning), even in pure tantalum, at doses of 10 dpa. The material begins to break down in the elastic region, at load levels below the yield point, resulting in brittle failure.
- Briefly analyzed physical mechanisms of influence of radiation defects, products of nuclear reactions, interstitial impurities on strain hardening of irradiated tantalum.
- A prediction was made regarding the behavior of the tantalum coating of the neutron-generating target of the NSC of the KIPT. Taking into account the high concentration of impurities in the material (oxygen), it can be assumed that the tantalum coating of the tungsten target will practically not have a reserve of plasticity already in the first year of operation of the neutron source.

Conflict of Interest

The authors declare that there is no conflict of interest regarding the publication of this paper.

ORCID

O.O. Parkhomenko, https://orcid.org/0000-0001-9671-8874; **V.V. Gann,** https://orcid.org/0000-0002-3451-1840;
B.W. Borts, https://orcid.org/0000-0003-0387-3491; **A.Yu. Zelinsky,** https://orcid.org/0000-0002-4110-8523;
Yu.O. Marchenko, https://orcid.org/0000-0002-9128-0372

REFERENCES

[1] C. Rubbia, J.A. Rubbio, and S. Buono, CERN/AT/95-44T.

[2] D. Ridicas, H. Safa, and M.L. Giacri, in: *Seven Information Exchange Meeting on Actinide and Fission Product*, (Jeju, Korea, 2002).

[3] A. Bykhun, P. Gladkikh, I. Karnaukhov, V. Lyashchenko, A. Mytsykov, V. Ridozub, V. Selivanov, *et al*., Ukr. J. Phys. **68**(3), 147 (2023). https://doi.org/10.15407/ujpe68.3.147

[4] I.M. Karnaukhov, O.P. Bezditko, B.V. Borts, O.V. Bykhun, V.T. Bykov, P.I. Gladkikh, L.I. Glushchenko, *et al*., Reports of the National Academy of Sciences of Ukraine, (3), 44 (2024). https://doi.org/10.15407/dopovidi2024.03.044

[5] M.S. Wecsler, J. Sommer, C. Lin, L.L. Daemen, and P.D. Ferguson, Journal of Nuclear Materials, **244**, 177 (1997). https://doi.org/10.1016/s0022-3115(96)00735-0

[6] M. Kawai, M.M. Kawai, M. Furusaka, K. Kikuchi, and H. Kurishita, Journal of Nuclear Materials, **318**, 38 (2003).

[7] C.P. Massey, C.K. Goetz, Y.-R. Lin, J. Werden, S. Curlin, and T.I. Siggillino, Journal of Nuclear Materials, **591**, 154906 (2024), https://doi.org/10.1016/j.jnucmat.2024.154906

[8] D. Wilcox, P. Loveridge, and T. Davenne, L. Jones, and D. Jenkins, Journal of Nuclear Materials, **506**, 76 (2018). https://doi.org/10.1016/j.jnucmat.2017.10.075

[9] J. Chen, P. Jung, M. Rödig, H. Ullmaier, and G.S. Bauer, Journal of Nuclear Materials, **343**, 227 (2005). https://doi.org/10.1016/j.jnucmat.2004.09.076

[10] T.S. Byun, and S. Maloy, Journal of Nuclear Materials, **377**, 72 (2008). https://doi.org/10.1016/j.jnucmat.2008.02.034

[11] E.L. Sola, M. Calviani, P. Avigni, M. Battistin, J.B. Descarrega, J.C. Espadanal, M.A. Fraser, *et al*., Physical Review Accelerators and Beams, **22**, 113001 (2019). https://doi.org/10.1103/PhysRevAccelBeams.22.113001

[12] D.B. Perlowitz, (April 2008), LA-CP-07-1473.

[13] V.V. Gann, A.V. Gann, B.V. Borts, I.M. Karnaukhov, and A.A. Parkhomenko, VANT**,** Ser. YFI. (6)(136), 17 (2025). https://doi.org/10.46813/2021-136-017

[14] S. Saito, K. Suzuki, H. Obata, and Y. Dai, Nuclear Materials and Energy, **34**, 101338 (2023), https://doi.org/10.1016/j.nme.2022.101338

[15] F.W. Fiffen, Proc. Conf. 730813.1973, 22p.

[16] R.D. Brown, M.S. Wecsler, and C. Tschalar, in: *Proceedings of the 13 International Symposium on Effects of Radiation on Material Properties, ASTM STP 956*, (Philadelphia, PA, 1987).

[17] R.L. Fleischer, in: *Strengthening of Metals*, edited by D. Peckner, (Reinhold Publishing Corporation, N.Y., 1964). pp. 93.

[18] M. Boček, H. Böhm, and W. Schnider, Journal of Nuclear Materials, **40**, 249 (1971). https://doi.org/10.1016/0022-3115(71)90093-6

[19] B.N. Singh, A.J.E. Foreman, and H. Trinkaus, Journal of Nuclear Materials, **249**, 103 (1997). https://doi.org/10.1016/s0022-3115(97)00231-6

[20] T.S. Byun, K. Farrel, E.H. Lee, J.D. Hunn, and L.K. Mansur, Journal of Nuclear Materials, **298**, 1269 (2001).

[21] M.I. Luppo, C. Bailat, R. Schaublin, and M. Victoria, Journal of Nuclear Materials, **283-287**, 483 (2000). https://doi.org/10.1016/S0022-3115(00)00370-6

[22] F.W. Wiffen, Journal of Nuclear Materials, **67**, 119 (1977). https://doi.org/10.1016/0022-3115(77)90168-4

[23] I.M. Laptev, and O.O. Parkhomenko, *Vacancies, martensitic transformation, and resource of nuclear reactors*, (Kharkiv National University, Kharkiv, 2018), pp. 170. (in Ukrainian)

[24] S. Maloy, M.R. James, G. Willcutt, W.F. Sommer, M. Sokolov, L.L. Snead, M.L. Hamilton, *et al*., J. Nucl. Mater. **296**, 119 (2001). https://doi.org/10.1016/S0022-3115(01)00514-1

[25] X. Wu, X. Pan, M. Li, and J.F. Stubbins, Journal of Nuclear Materials, **343**, 302 (2005). https://doi.org/10.1016/j.jnucmat.2004.12.015

[26] H. Sencer, S.A. Maloy, M.L. Hamilton, and F.A. Garner, Journal of Nuclear Materials, **345**, 136 (2005). https://doi.org/10.1016/j.jnucmat.2005.05.005

[27] D.S. Pudjorahardjo, T. Sujitno, and Suprapto. Journal of Physics: Conference Series, **2498**, 012020 (2023). https://doi.org/10.1088/1742-6596/2498/1/012020

РАДІАЦІЙНА КРИХКІСТЬ ТАНТАЛОВОГО ПОКРИТТЯ МІШЕНЕЙ ДЖЕРЕЛ НЕЙТРОНІВ

О.О. Пархоменко[1,2], В.В. Ганн[1], Б.В. Борц[1], А.Ю. Зелінський[1], І.М. Карнаухов[1], Ю.О. Марченко[1]
[1]ННЦ "Харківський фізико-технічний інститут", Харків, Україна
[2]Харківський національний університет імені В.Н. Каразіна, Харків, Україна

Представлено роботу в галузі радіаційного матеріалознавства матеріалів мішеней для джерел нейтронів на основі підкритичних збірок, керованих лінійними прискорювачами електронів або протонів, – так званих ADS-систем. Наразі електроядерні ADS системи є прототипом безпечних ядерних реакторів 5-го покоління. У зв'язку з фізичним пуском установки нейтронного джерела ННЦ «ХФТІ», мішень якого виготовлена з вольфраму покритого танталом, розглянуто вплив випромінювання на механічні властивості, та оцінено ресурс танталового покриття мішені.

Ключові слова: *джерело нейтронів; системи керовані лінійними прискорювачами; мішені; танталове покриття; радіаційне зміцнення; окрихчення; дозова залежність*

East European Journal of Physics. **2.** 498-507 (2026)
DOI:10.26565/2312-4334-2026-2-56 ISSN 2312-4334

APPLICATION OF SEMI-EMPIRICAL MODELS OF ELECTRON BEAM CONTROL IN RADIATION STERILIZATION TECHNOLOGY

Valentín T. Lazurik[1]*, **Igor O. Girka**[1], **Oleksandr O. Zolotukhin**[1], **Zbigniew Zimek**[2]
[1]*V.N. Karazin Kharkiv National University, Kharkiv, Ukraine*
[2]*Institute of Nuclear Chemistry and Technology, Warsaw, Poland*
**Corresponding Author e-mail: vtlazurik@karazin.ua*

Received February 3, 2026; revised March 30, 2026; accepted April 22, 2026

An application of semi-empirical models involves analyzing data regularly recorded during irradiation control and processing it to determine the values of the semi-empirical model parameters. In the present paper, the recorded data used present the depth dose curves measured at the INCT radiation sterilization center in Warsaw, Poland. The measurement method is described. The depth dose curves are analyzed using the dosimetric wedge method. The characteristics of the depth dose curves are presented. The depth ranges are determined within which the measurement results can be used without special processing as depth dose curve values in the dosimetric wedge. Special procedures are developed to approximate and extrapolate the measurement results. The objective of the procedures is to obtain the basic dependencies of semi-empirical models, namely the doses as a function of depth at normal incidence of the electron beam on a semi-infinite medium. Special procedures are developed to process measurement results using the PFSEM method (two-parameter fitting of a semi-empirical model of depth-dose curves). A procedure for excluding bremsstrahlung contributions from depth-dose curves is proposed and implemented. The value of this contribution is estimated as the average dose in the bremsstrahlung tail region. The change of the bremsstrahlung influence on the doses with depth is neglected. The method for selecting the values of model-fitting parameters is proposed based on the assumption that the fitting parameters depend weakly on electron energy. Based on the proposed method, the fitting parameters of semi-empirical models are determined from Monte Carlo simulations of depth-dose curves during irradiation of a layer with a monoenergetic electron beam. The measurement results are compared with depth-dose curves calculated using semi-empirical models for electron-beam irradiation at different angles of incidence on an aluminum dosimetric wedge. Based on the comparison results, the errors in model predictions and the feasibility of implementing methods to optimize irradiation processes by selecting the angle of electron incidence on the surface of the irradiated object are discussed.

Keywords: *Electron beam dosimetry; Depth Dose curve; Sterilization; Control of optimal modes; Semi-empirical model; Monte-Carlo method*
PACS: 87.53.Bn, 02.60.Cb

INTRODUCTION

Radiation technologies are widely used to sterilize pharmaceutical products and medical equipment and to disinfect food products. Optimizing irradiation is one of the main tasks in implementing radiation technologies [1-16]. In radiation technologies, the minimum level of dose uniformity (*DUR*) in the irradiated object corresponds to the optimal irradiation mode [17-25]. For electron beams, the two-sided irradiation method is the one that enables low *DUR* [4,5]. When using this method, the optimal irradiation mode of the layer is achieved when, at a given electron energy $\boldsymbol{E}$, the layer has an optimal thickness $\boldsymbol{H_{opt}(E)}$. At the same time, there is a strong dependence of *DUR* on layer thickness, which poses technical challenges to implementing the optimal mode of two-sided irradiation at fixed electron energy. Changing the angle of incidence of the electron beam on the surface of the irradiated object is one possible solution to the technical problems encountered in implementing the two-sided irradiation method [26-34]. The feasibility of this approach for optimizing irradiation was demonstrated by reviewing the results of Monte Carlo modeling of depth-dose curves [26]. It should be noted that the capabilities of such modeling of the depth dose distribution for given angles of incidence of the electron beam on the layer were implemented in the *RT-Office* software (*ModeRTL* module). However, these capabilities were not used to optimize the irradiation in radiation technologies, since such a knowledge-intensive optimization procedure is difficult to implement in technology centers.

Therefore, new tasks arose in electron radiation dosimetry related to the need to investigate the dependence of the depth dose distribution on the angle of incidence of the electron beam on the material layer. To carry out these studies, semi-empirical models of the depth dose curve caused by an electron beam incident on the surface of a layer at an angle θ were developed. In these semi-empirical models [27,28], the distribution of transferred energy in the volume of matter, which is initiated when a point beam of radiation strikes the surface of a semi-infinite medium at a normal angle, is the basic object (*Dose-Map* object). The following assumptions were used to develop the models. The *Dose-Map* object was assumed to have axial symmetry with respect to the beam particles' direction of incidence on the layer. The parameters of the object in its eigen coordinate system were assumed to be independent on the angle of incidence of the beam on the layer of substance. Finally, the dose distribution was assumed to be uniform or normal (Gaussian) across the object's cross-sections at all depths within the layer. Based on these assumptions, two two-parameter semi-

---

Cite as: V.T. Lazurik, I.O. Girka, O.O. Zolotukhin, Z. Zimek, East Eur. J. Phys. 2, 498 (2026), https://doi.org/10.26565/2312-4334-2026-2-56

empirical models were developed: *SEM2U* – a model with uniform dose distribution, and *SEM2N* – a model with normal dose distribution in the cross-sections of the *Dose-Map* object.

A comparison of the depth dose curves obtained using the developed semi-empirical models *SEM2U* and *SEM2N* with the depth dose curves obtained by Monte Carlo simulation at different angles θ of the electron beam incidence on the layer demonstrated satisfactory agreement of these results for cases of monoenergetic electron beams at incidence angles $0° < \theta < 60°$ on a semi-infinite layer. In [27], examples were given where the developed two-parameter models provided the correct calculation of two technological characteristics of the double-sided irradiation simultaneously (in a coordinated manner): the optimal target thickness and the dose uniformity ratio in the target.

To implement methods for optimizing irradiation based on selecting the angle of incidence of electrons on the surface of the irradiated object, the semi-empirical models and the software developed on the basis of these models can be used. However, for the practical implementation of these developments, the proposed optimization methods should be approved and the software should be verified. In the present paper, the semi-empirical models are validated by the results of dose depth distribution curve measurements carried out at the INCT radiation sterilization centre in Warsaw, Poland.

The data recorded during the control of irradiation at this radiation sterilization centre is analyzed. The measurement method used is described. The characteristics of the depth dose curve measurements carried out by the dosimetric wedge method are analyzed. The depth ranges within which the measurement results can be used without special processing as depth dose curve values in the dosimetric wedge are determined. Special procedures for approximation and extrapolation of measurement results are used to obtain the values of the basic model: the values of the doses subject to the depth at normal incidence of the electron beam on a semi-infinite medium. Special procedures for processing measurement results are developed based on the *PFSEM* method (fitting of semi-empirical model parameters) [8]. The special procedure is used to exclude the contribution of bremsstrahlung to the depth dose curves. The procedure is based on the estimate of this contribution as the average dose value in the bremsstrahlung tail region.

The methods for determining the fitting parameters of semi-empirical models are analyzed. The method is proposed for selecting the values of the model fitting parameters. The method is based on the assumption of a weak dependence of the fitting parameters on the electron energy. Based on the proposed method, the fitting parameters of semi-empirical models are determined based on the results of Monte Carlo simulation of depth dose curves during irradiation of a layer with electron beams of different energies. The possibilities of implementing various methods for determining model fitting parameters in the practical activities of radiation sterilization centers are discussed.

The measurement results are compared with the results of calculating depth dose curves using semi-empirical models, when irradiating a layer with electron beams at different angles of incidence on the layer. The errors in the model predictions are discussed and recommendations are given for the implementation of methods for optimizing irradiation processes based on the selection of the angle of incidence of electrons on the surface of the irradiated object.

METHOD FOR VALIDATION OF SEMI-EMPIRICAL MODELS IN A RADIATION STERILIZATION CENTER

Measurement of depth dose curves at specified angles of incidence of the electron beam on the surface of the irradiated object

To validate the semi-empirical models, the radiation characteristics recorded at the radiation sterilization center are determined first. This is necessary to reconcile the data on the characteristics of the irradiation process available at this centre with the parameters of the semi-empirical models, which are required to calculate these characteristics. To test the semi-empirical models, the results of measurements of depth dose distribution curves in objects exposed to radiation at the Radiation Sterilization Center of the Institute of Nuclear Chemistry and Technology in Warsaw, Poland, are used. At this centre, uniform irradiation of the surface of objects was ensured by the uniform motion of objects on a conveyor line and scanning with an electron beam in a direction perpendicular to the direction of the conveyor motion. Changes in the angle of incidence $\boldsymbol{\theta}$ of the electron beam on the surface of the object were achieved by changing the spatial orientation of the irradiated object on the conveyor. For this purpose, the object was placed on a platform with a specified angle of inclination. The schematic of the method for measuring depth dose curves at specified angles of incidence of the electron beam on the surface of the irradiated object is shown in Fig. 1.

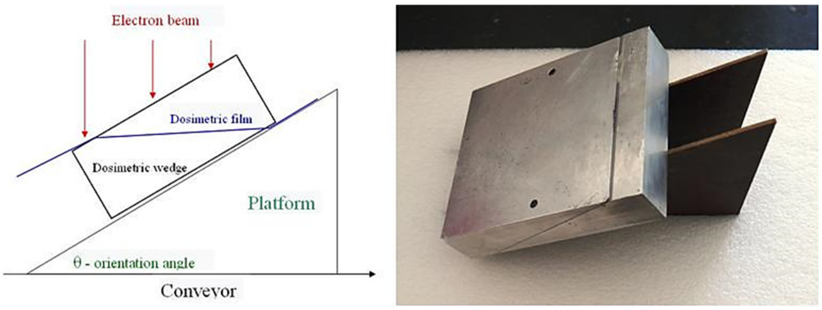

Figure 1. Schematic of measuring the depth dose curve at a given angle of incidence of the electron beam on the surface of the irradiated object

It should be noted that when using this method of measuring depth dose curves, it is necessary to take into account the change in the electron flux $\Phi(\theta)$ incident on the surface of the object when the angle θ of the irradiated object changes $\Phi(\theta) = \Phi_0 \cos(\theta)$.

The depth dose curves were measured using an aluminum dosimetric wedge from GEX Corporation, which characteristics are presented in Fig. 2.

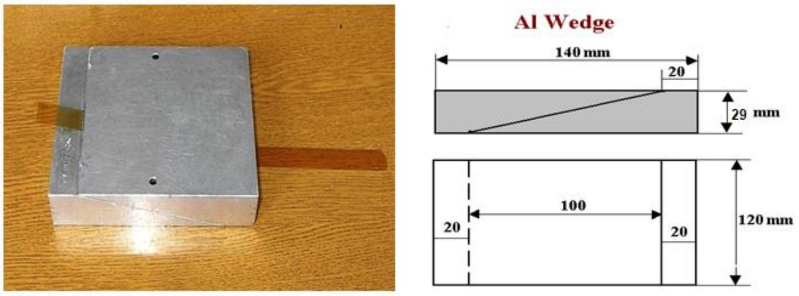

Figure 2. Aluminum dosimetric wedge for measuring depth dose curves

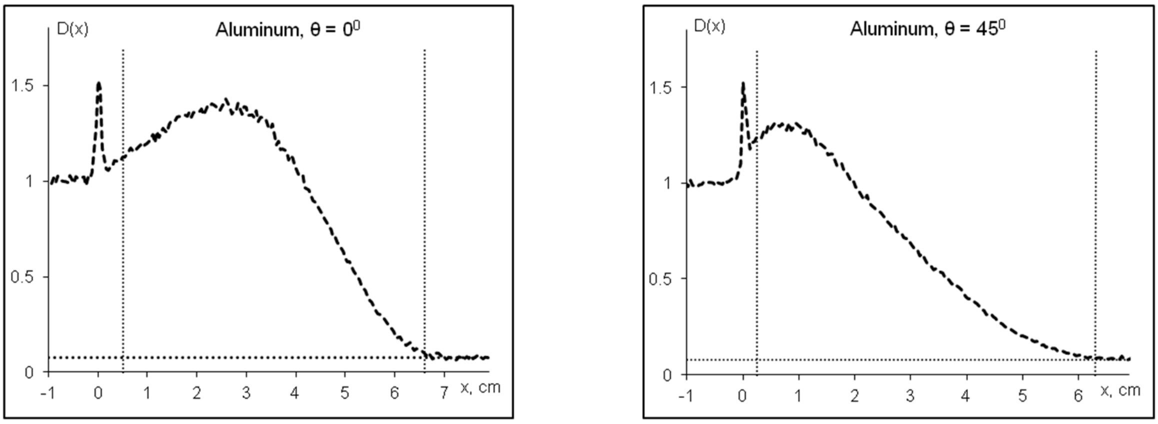

Figure 3. Results of measurements of depth dose curves in dosimetric film obtained by the dosimetric wedge method

The dose values D_i, determined at a set of points on the dosimetric film, are the measurement results. The starting point $x = 0$ of the depth dose curve is selected as the coordinate of the marker — the point at which the dose value is significantly greater than at neighboring points on the dosimetric film. Figure 3 shows the results of dose measurements for electron beam incidence angles $\theta = 0°$ and $45°$ on the surface of the dosimetric wedge, which are normalized to the average dose value on the upper surface of the dosimetric wedge (see Fig. 2).

To analyze the measurement results, we highlight three spatial areas, which are separated in the figure by vertical dotted lines.

Area 1 – the dose in the film located on the upper surface of the dosimetric wedge and that in the film when the film enters the dosimetric wedge. The measurement results in this area cannot be used to describe the depth dose curves, since they are distorted by boundary effects in the design of the dosimetric wedge and the positioning of the marker on the film.

Area 2 – the dose in the film located at a sufficient distance from the boundaries of the dosimetric wedge. The measurement results in this area are suitable for describing the depth dose curves.

Area 3 – the dose in the film, where the dose values are determined by the bremsstrahlung from the electron beam passing through the dosimetric wedge to this area, the so-called bremsstrahlung tail. The measurement results in this area cannot be used for comparison with the results of calculations based on semi-empirical models, since the models take into account the dose formation only due to the ionization losses of electrons.

Thus, the data obtained on the basis of measurements of depth dose curves by the dosimetric wedge method can be used to describe depth dose curves only in a limited depth range. To validate the models, it is necessary to extract the ionization component of the dose from this data.

Determination of the basic parameters of the model based on the results of measuring the depth dose curve

Semi-empirical models of the depth dose curve for an electron beam incident on a semi-infinite medium at an angle $\boldsymbol{\theta}$ are based on relationships in the form of integral transformations of the depth dose curve for normal incidence of the radiation beam on the medium [27,28]. Therefore, processing the measurement results with the objective to obtain the depth dose curve for normal incidence of the electron beam on a semi-infinite medium is the first step in determining the model parameters. As shown in the previous section, the data that can be obtained based on measurements by the dosimetric wedge method correctly describes the depth dose curve only at a sufficient distance from the irradiated surface of the dosimetric wedge. In the integral transformations applied in the models, the depth range near the surface of the irradiated object makes a significant contribution to the results. Therefore, special methods of processing the measurement results are required for the correct extrapolation of the depth dose curve in the shallow depth range in the wedge. For this purpose, the processing of the measurement results of the depth dose curve in the film at normal incidence of the electron beam on the wedge was carried out using a two-parameter electron beam model (PFSEM method), i.e., by fitting the parameters of a semi-empirical model [34].

The red solid curve in Fig. 4 presents the result of a two-parameter fit with the following *PFSEM* method parameters: monoenergetic electron beam energy is $E_0 = 9.84$ *MeV* and additional layer thickness corresponding to the displacement in the film is $X_0 = 0.87$ *cm*. The dotted curve is calculated in the result of a single-parameter fit with the following *PFSEM* method parameter value: monochromatic electron beam energy is $E_1 = 8.4$ *MeV*. As one can see in Fig. 4, the two-parameter fitting of *PFSEM* measurement results provides a more accurate approximation of measurement results and extrapolation of the depth dose curve to the shallow depth region in the wedge than standard one-parameter method.

It should be noted that the obtained approximation of the depth dose curve in the film under normal incidence of the electron beam on the wedge contains the contribution of bremsstrahlung to the dose value. In Fig. 4, the dotted horizontal line shows the level of the bremsstrahlung tail. Since the models take into account the dose formation only due to ionization losses of electrons, it is necessary to exclude the contribution of bremsstrahlung from the approximation of the depth dose curve. To do this, the value of the contribution of bremsstrahlung to the dose is assumed to be independent of the depth. The value of this contribution is calculated as the average dose in the region 3 - the tail of the bremsstrahlung and subtract the obtained value of the contribution from the dose values at all depths. The result of excluding the contribution of bremsstrahlung from the depth dose curve is shown in Fig. 5. The model parameter L_{max} is determined from the curve in Fig. 5. This parameter is the depth to which the values of the depth dose curve in the film are known. The parameter is determined as the maximum value of the depth *x* to which all dose values $D(x) > 0$. For the data in Fig. 5, the model parameter $L_{max} = 6.6$ *cm*.

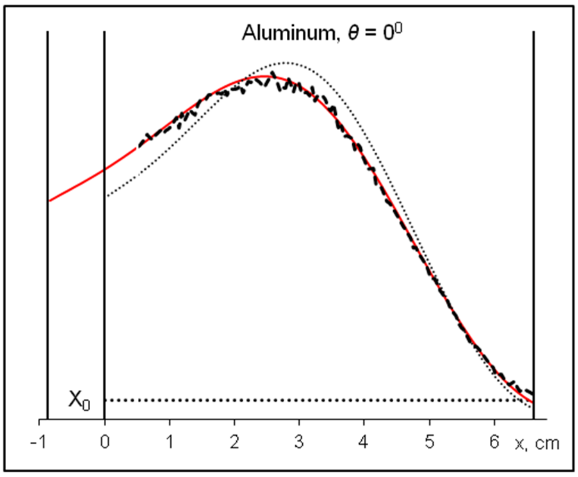

Figure 4. Results of processing the measurements of the depth dose curve in the film (dashed curve) using the ***PFSEM*** method. The red solid curve corresponds to the two-parameter fit. The dotted curve corresponds to the single-parameter fit.

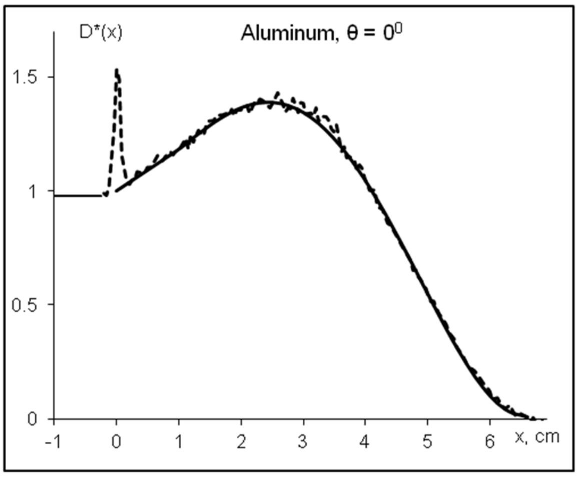

Figure 5. Depth dose curve in the film due to ionization losses of electrons, with normal incidence of the electron beam on the wedge – basic dependence for semi-empirical models.

The solid curve in Fig. 5 shows the depth-dose curves in the film when the electron beam strikes the wedge normally, which is prepared for use in semi-empirical models as basic data for calculations. In the following, the characteristics for these depth-dose curves are calculated in accordance with standards [4, 6]. These parameters are: the practical range of electrons R_p and the depth of half the maximum dose reduction R_{50}. The characteristics of the dose-depth dependence curves (R_p,R_{50}) relate to the parameters of the *PFSEM* method (E_0,X_0) by the following relationships [8]:

$$R_p = R_p(E_0) - X_0 \cdot K_w;\ R_{50} = R_{50}(E_0) - X_0 \cdot K_w, \tag{1}$$

where $R_p(E_0)$ is practical range of electrons and $R_{50}(E_0)$ is the depth of half the maximum dose reduction for electrons with energy E_0, K_w is the ratio of film distance to the depth in dosimetric wedge (for standard aluminum dosimetric wedge, this ratio is $K_w = 0.28$).

Using eq. (1) and the values of the parameters (E_0, X_0) determined during processing the measurement results (see Fig. 4) by the *PFSEM* method, one obtains $R_p = 1.75$ *cm*, $R_{50} = 1.32$ *cm*. Based on these values (R_p, R_{50}), according to the standard [6], characteristics of the electron energy: average energy E_{Av} and most probable energy E_p of the electron source, are determined: $E_{Av} = 8.47$ *MeV* $E_p = 8.77$ *MeV*. Note that the energy value $E_1 = 8.4$ *MeV*, calculated based on a single-parameter *PFSEM* fit, is close to the energy value E_{Av}.

Determination of fitting parameters for semi-empirical models of the depth dose curve

The basic relationship for the depth dose curve in a semi-infinite medium *D(x,θ,E)*, under uniform irradiation with a monoenergetic electron beam with energy *E* at an angle *θ* to the surface of the medium, can be represented as an integral transformation of the depth dose curve in a semi-infinite medium *D(x,0,E)*, when the medium is irradiated with a normally incident electron beam

$$D_i(x,\theta,E) = \int_0^{L_{\max}} D(t,0,E)\cdot K_i(t,x,\theta,\alpha_i(E),Q_i(E))dt \tag{2}$$

where $K_i(t,x,\theta,\alpha_i(E),Q_i(E))$ is the kernel of the integral transform; $\alpha_i(E),Q_i(E)$ are fitting parameters of semi-empirical models; for the *Dose-Map* object model with uniform dose distribution, the index *i=1,* and for Gaussian distribution, the index *i=2*.

In semi-empirical models [27], power functions are used to approximate the distribution of transmitted energy in the volume of matter, which is initiated by the normal incidence of a point beam of radiation on the surface of a semi-infinite medium (*Dose-Map* object).

$$F(x,\alpha,Q) = \alpha\cdot L_{\max}\left(\frac{x}{L_{\max}}\right)^{Q}, \qquad \alpha > 0, \quad Q \geq 0, \quad 0 < x \leq L_{\max} \tag{3}$$

Therefore, these models have two fitting parameters: *Q* - the exponent of the power function and *α* - a multiplier that determines the maximum value of the function $F_{max} = \alpha\cdot L_{max}$. Due to the axial symmetry of the *Dose-Map* object, the dependence of the radius $R(x) = F(x,\alpha_1,Q_1)$ of the circle is used to describe uniform distribution, and the dependence of the dispersion $\sigma(x) = F(x,\alpha_2,Q_2)$ on the depth *x* in the medium is used for Gaussian distribution.

The procedures for determining the fitting parameters of semi-empirical models were described in [28]. However, the calculation results were presented there only for monoenergetic electron beams. Industrial radiation facilities typically have electron beams with a fairly broad spectrum. In this case, the depth dose curve *D(x,θ)* can be calculated as the average of the depth dose curves *D(x,E,θ)* according to the spectral distribution of electrons *S(E)*:

$$D(x,\theta) = \int_{E_{\min}}^{E_{\max}} D(x,\theta,E)\cdot S(E)dE \tag{4}$$

Here E_{min}, and E_{max} are minimum and maximum electron energy in the beam.
Substituting Eq. (2) into Eq. (4) and changing the order of integration, one obtains

$$D_i(x,\theta) = \int_0^{L_{\max}}\int_{E_{\min}}^{E_{\max}} D(t,0,E)\cdot K_i(t,x,\theta,\alpha_i(E),Q_i(E))\cdot S(E)dEdt \tag{5}$$

If the spectral distribution *S(E)* and the fitting parameter functions of the models $\alpha_i(E)$ and $Q_i(E)$ are known for irradiation by the electron beam with the given spectrum, then eq. (5) makes it possible to calculate the depth dose curve $D_i(x,\theta)$. However, detailed information about the spectrum and the dependence of the model fitting parameters on electron energy is usually unavailable.

To develop the approximate calculation method, when integrating the energy in eq. (5), the model fitting parameters are assumed to be constants equal to $\alpha_i(E_{Av})$ and $Q_i(E_{Av})$. In this case, one derives the expression

$$D_i(x,\theta) = \int_0^{L_{\max}} D(t,0)\cdot K_i(t,x,\theta,\alpha_i(E_{Av}),Q_i(E_{Av}))dt \tag{6}$$

Here *D(t,0)* is the dose depth curve in semi-infinite medium under irradiation by normally incident electron beam with a given spectrum,

$$D(t,0) = \int_{E_{\min}}^{E_{\max}} D(t,0,E)\cdot S(E)dE \tag{7}$$

It should be noted that the simple method for calculating the depth dose curve in accordance with the following expression was suggested in [27]:

$$D(x,\theta) = \int_0^{L_{\max}} D(t,0,E_{Av})\cdot K_i(t,x,\theta,\alpha_i(E_{Av}),Q_i(E_{Av}))dt \tag{8}$$

However, the results obtained by this method appeared to be unsatisfactory because of the difference between the depth dose curve $\boldsymbol{D(t,0,E_{Av})}$ and the approximation of the dose measurement results ***D(t,0)***, which is shown in Fig. 4. The application of the exact dependence of the depth dose curve ***D(t,0)*** in eq. (6) ensures satisfactory accuracy of the model predictions.

In the proposed method based on eq. (6), to determine the fitting parameters of the semi-empirical model, it is sufficient to determine the values of these parameters for a monoenergetic electron beam with energy E_{Av}. The procedure for determining the fitting parameters of semi-empirical models, as described in [28], is used in the present paper.

The fitting parameters of the semi-empirical model are determined from the condition of equality of the value of the optimal layer thickness H_{opt} during two-side electron irradiation, obtained by modelling the depth dose curves using the Monte Carlo method, to the value of the optimal layer thickness calculated using the semi-empirical model with these parameters. The implemented method is as follows.

1. The irradiation mode is selected: electron energy E and angle θ of incidence of the beam on the surface of the object undergoing the radiation treatment. The selected irradiation mode of the object should ensure a strong dependence of the results of the depth dose curve calculation on the fitting parameters of the semi-empirical model.
2. The depth dose curve for the selected irradiation mode is determined based on modelling the electron passage through the semi-infinite medium by the Monte Carlo method. The depth dose curve calculated using the Monte Carlo method is shown in Fig. 6 in the form of the histogram.
3. The optimal layer thickness H_{opt} is determined for two-side electron irradiation using the depth dose curve calculated by the Monte Carlo method. The optimal layer thickness H_{opt} is determined by searching through layer thickness values with the step of 0.01 g/cm^2. The search for thicknesses is stopped when the layer thickness is found for which the difference between the dose at the centre and the dose at the surface of the layer has a minimum positive value. The depth dose curve in the layer of optimal thickness under two-side electron irradiation is shown in Fig. 7 by dashed curve.
4. The parameters of the semi-empirical models are determined from the condition of equality of the value of the optimal layer thickness H_{opt}, obtained on the basis of the depth dose curve calculated by the Monte Carlo method, to the value of the layer thickness obtained on the basis of calculations using the semi-empirical model. The parameters of the semi-empirical model are determined by searching through parameter values with the step of 0.01. The depth dose curves calculated with the selected parameters for the semi-empirical model with the uniform distribution (solid curves) and the Gaussian distribution (dotted curves) of the dose in the cross-sections of the *Dose-Map* object are shown in Figs. 6 and 7.

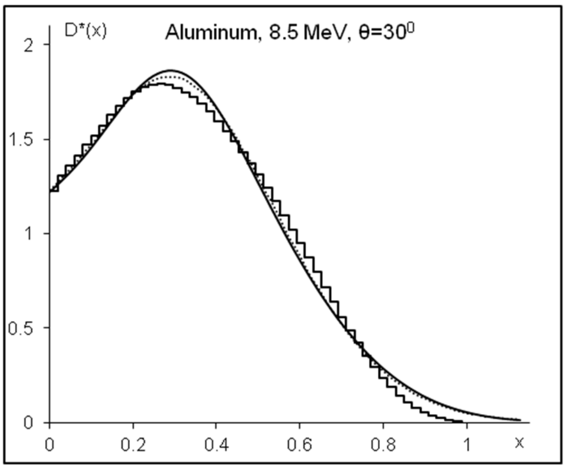

Figure 6. Depth dose curves calculated for a semi-infinite medium. A histogram corresponds to a Monte Carlo simulation.

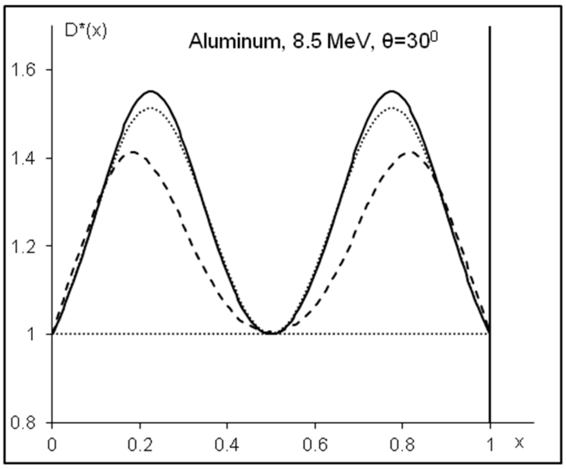

Figure 7. Depth dose curves in a layer of optimal thickness H_{opt}= 6.7 g/cm^2 with two-sided irradiation. The dashed curve corresponds to the Monte Carlo simulation.

COMPARISON OF MODELLING RESULTS WITH MEASUREMENT RESULTS

The depth dose curves are calculated in semi-empirical models using eq. (4). This equation uses $D(t,0)$ - the depth dose curve prepared on the basis of processing the measurement results described in the previous section of the present paper. To determine the fitting parameters of the models, the method proposed in the previous section of the present paper is used. The irradiation mode is selected: the energy of the monoenergetic electron beam is assumed to be equal to the average energy $E_{Av}= 8.5\ MeV$, calculated based on the processing of the deep dose curve measurement results. The angle θ of the beam incidence on the surface of the dosimetric wedge is assumed to be equal to $\theta = 30°$. The choice of this angle of orientation of the dosimetric wedge ensures sufficiently strong dependence of the results of the depth dose curve calculation on the fitting parameters of the semi-empirical model. However, at this angle of incidence of the electron beam on the layer, the influence of the layer boundary is still insignificant.

The equality of the values of the optimal layer thicknesses, the thickness obtained on the basis of Monte Carlo calculations, and the thickness obtained on the basis of calculations using a semi-empirical model is illustrated in Fig. 7. The depth dose curves shown in Fig. 7 are calculated with the selected parameters $\alpha_1 = 0.8$, and $Q_1 = 1$ for the model with a uniform distribution (solid curves) and with parameters $\alpha_2 = 0.4$, and $Q_2 = 1$ for the model with Gaussian distribution (dotted curves) of the dose in the cross-sections of the *Dose-Map* object. These values of the fitting parameters can be used to calculate depth-dose curves in semi-empirical models for any orientation angle of the dosimetric wedge.

The results of calculations of depth dose curves in semi-empirical models for angles $\theta = 10°, 20°, 30°, 45°$ of the dosimetric wedge orientation are shown in Figs. 8-11.

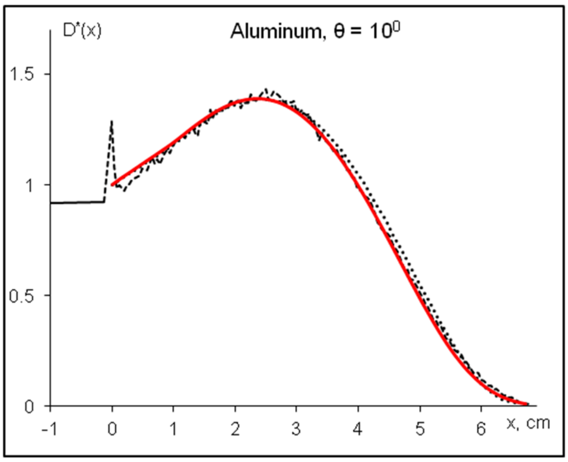

Figure 8. Depth dose curves calculated for a semi-infinite medium. The red curve corresponds to the calculation in the *SEM2U* model. The dotted curve relates to the base curve for the *SEM2U* and *SEM2N* models

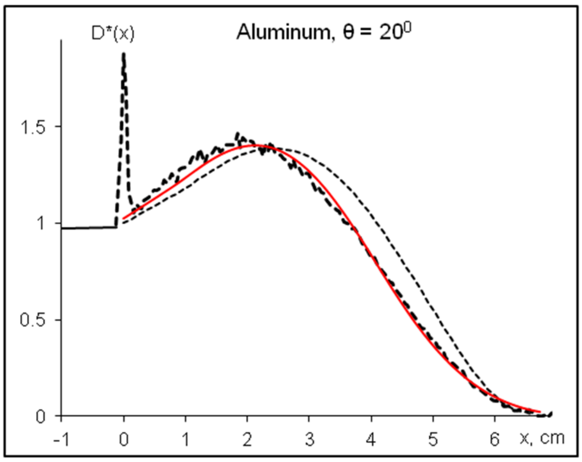

Figure 9. Depth dose curves calculated for a semi-infinite medium. The red curve relates to the calculation in the *SEM2U* model. The dotted curve corresponds to the baseline curve for the *SEM2U* and *SEM2N* models

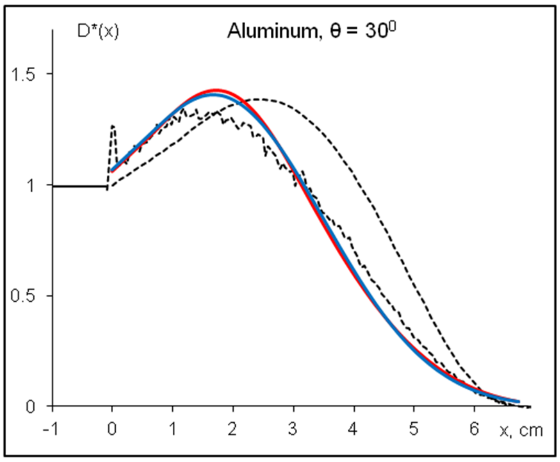

Figure 10. Depth dose curves calculated for a semi-infinite medium. The red curve relates to the calculation in the *SEM2U* model. The blue curve corresponds to the calculation in the *SEM2N* model

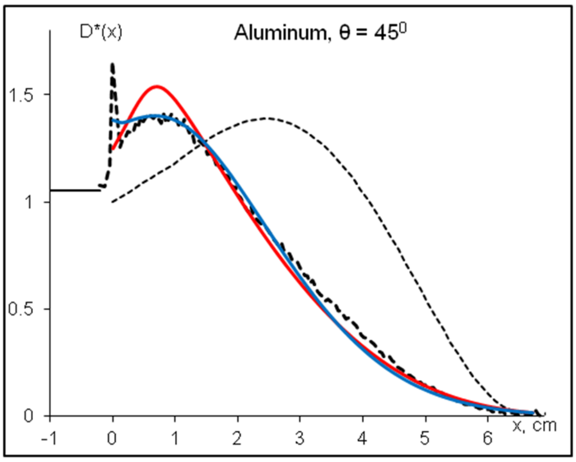

Figure 11. Depth dose curves calculated for a semi-infinite medium. The red curve represents the calculations in the *SEM2U* model. The blue curve relates to the calculations in the *SEM2N* model

The red curves represent calculations in a model with uniform dose distribution, and the blue curves represent calculations in a model with Gaussian dose distribution in the *Dose-Map* object cross-sections. The dashed curves represent depth-dose measurements carried out at different orientations of the dosimetric wedge. The dotted curves represent the depth-dose curve for normal incidence of the electron beam on the dosimetric wedge, which is used as baseline data for calculations in semi-empirical models.

As one can see in Figs. 8 and 9, at small angles of orientation of the irradiation object, the depth dose curve (red curve) does not differ significantly from the depth dose curve (dotted curve) at normal incidence of the electron beam. In this case, there is good agreement between the simulation results and the measurements. It should be noted that the results of calculations using the two models at small angles of orientation of the irradiation object differ only due to rounding errors in the calculations.

As the orientation angle increases, the difference between the results of calculations using the two models increases, as one can clearly see in Figs. 10 and 11. These differences are related to the influence of the boundary on the dose distribution in the cross-sections of the *Dose-Map* object. Therefore, the difference between the calculation results using the two models can serve as an indicator of the correctness of the basic assumption that the parameters of the *Dose-Map* object in its eigen coordinate system are independent on the angle of incidence of the beam on the layer. As one can see in Fig. 11, the model with a Gaussian distribution (blue curve) of the dose in the cross-sections of the *Dose-Map* object describes the results of measurements of the depth dose curve near the irradiation surface more adequately.

The large error in the model description of the measurement results should be noted in Fig. 10 at the orientation angle of 30°. This is explained by changes in the irradiation mode happened on different days. Such differences indicate instability in the radiation sterilization process during a single batch of the treated product.

CONCLUSIONS

The method of electron beam irradiation with specified beam-incidence angles on the surface of the irradiated object is proposed.

The object is assumed to be placed on a special platform with a variable angle of inclination. The platform is assumed to be installed on the conveyor line of the radiation technology unit.

The method is proposed to measure the depth-dose curve at specified object-orientation angles during electron-beam irradiation. The dosimetric wedge is assumed to be placed on a special platform with a specified angle of inclination, which is installed on the conveyor line of the radiation technology facility. For this method, the dependence of the electron flux $\Phi(\theta)$ incident on the surface of the object on the change in the orientation angle θ of the irradiated object is determined as $\Phi(\theta) = \Phi_0 \cos(\theta)$.

Based on the proposed method, measurements of depth dose curves are carried out in a standard aluminum dosimetric wedge at wedge orientation angles $\theta = 0°, 10°, 20°, 30°, 45°, 60°$.

The results of measurements across three spatial regions at different depths within the wedge are analyzed. It is shown that data obtained from depth-dose curve measurements using the dosimetric wedge method are applicable only within a limited depth range and that specialized methods for processing these data are required when testing semi-empirical models.

Special methods are developed for processing measurement results to correctly approximate and extrapolate the depth dose curve in the shallow depth region of the wedge, based on the *PFSEM* method, i.e. the two-parameter fitting method of the semi-empirical model. A method for excluding the contribution of bremsstrahlung from depth-dose curve measurements is proposed and implemented, as required for comparisons with model-based calculations. The basic depth-dose distribution curve is determined and serves as the basis for calculations in semi-empirical models.

The basic depth dose distribution curve is obtained using special methods developed in the present paper for processing measurements of depth dose distribution curves on a film under normal incidence of an electron beam on a wedge. For this curve, in accordance with the standard [6], the values of electron energy characteristics, such as the average energy E_{Av} and most probable energy E_p of the electron source, are determined. For this depth dose curve, the values of the electron energy characteristics, namely, average energy E_{Av} and most probable energy E_p of the electron source are determined.

A method for determining fitting parameters for semi-empirical models is proposed. It is based on the assumption that these parameters are independent of electron energy. In this method, a base curve derived from processed measurement results is used in the integral transformation. The fitting parameters of semi-empirical models $\alpha_i(E_{Av})$ and $Q_i(E_{Av})$ are determined based on the values of these parameters for the case of a monoenergetic electron beam with energy E_{Av}. The values of the fitting parameters are determined for the model with the uniform distribution ($\alpha_1 = 0.8, Q_1 = 1$) and for the model with the Gaussian distribution ($\alpha_2 = 0.4, Q_2 = 1$) of the dose in the cross-sections of the *Dose-Map* object.

The measurement results are compared with the simulation results from the depth dose curves in semi-empirical models for angles $\theta = 10°, 20°, 30°, 45°$ of the dosimetric wedge orientation. At small angles of orientation of the irradiated object, good agreement between the simulation and measurement results is observed. In these cases, the results of calculations using the two models differ only due to rounding errors.

As the orientation angle increases, the difference between the results of calculations using the two models widens due to the boundary's influence on the dose distribution in the *Dose-Map* object cross-sections. Therefore, the difference between the results of calculations using the two models can serve as an indicator of the model error. It should be noted that the model with a Gaussian dose distribution in the cross-sections of the Dose-Map object more adequately describes measurements of the depth dose curve near the irradiation surface.

It is found that changes in the irradiation regime during radiation sterilization can significantly increase the discrepancy between the model description and the measured depth-dose curve.

ORCID

Valentín T. Lazurik, https://orcid.org/0000-0002-8319-0764; **Igor O. Girka,** https://orcid.org/0000-0001-6662-8683;
Oleksandr O. Zolotukhin, https://orcid.org/0000-0003-4440-240X; **Zbigniew Zimek,** https://orcid.org/0000-0002-8653-5609

REFERENCES

[1] S. Schiller, U. Heisig, and S. Panzer, *Electron Beam Technology*, (John Wiley & Sons Inc, 1995).
[2] M. Reiser, *Theory and Design of Charged Particle Beams*, (John Wiley & Sons, 2008).

[3] R.C. Davidson, and H. Qin, *Physics of Intense Charged Particle Beams in High Energy Accelerators*, (World Scientific, Singapore, 2001).

[4] ICRU REPORT 35, *Radiation dosimetry: electron beams with energies between 1 and 50 MeV*, (ICRU, 1984), p. 168.

[5] R.J. Woods, and A.K. Pikaev, *Applied radiation chemistry: radiation processing*, (Wiley, New York, 1994).

[6] ISO/ASTM Standard 51649, *Practice for dosimetry in an e-beam facility for radiation processing at energies between 300 keV and 25 MeV*, (ASTM Standards, vol. 12.02, 2005).

[7] Yu. Pavlov, and P. Bystrov, "Software and hardware complex for radiation processing facility control," Radiation Physics and Chemistry, **196**, 110110 (2022). https://doi.org/10.1016/j.radphyschem.2022.110110

[8] V.T. Lazurik, V.M. Lazurik, G.P. Popov, and Z. Zimek, "Dosimetry method based on a two-parametric model of electrons beam for radiation processing," Problems of Atomic Science and Technology, 112(6), 137–141 (2017).

[9] J.E. Arellano, L.A. Diaz-Torres, J.P. Córdova, J.L. Cervantes, J.A. Elias, M.A. Sosa, and M.A. Vallejo, "Thermoluminescent properties of NASICON glass-ceramics under electron beam irradiation," Journal of Alloys and Compounds, **1056**, 186585, (2026). https://doi.org/10.1016/j.jallcom.2026.186585

[10] S. Howard, and V. Starovoitova, "Target optimization for the photonuclear production of radioisotopes," Applied Radiation and Isotopes, **96**, 162 (2015). https://doi.org/10.1016/j.apradiso.2014.12.003

[11] R. Pomatsalyuk, S. Romanovskyi, V. Shevchenko, and V. Uvarov, "Real Time Luminescent Dosimetry System for Product Processing at Aa Electron Accelerator," Problems of Atomic Science and Technology, (5), 131 (2024). https://doi.org/10.46813/2024-153-131

[12] R.I. Pomatsalyuk, S.K. Romanovsky, V.O. Shevchenko, V.Yu. Titov, D.V. Titov, and V.L. Uvarov, "Analysis of Uncertainty Sources in Dose Measurement at an Industrial Electron Accelerator," Problems of Atomic Science and Technology, (5), 117 (2024). https://doi.org/10.46813/2024-153-117

[13] I.V. Melnik, and S.B. Tugay, "Analytical calculations of anode plasma position in high-voltage discharge range in case of auxiliary discharge firing," Radioelectronics and Communications Systems, **55**, 514 (2012). https://doi.org/10.3103/S0735272712110064

[14] D. Gregocki, P. Köster, L.U. Labate, S. Piccinini, F. Avella, F. Baffigi, G. Bandini, *et al*., "Real-Time Dose Monitoring via Non-Destructive Charge Measurement of Laser-Driven Electrons for Medical Applications," Instruments, **9**, 25 (2025). https://doi.org/10.3390/instruments9040025

[15] I.A. Ivanov, "Application of the Lambert W Function to the Calculation of the Electron Transmission Coefficient and Bremsstrahlung Yield from the Bethe–Heitler Theory," Physics of Atomic Nuclei, (2025). https://doi.org/10.1134/S1063778825090212

[16] I.V. Melnyk, Radioelectronics and Communications Systems, **60**, 319, (2017). https://doi.org/10.3103/S0735272717070056

[17] ASTM E2232-21 *Standard Guide for Selection and Use of Mathematical Methods for Calculating Absorbed Dose in Radiation Processing Applications*, (ASTM, 2021), p. 19. https://doi.org/10.1520/E2232-21

[18] F. Salvat, J. Fernandez-Varea, J. Sempau, *PENELOPE 2011: A Code System for Monte Carlo Simulation of Electron and Photon Transport*, (Nuclear Energy Agency, 2012), p. 385.

[19] S.-T. Jung, S.-H. Pyo, W.-G. Kang, Y.-R. Kim, J.-K. Kim, C.M. Kang, Y.-C. Nho, and J.-S. Park, Radiation Physics and Chemistry, **186**, 109506 (2021). https://doi.org/10.1016/j.radphyschem.2021.109506

[20] M. Rezzoug, M. Zerfaoui, Y. Oulhouq, A. Rrhioua, S. Didi, and D. Bakari, Radiation Physics and Chemistry, **235**, 112828 (2025). https://doi.org/10.1016/j.radphyschem.2025.112828

[21] D.J.S. Findlay, Nucl. Instrum. Methods A, **276**(3), 598 (1989). https://doi.org/10.1016/0168-9002(89)90591-3

[22] V.L. Uvarov, A.A. Zakharchenko, N.P. Dikiy, Yu.V. Lyashko, R.I. Pomatsalyuk, V.A. Shevchenko, and Eu.B. Malets, Problems of Atomic Science and Technology, (6), 180 (2023). https://doi.org/10.46813/2023-148-180

[23] V.L. Uvarov, A.A. Zakharchenko, N.P. Dikiy, R.I. Pomatsalyuk, and Yu.V. Lyashko, Applied Radiation and Isotopes, **199**, 110890 (2023). https://doi.org/10.1016/j.apradiso.2023.110890

[24] V.L. Uvarov, A.A. Zakharchenko, N.P. Dikiy, YuV. Lyashko, and R.I. Pomatsalyuk, Radiation Physics and Chemistry, **214**, 111547 (2024). https://doi.org/10.1016/j.apradiso.2024.111547

[25] M. Rosenstein, H. Eisen, and J. Silverman, Journal of Applied Physics, **43**, 3191 (1972). https://doi.org/10.1063/1.1661684

[26] V.G. Rudychev, V.T. Lazurik, and Y.V. Rudychev, Radiation Physics and Chemistry, **186**, 109527 (2021). https://doi.org/10.1016/j.radphyschem.2021.109527

[27] I.O. Girka, V.T. Lazurik, Semi-empirical models of electron beam control for radiation sterilisation, East Eur. J. Phys. 3, 422 (2025), https://doi.org/10.26565/2312-4334-2025-3-45

[28] V. Lazurik, S. Sawan, V. Lazurik, and O. Zolotukhin, in: *4th International Maghreb Meeting of the Conference on Sciences and Techniques of Automatic Control and Computer Engineering Proceedings*, (IEEE, Maghreb, 2024), pp. 649–653. https://doi.org/10.1109/MI-STA61267.2024.10599694

[29] I.V. Melnyk, "Simulation of energetic efficiency of triode high voltage glow discharge electron sources with account of temperature of electrons and its mobility in anode plasma," Radioelectronics and Communications Systems, **56**, 592 (2013), https://doi.org/10.3103/S0735272713120066

[30] I. Melnyk, A. Pochynok, and M. Skrypka, "Comparison of methods for interpolation and extrapolation of boundary trajectories of short-focus electron beams using root-polynomial functions," System Research and Information Technologies, **3**, 77 (2024). https://doi.org/10.20535/SRIT.2308-8893.2024.3.05

[31] S.V. Denbnovetsky, V. I. Melnik, I.V. Melnik, B.A. Tugay, in: *XVIII-th International Symposium on Discharges and Electrical Insulation in Vacuum, Proceedings*, (ISDEIV, 1998), vol. 2, pp. 637–640. https://doi.org/10.1109/DEIV.1998.738530

[32] I. Melnyk, A. Pochynok, M. Skrypka, and O. Demyanchenko, "Method of interpolation using root-fractional-rational functions of different orders," Bulletin of Taras Shevchenko National University of Kyiv. Physics and Mathematics, **80**(1), 130-138. (2025). https://doi.org/10.17721/1812-5409.2025/1.17

[33] V. Lazurik, and V. Moskvin, “Monte Carlo calculation of charge-deposition depth profile in slabs irradiated by electrons,” Nucl. Instrum. Methods B, **108**(3), 276 (1996). https://doi.org/10.1016/0168-583X(95)01052-1

[34] T. Tabata, P. Andreo, and K. Shinoda, “An algorithm for depth–dose curves of electrons fitted to Monte Carlo data,” Radiation Physics and Chemistry, **53**, 205 (1998). https://doi.org/10.1016/S0969-806X(98)00102-9

ЗАСТОСУВАННЯ НАПІВЕМПІРИЧНИХ МОДЕЛЕЙ УПРАВЛІННЯ ПУЧКОМ ЕЛЕКТРОНІВ У ТЕХНОЛОГІЇ РАДІАЦІЙНОЇ СТЕРИЛІЗАЦІЇ

Валентин Т. Лазурик[1], Ігор О. Гірка[1], Олександр О. Золотухін[1], Збігнєв Зімек[2]
[1]Харківський національний університет імені В.Н. Каразіна, Харків, Україна
[2]Інститут ядерної хімії та технологій, Варшава, Польща

Для використання напівемпіричних моделей необхідно аналізувати дані, які регулярно реєструються під час контролю процесів опромінення, та обробляти ці дані для визначення значень параметрів напівемпіричних моделей. У цій роботі як реєстровані дані використано глибинні криві дози, виміряні у Центрі радіаційної стерилізації INCT, Варшава, Польща. Описано метод проведених вимірювань і представлено аналіз особливостей глибинних кривих дози, які було виміряно методом дозиметричного клина. Визначено області глибин, в яких результати вимірювань можуть бути використані без спеціальної обробки в якості значень глибинної кривої дози в дозиметричному клині. Розроблено спеціальні процедури апроксимації та екстраполяції результатів вимірювань для отримання значень базової залежності напівемпіричних моделей - значення глибинної кривої дози при нормальному падінні пучка електронів на напівнескінченне середовище. Розроблено спеціальні процедури обробки результатів вимірювань на базі методу PFSEM (двопараметрична підгонка параметрів напівемпіричної моделі глибинних кривих дози). Запропоновано та реалізовано процедуру виключення внеску гальмівного випромінювання зі значень глибинних кривих дози. Величину цього внеску оцінено як середнє значення дози в інтервалі хвоста гальмівного випромінювання, і припущено, що величина внеску гальмівного випромінювання в дозу не змінюється з глибиною. Запропоновано метод вибору значень параметрів підгонки моделей на основі припущення про слабку залежність параметрів підгонки від енергії електронів. На основі запропонованого методу визначено параметри підгонки напівемпіричних моделей за результатами моделювання методом Монте-Карло глибинних кривих дози при опроміненні шару моноенергетичним пучком електронів. Проведено порівняння результатів вимірювань із результатами розрахунку глибинних кривих дози, виконаних за напівемпіричними моделями, при опроміненні шару пучками електронів з різними кутами падіння на алюмінієвий дозиметричний клин. На основі результатів порівняння обговорено похибки прогнозів моделей і можливість реалізації методів оптимізації процесів опромінення на основі вибору кута падіння електронів на поверхню опромінюваного об'єкта.

Ключові слова: *електронно-променева дозиметрія; крива глибини-дози; процеси стерилізації; контроль оптимальних режимів; напівемпірична модель; метод Монте-Карло*

East European Journal of Physics. 2. 508-514 (2026)
DOI:10.26565/2312-4334-2026-2-57 ISSN 2312-4334

MORPHOLOGICAL FEATURES AND MICROSTRUCTURAL CHARACTERISTICS OF CRATERS ON THE SURFACE OF INDUSTRIAL ALUMINUM ALLOY AA6111 IRRADIATED WITH A HIGH-CURRENT PULSED ELECTRON BEAM

V.V. Bryukhovetsky[1], V.V. Lytvynenko[1]*, D.E. Myla[1], O.L. Rak[2]
[1]*Institute of Electrophysics and Radiation Technologies NAS of Ukraine, 13, Gudanova Str., 61024 Kharkiv, Ukraine*
[2]*NSC «Kharkiv Institute of Physics and Technology» NAS of Ukraine, 1, Akademicheskaya Str., 61108 Kharkiv, Ukraine*
**Corresponding Author e-mail: vvlytvynenko@ukr.net*

Received March 2, 2026; revised April 20, 2026; accepted May 19, 2026

Irradiation of the industrial aluminum alloy AA6111 with a high-current pulsed electron beam (HCPEB) with particle energy of 0.35 MeV, a beam current of 2.0 kA, a pulse duration of 5 μs, and a beam diameter of 3 cm results in the formation of a surface layer with improved physical and mechanical properties. However, the potential formation of craters on the surface of HCPEB-treated materials is one of the negative effects caused by HCPEB. This study examines the types and morphology of craters formed on the surface of AA6111 aluminum alloy after irradiation with HCPEB. The distribution of crater sizes and the crater density on the irradiated surface were studied. An analysis of the elemental composition of the crater walls and the adjacent melted surface was performed. The features of the grain microstructure, including shape and size, in the crater area were studied. The implications of these observations for a deeper understanding of the mechanisms underlying crater formation during HCPEB irradiation are discussed.

Keywords: *High-current pulsed electron beam; Aluminum alloy; Surface layer; Craters*
PACS: 29.25.Bx, 61.80.Fe, 62.20.−x

INTRODUCTION

The study of the morphology and mechanisms of formation of surface structures in metals and alloys resulting from irradiation with charged-particle flows is of great scientific and applied importance. The surface treatment of solid objects by high-current pulsed electron beams (HCPEB) significantly affects their physical and mechanical properties [1-8]. High-density energy is released in the process of HCPEB-irradiation at a shallow depth below the material's surface within a short period of time. This results in rapid heating and cooling with a high temperature gradient, leading to melting, vaporization, plasma ablation, and the formation of thermal stresses and shock waves. These non-equilibrium processes can alter the microstructure, chemical composition, phase structure, and stress state at the surface. In addition, the dynamic stress field triggers intense deformation processes on the material's surface due to the HCPEB effect [9,10]. It was established that the modified cross-sectional area following HCPEB treatment is divided into three zones: the remelted layer, the heat-affected zone, and the thermal stress wave zone [11]. Metastable structures form in the molten layer due to high heating and cooling rates. The presence of crater-like defects is the most characteristic feature of the microstructure of the remelted zone [12]. Moreover, crater formation is characteristic not only of HCPEB-irradiated steels and alloys, but also of pure metals. For example, craters were observed when irradiating pure nickel, aluminum, zirconium, and copper [13-16]. The size of the craters and the density of their distribution on the irradiated surface depend on the purity of the material, grain size, irradiation parameters, and other conditions [17-19]. Crater formation increases surface roughness and creates local areas with highly inhomogeneous stress states in the near layer [17-19].

Craters form as a result of a complex set of physical processes. However, a definitive answer to the mechanisms and causes of crater formation on the HCPEB-irradiated surface has not yet been found. Issues regarding crater size and density on the irradiated surface are also debatable. Therefore, further detailed studies of crater morphological features, microstructural characteristics in the crater-formation zone, and possible mechanisms of crater formation are required. Such experimental studies are of interest not only from a technological standpoint but also from a broader scientific perspective.

MATERIAL AND EXPERIMENTAL

The studied alloy AA6111 has such a chemical composition: Al; 0,5-1,0wt.%Mg; 0,5-0,9wt.%Cu; 0,1-0,4wt.%Mn; 0,15-0,44wt.%Fe; 0,7-1,1wt.%Si; 0,15wt.%Zn; 0,1wt.%Ti [20]. The initial microstructure of the AA6111 alloy had a grain size of approximately 40 μm [21]. The grains vary in size, but there is no distinct metallographic texture. The AA6111 alloy is classified as a medium-strength aluminum alloy. Tensile strength, $\sigma_t = 340$ MPa, and yield strength, $\sigma_y = 152$ MPa [22]. The microhardness of the studied AA6111 alloy, in the initial condition, is 70*HV*0.50. The microhardness of the HCPEB-irradiated layer of the AA6111 alloy increases and on average amounts to 101*HV*0.50 [3]. The results of diffraction studies of the initial microstructure of the AA6111 alloy, reported in [3,23], revealed that the initial microstructure is characterized by the presence of phases $Al_2Fe_3Si_4$ and $Al_4Cu_2Mg_8Si_7$. The maximum elongation at break at room temperature of the AA6111 alloy under study is 21%. At elevated temperatures, despite its coarse grain size, the

---

Cite as: V.V. Bryukhovetsky, V.V. Lytvynenko, D.E. Myla, O.L. Rak, East Eur. J. Phys. 2, 508 (2026), https://doi.org/10.26565/2312-4334-2026-2-57

alloy shows superplastic behavior [21,24]. At a temperature of $T = 793$ K and a true strain rate, $\dot{\varepsilon} = 5{,}2\cdot10^{-4}$ s^{-1}, the elongation of specimens made of this alloy at break is 180%.

Plates measuring 100×100 mm^2 were cut from AA611 alloy sheets (1.2 mm thick) for irradiation. The cladding layer on the plate surface was grinded off, and the plate surface was polished before irradiation. Irradiation of alloy sheets was performed by a high-current electron beam (HCPEB) at the TEMP-A accelerator in the NSC KIPT of the NAS of Ukraine [2,3,25]. The energy flux density at the target W is approximately 10^9W/cm^2 (beam energy E ~ 0.35 MeV, current I ~ 2000 A, pulse duration τ_i ~$5\cdot10^{-6}$ s, beam diameter ~ 3 cm). Irradiation was done by a single impulse in a vacuum at 1.310^{-3} Pa. Microstructural examinations were conducted with an optical microscope (Olympus GX51) and a scanning electron microscope (Tescan VEGA 3 LMH). Energy-dispersive X-ray microanalysis of local microvolumes in the irradiated alloy layers was performed using a Tescan VEGA 3 LMH scanning electron microscope equipped with a Bruker XFlash 5010 SSD EDS detector. The distribution of alloying elements across the cross-section was determined using mapping mode on a Tescan VEGA 3 LMH scanning electron microscope using energy-dispersive X-ray analysis method. To reveal the granular microstructure of the craters, the surface was chemically etched using Keller's etchant.

RESULTS AND DISCUSSION

The effect of HCPEB irradiation on materials comprises mechanical, thermal, and radioactive effects [1,11]. Under such irradiation, the alloy's heating rate is higher in the deeper layers. Maximum energy absorption occurs at a depth of approximately one-third of the electron path length in this material. This results in an explosive ejection of molten material and the subsequent rapid cooling of the alloy via heat transfer to the target's bulk. Cooling is accompanied by the crystallization of the molten material and structural and phase transformations. Previous studies [3, 23] have examined the characteristics of structural and phase changes in the surface layer of the HCPEB-irradiated AA6111 industrial aluminum alloy (Al-Mg-Cu-Si system). In particular, it was determined that the effect of HCPEB is accompanied by the formation of a complex surface topography on the AA6111 alloy plate and the appearance of microcracks and craters on its surface. The surface exhibits a wavy texture with localized protrusions exceeding 100 μm in height. The presence of these hemispherical protrusions is caused by the ejection of molten material from the area of maximum energy release and the ultra-rapid solidification of the molten material following irradiation. The local surface roughness does not exceed 1.7 μm. At the same time, the depth of the surface-modified layer reaches 200 μm.

Fig. 1 shows a panoramic micrograph of the crater distribution on the irradiated surface of a target made of AA6111 alloy. An analysis of these micrographs revealed that the craters are distributed fairly uniformly across the entire irradiated surface. Most craters are either perfectly round or elliptical. A visual inspection of the irradiated surface confirms that most craters appear exactly as shown in Fig. 1.

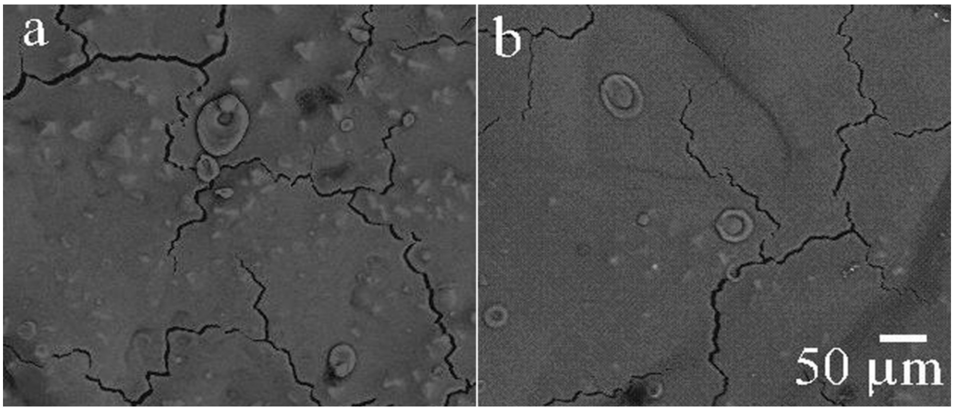

Figure 1. Appearance of craters on an irradiated target of AA6111 alloy: a and b are different areas of the irradiated surface

Fig. 2 shows an overview of the diameters of several craters, which vary significantly in size, for a more detailed analysis of their appearance. Thus, the diameter of the crater shown in Fig. 2a is approximately 100 μm, the diameter of the crater shown in Fig. 2b is approximately 65 μm, and the diameter of the crater shown in Fig. 2c is approximately 10 μm. That is, the diameters of the largest and smallest craters in Fig. 2 differ by an order of magnitude. An analysis of the overall appearance of all three craters shown in Fig. 2 suggests that the craters formed on the HCPEB-irradiated surface of the AA6111 alloy are characterized by central symmetry. Craters are typically multi-ringed and have a funnel-like morphology. The craters either have a distinct ring structure (see Fig. 2a) or feature blurred peripheral rings (see Fig. 2bc). The larger the crater's diameter, the more ring-like structures it has. The crater floor can be either flat, as in the crater shown in Fig. 2b; or parabolic, as in the crater shown in Fig. 2a. The edge of a crater is usually higher than the average surface level, while its center is lower.

The distribution of craters by size is an important parameter that can be quantified. Such data are of particular interest in predicting the mechanism of crater formation, which has not yet been fully studied and remains debatable [12,17-19]. To establish this relationship, the diameters of the craters were measured in two mutually perpendicular directions, and the average was calculated. The statistical results of a quantitative analysis of micrographs of craters on the irradiated surface are shown in Fig. 3. The block diagram shows the distribution of craters by size, expressed as percentages. It is evident that the resulting distribution of crater sizes is approximately Gaussian. It is also evident that most craters range in size from 20 μm to 50 μm, and that the average diameter of all craters, D, is 37 μm. Measuring the crater density *n* and the average crater size *D* allows determining the crater coverage ratio of the HCPEB-treated surface $S = \pi D^2 n/4$ [17]. This parameter is an important factor in determining the degree to which craters occupy the surface area of a HCPEB-modified surface and, as such, may be significant in determining certain properties of surfaces treated in this manner. The calculated value of *S* for the irradiated surface of the AA6111 alloy is 3.7%. That is, the craters occupy a negligible portion of the alloy's irradiated surface. However, based on the value of *S*, the presence of craters shall be taken into account when analyzing the physical and technological properties of the irradiated surface.

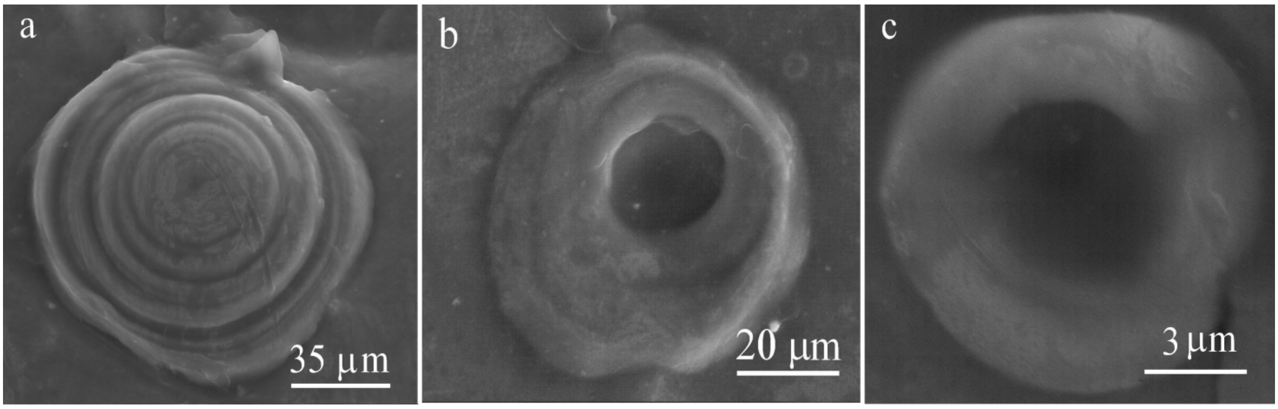

Figure 2. Appearance of craters on an irradiated target of AA6111 alloy

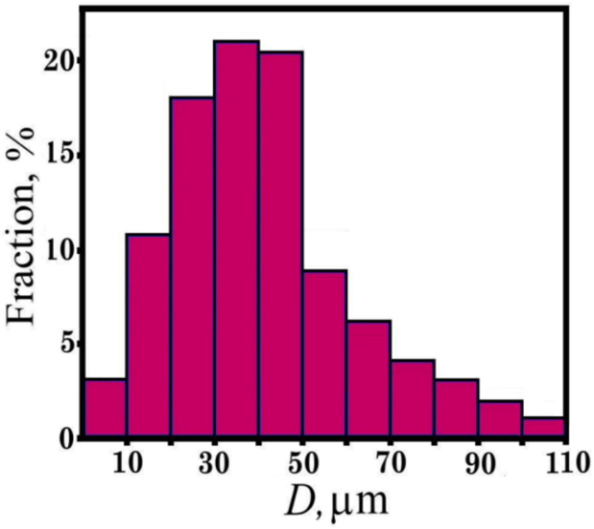

Figure 3. Size distribution of craters on an irradiated target of AA6111 alloy

It is known that chemical composition is an important indicator of a metal's structure following HCPEB treatment. Therefore, an analysis of the chemical composition was conducted on the crater walls and on the remelted surface adjacent to the crater. The studies were conducted on the crater shown in Fig. 4. Fig. 4c shows the EDS testing areas (labeled 1, 2, and 3). Data on the chemical composition of the selected areas are shown in Table 1. Each value shown in this table is an average value for the selected areas. An analysis of the data in Table 1 allows for the drawing of several conclusions about the chemical composition of the spectra studied. First and foremost, there are noticeable differences in the Mg and O content across the selected areas. Given the characteristic ratio of the mass fractions of oxygen and magnesium, it can be concluded that an oxide film consisting of MgO is present on the surface of the remelted layer. Irradiation was done by a single impulse in a vacuum at 1.3×10^{-3} Pa. At this pressure, oxidation will still occur due to the presence of oxygen in the residual vacuum. Magnesium oxidizes much more rapidly in the air than aluminum does. Magnesium oxide is easier to form than Al_2O_3, as magnesium is more reactive than aluminum. MgO is the initial product of the oxidation of a molten magnesium-containing aluminum alloy [26]. As for the other alloying elements present in the AA6111 alloy, there are minor differences in their distribution between the alloy's surface layer and the inner walls of the craters. In addition, the concentrations of Cu and Si on the inner walls of the crater are slightly higher than in the central part of the crater.

Fig. 4b shows the results of studies on the distribution of Mg atoms across the irradiated surface, conducted in mapping mode. Magnesium is distributed in patches over the surface. Thus, the differences in magnesium content in the spectrum are due to the patchy distribution of magnesium oxide over the surface, as shown in Fig. 4b. At the same time, the distribution of aluminum atoms on the irradiated surface is more uniform (see Fig. 4a) than that of magnesium atoms. It should be noted that similar studies were conducted in [27] using an Al-20%Si-5%Mg alloy as an example. This study also highlights that aluminum atoms are distributed more uniformly in the crater area than are Si and Mg atoms. The highest concentration of Si and Mg atoms was found at the crater floor [27]. At the same time, according to the energy-dispersive analysis data (Table 1), the central region of the crater was depleted in magnesium and silicon.

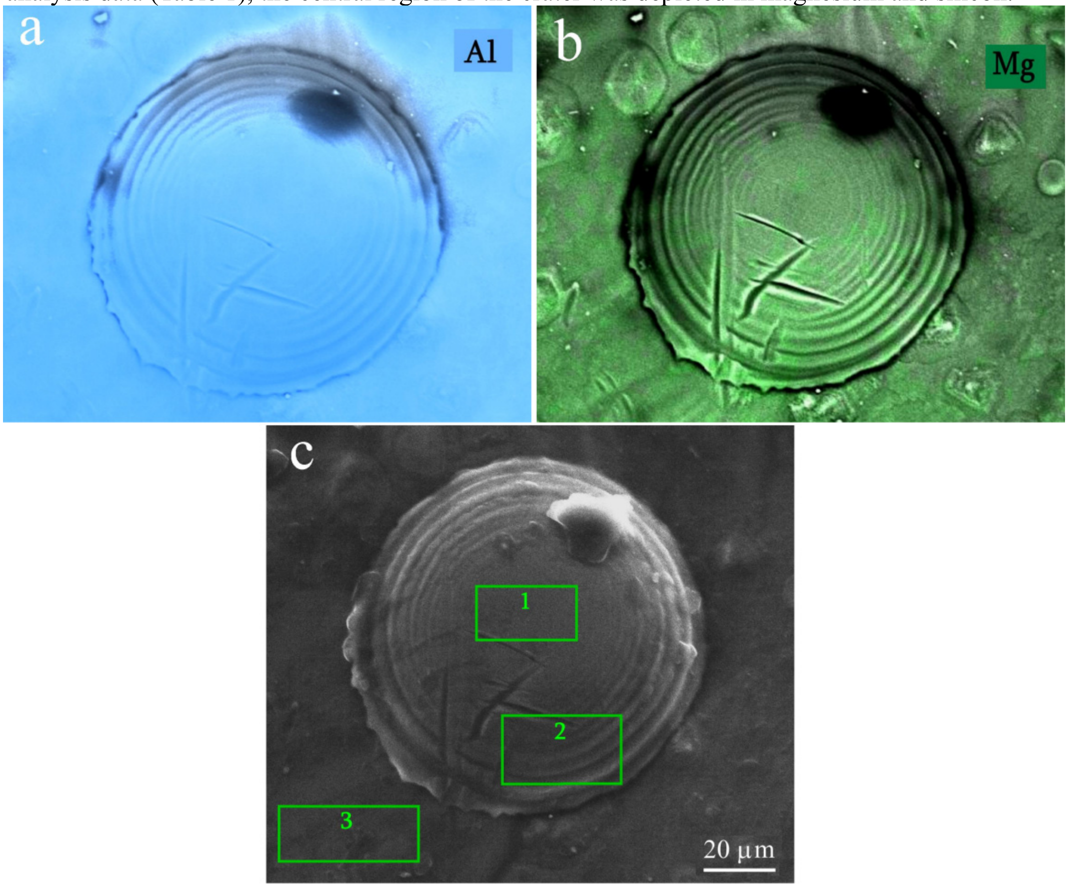

Figure 4. SEM image of a crater on the surface of the remelted alloy layer. Maps showing the distribution of magnesium (b) and aluminum (a) atoms across the surface

Table 1. EDS Analysis Results of Selected Areas in Fig. 4(c)

Spectrum	O	Mg	Al	Si	Mn	Fe	Cu
1	1.61	0.87	98.70	0.13	0.04	0.07	0.20
2	2.82	1.09	95.15	0.41	0.05	0.21	0.27
3	3.27	1.43	94.25	0.32	0.06	0.09	0.28

As shown in [28], crater formation alters the local stress state. Heterogeneity in the stress state can affect the appearance and shape of the grain structure in the vicinity of the crater formed during melt solidification. Fig. 5a shows the grain structure of the irradiated surface of the AA6111 alloy under study in the area where the crater is located. Asymmetrical, elongated grains, radiating outward from the central eruption zone, are visible near the center of the crater. Whereas smaller equiaxial grains are observed at the crater's rim. All of this suggests that solidification occurred quickly after the eruption that formed the crater. Thus, crater formation affects the course of the melt crystallization process and, consequently, the physical and technological properties of the surface after irradiation. A similar crater grain structure in type and shape was also observed in study [29]. Fig. 5b shows the granular microstructure on the surface away from the craters. An equiaxial, uniform microstructure is observed, which may indicate that the surface has uniform physical and technological properties and contains no craters. Thus, the craters introduce distortions in the surface properties of the HCPEB-irradiated surface.

Since craters significantly impact the surface properties of materials exposed to pulsed energy beams, understanding the mechanisms of crater formation is crucial for understanding the fundamental processes involved in HCPEB irradiation and, consequently, for predicting the potential applications of this technology. According to [17], non-uniform local melting in the near-surface layer of the target material, followed by the ejection of molten material through the solid outer surface, is the primary hypothesis for the crater formation. An alternative mechanism suggests that craters form due to uneven crystallization of the remelted layer [19]. Arguments in favor of one or another mechanism of crater formation during irradiation are crucial for further understanding the processes that occur when materials are irradiated with HCPEB.

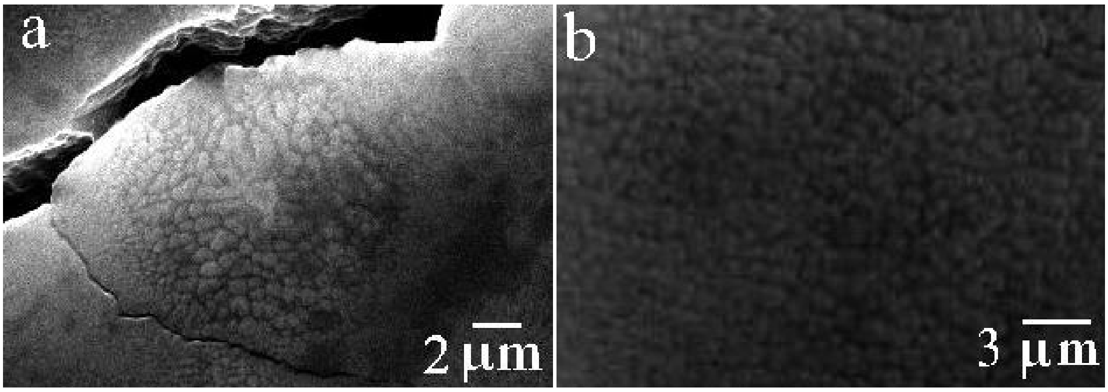

Figure 5. Appearance of the grain microstructure in the crater location area of an irradiated target of AA6111 alloy (a); general appearance of the grain microstructure on the irradiated surface of the AA6111 alloy (b)

It is known that the presence of surface cracks is a characteristic feature of many aluminum alloys and other metals and alloys irradiated with HCPEB [2,3,5,30]. As shown in Fig. 1 and Fig. 6, such cracks are also present on the irradiated surface of the AA6111 alloy under study. The zigzag-like pattern of cracks on the surface is caused by local inhomogeneities in the distribution of alloying elements within the solidified material and local variations in the strength and ductility properties of the solidified material across its various microvolumes. However, it is worth noting that some craters are crossed by fractures (see Fig. 6ab), whereas others lie atop fractures (see Fig. 6cd). In other words, some craters form during the crystallization of the molten layer, while others form after the surface layer has already crystallized. This may support the crater-formation mechanism proposed in [19], according to which craters form during crystallization of the molten target material due to uneven crystallization of the remelted layer.

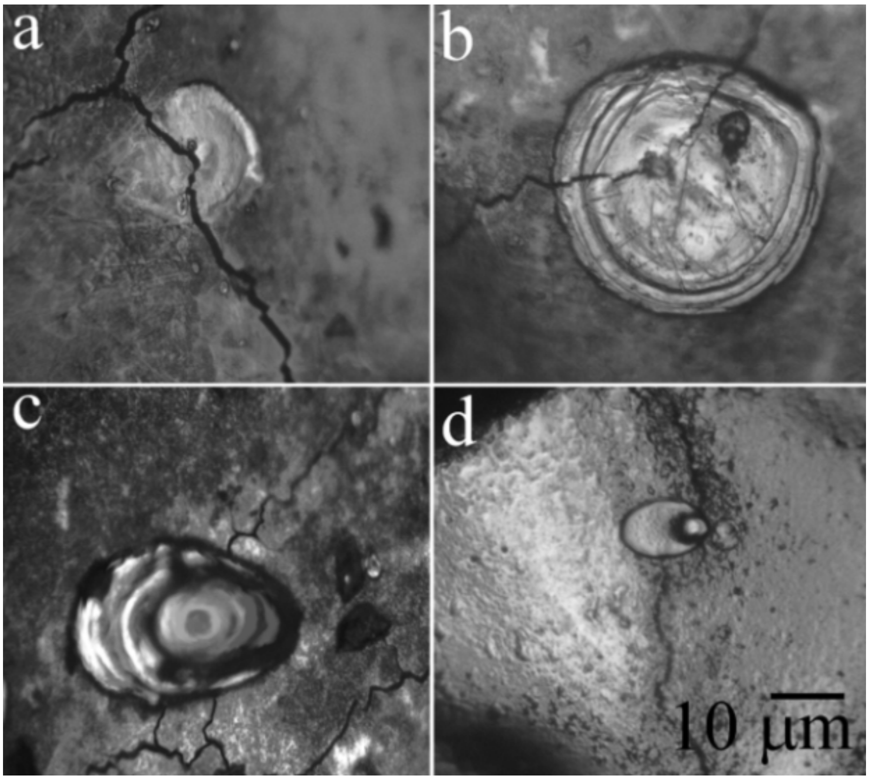

Figure 6. Appearance of craters on the irradiated surface of AA6111 alloy

CONCLUSIONS

It has been shown that HCPEB irradiation with a particle energy of 0.35 MeV, a beam current of 2.0 kA, a pulse duration of 5 μs, and a beam diameter of 3 cm results in the formation of craters on the surface of the AA6111 industrial aluminum alloy.

The craters are distributed fairly evenly across the entire irradiated surface of the AA6111 alloy target, and the size distribution of the craters, as a function of their fractional abundance, follows an approximately Gaussian distribution. Most craters range in size from 20 μm to 50 μm.

There is a non-uniform distribution of alloying elements in the alloy's surface layer and on the inner crater walls. The concentrations of Cu and Si on the inner crater walls are slightly higher than in the central part of the crater.

The grain structure of the irradiated surface in the crater region was studied. It has been established that asymmetrically elongated grains are observed near the crater center, radiating outward from the central eruption zone.

The overall appearance of the irradiated surface of the AA6111 alloy indicates that craters form during crystallization of the molten target material due to uneven remelting of the layer.

ORCID

Vasyl Bryukhovetsky, https://orcid.org/0000-0003-0423-8828; **Volodymyr Lytvynenko,** https://orcid.org/0000-0003-4850-2555
Diana Myla, https://orcid.org/0000-0003-2919-741X; **Oleg Rak,** https://orcid.org/0009-0000-6683-1235

REFERENCES

[1] Y. Qin, C. Dong, Z. Song, S. Hao, X. Me, J. Li, X. Wang, J. Zou, and Th. Grosdidier, J. Vacuum Sci. and Technol. A, **279**(3), 430 (2009). https://doi.org/10.1116/1.3093876
[2] V.V. Bryukhovetsky, V.F. Klepikov, V.V. Lytvynenko, D.E. Myla, V.P. Poyda, A.V. Poyda, V.T. Uvarov, *et al.*, Nucl. Instrum. Methods Phys. Res. Sect. B, **499**, 25 (2021). https://doi.org/10.1016/j.nimb.2021.02.011
[3] V.V. Bryukhovetsky, V.F. Klepikov, V.V. Lytvynenko, D.E. Myla, Yu.F. Lonin, and A.G. Ponomarev, Nucl. Instrum. Methods Phys. Res. Sect. B. **519**, 1 (2022). https://doi.org/10.1016/j.nimb.2022.03.008
[4] H. Xie, J. Cai, C. Yu, M. Feng, X. Li, S. Chen, W. Pu, *et al*., Journal of Alloys and Compounds, **1025,** 180201 (2025). https://doi.org/10.1016/j.jallcom.2025.180201
[5] D.E. Myla, V.V. Bryukhovetsky, V.V. Lytvynenko, V.P. Poyda, A.V. Poyda, V.F. Klepikov, V.T. Uvarov, *et al.*, Problems of Atomic Science and Technology, **2**(126), 33 (2020).
[6] Y. Hao, B. Gao, G.F. Tu, S.W. Li, C. Dong, and Z.G. Zhang, Nucl. Instrum. Methods Phys. Res. Sect. B, **269**, 1499 (2011). https://doi.org/10.1016/j.nimb.2011.04.010
[7] V.V. Bryukhovetsky, A.V. Poyda, V.P. Poyda, and D.E. Milaya, Problems of Atomic Science and Technology, **2**(120), 67 (2019).
[8] V.V. Bryukhovetsky, V.V. Lytvynenko, D.E. Myla, V.A. Bychko, Yu.F. Lonin, A.G. Ponomarev, and V.T. Uvarov, Physics and Chemistry of Solid State, **22**, 655 (2021), https://doi.org/10.15330/pcss.22.4.655-663
[9] J. Cai, L. Ji, S.Z. Yang, X.T. Wang, Y. Li, X.L. Hou, and Q.F. Guan, Chinese Science Bulletin, **58**, 2507 (2013). https://doi.org/10.1007/s11434-013-5848-5
[10] V.V. Bryukhovetsky, V.V. Lytvynenko, O.A. Startsev, D.E. Myla, Yu.N. Volkov, and O.L. Rak, Materials Letters, **367**, 136642 (2024). https://doi.org/10.1016/j.matlet.2024.136642
[11] D.I. Proscurovsky, and A.D. Pogrebnjak, Phys. Stat. Sol. A, **145**(1), 9 (1994). https://doi.org/10.1002/pssa.2211450103
[12] V.V. Bryukhovetsky, V.V. Lytvynenko, Yu.F. Lonin, D.E. Myla, A.G. Ponomarev, and V.T. Uvarov, Problems of Atomic Science and Technology, **2**(144), 24 (2023). https://doi.org/10.46813/2023-144-024
[13] C. Zhang, Y. Zhang, N. Tian, S. Chen, Z. Qian, P. Lv, and Q. Guan, Protection of Metals and Physical Chemistry of Surfaces, **52**, 869 (2016). https://doi.org/10.1134/S2070205116050269
[14] Z. Zhang, S. Yang, P. Lv, Y. Li, X. Wang, X. Hou, and Q. Guan, Applied surface science, **294**, 9 (2014). https://doi.org/10.1016/j.apsusc.2013.12.178
[15] L. Chai, B. Chen, S. Wang, Z. Zhang, and K.L. Murty, Applied Surface Science, **390**, 430 (2016). https://doi.org/10.1016/j.apsusc.2016.08.128
[16] J. Cai, Q. Guan, P. Lv, C. Zhang, and Y. Yin, High Temperature Materials and Processes, **37**(8), 777 (2018). https://doi.org/10.1515/htmp-2017-0067
[17] Y. Qin, Ch. Dong, X. Wang, Sh. Hao, A. Wu, J. Zou, and Y. Liu, J. of Vacuum Science & Technology A, **21**(6), 1934 (2003). https://doi.org/10.1116/1.1619417
[18] J. Zhang, X. Zou, T. Grosdidier, C. Dong, J. of Vacuum Sci. & Technol. A, **27**, 1217 (2009). https://doi.org/10.1116/1.3207948
[19] V.V. Bryukhovetsky, V.F. Klepikov, V.V. Lytvynenko, D.E. Myla, O.A. Startsev, Yu.F. Lonin, and A.G. Ponomarev, Vacuum, **215**, 112263 (2023). https://doi.org/10.1016/j.vacuum.2023.112263
[20] P.E. Fortin, M.J. Bull, and D.M. Moore, SAE Int. Congr. Exp., Detroit, MI, 1983, SAE Paper no. 830096. https://doi.org/10.4271/830096
[21] V.V. Bryukhovetskyy, V.P. Pojda, A.V. Poyda, D.R. Avramets', R.I. Kuznetsova, O.P. Kryshtal', O.L. Samsonnik, *et al.*, Metallofiz. Noveishie Tekhnol. **31**(9), 1289-1302 (2009).
[22] G.K. Quainoo, S. Yannacopoulos, and A.K. Gupta, Canadian Metallurgical Quarterly, **40**(2), 211 (2001). https://doi.org/10.1179/000844301794388515
[23] D.E. Myla, V.V. Bryukhovetsky, V.V. Lytvynenko, S.I. Petrushenko, O.O. Nevgasimov, Yu.F. Lonin, A.G. Ponomarev, *et al.*, Problems of Atomic Science and Technology, **2**(138), 25 (2022). https://doi.org/10.46813/2022-138-025
[24] V.V. Bryukhovetskij, Fizika Metallov i Metallovedenie, **92**(1), 107 (2001). (in Russian)
[25] V.V. Bryukhovetsky, S.E. Donets, S.A. Kniaziev, O.V. Subbotin, V.V. Lytvynenko, S.I. Bogatyrenko, O.L. Rak, *et al.*, Problems of Atomic Science and Technology, **6**(160), 76 (2025). https://doi.org/10.46813/2025-160-076
[26] K. Kim, Surface and Interface Analysis, **47**(4), 429 (2015). https://doi.org/10.1002/sia.5726
[27] B. Gao, K. Li, and P. Xing, Coatings, **9**(7), 413 (2019). https://doi.org/10.3390/coatings9070413
[28] P. Yan, T. Grosdidier, X. Zhang, and J. Zou, Materials & Design, **159**, 1 (2018). https://doi.org/10.1016/j.matdes.2018.08.033
[29] J. Zou, T. Grosdidier, K. Zhang, and C. Dong, Acta Materialia, **54**(20), 5409 (2006). https://doi.org/10.1016/j.actamat.2006.05.053
[30] V.V. Bryukhovetsky, V.V. Lytvynenko, D.E. Myla, Yu.F. Lonin, A.G. Ponomarev, and V.T. Uvarov. J. Nano- and Electronic Physics, **13**(6), 06025-1 (2021). https://doi.org/10.21272/jnep.13(6).06025

МОРФОЛОГІЧНІ ОСОБЛИВОСТІ ТА ХАРАКТЕРИСТИКИ МІКРОСТРУКТУРИ КРАТЕРІВ НА ОПРОМІНЕНІЙ СИЛЬНОСТРУМОВИМ ІМПУЛЬСНИМ ПУЧКОМ ЕЛЕКТРОНІВ ПОВЕРХНІ ПРОМИСЛОВОГО АЛЮМІНІЄВОГО СПЛАВУ АА6111

В.В. Брюховецький[1], В.В. Литвиненко[1], Д.Є. Мила[1], О.Л. Рак[2]
[1]Інститут електрофізики і радіаційних технологій НАН України, вул. Гуданова, 13, 61024 Харків, Україна
[2]ННЦ «Харківський фізики-технічний інститут» НАН України, вул. Академічна, 1, 61108 Харків, Україна

Опромінення промислового алюмінієвого сплаву АА6111 сильнострумовим імпульсним електронним пучком з енергією частинок 0,35 МеВ, струмом пучка 2,0 кА, тривалістю імпульсу 5 мкс та діаметром пучка 3 см призводить до формування поверхневого шару з покращеними фізико-технологічними властивостями. Однак одним із негативних ефектів, спричинених імпульсним електронним опроміненням, є потенційне утворення кратерів на поверхні опроміненого матеріалу. В роботі вивчені типи та морфологія кратерів на поверхні алюмінієвого сплаву АА6111, що виникають внаслідок опромінення поверхні цього сплаву. Вивчено розподіл кратерів за розмірами та щільність кратерів на опроміненій поверхні. Проведено аналіз складу хімічних елементів на поверхні стінок кратера та на прилеглій до кратера переплавній поверхні. Вивчено особливості форми та розмірів мікроструктури зерен у зоні розташування кратера. Обговорюється значення цих спостережень для глибшого розуміння механізмів утворення кратерів під час опромінення сильнострумовим імпульсним електронним пучком.

Ключові слова: *сильнострумовий імпульсний електронний пучок; алюмінієвий сплав, поверхневий шар; кратери*

East European Journal of Physics. **2.** 515-519 (2026)
DOI:10.26565/2312-4334-2026-2-58 ISSN 2312-4334

COMPARISON OF Sn AND As EFFECT ON TENSILE PROPERTIES OF Pb–3.5%Sb GRID ALLOY FOR LEAD-ACID BATTERIES

Victor O. Dzenzerskiy, Serhii V. Tarasov, Olena V. Sukhova*, Volodymyr A. Ivanov
Institute of Transport Systems and Technologies of National Academy of Sciences of Ukraine
5, Pisarzhevsky St., Dnipro, 49005, Ukraine
**Corresponding Author email: sukhovaya@ukr.net*

Received January 15, 2026; revised April 20, 2026; accepted May 11, 2026

In this work, the effects of 0.5 wt.% Sn and 0.16–0.23 wt.% As on tensile properties of Pb–3.5%Sb grid alloy for lead-acid batteries were compared in the as-cast condition. The alloys were melted under different cooling-rate conditions in a casting mold preheated between 50°C and 170°C, with cooling rates ranging from 100 °C/s to 50 °C/s. Mechanical properties, such as ultimate tensile strength and percentage elongation, were measured at room temperature using the TIRAtest 2300 universal testing machine at a constant crosshead speed of 10 mm/min. It was established that as mold preheating temperatures rise, the elongation and ultimate tensile strength of the Pb–3.5%Sb–0.23%As alloy decrease by 13.9% and 11.8%, respectively. Addition of tin in place of some arsenic causes a decrease in ultimate tensile strength of the Pb–3.5%Sb–0.5%Sn–0.16%As alloy, but only by 2.8 %, whereas elongation increases by 2.4 %. It was concluded that additions of tin compensate for the negative effect of arsenic on the tensile properties of the Pb–3.5%Sb grid alloy, which relates to the formation of brittle arsenic-containing phases at the grain boundaries. Tin addition to the Pb–3.5 %Sb alloy produces higher tensile properties at room temperature than those obtained by the addition of arsenic.

Keywords: *Lead-acid batteries; Pb–Sb based grid alloys; Casting mold preheating temperature; Cooling rate; Tensile tests; Ultimate tensile strength; Elongation*
PACS: 61.82.Bg, 61.66.Dk, 62.20.-x, 62.20.Fe, 62.20.Mk, 64.70.Dv, 81.70.Bt, 81.40.Cd, 81.40.Lm

Lead-acid batteries are the most widely used rechargeable batteries in the automotive and industrial sectors, powering many appliances and grid-scale power systems for decades [1-6]. Irrespective of the environmental hazards they pose, lead-acid batteries remain ahead of their peers because of their lower cost compared with lithium-ion or nickel-cadmium batteries. Industry will still have to deal with millions of lead-acid batteries, already existing and those planned to be produced in the next few years. The increasing demand for motor vehicles as countries undergo economic development and growth in the use of renewable energy sources, with the need for storage batteries, is directly proportional to the increasing demand for lead-acid batteries.

Lead-acid batteries contain cast lead alloy grids, packed with varying amounts of Pb, PbO2, or other active pastes to form the positive and negative grids. The grid is the most critical non-active component in a lead-acid battery. This is used to support the positive and negative active materials and to provide a conductive path for current to and from the plates during charging and discharging.

Lead grids alloyed with antimony are commonly used in batteries today. Lead-antimony grids have been well-researched and are known for their use in the positive electrode grids of lead-acid batteries, as antimony enables high charge-discharge performance and good castability [7-10]. However, high-antimony lead alloys are prone to sulfation and should not be left at low states of charge for extended periods of time [11-13]. These alloys increase battery gassing during charging, leading to high water loss. Because water must be added to these batteries, they have higher maintenance costs. Furthermore, high-antimony lead batteries have a high discharge rate and a short lifetime. These problems are caused by the dissolution of antimony from one electrode and its deposition on the other electrode [14]. Therefore, lead-antimony alloys for battery grids in automotive applications are produced only up to 3.5 wt.% Sb [15].

Medium-antimony lead alloys (containing 3.0–4.0 wt.% Sb) reduce the transfer of antimony to the negative plate and thus reduce water loss of the battery [16], especially when alloyed with additions of such elements as arsenic and tin [17-21]. The combination of these alloying elements with antimony enables the manufacture of battery grids with lower antimony content that meet the necessary mechanical strength and quality requirements.

The main difficulty with casting lead-antimony alloys is that the decrease in antimony content is accompanied by the appearance of hot cracks. Solidification occurs in a coarse dendritic structure with cracks along grain boundaries [9]. Tin additions have been shown to improve castability, mechanical properties, deep cycling and to reduce the tendency towards passivation and corrosion [22-25]. Another element, arsenic, has been added to lead-acid batteries and is currently used mostly with lead-antimony grids because it allows for lower antimony content which minimizes the self-discharging characteristics of higher antimony composition batteries [26-31]. In addition to improving lead-antimony grids, alloying lead grids with arsenic at low percentages (<0.1%) increases hardness, yields finer grains, and improves casting properties in lead-arsenic grids.

Cite as: V.O. Dzenzerskiy, S.V. Tarasov, O.V. Sukhova, V.A. Ivanov, East Eur. J. Phys. 2, 515 (2026), https://doi.org/10.26565/2312-4334-2026-2-58

Suitable grid alloys must possess acceptable tensile properties for processability, enabling the alloys to be cast into plates of the desired configuration [32]. In other words, the alloys can be processed under desired battery assembling and manufacturing conditions [33-35]. Ultimate tensile strength and elongation are among the mechanical properties important to grid performance. Among the factors that can affect these properties is the cooling rate of the alloys during casting, which is regulated by the mold preheating temperature [35-38]. Changes in this parameter has been commonly used to control grain size and second phase dispersion that are responsible for achieving the required mechanical properties [39-42]. Although much attention has focused on lead-antimony grid alloys for lead-acid batteries, research on the factors influencing tensile properties remains scarce. Currently, the microstructure and hardening mechanisms are mostly determined using metallography, hardness measurements, and/or electrical resistivity measurements [43-45]. But studying the tensile properties of these grid alloys is indispensable for ensuring their safe and reliable application and has important research value and practical significance. Therefore, this work focuses on comparative analysis of the effect of tin and arsenic additions to the Pb–3.5%Sb grid alloy on tensile properties as a function of mold preheating temperature during conventional casting.

MATERIALS AND METHODS

The alloys for this study were cast in the melt pot of the cast-on-strap machine on the production line of BM Company (Austria) for lead-acid battery grids at Westa Corp. (City of Dnipro, Ukraine). The molten alloys maintained at the temperature of 450±10 °C were poured in different cooling rate conditions into a preheated mold, which temperature was changed in the range between 50 °C and 170 °C with an interval of 5 °C. Then the casting mold was left to cool to room temperature at different rates, ranging from 100 °C/s to 50 °C/s. The temperature was measured using a K-type chromel-alumel thermocouple with a standard error of ±5 °C. The diameters of the thermocouple electrode wires and their junction were 1 mm and 2 mm, respectively. For each mold preheating temperature, six specimens were collected from each casting for further investigation.

The weight values of alloy chemical composition determined by atomic absorption spectroscopy using ARL 3460 instrument were 3.5 wt.% Sb, 0.5 wt.% Sn, 0.16–0.23 wt.% As, and Pb – the balance. Trace amounts of impurities, such as Al and Se, amounted to less than 0.02 wt.%. The additional amount of trace elements was a factor that largely fluctuated depending on the blending ratio of scrap. Samples were obtained from a same casting batch to guarantee an identical chemical composition. Three samples for chemical analysis were taken at the time of the casting to ascertain the exact chemical composition of each alloy.

The tensile tests were conducted at room temperature on a TIRAtest 2300 PC-controlled testing system at a constant crosshead speed of 10 mm/min. The ultimate tensile strength (σ_U) and percentage elongation (σ) were determined one day after casting. Standard flat samples with a total length of 60 mm, a gage length of 45 mm, and a thickness of 3 mm were prepared for tensile tests. For this purpose, casting mold made of structural carbon steel that had 2.5 mm thick thermal coating of cork suspension inside was designed (Fig. 1). Each reported value of tensile properties corresponded to the mean of six measurements. The average uncertainty of measurements was estimated at approximately ±5 %.

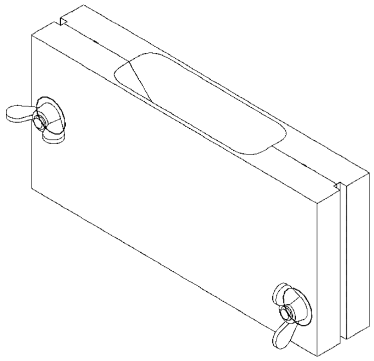

Figure 1. General view of casting mold

RESULTS AND DISCUSSION

Variation of the preheating temperatures of a casting mold has the potential for influencing the tensile properties of the studied grid alloys to a noticeable extent. As the mold preheating temperature increases from 50 °C to170 °C, the values of ultimate tensile strength for Pb–3.5%Sb–0.23%As alloy decrease from 38.9 MPa to 34.8 MPa (by 11.8 %) with an average decrement equaling to 0.03 MPa per 1 °C (Fig. 2a). The percentage elongation of the alloy exhibits the same trend with respect to mold preheating temperature. The elongation decreases from 8.2 % to 7.2 % (by 13.9 %) with an average decrement of about 0.008 % per 1 °C (Fig. 2b). So, the alloy tends to become more brittle, less prone to deformation, as shown by the decreased elongation [46]. The tensile properties of the Pb–3.5%Sb–0.23%As alloy are less influenced by cooling conditions between 50 °C and 110 °C.

Considering that elongation and ultimate tensile strength of the alloy are nearly the same at mold temperatures lower 110 ºC, a mold during casting should be preheated over the temperature range between 50 ºC and 110 ºC. Besides, this ensures 1.5 times higher cooling rates of the alloy and enhances the supersaturation of the lead-based solid solution [47]. As a result, less brittle arsenic precipitates can form at the grain boundaries in the as-cast structure [27].

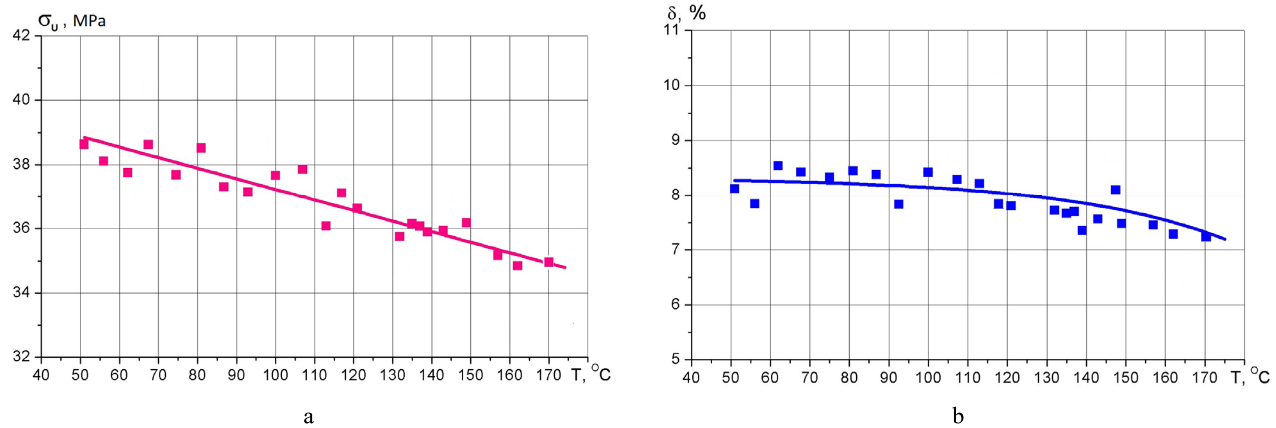

a

b

Figure 2. Effect of preheating temperature of casting mold on tensile properties of Pb–3.5%Sb–0.23%As alloy: a – ultimate tensile strength; b – elongation

When Pb–Sb–As grid alloy contains up to 0.5 wt.% tin in place of some of the arsenic, provided that the arsenic level is at least 0.16 wt.%, the ultimate tensile strength slightly decreases from 40.0 MPa to 38.9 MPa (by 2.8 %) while elongation insignificantly increases from 8.1 % to 8.3 % (by 2.4 %) with higher mold temperature (Fig. 3). The temperature dependencies of tensile properties are approximately 0.012 MPa/ºC and 0.002 %/ºC, respectively. So, these characteristics remain virtually unchanged, which correlates with insignificant changes in the grain size of the Pb–3.5%Sb–0.5%Sn–0.16%As grid alloy as the mold temperature increases from 75 °C to 165 °C. As shown, the tensile properties are more stable between 140 °C and 165 °C. Considering that elongation of the alloy is nearly the same at mold temperatures above 110 ºC, while ultimate tensile strength tends to slight decrease up to 140 ºC, a mold during casting should be preheated over the temperature range between 140 ºC and 165 ºC.

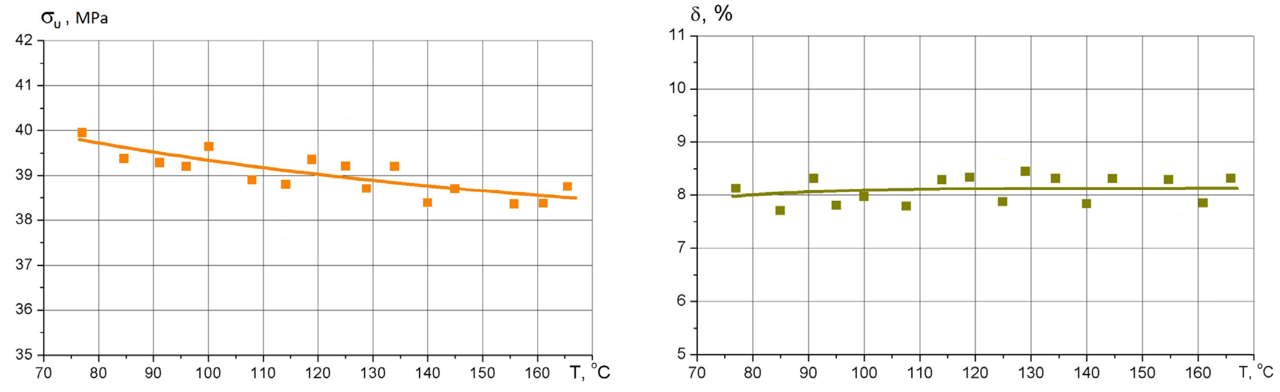

a

b

Figure 3. Effect of preheating temperature of casting mold on tensile properties of Pb–3.5%Sb–0.5%Sn–0.16%As alloy: a – ultimate tensile strength; b – elongation

Considering obtained results, it may be assumed that with preheating temperature of the mold increasing, the cooling conditions become closer to an equilibrium kinetic. The effect of the slower cooling rate results in the decreased distortion in the alloys' crystal structure, so the dislocation motion occurs easily, hence the tensile strength decreases. Since mold temperature is related to the cooling rate, the increase in the mold temperature enlarges grains in the structure of the alloys [48]. By increasing the grain size, the area of grain boundaries which can block dislocations and impede their movement decreases, which is disadvantageous for the strength as well. As a result, ultimate tensile strength of both alloys tends to reduce.

Besides the slower cooled alloys have a less uniform structure due to more severe segregation effects. The grain boundaries contain relatively higher arsenic and tin content [25-27]. Due to the segregation, grain boundaries become weaker than similar boundary areas (which contain fewer alloying elements) in rapidly cooled alloys. The segregated arsenic forms own phases which can make the Pb–3.5%Sb–0.23%As alloy more brittle as confirmed by its decreased elongation. When the preheating temperature of the casting mold is higher, the slight increase in elongation of the Pb-3.5%Sb–0.5%Sn–0.16%As alloy indicates that arsenic contributes more to the embrittlement of grain boundaries than tin. Tin may also prevent the migration of arsenic towards the boundaries, thereby ensuring a more uniform structure of the Pb–3.5%Sb–0.5%Sn–0.16%As alloy. As a result, tensile properties of this alloy show less noticeable changes with variation of mold preheating temperatures as compared with those of the Pb–3.5%Sb–0.23%As alloy.

CONCLUSIONS

The tensile properties of the Pb–3.5%Sb–0.23%As and Pb–3.5%Sb–0.5%Sn–0.16%As grid alloys are found to be sensitive to the temperature parameters of the casting procedure. Changing the preheating temperature of the casting mold in the range 50 –170 °C reduces the ultimate tensile strength of both alloys by 11.8% and 2.8%, respectively. At the same time, elongation of the Pb–3.5%Sb–0.23%As decreases by 13.9 %, but that of the Pb–3.5%Sb–0.5%Sn–0.16%As increases by 2.4 %, exhibiting an inverse trend compared to the strength with respect to preheating mold temperature. Based on the results obtained, it is assumed that tin has a positive effect on the tensile properties of the Pb–Sb–As alloy. The improvement in tensile properties can be attributed to a more uniform structure and less brittle arsenic phases at the grain boundaries of the tin-containing alloy.

Within the range of 110 °C to 170 °C, the Pb–3.5%Sb–0.23%As alloy is more sensitive to cooling conditions in the mold. But when a mold is maintained at temperatures below 110°C, the ultimate tensile strength and elongation generally stabilize. For the same reason, the casting parameters for the Pb–3.5%Sb–0.5%Sn–0.16%As alloy, should be kept in a range 140 ºC–165 ºC.

The work was performed within the framework of research projects of the National Academy of Sciences of Ukraine No. 1.3.6.18 “Development of new methods and improvement of known ones to investigate mechanics of transport and energetic systems“ (2017-2021) and No. 1.3.6.22 “Development of mathematical models and investigation of ground transport and energetic systems“ (2022-2026).

ORCID

Victor O. Dzenzerskiy, https://orcid.org/0000-0002-9722-1920; **Sergei V. Tarasov,** https://orcid.org/0000-0002-9254-1503; **Olena V. Sukhova,** https://orcid.org/0000-0001-8002-0906; **Volodymyr A. Ivanov,** https://orcid.org/0009-0008-9836-6508

REFERENCES

[1] S. Guruswamy, *Engineering Properties and Applications of Lead Alloys*, (CRC Press, New York, 2000), https://doi.org/10.1201/9781482276909
[2] D.A.J. Rand, T. Moseley, J. Garche, and C.D. Parker, *Valve-Regulated Lead-Acid Batteries*, (Elsevier, Amsterdam, 2004), https://doi.org/10.1016/B978-0-444-50746-4.X5000-4
[3] V.A. Dzenzerskiy, S.V. Tarasov, D.O. Redchyts, V.A. Ivanov, and O.V. Sukhova, J. Nano-Electron. Phys. **16**(1), 01003 (2024). https://doi.org/10.21272/jnep.16(1).01003
[4] V.O. Dzenzerskiy, S.V. Tarasov, O.V. Sukhova, and V.A. Ivanov, East Eur. J. Phys. **2023**(4), 182-188 (2023). https://doi.org/10.26565/2312-4334-2023-4-21
[5] V. Dzenzerskiy, S. Tarasov, O. Sukhova, and V. Ivanov, Rom. J. Phys. **69**(1-2), 605, (2024). https://doi.org/10.59277/RomJPhys.2024.69.605
[6] D.O. Redchyts and S.V. Moiseienko, Space Sci. Technol. **27**(1), 85-96 (2021). https://doi.org/10.15407/knit2021.01.085.
[7] A.H. Seikh, E.-S.M. Sherif, S.M.A. Khan Mohammed, M. Baig, M.A. Alam, and N. Alharthi, PLOS One, **13**(4), 1-14 (2018). https://doi. org/10.1371/journal.pone.0195224
[8] H.T. Liu, C.X. Yang, H.H. Liang, J. Yang, and W.F. Zhou, J. Power Sources, **103**(2), 173-179 (2002). https://doi.org/10.1016/S0378-7753(01)00839-4
[9] F. Tariq, S.U. Azher, and N. Naz, J. Fail. Anal. Preven. **10**(2), 152-160 (2010), https://doi.org/ 10.1007/s11668-010-9331-1
[10] R. Mahmudi, A.R. Geranmayeh, and A. Rezaee-Bazzaz, J. Alloys Compd. **427**, 124-129 (2007). https://doi.org/10.1016/j.jallcom.2006.02.053
[11] S.P. O'Dell, G.L. Ding, S.N. Tewari, Metall. Mater. Trans. A, **30**, 2159-2165 (1999). https://doi.org/10.1007/s11661-999-0027-7
[12] T. Gancarz and W. Gasior, J. Chem. Eng. Data, **63**(5), 1471-1479 (2018). https://doi.org/10.1021/acs.jced.7b01049
[13] S.E. Kisakurek, J. Mater. Sci. **19**(7), 2289-2305 (1984). https://doi.org/10.1007/BF01058106
[14] T. Hirasawa, K. Sasaki, M. Taguchi, and H. Kaneko, J. Power Sources, **85**(1), 44-48 (2000). https://doi.org/10.1016/S0378-7753(99)00380-8
[15] H. Li, W.X. Guo, H.Y. Chen, D.E. Finlow, H.W. Zhou, C.L. Dou, G.M. Xiao, S.G. Peng, W.W. Wei, and H. Wang, J. Power Sources. **191**(1), 111-118 (2009), https://doi.org/10.1016/j.jpowsour.2008.10.059
[16] W.-B. Cai, Y.-Q. Wan, H.-T. Liu, and W.-F. Zhou, Chin. J. Chem. **14**(2), 138-146 (1996). https://doi.org/10.1002/cjoc.19960140208
[17] R.K. Shervedani, A.Z. Isfahani, R. Khodavisy, and A. Hatefi-Mehrjardi, J. Power Sources, **164**(2), 890-895 (2007). https://doi.org/10.1016/j.jpowsour.2006.10.105
[18] M. Matrakova, A. Aleksandrova, P. Nikolov, O. Saoudi, and L. Zerroual, Bulg. Chem. Commun. **52** (A), 74-79 (2020). https://doi.org/10.34049/bcc.52.A.232 74
[19] S. Khatbi, Y. Gouale, S. Mansour, A. Lamiri, and M. Essahli, Port. Electrochim. Acta, **36**(2), 133-146 (2018). https://doi.org/10.4152/pea.201802133
[20] Y.B. Zhou, C.X. Yang, W.F. Zhou, and H.T. Liu, J. Alloys Compd. **365**(1-2), 108-111 (2004). https://doi.org/10.1016/S0925-8388(03)00649-2
[21] B. Yang, C. Xianyu, Y. Shaoqiang, L. Wei, D. Changsong, and Y. Geping, J. Energy Storage, **25**, 100908 (2019). https://doi.org/10.1016/j.est.2019.100908

[22] D. Slavkov, B.S. Haran, B.N. Popov, and F. Fleming, J. Power Sources. **112**(1), 199-208 (2002). https://doi.org/10.1016/S0378-7753(02)00368-3
[23] E. Rocca, G. Bourguignon, and J. Steinmetz, J. Power Sources. **161**(2), 666-675 (2006). http://dx.doi.org/10.1016/j.jpowsour.2006.04.140
[24] E.A.M. Ali, M.M. Hameed, M.S. Gumaan, A. Alameri, S.M.A.M. Alsowidy, N.Q. Al Naggar, and R.M. Shalaby, Results Mater. **16**(12), 100307 (2022). https://doi.org/10.1016/j.rinma.2022.100307
[25] M.T. Wall, Y. Ren, T. Hesterberg, T. Ellis, and M.L. Young, J. Energy Storage. **55**, 105569 (2022). https://doi.org/10.1016/j.est.2022.105569
[26] Z. Ghasemi and A. Tizpar, Int. J. Electrochem. Sci. **2**, 700-720 (2007). https://doi.org/10.1016/S1452-3981(23)17106-9
[27] Z. Ghasemi and A. Tizpar, Int. J. Electrochem. Sci. **3**, 727-745 (2008). https://doi.org/10.1016/S1452-3981(23)15476-9
[28] E. Gullian, L. Albert, and J.L. Caillerie, J. Power Sources. **116**(1-2), 185-192 (2003). http://dx.doi.org/10.1016/S0378-7753(02)00705-X
[29] S. El-Gamal, G. Mohammed, and E.E. Abdel-Hady, Am. J. Mater. Sci. **5**(5), 97-105 (2015). https://doi.org/10.5923/j.materials.20150505.01
[30] J.P. Hilger, J. Power Sources. **53**(1), 45-51 (1995). https://doi.org/10.1016/0378-7753(94)01977-4
[31] G.S. Al-Ganainy, M.T. Mostafa, and F. Abd El-Salam, Physica B **348**(1-4), 242-248 (2004). https://doi.org/10.1016/j.physb.2003.11.096.
[32] B. Trembach, M. Krbata, B. Haibadulov, O. Iokhov, I. Tsebriuk, I. Pomohaiev, Y. Korobkov, L. Neduzha, *et al.*, Eng. **7**, 139 (2026). https://doi.org/10.3390/eng7030139
[33] B. Trembach, B. Mordyuk, M. Krbata, M. Skoryk, A. Volovodiuk, O. Reshetnyk, V. Zakiev, *et al.*, J. Manuf. Mater. Process. **10**, 108 (2026). https://doi.org/10.3390/jmmp10030108
[34] D. Redchyts, S. Dovgiy, U. Tuchyna, and S. Moiseienko, in: *Applied innovations in information and communication technology*, edited by S. Dovgiy, E. Siemens, L. Globa, O. Kopiika, end O. Stryzhak, (Cham, Springer, 2025), pp. 672-694. https://doi.org/10.1007/978-3-031-89296-7_34
[35] B. Trembach, I. Trembach, A. Grin, N. Makarenko, O. Rebrov, Y. Musairova, N. Kuravska, *et al.*, Int. J. Adv. Manuf. Technol. **140**, 1367-1408 (2025). https://doi.org/10.1007/s00170-025-16325-w
[36] O. Sukhova, and Yu. Syrovatko, Metallofiz. Noveishie Technol. **33**(Special Issue), 371-378 (2011). (in Russian)
[37] I.M. Spiridonova, E.V. Sukhovaya, and V.F. Balakin, Metallurgia, **35**(2), 65-68 (1996).
[38] B. Trembach, I. Trembach, A. Grin, N. Makarenko, O. Babych, S. Knyazev, Y. Musairova, *et al.*, Eng. **6**, 125 (2025). https://doi.org/10.3390/eng6060125
[39] I. Spiridonova, O. Sukhova, and O. Vashchenko, Metallofiz. Noveishie Technol. **21**(2), 122-125 (1999).
[40] O.V. Sukhova, and K.V. Ustinova, Funct. Mater. **26**(3), 495-506 (2019). https://doi.org/10.15407/fm26.03.495
[41] O.V. Sukhova, Probl. At. Sci. Technol. **128**(4), 77-83 (2020). https://doi.org/10.46813/2020-128-077
[42] I.M. Spyrydonova, O.V. Sukhova, and G.V. Zinkovskij, Metall. Min. Ind. **4**(4), 2-5 (2012). (in Russian)
[43] R.S. Hixson, D.D. Koller, G.T. Gray, and D.B. Hayes, AIP Conf. Proc. **955**, 51-54 (2007). https://doi.org/10.1063/1.2833128
[44] L. Albert, A. Goguelin, and E. Jullian, J. Power Sources. **78**(1-2), 23-29 (1999). https://doi.org/10.1016/S0378-7753(99)00006-3
[45] D.M. Rosa, J.E. Spinelli, I.L. Ferreira, and A. Garcia, Metall. Mater. Trans. A, **39**(9), 2161-2174 (2008). https://doi.org/10.1007/s11661-008-9542-1
[46] O.V. Sukhova, East Eur. J. Phys. (2), 115-121 (2021). https://doi.org/10.26565/2312-4334-2021-2-08
[47] O.V. Sukhova, Metallofiz. Noveishie Technol. **43**(3), 355-365 (2021). https://doi.org/10.15407/mfint.43.03.0355
[48] O.V. Sukhova, Phys. Chem. Solid St. **22**(3), 487-493 (2021). https://doi.org/10.15330/pcss.22.3.487-493

ПОРІВНЯННЯ ВПЛИВУ Sn ТА As НА ВЛАСТИВОСТІ НА РОЗТЯГ СПЛАВУ Pb–3,5%Sb ДЛЯ СТРУМОВІДВОДІВ СВИНЦЕВО-КИСЛОТНИХ АКУМУЛЯТОРІВ

Віктор О. Дзензерський, Сергій В. Тарасов, Олена В. Сухова, Володимир А. Іванов
Інститут транспортних систем і технологій Національної Академії наук України
49005, Україна, м. Дніпро, вул. Писаржевського, 5

В роботі порівнювали вплив 0,5 ваг.% Sn та 0,16–0,23 ваг.% As на властивості на розтяг литого сплаву Pb–3,5%Sb для струмовідводів свинцево-кислотних акумуляторів. Сплави виплавляли в умовах охолодження з різною швидкістю в ливарних формах, попередньо підігрітих в інтервалі температур від 50 °C до 170 °C, що відповідало швидкості охолодження в діапазоні від 100 °C/с до 50 °C/с. Механічні властивості, а саме межу міцності на розтяг і відносне подовження, вимірювали за кімнатної температури на універсальній випробувальній машині TIRAtest 2300 за сталої швидкості траверси 10 мм/хв. Встановили, що зі збільшенням температури підігріву ливарної форми подовження і межа міцності на розтяг сплаву Pb–3,5%Sb–0,23%As зменшуються на 13,9 % та 11,8 %, відповідно. Додавання олова замість миш'яку знижує межу міцності на розтяг лише на 2,8 %, тоді як подовження збільшується на 2,4 %. Зроблено висновок, що додавання олова компенсує негативний вплив миш'яку на властивості на розрив сплаву Pb–3,5%Sb для струмовідводів, пов'язаний з утворенням крихких фаз із вмістом миш'яку на границях зерен сплавів. Додавання олова до сплаву Pb–3,5%Sb забезпечує кращі властивості на розтяг за кімнатної температури, ніж додавання миш'яку.

Ключові слова: *свинцево-кислотні акумулятори; сплави на основі системи Pb–Sb для струмовідводів; температура підігріву ливарної форми; швидкість охолодження; випробування на розрив; межа міцності на розрив; подовження*

EAST EUROPEAN JOURNAL OF PHYSICS. **2.** 520-527 (2026)
DOI:10.26565/2312-4334-2026-2-59 ISSN 2312-4334

CHARACTERISTICS OF RADIATED FIELDS FORMED BY PATCH ANTENNA WITH COMPLICATED APERTURE

Sergey A. Pogarsky*, Dmitry V. Mayboroda, Mikhail V. Nesterenko,
Serhii M. Mykhaliuk, Oleksander A. Biloshenko
V.N. Karazin Kharkiv National University, 4, Svobody Sq., Kharkiv, Ukraine, 61022
**Corresponding Author e-mail: spogarsky@gmail.com*

Received March 9, 2026; revised May 2, 2026; accepted May 20, 2026

The paper considers issues related to simulating the electrodynamic characteristics of a patch antenna based on a microstrip disc resonator with a complex topology of the radiating aperture in the form of three slot log-periodic discontinuities, oriented at an angle of 120° with the scaling factor $\tau = 0.8$ and the spacing factor $\sigma = 0.15$. Three concentric ring slot discontinuities are located in a grounded base at a certain distance from the dielectric substrate, the centers of which coincide with the center of the microstrip disc. The antenna was fed by a section of a coplanar line with a stepped profile of the central conductor. The calculations used two methods: the magnetic wall model (semi-open resonator model) and the finite element method. After optimization procedures were carried out for the selected parameters, it was established that compromise parameter sets were necessary to obtain the required characteristics.

Keywords: *Ring resonator; Slot discontinuity; Coplanar line; Matching; Frequency characteristics; Energy characteristics*
PACS: 84.40.Ba; 41.20.Jb

Patch monopole antennas, which appeared in the mid-20th century, became a fundamental design for creating radiating systems for various purposes, thanks to their simplicity, low cost, relatively straightforward matching, and fairly easy parameter optimization. Since their appearance, the design of such antennas has been constantly evolving. This process affects not only changes in the topology of radiating elements – from the simplest canonical forms (rectangular, circular, ring-shaped, and their modifications) [1-3] to fairly complex ones in terms of topology (including fractal ones) [4-12], but also the process of searching for and using new substrate materials with unique characteristics [13-15]. A separate niche is occupied by so-called conformal antennas [16-18], whose geometry is matched to the curved surfaces on which they are placed.

The directions of antenna modifications were almost always determined by the need to solve specific problems. This was either the formation of specific directional patterns [19-21], or the creation of designs that provided the radiation (reception) of signals with circular polarization [22-24], or ensuring high gain values [25, 26], or ensuring the reconfigurability of the antenna design through the use of semiconductor elements [27, 28], and others. However, in solving all these problems, the important issue remained ensuring an acceptable level of antenna matching to external circuits.

Recently, there has been a real need to develop so-called ‘wearable’ small-sized antennas for both individual identification and common communication tasks [29, 30]. Given the specifics of this type of task, at least two non-standard requirements for the characteristics of such antennas can be formulated. The first requirement is that, depending on the antenna's location, the surface's radius of curvature at that location must be taken into account. This factor will be particularly relevant when the antenna's geometric dimensions increase relative to the wavelength. In cases where the geometric dimensions of the antenna are comparable to (or smaller than) the wavelength, flat antennas can be considered. The second requirement concerns the need to form a specific directional pattern. The specificity is that reception (radiation) in a direction perpendicular to the antenna plane is not predominant. The reason is that the transmitter (receiver) will almost always be at some angle of elevation above the horizon (above the antenna plane). Of course, with all this, it is necessary to ensure satisfactory matching with external circuits. It is desirable to ensure circular (elliptical) polarization within a certain angle range and a sufficiently high antenna gain.

It is clear that such a set of requirements cannot be implemented using trivial (classical) designs. It can be assumed that the potential design should have both a sufficiently non-trivial topology of the radiating aperture and additional design elements that enable the formation of the required directional pattern.

In this paper, the results of a simulation of the characteristics of a planar monopole antenna with a complex radiating aperture topology consisting of three slot log-periodic radiators oriented at an angle of 120° to each other, and a grounding screen with a set of slot discontinuities in the form of concentric circles, are presented. The antenna was fed using a section of a coplanar line.

STRUCTURE UNDER CONSIDERATION

We will consider a monopole planar antenna, the design of which is based on a disc microstrip resonator with three slot apertures in the form of log-periodic elements oriented at an angle of 120° with a scale factor $\tau = 0.8$ and a

---

Cite as: S.A. Pogarsky, D.V. Mayboroda, M.V. Nesterenko, S.M. Mykhaliuk, O.A. Biloshenko, East Eur. J. Phys. 2, 520 (2026), https://doi.org/10.26565/2312-4334-2026-2-59

spacing factor $\sigma = 0.15$. The element standard for all microstrip structures – a grounded base – is located at a certain distance from the dielectric substrate. It is assumed that the geometric dimensions of the grounded base significantly exceed the geometric dimensions of the substrate, and they are significantly larger than the wavelength. This choice of dimensions eliminates specific effects (diffraction effects at the edges of metal elements and the so-called 'flow' of currents to the opposite side of the grounded plane). The grounded base has three concentric slot irregularities, the geometric centers of which coincide with the geometric center of the disc resonator. The width of the slot elements is 1 mm, and the radii are selected so that the slot discontinuities intersect the projections of the log-periodic apertures in three characteristic areas. The antenna is fed using a section of a coplanar line, the inner conductor of which has a stepped profile. The antenna design is shown in Fig. 1. Fig. 1a – the image of antenna, Fig. 1b – the topology of aperture on the top part of the substrate, Fig. 1c – the grounded base with concentric slot discontinuities.

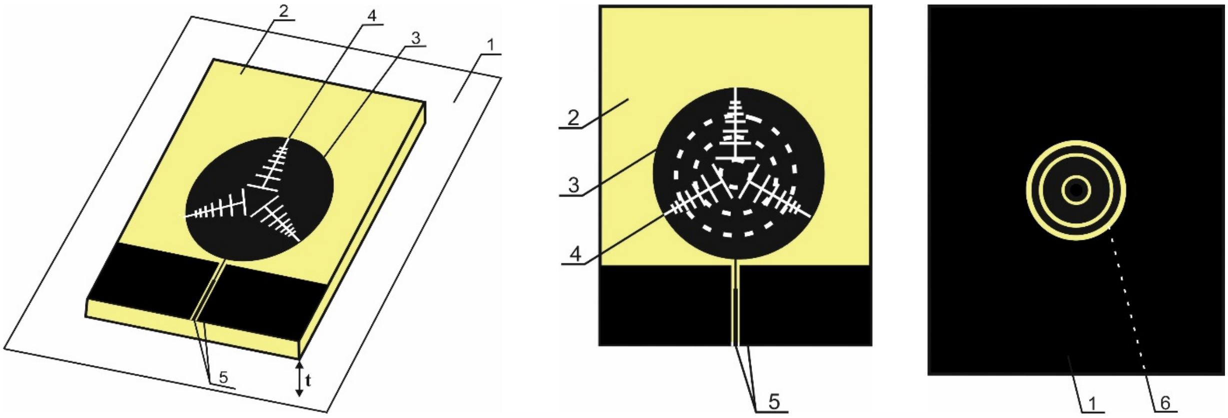

a) b) c)

Figure 1. The design of the antenna
The following symbols are used in the figure: 1 – grounded base, 2 – dielectric substrate, 3 – disc resonator, 4 – log-periodic discontinuities, 5 – coplanar elements, 6 – additional slot discontinuities in the metalized screen

The geometric dimensions of the disc resonator and the material constants of the dielectrics were selected based on the assumption that the antenna would operate in the microwave range. The use of slot discontinuities in the screen provides additional opportunities for solving problems such as matching the antenna to external circuits and adjusting the antenna's energy characteristics (directivity pattern, gain coefficient, and polarization characteristics). The gap between the dielectric substrate and the grounded base is easily achieved by using an additional dielectric layer. In cases where the required characteristics are achieved at $\varepsilon_r = 1$, it is possible to use special dielectrics, such as expanded polystyrene foam or polyurethane foam with parameters $\varepsilon_r = 1.02...1.06$ and $tg\,\delta = (1...5)10^{-4}$ (the parameters remain virtually unchanged in the frequency range from 100 MHz to 10 GHz). It is assumed that the conductivity of all metal elements is infinite (ideal metal).

NUMERICAL MODELLING RESULTS

Complete information about the electrodynamic characteristics of any electrodynamic structure can only be obtained by solving the corresponding boundary value problem formulated for a model that takes into account the maximum set of factors and features of the object itself. The antenna under consideration is a rather complex 3D structure, which makes it extremely difficult to build a model that takes all factors into account. In this situation, it can be argued that a rigorous solution to such an electrodynamic problem, which is currently unavailable, is unlikely to be found in the near future. A realistic solution in this situation is numerical simulating of the antenna's characteristics based on a model that takes into account the most significant parameters and the relationships between them. An important step in constructing such a model is to identify the most characteristic variable parameters, which are used to optimize the characteristics. However, it should be noted that the optimal set of parameters obtained for a particular antenna characteristic does not guarantee the optimality of other antenna characteristics.

The complexity of constructing a generalized model lies in the fact that the structure is a combination of resonators. In the plane of the microstrip patch, the first resonances are those of the aperture of the microstrip disc itself, and the second are those of the slot discontinuities. Resonance may also occur in the dielectric substrate and in the gap between the substrate and the grounded base (especially with increasing frequency). In the grounded base itself, where the ring slot discontinuities are located, resonances may occur at certain frequencies. Resonances in the coplanar line segment can be disregarded, since it has relatively small linear dimensions, which shifts the resonance frequencies beyond the range under consideration. The overall characteristics of the antenna will be formed taking into account all these factors, which is why it is mandatory to optimize the parameters according to the selected variable parameters.

It is obvious that the optimal model cannot be based on the use of only one approach or method (even numerical), since such implementation would lead to high demands on computer resources and calculation time. The most rational approach seems to be the use of a combination of several methods. The calculations use a model based on two methods: the magnetic wall model (sometimes called the semi-open resonator model) [31] and the finite element method (FEM), implemented in the commercial ANSYS HFSS package [32]. The following parameters were selected as significant variables: t – the gap between the dielectric substrate and the grounded base, and ε_r – the relative dielectric permittivity of the substrate itself. The substrate thickness parameter h was excluded from the variable parameters, since the thin substrate approximation is used exclusively for calculating the parameters of real antennas $h << \lambda_r$, where λ_r is the resonant wavelength of the excited oscillations. This approximation minimizes the possibility of surface waves being excited in the dielectric layer of the substrate [33].

Considering all physical aspects affecting the antenna's operating mode, the natural first step in the study would be to examine the spectral composition of the oscillations excited in the structure. It is the presence of certain types of oscillations and their mutual influence (taking into account possible dispersion) that will determine the potential capabilities of such an antenna.

The main variable parameter selected t is the distance between the dielectric substrate and the grounded base. This parameter will have a decisive influence on the entire spectral composition, since with a fixed geometry, the resonant frequencies of the microstrip patch itself and the slot discontinuities will not change, and a change in the dielectric permittivity of the substrate itself can only lead to a trivial shift in the characteristics along the frequency axis (without changing the spectral composition). Figure 2 shows the spectral characteristics of the antenna when the parameter t varies in the frequency range from 0.7 GHz to 13 GHz.

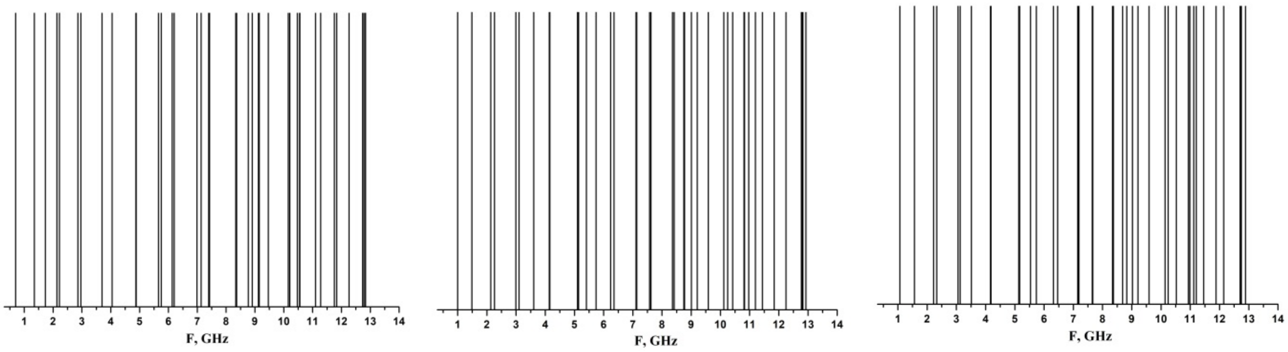

$\varepsilon_r = 2.4, t = 1\ mm$ $\varepsilon_r = 2.4, t = 1.5\ mm$ $\varepsilon_r = 2.4, t = 2\ mm$

Figure 2. Spectral characteristics of the antenna with parameter t variation

The characteristics given include 40 spectral lines in this range. The relative error in calculating the natural resonance frequencies does not exceed 10^{-7}, yielding a maximum error of no more than 1.4 kHz in the high-frequency part of the range under consideration.

A comparative analysis of the characteristics allows us to draw a general conclusion that, with the selected parameter t values, the radiating structure can operate in various modes: single-frequency with relatively narrow bands (corresponding to single spectral lines), multi-frequency with relatively wide bands (corresponding to frequency bands with a condensed spectrum or to individual frequencies with degenerate types of oscillations), and mixed mode. Modeling the spectrum above 13 GHz is not advisable due to strong spectral condensation and degenerate oscillation types, which greatly complicate type identification.

The conclusion about possible operating modes is illustrated by comparing the mutual arrangement of spectral lines in the characteristic near frequencies of 5.1 GHz and 7.5 GHz at a fixed value of the parameter t (for example, at $t = 1.5\ mm$). Near these frequencies, the spectral lines are located quite close to each other (5.10379 GHz, 5.13788 GHz and 7.5732 GHz, 7.61883 GHz), and there is no degeneration. It is precisely near these frequencies that the antenna can operate effectively. It can be argued that the value $t = 1.5\ mm$ is optimal in terms of spectral characteristics.

Another indirect indication of the optimality of certain parameter values is the structure of current densities on the surfaces of radiating apertures. The efficiency of their excitation may indicate the possibility of forming the necessary field distributions in the far field. Fig. 3 shows the structures of current density distributions on the surfaces of apertures (in the background, you can see the distribution of current densities on the surface of the grounded plane and on the slot discontinuities in it).

Frequencies close to the natural frequencies in the spectrum were selected for distribution, with a parameter value of $t = 1.5\ mm$. As can be seen from the distributions shown, the excitation of the aperture elements is sufficiently intense and sufficiently uniform. There are only slight differences in the excitation intensity of the slot log-periodic aperture element most distant from the microwave energy input point. Evidence that the ring-shaped slot discontinuities in the grounding screen actively influence on the formation of the radiated fields and other characteristics is their sufficiently effective excitation.

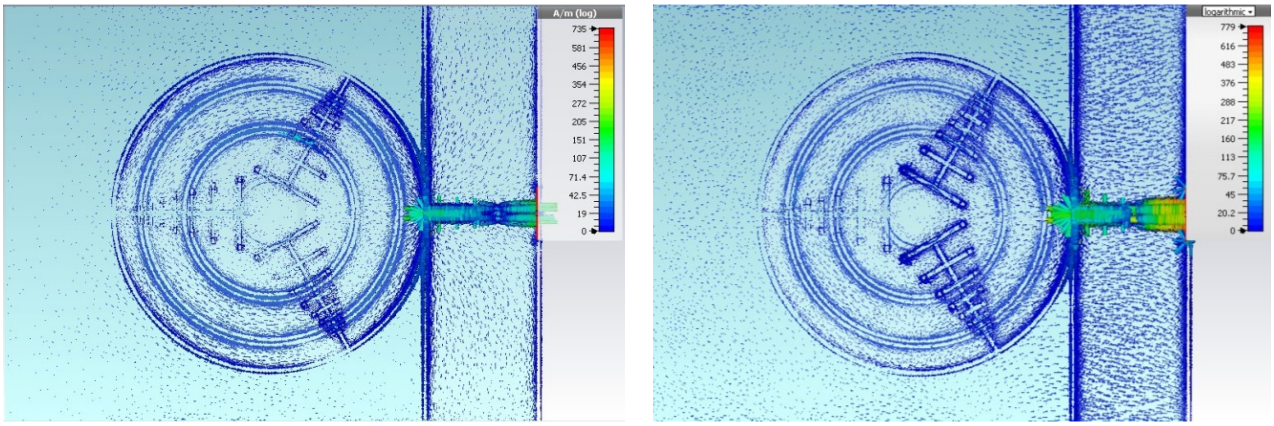

$F = 5.138$ GHz $F = 7.573$ GHz

Figure 3. Distribution of current densities on radiating apertures

The peculiarities of the current density distribution on the central conductor of the coplanar line necessitate additional research of the degree of antenna matching with external circuits. In addition, the degree of matching will indirectly indicate the efficiency of aperture excitation.

Fig. 4 shows the dependencies $|S_{11}|$ in the frequency range under consideration on the variable parameters t and ε_r. These dependencies allow us to assess the nature of the influence of the selected variable parameters on the reverse loss modulus, the presence of satisfactory matching bands, and the width of these bands.

Both dependencies are oscillatory in nature, with a significantly greater number of sharp fluctuations in value $|S_{11}|$ observed depending on ε_r. Absolute minima in dependencies $|S_{11}|$ on t at a fixed $\varepsilon_r = 2.4$ are observed near certain natural frequencies. And, if near the frequency $F = 5.5$ GHz the frequency distance of the minima is about 200 MHz, then near the frequency $F = 7.5$ GHz the distance does not exceed 80 MHz. In this situation, we can say that value of $|S_{11}|$ practically does not depend on the distance to the ground plane. The value ε_r has a significantly greater influence on the characteristic of $|S_{11}|$. If at a low value of $\varepsilon_r = 1.1$ the characteristic has a fairly wide frequency band with an acceptable level of matching (near the frequency $F = 6.5$ GHz, $\Delta F \approx 778$ MHz).

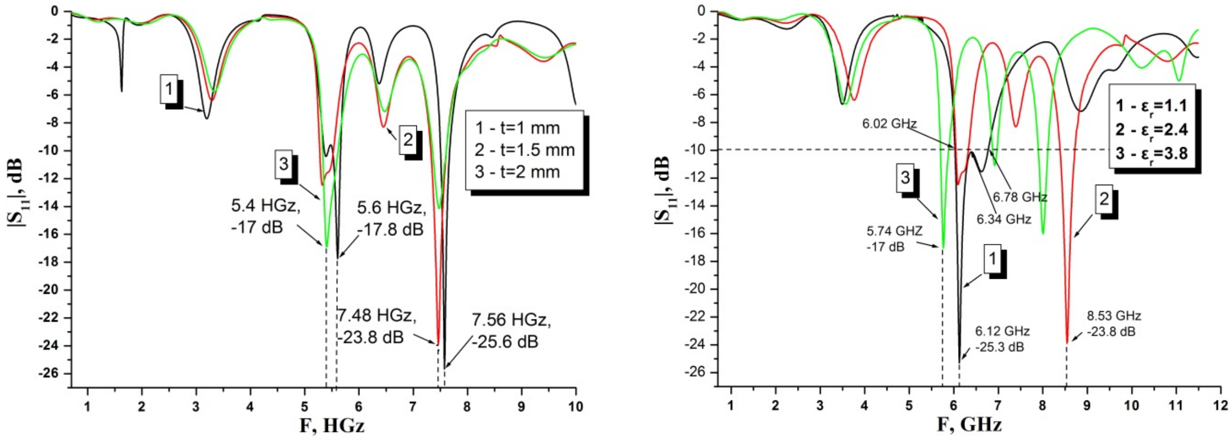

$\varepsilon_r = 2.4$ $t = 1.5\,mm$

Figure 4. Dependencies of $|S_{11}|$ on variable parameters t and ε_r

At the value of $\varepsilon_r = 2.4$ the band near this spectral line narrows significantly, but a relatively narrow band appears near the spectral line at a frequency of $F = 7.5$ GHz. That is, with this value of relative dielectric permittivity, the antenna can already operate in dual-band mode. A further increase ε_r to a value of 3.8 leads to the appearance of three narrow bands with an acceptable level of matching. However, when moving away from the center frequencies of these bands, there are quite sharp changes in the value $|S_{11}|$, which is generally unacceptable.

The functional purpose of any antenna is to form fields with specified energy characteristics in a certain part of space. These characteristics are: directivity pattern, gain coefficient, polarization characteristics. The synthesis of antennas taking these characteristics into account has always been a complex electrodynamic task, since each of the characteristics is described by a function that is multi-parametric, depending on the type of antenna, the features of the form factor of the radiating apertures, the material constants of the substrates (in the case of planar antennas), and the possible presence of auxiliary structural elements.

Fig. 5 shows the directional patterns at a frequency of $F = 7.5$ GHz with variation of the parameter t. Curve 1 corresponds to the value $t = 1mm$, curve 2 corresponds to $t = 1.5mm$, and curve 3 corresponds to $t = 2mm$. The curves are normalized to the absolute maximum (observed at $t = 1.5mm$) to enable the evaluation of radiation efficiency.

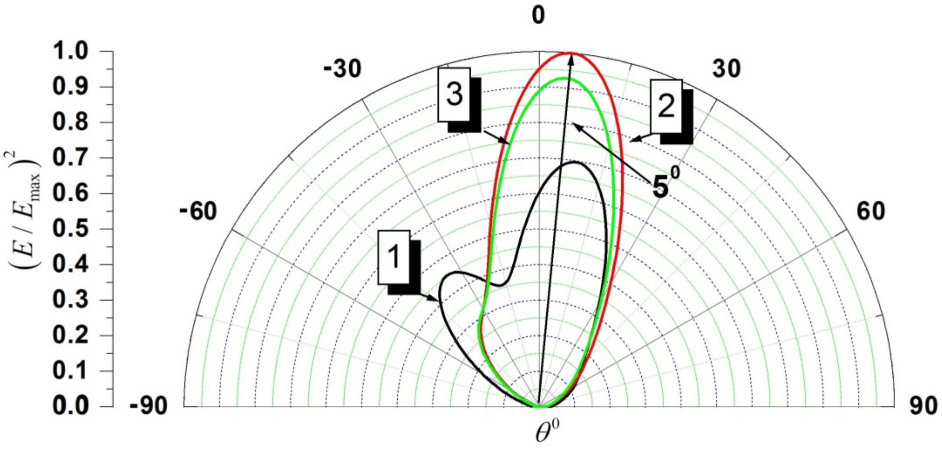

Figure 5. Directivity diagrams in the angular plane with parameter t variation

As shown in the figure, the distance to the grounded plane significantly affects both the shape of the directional pattern and the radiated power level. At a short distance ($t = 1mm$), the pattern has an almost two-lobe shape (curve 1). The main lobe is shifted relative to the normal by an angle of 9^0, and the amplitude is 0.69 of the maximum value. As the distance increases (curve 2 – $t = 1.5mm$, curve 3 – $t = 2mm$), the patterns transform into single-lobe patterns, the offset from the normal is practically the same, and is 5^0, and the maximum amplitude is observed at $t = 1.5mm$, while the width of the main lobe at a level of 0.707 is 27.8^0. Increasing the distance to the grounded plane to 2 mm leads to a slight narrowing of the main lobe.

It is clear that the total diagram is formed taking into account both elevation dependence and azimuthal dependence. Figure 6 shows two 3D directional diagrams at a frequency of $F = 7.5$ GHz for two values of the parameter t .

Analysis of the diagrams shows that, in principle, the type of diagrams is the same and largely repeats the type of diagrams in the elevation plane (Fig. 5). However, the amplitude values differ significantly, which indicates that the azimuthal components of the fields vary greatly.

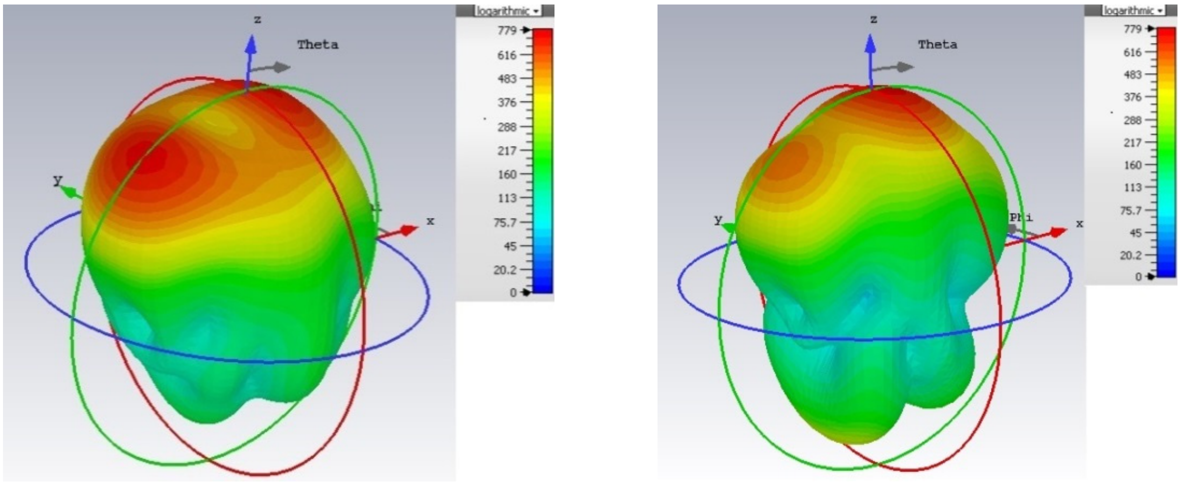

$t = 1.5mm$ $t = 2mm$

Figure 6. 3D directional diagrams at a frequency of F=7.5 GHz with parameter variation

Another energy parameter that determines an antenna's efficiency is the gain coefficient. Any antenna must provide an acceptable input signal level for subsequent processing. An important requirement for this characteristic is maintaining certain values above a specified level. Fig. 7 shows the dependence of the gain coefficient on the variation of the parameter t.

The behavior of the gain coefficient dependencies when varying the parameter t in the frequency range under consideration is fairly uniform. In the frequency range below 1.5 GHz, the gain coefficient values either fluctuate near zero or are negative. This behaviour is primarily due to the strong mismatch between the antenna and the exciting coplanar line (Fig. 4). With increasing frequency, a monotonic increase in the value of α begins. The maximum values for all values of the parameter α are reached near the frequency $F = 8.3$ GHz. From the point of view of the maximum gain coefficient, the optimal value is $t = 1.5mm$ with $\alpha = 9.22$ dBi.

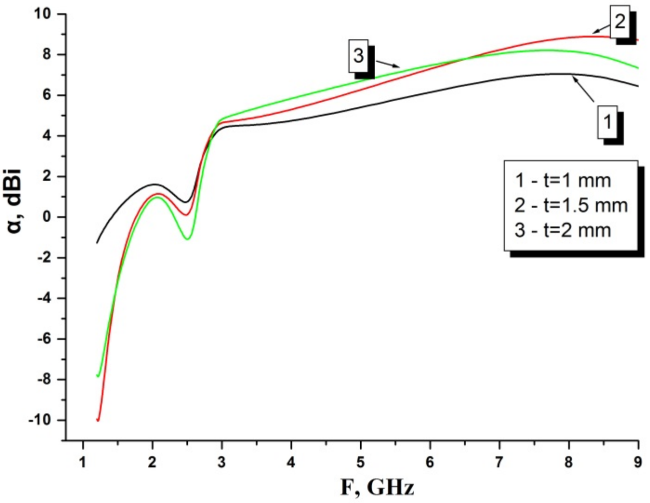

Figure 7. Dependencies of the antenna gain coefficient with parameter t variation

Another important energy characteristic is the so-called polarization characteristic, which shows the possibility of forming fields with a given polarization for transmission (reception). If we focus on the criterion of universality, then an antenna with circular (or elliptical, close to circular) polarization would be preferable. In most known designs, planar patch antennas form linearly polarized radiated fields, unless complex apertures, auxiliary elements or special excitation methods are used. Fig. 8 shows the polarization characteristics (according to the IEEE criterion in dB) for variations in the parameters t, $F = 7.5$ GHz $\varepsilon_r = 2.4$.

Figure 8 confirms the existence of a fairly strong dependence of the ellipticity coefficient function η on the observation angle θ (the angle of elevation, measured from the normal to the antenna plane). The optimal option in terms of minimum ellipticity coefficient is the close location of the grounding plane ($t = 1mm$). At an observation angle $\theta = 68.3^0$, an ellipticity coefficient of $\eta = 1.2$ dB is achieved. Moreover, in the angle range from 55^0 to 78.5^0, the ellipticity coefficient does not exceed 3 dB.

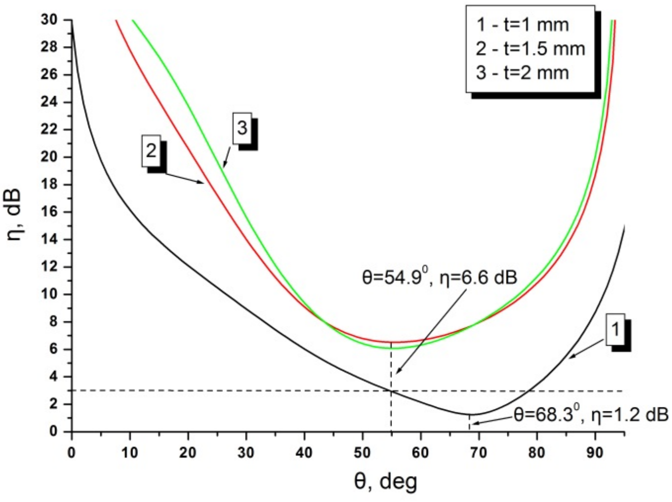

Figure 8. Polarization characteristics with parameter t variation

When the observation angle deviates from these values, the polarization becomes linear. For other tested parameter values, the ellipticity coefficients do not differ significantly from each other. The minimum achievable value is $\eta = 6.6$ dB at an observation angle of $\theta = 54.9^0$, which is quite far from the desired ellipticity coefficient value.

CONCLUSIONS

This paper presents the results of numerical modeling of the main characteristics of a patch antenna with a complex radiating aperture in the form of three sets of slot discontinuities in a microstrip disc with a log-periodic profile and oriented at an angle of 120^0 relative to each other. A ground plane located at a certain distance from a dielectric substrate with three ring slot discontinuities is used as an auxiliary element to influence the main characteristics. Using procedures for optimizing the electrodynamic characteristics of the antenna according to selected variable parameters, it was established that it is necessary to use a certain compromise set of parameters capable of ensuring the formation of the specified distributions of radiated (received) fields, an acceptable level of matching with external circuits, and acceptable values of the gain coefficient.

Acknowledgements

This work was supported by the Ministry of Education and Science of Ukraine, grant 0126U000999.

ORCID

Sergey A. Pogarsky, https://orcid.org/0000-0003-0833-1421; **Dmitry V. Mayboroda,** https://orcid.org/0000-0002-9564-2369
Mikhail V. Nesterenko, https://orcid.org/0000-0002-1297-9119

REFERENCES

[1] K.-L. Wong, *Compact and Broadband Microstrip Antennas*, (John Wiley & Sons, 2002). https://doi.org/10.1002/0471221112
[2] G. Kumar, and K.P. Ray, *Broadband microstrip antennas*, (Artech House, 2003). http://read.pudn.com/downloads150/ebook/652719/Broadband%20microstrip%20antennas.pdf
[3] R. Garg, P. Bhartia, I. Bahl, and A. Ittipiboon, *Microstrip Antenna Design Handbook*, (Artech House, 2001). https://uodiyala.edu.iq/uploads/PDF%20ELIBRARY%20UODIYALA/EL37/Microstrip%20Antenna%20Design%20Handbook.pdf
[4] J. Liu, Q. Xue, H. Wong, H.W. Lai, and Y. Long, IEEE Trans. Antennas Propag., **61**, 11 (2013). https://doi.org/10.1109/TAP.2012.2214996
[5] X. Ma, Y Zong, P. Zhang, J. Chen, and Z. Ren, IEEE Trans. Antennas Propag. **74**, 38 (2026). https://doi.org/10.1109/TAP.2025.3623329
[6] S. Lin, Progress in Electr. Res. **90**, 369 (2009). http://dx.doi.org/10.2528/PIER09020503
[7] R. Li, Y.-X. Guo, B. Zhang, and G. Du, IEEE Antennas and Wireless Propag. Lett. **16**, 2566 (2017). https://doi.org/10.1109/LAWP.2017.2734246
[8] D.V. Maiboroda, and S.A. Pogarsky, Telecom. and Radio Eng. **73**(19), 1713 (2014). https://doi.org/10.1615/TelecomRadEng.v73.i19.20
[9] S.A. Pogarsky, D.V. Mayboroda, and S.M. Mikhaliuk, East Eur. J. Phys. (4), 274 (2023). https://doi.org/10.26565/2312-4334-2023-4-34
[10] T.-S. Wang, C.-Z. Du, H.-F. Shu, and Z.-H. Yue, PIER C, **140**, 127 (2024). https://doi.org/10.2528/PIERC23111602
[11] Y. Liu, S. Gong, and H.-B. Zhang, in: *2006 IEEE Antennas and Propagation Society International Symposium (IEEE, 2006)*, 2603–2606. https://doi.org/10.1109/APS.2006.1711133
[12] S. A. Pogarsky, D. V. Mayboroda, and S. N. Mykhaliuk, in: *2024 IEEE 29th International Seminar/Workshop on Direct and Inverse Problems of Electromagnetic and Acoustic Wave Theory (DIPED)*, (IEEE, 2024), pp. 103–106. https://doi.org/10.1109/DIPED63529.2024.10706159
[13] S. Zhang, and D. Zhao, *Aerospace materials handbook*, (CRC Press, 2012). https://www.zlibrary.to/filedownload/aerospace-materials-handbook-2.
[14] R.P. Owens, J.E. Aitken, and T.C. Edwards, IEEE Trans. MTT, **24**, 499 (1976). https://doi.org/10.1109/TMTT.1976.1128887
[15] Y. Tokumitsu, M. Ishizaki, M. Iwakuni, and T. Saito, IEEE MTT, **31**, 121 (1983). https://doi.org/10.1109/TMTT.1983.1131445
[16] P. Muthusamy, S. Shaik, and M. Reddy, in: *2025 IEEE Wireless Antenna and Microwave Symposium (WAMS)*, (2025). https://doi.org/10.1109/WAMS64402.2025.11158849
[17] S. Yuanhua, and L. Yihe, in: *2019 2nd International Conference on Communication Engineering and Technology (ICCET)*, (2019). https://doi.org/10.1109/ICCET.2019.8726870
[18] B. Mohamadzade, Roy B. V. B. Simorangkir, R. Maqsood Hashmi, Y. Chao-Oger, M. Zhadobov, and Ronan Sauleau, IEEE Antennas and Wireless Propag. Lett. **19**, 203 (2020). https://doi.org/10.1109/LAWP.2019.2958036
[19] N. Khalid, S. Z. Ibrahim, and M. N. A. Karim, in: *2016 3rd International Conference on Electronic Design (ICED)*, (2016). https://doi.org/10.1109/ICED.2016.7804637
[20] O. A. Al Kaladi, and A. S. M. Alqadami, in: *2025 IEEE International RF and Microwave Conference (RFM)*, (2025). https://doi.org/10.1109/RFM67034.2025.11284496
[21] X. Zhang, Y. Liu, J. Q. Zhu, and W. Cui, in: *2023 16th UK-Europe-China Workshop on Millimetre Waves and Terahertz Technologies (UCMMT)*, (2023). https://doi.org/10.1109/UCMMT58116.2023.10418967
[22] W.-S. Yoon, D.-H. Lee, K.-J. Lee, S.-H. Kim, S.-M. Han, and Y.-S. Kim, in: *2009 Loughborough Antennas & Propagation Conference*, (2009). https://doi.org/10.1109/LAPC.2009.5352514
[23] H. J. Kim, S. M. Kim, J. M. Son, and W. G. Yang, in: *2005 Asia-Pacific Microwave Conference Proceedings*, (2005). https://doi.org/10.1109/APMC.2005.1606902
[24] T.-C. Yo, C.-M. Lee, and C.-H. Luo, in: *2007 International workshop on Antenna Technology: Small and Smart Antennas Metamaterials and Applications*, (2007). https://doi.org/10.1109/IWAT.2007.370167
[25] G. Idayachandran, E. Ramassamy, M. Sivaraj, and V. Rajesh, in: *2019 IEEE International Conference on System, Computation, Automation and Networking (ICSCAN)*, (2019). https://doi.org/10.1109/ICSCAN.2019.8878715
[26] J. P. Zhang, and J. J. Mao, in: *2020 International Conference on Microwave and Millimeter Wave Technology (ICMMT)*, (2020). https://doi.org/10.1109/ICMMT49418.2020.9386991

[27] R. George, C. R. S. Kumar, and S.A. Gangal, in: *2016 International Conference on Communication and Signal Processing (ICCSP)*, (2016). https://doi.org/10.1109/ICCSP.2016.7754451
[28] N. EL Anzoul, Y. K. Bekali, and K. Minaoui, in: *2025 12th International Conference on Wireless Networks and Mobile Communications (WINCOM)*. (2025). https://doi.org/10.1109/WINCOM65874.2025.11313447
[29] M. Schubler, M. Maasch, C. Damm, and R. Jakoby, in: *2009 European Microwave Conference (EuMC)*, (2009). https://doi.org/10.23919/EUMC.2009.5296144
[30] S. Sharma, M. Kumar, H. Nigam, and M. Mathur, in: *2021 IEEE Indian Conference on Antennas and Propagation (InCAP)*, (2021). https://doi.org/10.1109/InCAP52216.2021.9726406
[31] G. Kompa, and R. Mehran, Electron. Lett. **11**, 459 (1975). https://doi.org/10.1049/el:19750352
[32] Ansoft HFSS /ANSYS Academic Research HF (5 tasks): 1 task(s) Permanent Customer #1076710.
[33] V.R. Komanduri, V.R. Jackson, J.T. Williams, and A.R. Mehrotra, IEEE Trans. on Antennas and Propag. **61**, 2887 (2014). https://doi.org/10.1109/TAP.2013.2254441

ХАРАКТЕРИСТИКИ ВИПРОМІНЮВАНИХ ПОЛІВ, СФОРМОВАНИХ ПАТЧ-АНТЕНОЙ ЗІ СКЛАДНОЮ АПЕРТУРОЮ

Сергій О. Погарський, Дмитро В. Майборода, Михайло В. Нестеренко, Сергій М. Михалюк, Олександр А. Білошенко
Харківський національний університет імені В.Н. Каразіна, майдан Свободи, 4, Харків, Україна, 61022

У статті розглянуто питання, пов'язані з моделюванням електродинамічних характеристик смужкової антени на основі мікросмужкового дискового резонатора зі складною топологією випромінюючої апертури у вигляді трьох щілинних логарифмічно-періодичних неоднорідностей, орієнтованих під кутом 120^0 з масштабним коефіцієнтом $\tau = 0,8$ і коефіцієнтом кроку $\sigma = 0,15$. У заземленій основі на певній відстані від діелектричної підкладки розташовані три концентричні кільцеві щілинні розриви, центри яких збігаються з центром мікросмужкового диска. Антена живилася відрізком компланарної лінії зі ступінчастим профілем центрального провідника. У розрахунках використовувалася модель, побудована на основі двох методів: моделі магнітної стінки (модель напіввідкритого резонатора) та методу скінченних елементів. Після проведення оптимізаційних процедур для вибраних параметрів було встановлено, що для отримання необхідних характеристик необхідні компромісні набори параметрів.

Ключові слова: *кільцевий резонатор; щілинний розрив; компланарна лінія; узгодження; частотні характеристики; енергетичні характеристики*

East European Journal of Physics. **2.** 528-540 (2026)
DOI:10.26565/2312-4334-2026-2-60 ISSN 2312-4334

FORMATION OF AN K_a AXIALLY SYMMETRIC FIELD DISTRIBUTION USING RECTANGULAR APERTURE RADIATORS

I.K. Kuzmychov[1]*, O.A. Voitovych[1], O.S. Lukash[1], E.M. Khutoryan[1], V.P. Maltsev[1], O.V. May[2]
[1]*O.Ya. Usikov Institute for Radiophysics and Electronics of National Academy of Sciences of Ukraine,*
12, Ac. Proskura str., Kharkiv, 61085, Ukraine
[2]*"Actox Ukraine" LLC, 1, Ivana Honty Str., Kyiv, 04112, Ukraine*
**Corresponding Author e-mail: kuzmichev.igr@gmail.com*

Received February 24, 2026; revised May 2, 2026; accepted May 22, 2026

Using the aperture method, radiation from the open end of a rectangular waveguide was studied. Expressions were derived to describe the radiation pattern of such an aperture in the far-field region in two mutually perpendicular planes. Numerical studies of the radiation pattern cross-sections in the image plane were performed for two rectangular apertures, 40×33 mm and 30×21.6 mm, with varying aperture widths and heights. A comparison of the obtained radiation pattern cross-sections with a Gaussian field distribution showed that up to the –11 dB level, the radiation pattern cross-sections in both image planes practically coincide with the Gaussian field distribution. This result is particularly important when a wave beam is incident on the flat face of an axicon. It was also shown that varying the smaller dimension of the rectangular aperture can yield an axially symmetric radiation pattern. Experimental studies of these apertures in the K_a band were conducted. Good agreement between the experimental results and theoretical calculations was demonstrated. It was found that when the geometric dimensions of the rectangular aperture exceed two wavelengths, a traveling-wave regime is established in the waveguide section. Experimentally, it was found that the amplitude distribution of the field for both apertures in the far-field region coincides with the Gaussian distribution down to –8.7 dB. It was shown that the use of rectangular apertures to illuminate the flat face of an axicon with a wave beam is impractical.

Keywords: *Aperture method; K_a-band; Rectangular aperture; Radiation pattern; Gaussian field distribution; Axicon*
PACS: 41.20.Cq, 07.57.Hm

1. INTRODUCTION

When exposed to high-power pulsed electromagnetic radiation, voltages on semiconductor components can reach hundreds of volts, potentially causing a malfunction. If the affected equipment contains such components — for example, communications hardware or the input circuits of unmanned aerial vehicles (UAVs) — pulsed irradiation can drive devices into saturation or cause outright failure, effectively disabling them. Compact pulsed sources with high peak power are available in the X-band [1-3], but producing comparable devices in the K_a-band presents challenges. These difficulties stem from increased ohmic losses in electrodynamic elements as frequency rises and from reduced efficiency of energy exchange between the electron beam and the high-frequency field in resonant structures [4]. Consequently, the output pulse power typically decreases in the K_a-band.

Therefore, investigating the effects of high-power pulsed electromagnetic radiation on UAV input circuitry is an important and timely research topic. Several high-power pulse systems have been reported in the literature and open sources. One example is the THOR (Tactical High-Power Microwave Operational Responder) system developed at the U.S. Air Force Research Laboratory. THOR employs ultra-wideband pulses to disrupt UAV operation and reportedly can protect airspace out to approximately 5 km, with peak pulse powers on the order of 150 kW.

The PHASER system, developed by Raytheon, is another well-known, powerful microwave source mounted on top of a six-meter shipping container-like box coupled with radar (e.g., the MPQ-64 Sentinel or Close Combat Tactical Radar) to detect and localize UAVs and to direct pulses toward them. Publicly available information on PHASER's radiator parameters, pulse duration, and output power is limited; its antenna is described as a rectangular panel used with a steerable reflective mirror. The Tesla transformer is apparently used in both systems to generate powerful ultra-wideband pulses.

Epirus Technologies' Leonidas anti-drone system is an example of a compact, high-power X-band microwave solution. Leonidas is lightweight and vehicle-mountable, facilitating rapid deployment. The system has been procured by the U.S. Army; compared with earlier Epirus designs, its effective range against UAVs is reported to have doubled to about 2 km and its output power to have increased by roughly 30% (contract signed on 17 July 2025).

Given these constraints, operation in the K_a-band is attractive. K_a-band waves can penetrate small openings and shielding in UAV enclosures, potentially damaging both input circuits and shielded microelectronics. The principal obstacle is the lack of compact, high-power K_a-band sources. An alternative to increasing source pulse power is to employ low-divergence beams. Bessel beams are a promising candidate: their weakly diverging spatial profiles can concentrate field strength at a target location more efficiently, allowing lower source power to achieve the electric-field intensities needed to affect UAV electronics.

Cite as: I.K. Kuzmychov, O.A. Voitovych, O.S. Lukash, E.M. Khutoryan, V.P. Maltsev, O.V. May, East Eur. J. Phys. 2, 528 (2026), https://doi.org/10.26565/2312-4334-2026-2-60

The propagation of such beams in open resonators has been studied in the K_a-band [5-7]. Several works have also reported the spatial formation of Bessel beams [8,9]. In particular, the authors of [9] demonstrated a Bessel beam with a diameter of 5.5 mm at a distance of 100 mm in the W-band using a diagonal horn, a convex lens, and an optical element (axicon). In all such implementations, an optical element is required to convert a Gaussian beam into a Bessel beam [10, 11]. It has also been shown [12] that circular waveguides can be effectively used for exciting Bessel beams with the aid of optical elements. This requires that the waveguide's operating mode exhibit an axially symmetric electric-field distribution in the plane of the optical element. In the K_a-band, the most commonly used transmission lines are rectangular waveguides, such as the EIA standard WR-28 (7.11 × 3.56 mm^2) and 7.2 × 3.4 mm^2 waveguides. In these waveguides, the dominant TE$_{10}$ mode supports a linearly polarized electric field. As demonstrated in [13-15], the laser output radiation, which is a circular Gaussian beam, is incident on the flat face of an optical element to efficiently form a Bessel beam at its output. Consequently, in the K_a-band, the optical element must likewise be illuminated by an axially symmetric field in order to generate a Bessel beam. Unlike the optical regime, however, a waveguide radiator is required in the K_a-band to produce such an electric-field distribution.

Two key questions arise in this context: whether it is practically feasible to generate an axially symmetric field using a waveguide radiator, and what the diameter of the corresponding Gaussian-like beam will be in the far field (Fraunhofer zone). Therefore, the objective of this paper is to analyze aperture geometries capable of producing axially symmetric field distributions in the far field that closely approximate a Gaussian profile while maintaining a relatively small diameter at the $1/e$ intensity level.

2. RECTANGULAR APERTURE WITH THE TE$_{10}$ MODE

Radiation from the open end of a rectangular waveguide remains of considerable practical interest [16]. However, the problem of forming a far-field radiation pattern (RP) of a rectangular aperture that closely approximates a Gaussian field distribution has not been fully resolved.

Let us therefore consider radiation from the open end of a rectangular waveguide. The origin of the Cartesian coordinate system is placed in the plane of the waveguide aperture (Fig. 1). The z-axis coincides with both the waveguide axis and the direction of propagation of the TE$_{10}$ mode. Since an electric field exists in the aperture (at $z = 0$), a corresponding field is also present in the external region. For this configuration, the aperture field method is most commonly applied. Its use is based on the following assumptions [17]:

- the waveguide opening serves as the radiating aperture;
- the exciting field is zero outside the waveguide aperture ($z > 0$);
- the electric field in the aperture plane ($z = 0$) is identical to that in a waveguide cross-section located several wavelengths away from the opening;
- the waveguide operates in a single mode, namely TE$_{10}$.

It should be noted that for a specific mode (TE$_{10}$), the accuracy of the results increases as the aperture size becomes large compared with the wavelength λ.

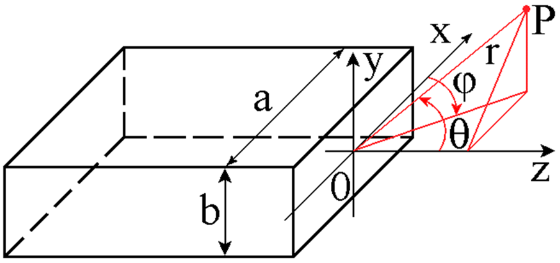

Figure 1. Coordinate systems for studying the radiation of TE$_{10}$ mode from the open end of a waveguide

In the Cartesian coordinate system, the electric-field strength at a point P (Fig. 1) can be expressed as follows

$$\vec{E}(P) = E_x(P)\vec{i} + E_y(P)\vec{j} + E_z(P)\vec{k} \tag{1}$$

By analogy with (1), the electric field strength at point P in the spherical coordinate system is expressed as follows

$$\vec{E}(P) = E_\theta(P)\vec{e}_\theta + E_\varphi(P)\vec{e}_\varphi + E_r(P)\vec{e}_r \tag{2}$$

The angles θ and φ for the spherical coordinate system are shown in Fig. 1. Let us express the Cartesian coordinates of point P through spherical ones

$$\begin{cases} E_x(P) = E_r(P)\sin\theta\cos\varphi - E_\varphi(P)\sin\varphi + E_\theta(P)\cos\varphi\cos\theta, \\ E_y(P) = E_r(P)\sin\varphi\sin\theta + E_\varphi(P)\cos\varphi + E_\theta(P)\sin\varphi\cos\theta, \\ E_z(P) = E_r(P)\cos\theta - E_\theta(P)\sin\theta. \end{cases} \tag{3}$$

A rectangular waveguide supporting the dominant TE₁₀ mode ($m = 1$, $n = 0$) is considered. In this case, the electric field has only one nonzero component E_y, while the remaining components $E_x=E_z=H_y=0$. Therefore, in the spherical coordinate system (see Fig. 1), the radial component can be set to zero, $E_r=0$. Taking this into account, expression (3) for the electric-field components of the mode at point P can be written as follows:

$$\begin{cases} E_x(P) = -E_\varphi(P)\sin\varphi + E_\theta(P)\cos\varphi\cos\theta, \\ E_y(P) = E_\varphi(P)\cos\varphi + E_\theta(P)\sin\varphi\cos\theta, \\ E_z(P) = -E_\theta(P)\sin\theta. \end{cases} \tag{4}$$

After substituting the expressions for the electric-field components from equation (4) into equation (1), we obtain a relation in the Cartesian coordinate system that defines the electric-field strength of the TE₁₀ mode at point P in terms of spherical coordinates.

$$\vec{E}(P) = \left(E_\theta(P)\cos\varphi\cos\theta - E_\varphi(P)\sin\varphi\right)\vec{i} + \left(E_\varphi(P)\cos\varphi + E_\theta(P)\sin\varphi\cos\theta\right)\vec{j} - E_\theta(P)\sin\theta\vec{k} \tag{5}$$

Taking into account the simplification made ($E_r=0$), the components of the electric field E_θ and E_φ at point P, determined by the electric-field distribution of the TE₁₀ mode in a rectangular aperture of cross-section $a \times b$, can be written in the following form in the spherical coordinate system [17]:

$$E_\theta(P) = AZ_0\frac{a^2 b}{\lambda_0^2}\sin\varphi\left(1+\frac{\lambda_0}{\lambda_g}\cos\theta\right)\frac{\cos\alpha}{\alpha^2-(\pi/2)^2}\cdot\frac{\sin\beta}{\beta}, \tag{6}$$

$$E_\varphi(P) = AZ_0\frac{a^2 b}{\lambda_0^2}\cos\varphi\left(\cos\theta+\frac{\lambda_0}{\lambda_g}\right)\frac{\cos\alpha}{\alpha^2-(\pi/2)^2}\cdot\frac{\sin\beta}{\beta}. \tag{7}$$

Here A is the amplitude coefficient, $Z_0=120\pi$ is the wave impedance of free space, $\alpha=(\pi a/\lambda_0)\sin\theta\cos\varphi$, $\beta=(\pi b/\lambda_0)\sin\theta\sin\varphi$, λ_0 is the wavelength in free space, $\lambda_g=\lambda_0\big/\sqrt{1-(\lambda_0/2a)^2}$ is the waveguide wavelength.

Let us now consider the electric-field component $E_x(P)$ that appears in equations (1) and (5). Substituting into (5) the expressions for $E_\theta(P)$ and $E_\varphi(P)$ given by equations (6) and (7), and omitting the intermediate steps, we can write the result in the following final form:

$$E_x(P) = E_\theta(P)\cos\varphi\cos\theta - E_\varphi(P)\sin\varphi = -D\frac{\lambda_0}{\lambda_g}\sin\varphi\cos\varphi\sin^2\theta, \tag{8}$$

where

$$D = AZ_0\frac{a^2 b}{\lambda_0^2}\frac{\cos\alpha}{\alpha^2-(\pi/2)^2}\cdot\frac{\sin\beta}{\beta}. \tag{9}$$

The expressions for the components of the electric field E_y and E_z, which appear in (1), (5), have the following form

$$E_y(P) = E_\varphi(P)\cos\varphi + E_\theta(P)\sin\varphi\cos\theta = D\left[\cos^2\varphi\left(\cos\theta+\frac{\lambda_0}{\lambda_g}\right)+\sin^2\varphi\cos\theta\left(1+\frac{\lambda_0}{\lambda_g}\cos\theta\right)\right], \tag{10}$$

$$E_z(P) = -E_\theta(P)\sin\theta = -D\sin\varphi\sin\theta\left(1+\frac{\lambda_0}{\lambda_g}\cos\theta\right). \tag{11}$$

By substituting the obtained expressions for the electric-field components $E_x(P)$, $E_y(P)$ and $E_z(P)$, as defined by equations (8), (10), and (11), into equation (5), we obtain the expression for the electric-field strength at point P in the Cartesian coordinate system, expressed in terms of spherical coordinates, as follows:

$$\vec{E}(P) = \left(-D\frac{\lambda_0}{\lambda_g}\sin\varphi\cos\varphi\sin^2\theta\right)\vec{i} + D\left[\cos^2\varphi\left(\cos\theta+\frac{\lambda_0}{\lambda_g}\right)+\sin^2\varphi\cos\theta\left(1+\frac{\lambda_0}{\lambda_g}\cos\theta\right)\right]\vec{j} - D\sin\varphi\sin\theta\left(1+\frac{\lambda_0}{\lambda_g}\cos\theta\right)\vec{k}. \tag{12}$$

By setting $\varphi = 0$ in equation (12), we obtain an expression that describes the RP of a rectangular aperture of cross-section $a \times b$ excited by the TE_{10} mode in the plane of the magnetic-field vector $\vec{H}$ **(**Fig. 1). Taking this into account, equation (12) can be rewritten in the following form:

$$\vec{E}(H) = D\left(\cos\theta + \frac{\lambda_0}{\lambda_g}\right)\vec{j}\,. \tag{13}$$

Let us now consider equation (9). taking into account the notations introduced above:

$$D = AZ_0\frac{a^2 b}{\lambda_0^2}\cdot\frac{\cos\left[(\pi a/\lambda_0)\sin\theta\cos\varphi\right]}{\left[(\pi a/\lambda_0)\sin\theta\cos\varphi\right]^2 - (\pi/2)^2}\cdot\frac{\sin\left[(\pi b/\lambda_0)\sin\theta\sin\varphi\right]}{\left[(\pi b/\lambda_0)\sin\theta\sin\varphi\right]}$$

Since both the ratio $\sin\left[(\pi b/\lambda_0)\sin\theta\sin\varphi\right]\big/\left[(\pi b/\lambda_0)\sin\theta\sin\varphi\right]$ and $\cos\varphi = 1$ tend to unity at $\varphi \to 0$, we write (9) in its final form

$$D = AZ_0\frac{a^2 b}{\lambda_0^2}\cdot\frac{\cos\left[(\pi a/\lambda_0)\sin\theta\right]}{\left[(\pi a/\lambda_0)\sin\theta\right]^2 - (\pi/2)^2}\,. \tag{14}$$

By substituting equation (14) into equation (13), we obtain:

$$\vec{E}(H) = AZ_0\frac{a^2 b}{\lambda_0^2}\frac{\cos\left[(\pi a/\lambda_0)\sin\theta\right]}{\left[(\pi a/\lambda_0)\sin\theta\right]^2 - (\pi/2)^2}\left(\cos\theta + \frac{\lambda_0}{\lambda_g}\right)\vec{j}\,. \tag{15}$$

An important practical conclusion can be drawn from the analysis of equation (15). The angular dependence of the electric-field strength in the plane of the magnetic-field vector $\vec{H}$ of the TE_{10} mode in a rectangular waveguide of cross-section $a \times b$ is given by the following relation:

$$\cos\left[(\pi a/\lambda_0)\sin\theta\right]\big/\left[(\pi a/\lambda_0)\sin\theta\right]^2 - (\pi/2)^2\,.$$

This relation is valid for in-phase excitation of a rectangular aperture and for an amplitude distribution of the field within it following the law $\cos(\pi x/a)$. The TE_{10} mode exhibits exactly this distribution of the electric-field strength in the aperture, in the plane of the magnetic-field vector $\vec{H}$.

Upon transitioning to scalar quantities and substituting the meridional angle $\theta=0$ into equation (15), the following expression is obtained:

$$E^{\max}(H) = AZ_0\frac{a^2 b}{\lambda_0^2}\cdot\frac{1}{-(\pi/2)^2}\left(1 + \frac{\lambda_0}{\lambda_g}\right). \tag{16}$$

Using equations (15) and (16), we can write an expression that defines the normalized RP of a rectangular aperture of cross-section $a \times b$, excited by the TE_{10} mode, in the plane of the magnetic-field vector $\vec{H}$ (Fig. 1, $x0z$ plane):

$$\frac{E(H)}{E^{\max}(H)} = 20\lg\left[\frac{\cos\left[(\pi a/\lambda_0)\sin\theta\right]}{\left[(\pi a/\lambda_0)\sin\theta\right]^2 - (\pi/2)^2}\left(\cos\theta + \frac{\lambda_0}{\lambda_w}\right)\times\frac{\left(-\pi^2/4\right)}{\left[1 + \left(\lambda_0/\lambda_g\right)\right]}\right]. \tag{17}$$

Let us now set the azimuthal angle $\varphi=\pi/2$ and analyze the RP produced by a rectangular aperture excited by the TE_{10} mode, in the plane of the electric-field vector $\vec{E}$ (Fig. 1, $y0z$ plane). In this case, equation (12) can be rewritten in the following form:

$$\vec{E}(E) = D\cos\theta\left(1 + \frac{\lambda_0}{\lambda_g}\cos\theta\right)\vec{j} - D\sin\theta\left(1 + \frac{\lambda_0}{\lambda_g}\cos\theta\right)\vec{k}\,. \tag{18}$$

In equation (18), the electric-field component E_z is neglected, since this component is zero in a rectangular waveguide operating in the TE_{10} mode. Then, expression (18) can be written as

$$\vec{E}(E)=D\cos\theta\left(1+\frac{\lambda_0}{\lambda_g}\cos\theta\right)\vec{j}\,. \tag{19}$$

When $\varphi=\pi/2$, expression (9) is significantly simplified and takes the form

$$D=AZ_0\frac{a^2b}{\lambda_0^2}\cdot\frac{1}{\left(-\pi^2/4\right)}\cdot\frac{\sin\left[\left(\pi b/\lambda_0\right)\sin\theta\right]}{\left[\left(\pi b/\lambda_0\right)\sin\theta\right]}\,. \tag{20}$$

After substituting (20) into (19) we obtain

$$\vec{E}(E)=AZ_0\frac{a^2b}{\lambda_0^2}\cdot\frac{1}{\left(-\pi^2/4\right)}\cdot\frac{\sin\left[\left(\pi b/\lambda_0\right)\sin\theta\right]}{\left[\left(\pi b/\lambda_0\right)\sin\theta\right]}\times\left[\cos\theta\left(1+\frac{\lambda_0}{\lambda_g}\cos\theta\right)\right]\vec{j}. \tag{21}$$

Expression (21) determines the RP of a rectangular aperture with the TE_{10} mode in the plane of the $\vec{E}$ vector (Fig. 1, the $y0z$ plane). From (21) it is clear that in this plane the RP is determined by the relation

$$\sin\left[\left(\pi b/\lambda_0\right)\sin\theta\right]\Big/\left[\left(\pi b/\lambda_0\right)\sin\theta\right].$$

This behavior of the radiation pattern in the specified plane occurs when a rectangular aperture is excited by a mode with uniform amplitude and phase. The TE_{10} mode exhibits exactly this field distribution.

In (21) set $\theta=0$. Then, transitioning to scalar quantities and taking into account that at $\theta\to 0$ both the ratio $\sin\left[\left(\pi b/\lambda_0\right)\sin\theta\right]\Big/\left[\left(\pi b/\lambda_0\right)\sin\theta\right]$ and $\cos\theta=1$ tend to unity, we write (21) in its final form

$$E^{\max}(E)=AZ_0\frac{a^2b}{\lambda_0^2}\cdot\frac{1}{\left(-\pi^2/4\right)}\cdot\left(1+\frac{\lambda_0}{\lambda_g}\right). \tag{22}$$

Using equations (21) and (22), expression that defines the normalized RP of a rectangular aperture of cross-section $a \times b$, excited by the TE_{10} mode, in the plane of the electric-field vector $\vec{E}$ (Fig. 1, plane $y0z$) can be written:

$$\frac{E(E)}{E^{\max}(E)}=20\lg\left[\frac{1}{\left[1+\left(\lambda_0/\lambda_g\right)\right]}\cdot\frac{\sin\left[\left(\pi b/\lambda_0\right)\sin\theta\right]}{\left[\left(\pi b/\lambda_0\right)\sin\theta\right]}\times\cos\theta\left(1+\frac{\lambda_0}{\lambda_g}\cos\theta\right)\right]. \tag{23}$$

Equations (18) and (24) describe the RP of a rectangular aperture excited by the TE_{10} mode in two mutually perpendicular planes, ($\vec{H}$) and ($\vec{E}$).

We now analyze the RP of a pyramidal horn with transverse aperture dimensions $a_{aperture}\times b_{aperture}$ of 40 × 33 mm^2. The horn transitions into a rectangular waveguide with a cross-section of $a \times b = 7.2 \times 3.4$ mm^2, which supports the propagation of the TE_{10} mode. The external appearance of the horn is shown in Fig. 2. For the RP calculation, we employ equations (17) and (23).

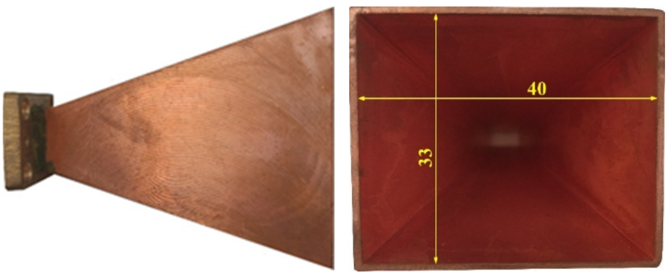

Figure 2. Pyramidal horn

The operating frequency in the K_a-band is chosen within the atmospheric transparency window. To determine this, we use the dependency constructed based on the results reported in [18]. Its behavior is described using an approximate physical model based on the recommendations of ITU-R P.676-12, combined with an absorption continuum model for water vapor and oxygen (Fig. 3).

The figure shows that the minimum atmospheric attenuation occurs in the 30–35 GHz frequency range. The narrow absorption peak at 35.5 GHz corresponds to the water-vapor line, while near 40 GHz the attenuation gradually increases due to the oxygen absorption continuum. Based on these data, the operating frequency was selected as 34 GHz (λ_0 = 8.824 mm). As seen in Fig. 3, the atmospheric attenuation at this frequency is approximately 0.04 dB/km. Using the expression provided above, the wavelength in the rectangular waveguide, λ_g is equal to 11.166 mm (a = 7.2 mm). To construct the RP (Fig. 2) in two mutually perpendicular planes, it is necessary to determine the distance R from the aperture to the far-field zone. This distance is given by the following expression [19]:

$$R \geq 2a_{aperture}^2 / \lambda_0 . \tag{24}$$

Here, $a_{aperture}$ = 40 mm is the larger aperture dimension. The far-field region is of particular interest when analyzing the RP of any antenna, since the angular distribution of the electric field strength in this region is practically independent of the distance from the antenna. For the radiator under consideration, this region can be determined from inequality (24) and begins at a distance of $R \geq 362.647$ mm. For further analysis, a distance of R = 363 mm was selected. Let us now examine the radiation pattern of the pyramidal horn (Fig. 2).

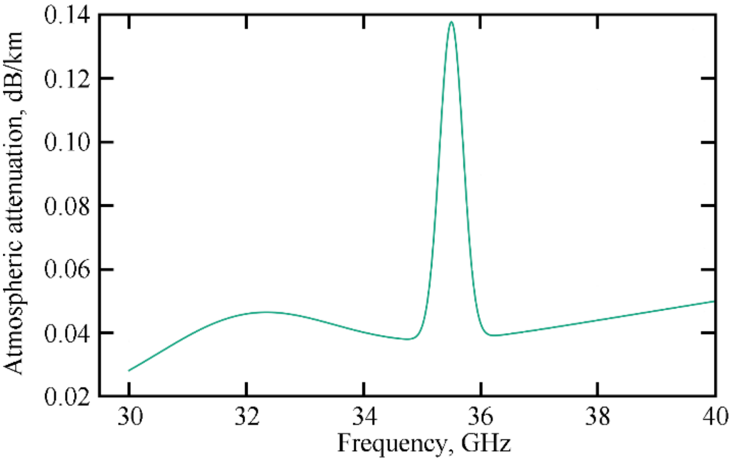

Figure 3. Atmospheric attenuation of electromagnetic radiation in the 30–40 GHz frequency range

In this analysis, we are interested not in the angular dependence itself, but in the cross section of the RP in the $x0z$ plane (the $\vec{H}$ -plane). The meridional angle θ appearing in equation (17) is defined as $\theta = \arctan(x/R)$ (Fig. 1). The calculation results, taking into account this definition, are shown in Fig. 4 ($a_{aperture}$ = 40 mm, red curve). As the next step, the cross section of the pyramidal horn pattern (Fig. 2) was constructed in the $y0z$ plane (the $\vec{E}$ -plane). In this case, the angle $\theta = \arctan(y/R)$ is defined accordingly. The calculation results obtained using equation (24) are presented in Fig. 4 ($b_{aperture}$ = 33 mm, blue curve).

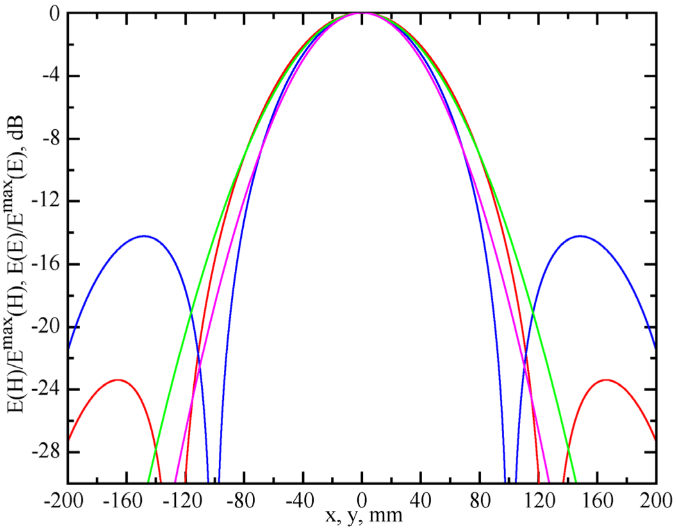

Figure 4. Cross sections of the RP of the pyramidal horn in the image plane

As can be seen, the cross section of the RP of the horn radiator in the image plane of the $\vec{E}$ vector is narrower than that in the $\vec{H}$ -plane. This behavior is explained by the different amplitude variation of the electric field in the aperture of the radiator excited by the TE₁₀ mode along the $x0z$ and $y0z$ planes (Fig. 1). Consequently, the RP of the pyramidal horn (Fig. 2) is not axially symmetric in the far-field region (R = 363 mm). In the $\vec{E}$ -plane, an increase in the side-lobe level is observed: −14.23 dB compared to −23.45 dB in the $\vec{H}$ -plane (Fig. 4). The Gaussian beam radius is determined at the $1/e$ level corresponding to −8.686 dB. Let us compare the RP cross section of the pyramidal horn in the $\vec{H}$ -plane with a Gaussian field distribution. In this plane, the half-width of the main lobe of the RP, determined at the −8.686 dB level, is taken to correspond to the beam radius w of the Gaussian field distribution. The calculated value of w is 78.351 mm (Fig. 4). The Gaussian field distribution is represented in the form $\exp\left(-x^2/78.351^2\right)$, and the results obtained using equation $E_G\left(H\right) = 20\lg\left[\exp\left(-x^2/78.351^2\right)\right]$ are shown in Fig. 4 (green curve). Next, let us compare the RP cross section in the image plane of the $\vec{E}$ vector with the Gaussian field distribution. In this plane, the value of w at the −8.686 dB level is 68.467 mm. The calculation results obtained using equation $E_G\left(E\right) = 20\lg\left[\exp\left(-x^2/68.467^2\right)\right]$ are shown in Fig. 4 (pink curve). As can be seen, up to the level of $20\lg\left[E\left(H\right)/E^{\max}\left(H\right)\right] = -10$ dB, the amplitude distribution of the electric-field component of the pyramidal horn in the far-field region in both the $\vec{H}$ - and $\vec{E}$ -planes coincides with the Gaussian field distribution. The main drawback of such a pyramidal horn is its axially asymmetric RP. This limitation can be mitigated by reducing the aperture dimension $b_{aperture}$.

The paper [20] shows that the condition for negligible diffraction losses in an open resonator supporting oscillations with a Gaussian field distribution is determined by the relation $G = 4w$, where G is the resonator mirror diameter. Therefore, the condition for negligible diffraction losses during the incidence of a Gaussian beam on an optical element with the specified dimensions in the $\vec{H}$ -plane is satisfied if the beam diameter is at least 313.4 mm. This plane is considered because its RP cross section in the image plane is larger. As can be seen, this is a rather large diameter for the K_a-band. To reduce it, the size of the wide side of the pyramidal horn $a_{aperture}$ must be increased. However, doing so leads to an increase in the parameter R according to inequality (24) and, consequently, to an increase in the Gaussian beam radius. Therefore, a reasonable compromise between these parameters is required.

Fig. 5 shows cross sections of the RP of the pyramidal horn in the image plane of the $\vec{H}$ vector for the TE_{10} mode of a rectangular aperture at three values of the wide-side dimension: $a_{aperture}$ = 40 mm (R = 363 mm, red curve), $a_{aperture}$ = 50 mm (R = 567 mm, blue curve), and $a_{aperture}$ = 60 mm (R = 816 mm, green curve).

It can be seen from the figure that the Gaussian spot diameter increases as the value of $a_{aperture}$ increases. It is also evident that enlarging the dimension $a_{aperture}$ makes it impossible to achieve an axially symmetric field distribution.

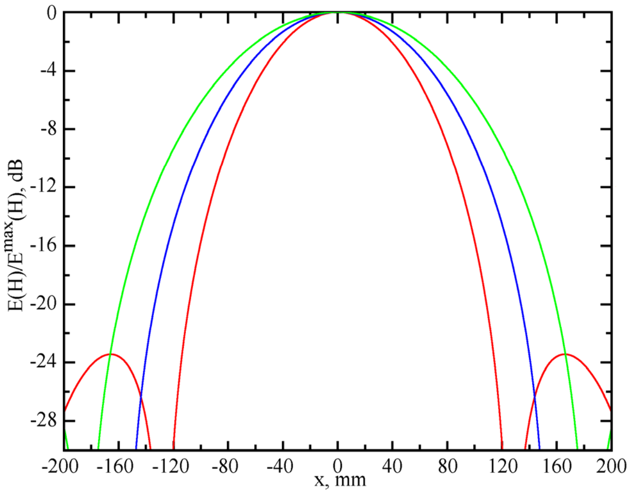

Figure 5. Cross sections of the RP of the pyramidal horn in the image $x0z$ plane for increasing values of the wide side $a_{aperture}$

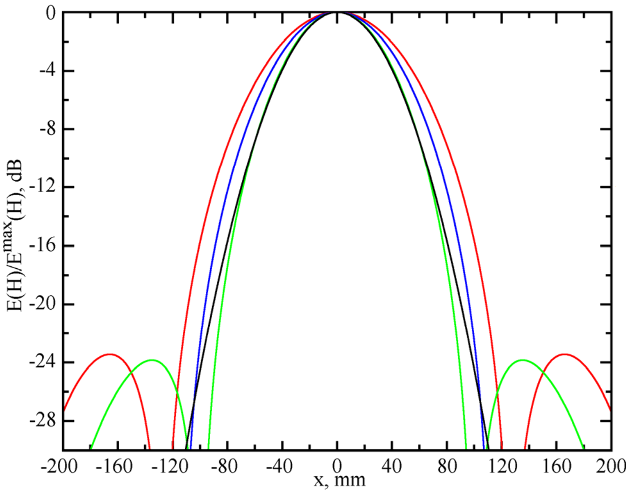

Figure 6. Cross sections of the RP of the pyramidal horn in the image $x0z$ plane for decreasing values of the wide side $a_{aperture}$

Let us now consider the case when the larger side of the rectangular aperture $a_{aperture}$ is reduced. The calculation results in the plane of the $\vec{H}$ vector, obtained using expression (18), are presented in Fig. 6. The cross-sections of the RP in the image plane are shown for the following cases: $a_{aperture}$ = 40 mm (R = 363 mm, red curve); $a_{aperture}$ = 35 mm (R = 278 mm, blue curve); and $a_{aperture}$ = 30 mm (R = 204 mm, green curve). It is clearly seen that as $a_{aperture}$ decreases, the RP becomes narrower in the far-field region. This occurs due to the corresponding decrease of the parameter R (see (24)). Let us now compare the field distribution in the $\vec{H}$ -plane for $a_{aperture}$ = 30 mm with the Gaussian distribution. As before, the field spot radius w is determined at the –8.686 dB level and is equal to 59.527 mm (Fig. 6). The distribution of the electric field component according to the Gaussian law $E_G(H) = 20\lg\left[\exp\left(-x^2/59.527^2\right)\right]$, is shown in Fig. 6 (black curve). It follows from the figure that the cross-section of the RP in the image $\vec{H}$ -plane when $E_G(H) = 20\lg\left[\exp\left(-x^2/59.527^2\right)\right]$ = 30 mm coincides with the Gaussian field distribution down to approximately the –10 dB level. This result confirms the earlier conclusion that the RP of a rectangular aperture in the $\vec{H}$ - and $\vec{E}$ -planes exhibits an electric field distribution that agrees with the Gaussian one up to the –10 dB level.

Let us determine the required diameter of the optical element placed at a distance of R = 204 mm from the aperture (in the Fraunhofer zone). The condition for negligible diffraction losses of a Gaussian beam incident on the optical element will be satisfied if the beam diameter equals 4w=238.084 mm [20]. Therefore, the optical element diameter is chosen to be 240 mm. It follows that, in this case, the optical element also has considerable geometric dimensions in the K_a-band, approximately 27λ_0.

To obtain an axially symmetric distribution of the electric field component in the far-field region at a distance of 204 mm from the aperture ($a_{aperture}$ =30 mm), it is necessary to reduce the size of its narrow side $b_{aperture}$. The results of the calculations in the plane of the E-vector, performed in accordance with (23), are presented in Fig. 7. The red curve corresponds to the RP cross-section in the H-plane ($a_{aperture}$ =30 mm). As can be seen from Fig. 7, side lobes appear in the RP cross-section, with an amplitude of –23.85 dB. When the narrow side of the pyramidal horn is reduced to $b_{aperture}$ =21.539 mm, the RP cross-section in the E-plane (blue curve) at a distance of 204 mm from the aperture increases to the –12 dB level and practically coincides with the RP cross-section in the H-plane. This correspondence holds for the main lobe of the RP. The side-lobe level for this value of $b_{aperture}$ decreases to –15.73 dB, compared to –14.23 dB for $b_{aperture}$ =33 mm (see Fig. 4).

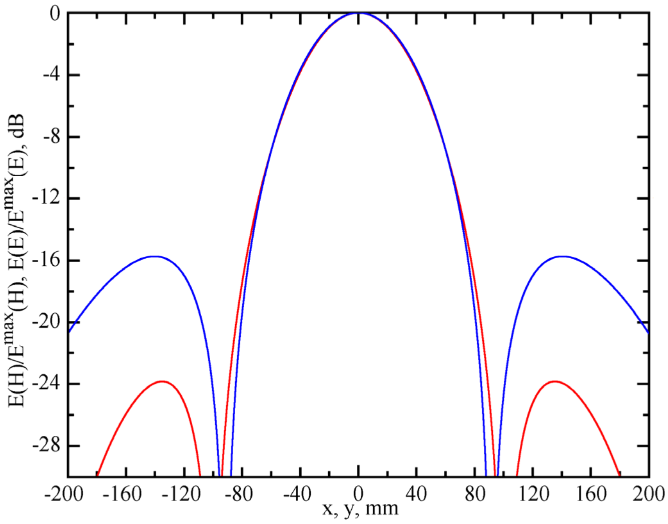

Figure 7. Cross sections of the RP of the pyramidal horn in the $x0z$ and $y0z$ planes when the aperture dimension was decreased down to $b_{aperture}$ = 21.539 mm

The calculations were performed under the assumption that the TE$_{10}$ mode exists in both the aperture and the waveguide. The electric field distribution of this mode in the aperture, in the $x0z$ plane (Fig. 1), must be in phase. The length of the horn radiator should therefore be chosen to ensure the required phase distribution across the aperture.

The maximum phase error in the aperture is determined by the geometric dimensions of the horn. Its permissible value must satisfy the following condition [19]:

$$\zeta_{\max} = \frac{\pi a^2_{aperture}}{4\lambda_0 R_H} \le \frac{3}{4}\pi , \qquad (\vec{H}\text{ -plane}) \qquad (25)$$

$$\xi_{\max} = \frac{\pi b^2_{aperture}}{4\lambda_0 R_E} \le \frac{\pi}{2} . \qquad (\vec{E}\text{ -plane}) \qquad (26)$$

Here: R_H and R_E are the distances from the aperture to the point where the edges of the horn converge in the planes of the $\vec{H}$ and $\vec{E}$ vectors of TE$_{10}$ mode in the waveguide.

On the other hand, the quantities R_H and R_E are related to the aperture dimensions $a_{aperture}$, $b_{aperture}$ and to the waveguide dimensions a, b by the relation [19]:

$$\frac{R_H}{R_E}=\frac{a_{aperture}}{b_{aperture}}\cdot\frac{\left(b_{aperture}-b\right)}{\left(a_{aperture}-a\right)}. \tag{27}$$

From inequality (24) it follows that $R_H \geq 34$ mm that allows us to select R_H=40 mm. The cross sections of the rectangular waveguide and of the radiating aperture are $a \times b$ = 7.2 × 3.4 mm^2 and $a_{aperture} \times b_{aperture}$ =30×21.539 mm respectively. Then, from (27), it follows that R_E=36 mm that satisfies inequality (26).

Let us estimate the reflection coefficient from the designed radiator. This is necessary to determine what fraction of the generator power is actually radiated into free space. In general, reflection in such a radiator occurs at two regions: at the aperture itself ($\dot{\Gamma}_{aperture}$) and at its neck ($\dot{\Gamma}_{neck}$). The reflection coefficient at the aperture, $\dot{\Gamma}_{aperture}$, is a complex quantity whose magnitude and phase depend on the aperture dimensions. As shown in [17, 19], with increasing aperture size, the magnitude of the reflection coefficient decreases, and the phase difference between the aperture center and the edge decreases. For apertures with dimensions of several wavelengths, $\dot{\Gamma}_{aperture}$ can be considered approximately zero. This condition is satisfied for the rectangular aperture under consideration, where $a_{aperture}$ =30 mm (≈3.4 λ_0) and $b_{aperture}$ =21.539 mm (≈2.45 λ_0).

To determine the magnitude of the reflection coefficient of the designed radiator, the following relation is used:

$$\left|\dot{\Gamma}_{aperture}\right|=\left[1-(\gamma/k)\right]/\left[1+(\gamma/k)\right], \tag{28}$$

where $\gamma=2\pi\sqrt{1-\left(\lambda_0/2a_{aperture}\right)^2}\Big/\lambda_0$ is the propagation constant in a rectangular waveguide whose cross-section is equal to the aperture of the horn ($a_{aperture}$ =30 mm), $k=2\pi/\lambda_0$.

The calculation using (28) at a frequency of 34 GHz (λ_0=8.824 mm) resulted in $\left|\dot{\Gamma}_{aperture}\right|$=0.006. Therefore, reflection from a rectangular aperture can be neglected.

Let us now estimate the fraction of the generator power reflected from the neck (phase focus) of the radiator under consideration. The absolute value of the reflection coefficient at the neck $\left|\dot{\Gamma}_{neck}\right|$ can be determined from the following expression [19]:

$$\left|\dot{\Gamma}_{neck}\right|=\left(Z_{equiv}-1\right)/\left(Z_{equiv}+1\right), \tag{29}$$

where

$$Z_{equiv}=1+\frac{1}{a\left(2\pi/\lambda_w\right)\mathrm{ctg}\alpha_0\left(1-\left(\lambda_0/2a\right)^2\right)}-\frac{1}{b\left(2\pi/\lambda_w\right)\mathrm{ctg}\beta_0},$$

$2\alpha_0$ and $2\beta_0$ are the radiator aperture angles in the $\vec{H}$ and $\vec{E}$ planes, respectively; $\alpha_0=\arctan\left(\left(a_{aperture}/2\right)/R_H\right)$, $\beta_0=\arctan\left(\left(b_{aperture}/2\right)/R_E\right)$. For the given dimensions $Z_{equiv}=0.991$ and $\left|\dot{\Gamma}_{neck}\right|=0.005$ and therefore, reflections from both the aperture and the neck can be neglected. This indicates that almost all of the source power is radiated into free space, i.e., a traveling-wave regime is established in the waveguide section.

3. EXPERIMENTAL STUDY

To verify the above calculations, an experimental study was conducted using two pyramidal horns, one of which is shown in Fig. 2. The dimensions of the second radiator which appearance is shown in Fig. 8 were chosen based on the theoretical analysis of the rectangular aperture.

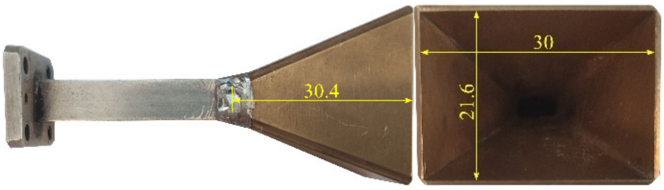

Figure 8. Pyramidal horn with a rectangular waveguide section

Let us consider a horn with rectangular aperture dimensions $a_{aperture}\times b_{aperture}$ =40×33 mm. Using a panoramic VSWR meter R2-65, the VSWR in the waveguide section loaded with this pyramidal horn was measured in the 33–35 GHz frequency range. The measurement results are presented in Fig. 9.

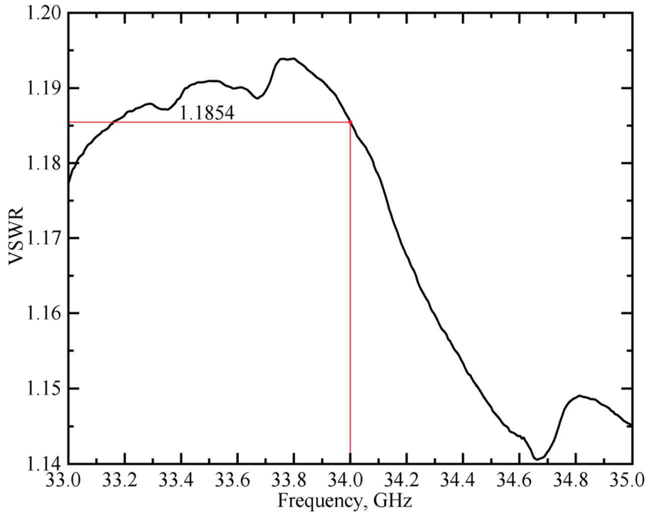

Figure 9. Dependence of the VSWR on frequency in the waveguide section loaded with a rectangular horn having aperture dimensions of 40×33 mm

As can be seen from the figure, at a frequency of 34 GHz the VSWR is 1.1854, which corresponds to a field reflection coefficient from the given aperture of $\Gamma = 0.0848$. The obtained result is in good agreement with the results of [17, 19], where it was shown that the reflection from a rectangular aperture can be neglected if its dimensions exceed several wavelengths.

To measure the RP cross-section of the pyramidal horn in the image plane, an experimental setup was assembled, the block diagram of which is shown in Fig. 10.

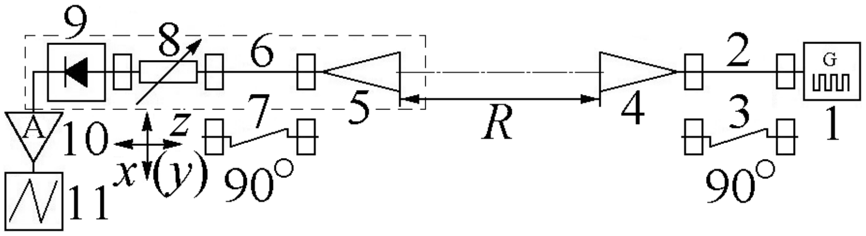

Figure 10. The experimental setup block diagram

As the source 1 of 34 GHz radiation, a high-frequency signal generator G4-156 was used. The main parameters of this generator are as follows: frequency range 29.95–37.5 GHz; output power not less than 5 mW; frequency setting error ±1%. To expand the dynamic range, the output signal was modulated by a rectangular waveform (square wave) with a frequency of 1 kHz.

Between the generator and the investigated horn 4, a 60 mm long section of rectangular waveguide 2 was inserted. In this configuration, the setup makes it possible to measure the RP cross-section of the pyramidal horn in the image plane of the $\vec{H}$ vector of the TE$_{10}$ mode in the waveguide, i.e., in the $x0z$ plane. The receiving path includes: a receiving horn 5, a section of rectangular waveguide 6 identical to the section 2, a polarization attenuator 8, and a detector section 9. The signal from the detector is fed to a resonant amplifier 10 tuned to a frequency of 1 kHz. An oscilloscope 11 is used for visual monitoring of the signal level. Both pyramidal horns 4 and 5 have identical apertures of 40×33 mm. For the investigated horn, the distance R determining the far-field region is 363 mm. The part of the measuring setup enclosed by the dashed line in Fig. 10 allows the receiving horn to be moved along the z-axis over a range of ±25 mm and along the x-axis over a range of ±80 mm.

The results of measuring the RP cross-section of horn 4 in the image plane of the $\vec{H}$ vector are presented in Fig. 11. The experimental values are shown by green circles. The figure also presents the theoretically calculated RP cross-section in the same plane for a horn of the specified dimensions, obtained using formula (17) (red curve).

As can be seen from the figure, there is good agreement between the calculated and measured cross-sections of the RP.

To measure the RP cross-section of horn 4 in the image plane of the $\vec{E}$ vector (the $y0z$ plane), it is necessary to replace the waveguide sections 2 and 6 with 90° waveguide twists 3 and 7 of the same length (Fig. 10). The measurement results are shown in Fig. 12. As in the previous case, good agreement is observed between the measured (green circles) and the calculated, according to formula (23), (blue curve) RP cross-sections in the image plane of the $\vec{E}$ vector.

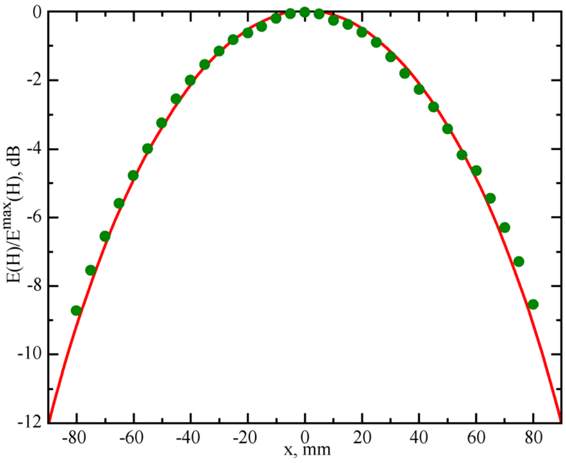

Figure 11. The measured RP cross-section of the pyramidal horn having aperture dimensions of 40×33 mm in the image plane *x*0*z*

From the presented figures, it follows that the RP cross-section of the considered pyramidal horn in the *x*0*z* image plane at the –8.7 dB level (corresponding to the Gaussian field distribution) is wider than in the *y*0*z* image plane. In this case, these cross-sections are 160 mm and 140 mm, respectively. Thus, the experimental results confirm the theoretical conclusion that the pyramidal horn with an aperture of 40×33 mm^2 has an axially asymmetric radiation pattern. In the previous section, a pyramidal horn was designed to provide an axially symmetric RP in the far-field region (Fig. 8).

Using a panoramic VSWR meter R2-65, the VSWR was measured in a waveguide line loaded with a pyramidal horn having an aperture of 30×21.6 mm^2 in the same frequency band. The measurement results are shown in Fig. 13.

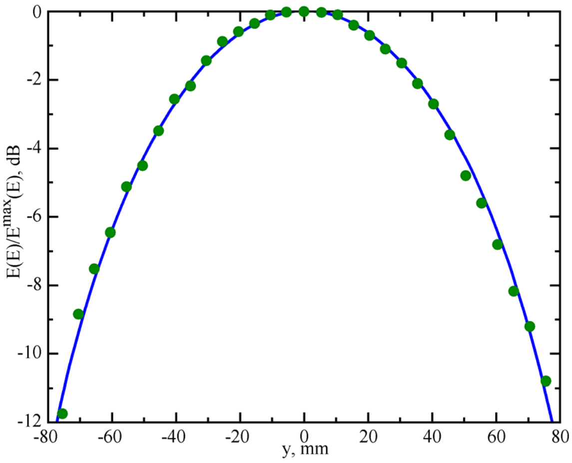

Figure 12. The measured RP cross-section of the pyramidal horn having aperture dimensions of 40×33 mm^2 in the image plane *y*0*z*

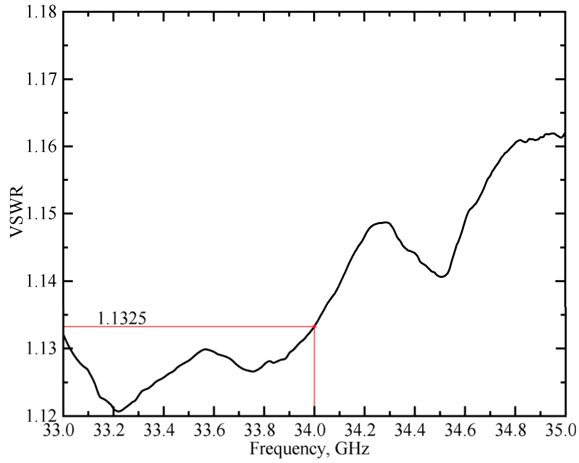

Figure 13. The measured VSWR dependence on frequency in the waveguide line loaded with a rectangular horn having an aperture size of 30×21.6 mm^2

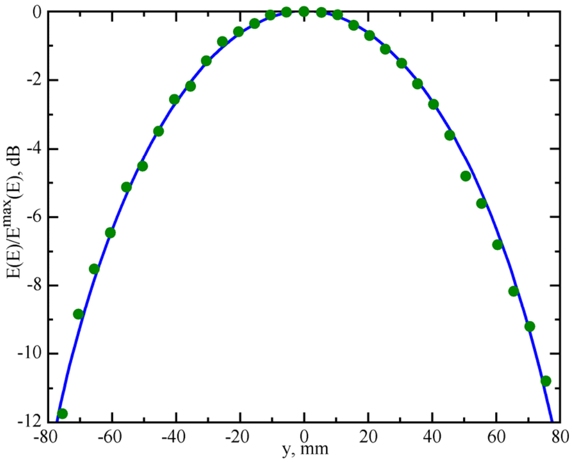

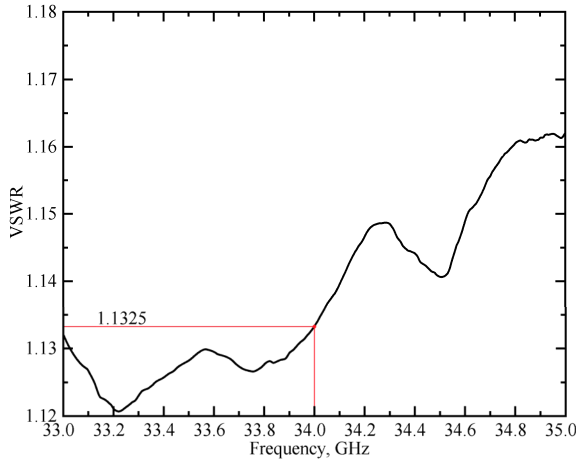

Figure 12. The measured RP cross-section of the pyramidal horn having aperture dimensions of 40×33 mm^2 in the image plane *y*0*z*

Figure 13. The measured VSWR dependence on frequency in the waveguide line loaded with a rectangular horn having an aperture size of 30×21.6 mm^2

As can be seen from the figure, in this case, at a frequency of 34 GHz, the VSWR = 1.1325, which corresponds to a field reflection coefficient of $\Gamma = 0.0621$. The obtained result correlates well with the calculated data for this horn presented in the previous section. Thus, the reflection from the aperture of such a radiator can be neglected.

Now let us consider the RP cross-section of this horn in the image plane. To carry out the measurements on the experimental setup, horn 4 was replaced with the test radiator having the specified aperture dimensions. For this horn, the distance R=204 mm. Instead of the receiving horn 5, an open end of a rectangular waveguide with a cross-section of 7.2×3.4 mm^2 was placed at the specified distance. The results of the radiation pattern cross-section measurements in the image plane of the $\vec{H}$ -vector of the TE_{10} mode in waveguide 2 are shown in Fig. 14.

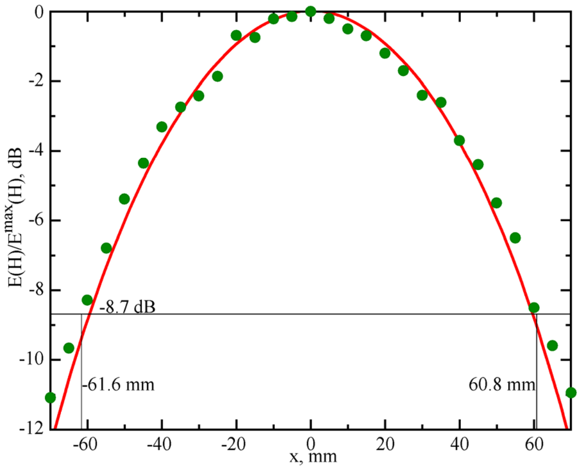

Figure 14. The measured RP cross-section of the pyramidal horn having aperture dimensions of 30×21.6 mm^2 in the image plane $x0z$

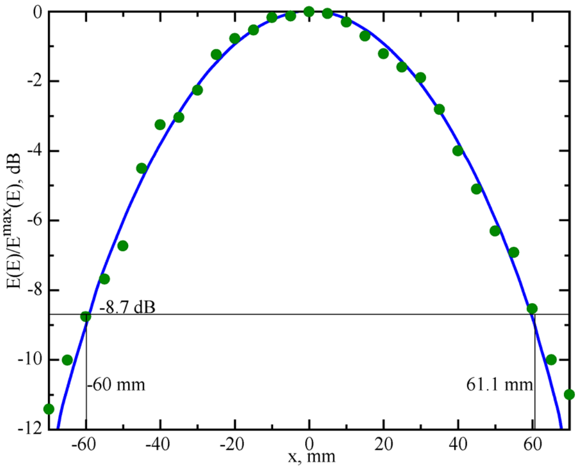

Figure 15. The measured RP cross-section of the pyramidal horn having aperture dimensions of 30×21.6 mm^2 in the image plane $y0z$

From the figure, a good agreement can be seen between the measured RP cross-section in the specified image plane (green circles) and the one calculated using formula (18) (red curve). At the –8.7 dB level (corresponding to the Gaussian field distribution), the radiation pattern cross-section width is 122.4 mm. For comparison, let us consider the RP cross-section of the rectangular aperture in the picture plane of the $\vec{E}$ vector. As in the previous case, the waveguide sections 2 and 6 are replaced with 90° waveguide twists 3 and 7 of the same length (see Fig. 10). The measurement results are shown in Fig. 15. In this case, there is also good agreement between the experimentally measured and the calculated radiation pattern cross-sections in the image plane $y0z$. The RP cross-section width at the –8.7 dB level is 121.1 mm. Thus, the designed pyramidal horn produces an axially symmetric radiation pattern in the far-field region. However, using such a pyramidal horn for the intended purpose is impractical due to the large field spot size at the –8.7 dB level in the far-field region. In this case, to ensure negligible diffraction losses when a Gaussian beam is incident on the flat face of the axicon, its diameter must be approximately1 240 mm. This represents unreasonably large geometric dimensions of the optical element in the K_a-band.

4. CONCLUSIONS

The studies of the rectangular aperture performed in the first part of the paper make it possible to draw several important practical conclusions.

1. By varying the aperture dimensions $a_{aperture} \times b_{aperture}$, it is always possible to obtain an axially symmetric radiation pattern of such a radiator in the far-field region. This is due to the linear distribution of the electric field in the aperture.
2. Up to the –8.7 dB level, the radiation pattern cross-sections of such a radiator in two mutually perpendicular planes coincide with the Gaussian field distribution.
3. Depending on the specific application, it is always necessary to find a compromise between the aperture dimensions $a_{aperture} \times b_{aperture}$ and the distance R to the far-field region.
4. For the chosen geometric dimensions of rectangular apertures in the K_a-band, a traveling-wave regime is established in the waveguide section.
5. In the K_a-band, the optical element must have large geometric dimensions (~$27\lambda_0$) in order to minimize diffraction losses when a Gaussian beam is incident on its flat surface. Therefore, when using a rectangular aperture with an axially symmetric radiation pattern in the far-field region and an acceptable distance $R = (20 \div 23)\lambda_0$, the geometric dimensions of the axicon become unreasonably large.
6. It is of practical interest to consider radiating apertures of other shapes that would allow obtaining narrower radiation pattern cross-sections in the far-field region.

Acknowledgement

This work was supported by the National Research Foundation of Ukraine (Project No. 2025.06/0011).

ORCID

I.K. Kuzmychov, https://orcid.org/0000-0002-6870-5491; **O.A. Voitovych,** https://orcid.org/0000-0001-7530-5149; **O.S. Lukash,** https://orcid.org/0009-0008-2408-3644; **E.M. Khutoryan,** https://orcid.org/0000-0002-0727-7753; **V.P. Maltsev,** https://orcid.org/0009-0002-7523-7603

REFERENCES

[1] Y. Dewen, T. Yan, C. Changhua, Z. Feng, and H. Lei, High Power Laser and Particle Beams, **37** (2025). https://doi.org/10.11884/HPLPB202537.240374
[2] S. Mumtaz, H.S. Uhm, and E.H. Choi, Physics Reports, **1069**, 1 (2024). https://doi.org/10.1016/j.physrep.2024.03.003
[3] C.-H. Zhan, T.-M. Li, L. Meng, Z.-H. Li, Y. Wu, and J.-B. Shao, Acta Phys. Sin. **63**, 238405 (2014). https://doi.org/10.7498/aps.63.238405
[4] Y. Xu, Review of the high-power vacuum tube microwave sources, arXiv:2003.04288 [physics.plasm-ph] (2024).
[5] E. Negri, W. Fuscaldo, P. Burghignoli, and A. Galli, Micromachines, **13**, 2230 (2022). https://doi.org/10.3390/mi13122230
[6] Z. Yu, and W.B. Dou, Prog. Electromagn. Res. **93**, 205 (2009). https://doi.org/10.2528/PIER09032303
[7] H. Huang, and Y. Yu, Acta Tech. **62**, 107 (2017).
[8] S. Monk, J. Arlt, D.A. Robertson, J. Courtial, and M.J. Padgett, Opt. Commun. **170**, 213 (1999). https://doi.org/10.1016/S0030-4018(99)00297-7
[9] H. Meng, B. Xiang, J. Zhang, W. Dou, and Y. Yu, J. Infrared Millim. Terahertz Waves, **35**, 208 (2014). https://doi.org/10.1007/s10762-013-0044-3
[10] V. Jarutis, R. Paskauskas, and A. Stabinis, Opt. Commun. **184**, 105 (2000). https://doi.org/10.1016/S0030-4018(00)00945-4
[11] S. Cabrini, C. Liberale, D. Cojoc, A. Carpentiero, M. Prasciolu, S. Mora, V. Degiorgio, *et al.*, Microelectr. Engineer. **83**(4-9), 804-807 (2006). https://doi.org/10.1016/j.mee.2006.01.247
[12] M. Ettorre, S. Pavone, M. Casaletti, M. Albani, A. Mazzinghi and A.Freni, *Aperture Antennas for Millimeter and Sub-Millimeter Wave Applications*, (Springer, Cham, 2017). https://doi.org/10.1007/978-3-319-62773-1_8
[13] Z. Zhai, Z. Cheng, Q. Lv, and X. Wang, Appl. Sciences, 10(15), 1-11 (2020). https://doi.org/10.3390/app10155127
[14] J. Dudutis, M. Mackevičiūtė, J. Pipiras, R. Stonys, V. Stankevič, G. Račiukaitis, and P. Gečys, Opt. Express, **30**(2), 1860-1874 (2022). https://doi.org/10.1364/OE.447035
[15] C. Lyu, M. R. Belić, Y. Li, and Y. Zhang, Optics & Laser Technology, **164**, 109548 (2023). https://doi.org/10.1016/j.optlastec.2023.109548
[16] M. Eskandari, M. Joodaki, and A.R. Attari, arXiv:2408.03333 [physics.app-ph], 1-11 (2024). http://dx.doi.org/10.1109/TMTT.2024.3449650
[17] R. Kühn, *Mikrowellenantennen*, (VEB Verlag Technik, Berlin, 1964).
[18] J.R. Pardo, J. Cernicharo, and E. Serabyn, IEEE Trans. Antennas Propag., **49**(12), 1683-1694 (2001). http://dx.doi.org/10.1109/8.982447
[19] C.A. Balanis, *Antenna Theory: Analysis and Design*, 3rd ed. (Wiley, Hoboken, NJ, 2005). https://doi.org/10.1002/0471654507
[20] D. Gloge, *Proceedings of the symposium on quasi-optics*, (Polytechnic Press, Brooklyn, 1964).

ОТРИМАННЯ АКСІАЛЬНО-СИМЕТРИЧНОГО РОЗПОДІЛУ ПОЛЯ З ВИКОРИСТАННЯМ ПРЯМОКУТНИХ АПЕРТУРНИХ ВИПРОМІНЮВАЧІВ

І.К. Кузьмичов[1], О.А. Войтович[1], О.С. Лукаш[1], Е.М. Хуторян[1], В.П. Мальцев[1], О.В. Май[2]
[1]Інститут радіофізики та електроніки ім. О. Я. Усикова НАН України,вул. Ак. Проскури 12., Харків, 61085, Україна
[2]ТОВ "Актокс Україна", вул. І. Гонти, 1, Київ, 04112, Україна

У роботі з використанням апертурного методу досліджено випромінювання з відкритого кінця прямокутного хвилеводу. Отримано вирази, що описують діаграму спрямованості (ДС) такої апертури в дальній зоні у двох взаємно перпендикулярних площинах. Для конкретних розмірів двох прямокутних апертур 40×33 мм та 30×21,6 мм проведено чисельні дослідження перерізів ДС у картинній площині за змінних ширини та довжини сторін розкривів. Зроблено порівняння отриманих перерізів ДС з Гаусовим розподілом поля та встановлено, що до рівня -11 дБ, перерізи ДС в обох картинних площинах практично збігаються з Гаусовим розподілом поля. Це особливо важливо під час падіння хвильового пучка на плоску грань аксікону. При зміні розміру вузької сторони прямокутної апертури можна отримати аксіально-симетричну ДС. Проведено експериментальні дослідження цих прямокутних апертур у K_a діапазоні. Показано гарний збіг експериментальних результатів із розрахунковими даними. Встановлено, що якщо геометричні розміри прямокутної апертури перевищують дві довжини хвилі, то в хвилеводному тракті встановлюється режим біжучої хвилі. Експериментально виявлено, що амплітудний розподіл поля обох апертур у дальній зоні до рівня −8,7 дБ збігається з Гауссовим розподілом поля. Показано, що для опромінення плоскої грані аксікону хвильовим пучком використовувати прямокутні апертури не доцільно.

Ключові слова: *апертурний метод; K_a діапазон; прямокутна апертура; діаграма спрямованості; Гауссовий розподіл поля; аксікон*

EAST EUROPEAN JOURNAL OF PHYSICS. 2. 541-553 (2026)
DOI:10.26565/2312-4334-2026-2-61 ISSN 2312-4334

ESTIMATION OF THE GAMMA EXPOSER RATE CONSTANT FOR CLINICALLY RELEVANT RADIONUCLIDES IN NUCLEAR MEDICINE USING GATE/GEANT4 MONTE CARLO SIMULATION

Abdulkhaleq O. Jaralah[1], **Alaa M. Elgohary**[1], **Monira M. Rageh**[1], **Magdy M. Khalil**[2,3]
[1]Department of Biophysics, Faculty of Science, Cairo University, Egypt
[2]Medical Biophysics, Department of Physics, Faculty of Science, Helwan University
[3]School of Applied Health Sciences, Badr University in Cairo (BUC), Cairo, Egypt
**Corresponding Author E-mail: magdy_khalil@hotmail.com*

Received March 4, 2026; revised April 15, 2026; accepted May 20, 2026

Purpose. To establish a reliable computational method for calculating external radiation dose rates from nuclear medicine patients using Monte Carlo simulation and to systematically evaluate the effects of phantom geometry and detector characteristics on occupational exposure. **Methods:** MC GATE simulations version 9.1 (Geant4 10.7) calculated external dose rate constants for most clinical radionuclides: ^{99m}Tc, ^{67}Ga, ^{18}F, ^{11}C, ^{131}I, and ^{123}I. Two phantoms were used, one with dimensions of (25×15×20, 30×20×25, and 35×25×30 cm^3), and the other with a fixed length of 170 cm and variable width (15×20, 20×25, and 25×30 cm^3), specific to the ^{99m}Tc nuclide. Detector sizes (3×3×3 to 10×10×10 cm^3) were evaluated at distances of 1, 2, and 3 m. Different detector media (air, argon, and neon) were assessed for photon sensitivity. The results were compared with experimental data. **Results:** Simulated results agreed with experimental data within ±10%. Argon demonstrated superior sensitivity compared with air and neon detector media. Phantom dimensions increased overall, resulting in a 36.8% reduction due to self-attenuation. Radionuclides of ^{18}F and ^{11}C, followed by ^{67}Ga, ^{131}I, ^{123}I, and ^{99m}Tc, posed the highest occupational exposure hazard. Patient body thickness was a more significant attenuation factor than patient height. **Conclusion:** GATE/Geant4 simulations provide a reliable and accurate tool for evaluating external dose rates in nuclear medicine departments. These findings underscore the importance of using appropriate detector sizes and media, as well as realistic patient geometry, in occupational dose assessments and provide essential data to improve radiation protection protocols.

Keywords: *External dose rate; Nuclear Medicine; Radiation Protection; Monte Carlo simulation; Gamma rate constant*
PACS: 02.70.Uu, 07.05Tp

1. INTRODUCTION

Nuclear medicine is an important medical specialty that uses radioactive substances for diagnostic and therapeutic procedures [1]. Fluorodeoxyglucose (F18-FDG) has a specific role in clinical oncology for patient stratification, diagnosis, staging, restaging, and management [2]. Technetium (^{99m}Tc) is the workhorse of most nuclear medicine examinations in the diagnosis of many diseases, including orthopedic, cardiac, urological, endocrine, and other pathologies [1]. Gallium-67 (67Ga) has been used to image inflammation and infection, as well as various solid neoplasms, particularly lymphomas [3].

An iodine-131 (131I) and iodine-123 (^{123}I) nuclide scan is a noninvasive imaging procedure used to detect metastatic thyroid cancer and assess the remaining thyroid tissue after thyroidectomy and thyroid cancer treatments [4,5]. The carbon-11 (^{11}C) nuclide makes an ideal non-invasive option for targeted labeling molecules in PET imaging [6].

After patients are injected with radiopharmaceuticals, they become a source of contamination, emitting ionizing radiation to those who come into contact with them [7].

Each radiation exposure in nuclear medicine, even if minimal, potentially carries an inherent risk. This risk, primarily the potential for genetic alterations or malignancies, requires careful use of radionuclides by medical staff when administering pharmaceuticals [8].

The reduction of occupational exposure is by the ALARA acronym, which stands for “As Low As Reasonably Achievable” principles, optimizing dose in any work that includes radiation exposure. This crucial endeavor in radiation safety helps reduce occupational exposure. ALARA encapsulates the obligation to avoid unnecessary radiation exposure, emphasizing that any exposure should be clinically indicated and provide a direct benefit to the ALARA principles, which manifest through three essential strategies (Time, Distance, Shielding), each designed to reduce radiation exposure consistently, which are dependent on precise dose rate [9]. The exposure dose rate constant (Γ) is essential in dosimetry for estimating dose rate at distance (usually at 1 m from the source) to ensure a safe environment and monitoring, by ICRP and IAEA [10,11]

The International Commission on Radiological Protection (ICRP) has established a radiation dose rate of 20 μSv h^{-1} at a distance of 1m from the patient as one of the criteria for discharging patients after injection with radioactive isotopes [12].

Some researchers have adopted a dose calculation method whereby radioactivity within the patient, as a point source, is subject to the inverse-square law, and the physical half-life is taken into account instead of the effective half-life [13,14].

Cite as: A.O. Jaralah, A.M. Elgohary, M.M. Rageh, M.M. Khalil, East Eur. J. Phys. 2, 541 (2026), https://doi.org/10.26565/2312-4334-2026-2-61

Monte Carlo simulation has emerged as a prominent tool in radiation protection and dosimetry, capable of simulating complex scenarios that are otherwise infeasible due to ethical or spatial constraints. One such Monte Carlo simulation platform, specializing in nuclear medicine, is GATE (GEANT4 Application to Tomographic Emission). Based on the Geant4 (GEometry ANd Tracking) libraries, it offers a scripting interface with numerous advantages for simulating SPECT and PET systems. It boasts high performance in measuring internal and external radiation doses [15].

Despite previous studies investigating external radiation exposure from nuclear medicine patients using MCNP simulation, a clear lack of understanding persists. Simple geometry was used to calculate dose rates, employing a point source without any attenuation to ensure realism. This leads to significant overestimation of dose rates, especially at short distances. While some studies have suggested simulating linear or point sources to improve exposure accuracy, systematic evaluation of the impact of patient dimensions, such as thickness and height, remains limited [15,16]. In the Soares et al. 2018 study, which used MCNPX and employed anthropomorphic voxel phantoms based on ICRP-110, although the study was comprehensive, it did not assess the dose rate on the effect of anatomical differences, such as variations in height and width [18].

This focused on the need to use Monte Carlo simulation to assess the impact of phantom geometry and varying distances between the source and detector, comparing dose rates between the bare source and the phantom to better support radiation protection and enhance the safety of workers and the public.

This study aimed to use the Geant4/Gate Monte Carlo simulation to calculate dose rates for most radionuclides employed in nuclear medicine by systematically varying phantom dimensions and detector-phantom distances, and employing different detector media (air, argon, and neon) to evaluate detector media and responses on dose rate values.

2. MODELING AND METHODS

2.1 GATE simulation setup

The simulations were performed using GATE (version 9.1) installed in combination with Geant4 (version 10.7) [19]. The simulation was run on an HP laptop with an Intel Core i5-7Y54 processor and 8 GB of RAM. The GATE was operated on an Ubuntu Oracle virtual machine hosted on a Windows 10 Pro operating system.

2.2 World Geometry

In the MC GATE simulation, a cubic environment with equal dimensions of 6×6×6 m^3 was created and filled with air, as specified in the GateMaterials database. These dimensions were chosen to ensure accurate and complete containment and tracking of primary and secondary particles, thereby enabling accurate analysis of energy distribution across the entire simulation domain and eliminating boundary-related photon-scattering artifacts that affect dose calculation accuracy.

2.3 Physics List

The physics list was used in this simulation, and all electromagnetic interactions involving transport particles and photons are consistent with those of the radionuclide used in nuclear medicine. Regarding photon transport, Compton scattering and the photoelectric effect were implemented, and Rayleigh scattering was implemented using the Penelope model [11]. Charged-particle interactions, positron and electron decays, bremsstrahlung, and high-energy annihilation (511 keV) were also implemented. A physics list for radioactive decay was also used to accurately simulate this process, resulting in the emission of gamma rays [20]. This approach ensures the optimal balance between dose recorder accuracy and computational efficiency.

2.4 Phantom Geometry and Dimension

In this study, a water-based phantom with a water density of 1.0 g/cm^3, equivalent to human soft tissue, was used. The phantom was modeled using geometric shapes with varying length and width to assess changes in external exposure across different phantom dimensions. Two sets of phantom configurations were used in this study. The first set of phantoms, based on the ICRP-110 report for the adult voxel phantom, has a height of 176 cm for males and 168 cm for females.

In this work, the mean ICRP-110 report tall phantom, with a fixed height of 170 cm and variable width (15×20, 20×25, and 25×30 cm^3), was used to ensure optimal assessment of the external radiation dose rate. This largely simulated the variable dimensions of the human thorax. The second set of phantoms had smaller overall dimensions (25×15×20, 30×20×25, and 35×25×30 cm^3). The phantom dimensions were derived from the transverse thoracic diameter of an adult Nigerian population [20].

However, the effect of varying the phantom length and width on the external dose rate was evaluated under the same radiation conditions. A point source was placed inside the phantom at a predetermined position. Using a point source enables precise calculations and facilitates the evaluation of how variations in geometric shape affect the dose rate.

2.5 Source Configuration

In this study, the source was modeled as a point source and defined as an ion source with isotropic emission in all directions, using a general particle source (GPS). The point source emits particles and photons of each radionuclide according to the physics decay scheme. Fluorine-18 and Carbon-11, the positron-emitting radionuclides, undergo β^+

decay, producing positrons and neutrinos, which generate two gamma photons with an energy of 511 keV. In contrast, Iodine-123 emits gamma photons with an energy of 159 keV. Iodine-131 emits beta particles accompanied by gamma photons at 364 keV.

Gallium-67 decays by electron capture and emits photons with energies around 93, 184, and 300 keV. Technetium-99m emits a gamma photon with an energy of 140 keV [1]. The source was placed in two conditions: in the first, it was an unshielded source to ensure the absence of Compton scattering or attenuation that might absorb a portion of the photons, and to calculate an external dose rate constant (Γ) to be used as a reference and compared with previous studies.

In the second, the source was placed inside the phantom to calculate the dose and determine the extent to which self-attenuation and scattering affect radiation exposure under realistic clinical conditions. The radioactivity used in the simulation was 100 kBq for an acquisition time of 60 s to produce 6×10^6 particle histories. This event number was used in the simulation to ensure the statistical uncertainties in the dose rate values, resulting in a maximum relative standard deviation of 1.5%.

2.6 Detector Geometry and Dose Calculation

A detector was modeled to measure radiation exposure. The detector was designed to operate with different gaseous media: air, argon, and neon. Each gas detector was assigned to a specific boundary, and its physical properties were specified. The densities of air, argon, and neon were set to 1.22×10^{-3} g/cm³, 1.61×10^{-3} g/cm³, and 8.39×10^{-4} g/cm³, with effective atomic numbers $Z_{eff} \approx 7.6$, $Z = 18$, and $Z = 10$, respectively.

The purpose of this study was to examine the effect of gas type on photon energy deposition. The detector was placed at distances of 1, 2, and 3 m from the source to evaluate the effect of distance on the external radiation dose. The detector size was varied from (3×3×3 cm³ to 10×10×10 cm³) to assess the measurement response and the accuracy of dose calculation. The detector was coupled within a Geant4 Gate simulation with a Dose Actor to calculate photon energy deposition within the detector volume. The effect of low-energy interactions, which are not scientifically significant at doses below 10 keV, was neglected to ensure high consistency with previous studies, including Unger & Trubey (1982) [21]. In the dose actor, the energy of the deposit was converted into a radiation dose according to the following equation:

$$\mathrm{D} = \frac{\mathrm{E}_{dep}}{\mathrm{m}} \tag{1}$$

Where D represents the absorbed dose (Gy), E_{dep} is the energy deposited within the detector volume (J), and m is the detector mass (kg), calculated using the previously defined detector volume and density [22].

3. RESULTS

3.1 Unshielded point source

Figure 1 shows six separate graphs (a-f) comparing dose-rate constant values from GATE/Geant4 simulations with previous experimental studies for the six nuclides across different detector media (air, argon, neon) and multiple detector sizes at 1 m from an unshielded point source.

Table 1 shows a comparison of GATE simulations using different detector dimensions and gas media with published data. The optimal detector size that gave results closest to experimental values was selected. The matching results showed variation in the detector dimensions and media depending on the specific radionuclide; the agreement ratio was calculated between the simulation and published data, and the deviation was within ±10% of the total experimental data. In the study by Unger & Trubey (1982) [21], the mean overall agreement ratio and standard deviation (SD) were 1.089±0.120, in the study by Tschurlovits et al. (1992) [23], it was 1.127±0.194, and in the study by Smith & Stabin (2012), it was 1.114±0.241[24].

Table 1. Validation of the MC Gate simulation of dose rate constants for radionuclides with experimental published previous studies at 1 m.

Nuclide	**Experimental**		**Simulation**			**Ratio**
	Reference	**Γ (mSv·m²/MBq·h)**	**Detector Size (cm³)**	**Media Detector**	**Γ (mSv·m²/MBq·h)**	
^{11}C	Unger & Trubey (1982)	1.91×10^{-4}	8×8×8	Argon	1.86×10^{-4}	0.973
	Tschurlovits et al. (1992)	1.39×10^{-4}	9×9×9	Air	1.36×10^{-4}	0.978
	Smith & Stabin (2012)	1.54×10^{-4}	7×7×7	Argon	1.66×10^{-4}	1.078

Nuclide	**Experimental**		**Simulation**			**Ratio**
	Reference	**Γ (mSv·m²/MBq·h)**	**Detector Size (cm³)**	**Media Detector**	**Γ (mSv·m²/MBq·h)**	
^{18}F	Unger & Trubey (1982)	1.85×10^{-4}	6×6×6	Argon	1.77×10^{-4}	0.956
	Tschurlovits et al. (1992)	1.37×10^{-4}	8×8×8	Air	1.40×10^{-4}	1.022
	Smith & Stabin (2012)	1.49×10^{-4}	10×10×10	Argon	1.49×10^{-4}	1.000
^{67}Ga	Unger & Trubey (1982)	3.00×10^{-5}	9×9×9	Argon	3.57×10^{-5}	1.190
	Tschurlovits et al. (1992)	3.10×10^{-4}	4×4×4	Argon	3.42×10^{-4}	1.103
	Smith & Stabin (2012)	2.08×10^{-5}	9×9×9	Neon	2.02×10^{-5}	0.971
^{123}I	Unger & Trubey (1982)	7.48×10^{-5}	7×7×7	Air	9.21×10^{-5}	1.231
	Tschurlovits et al. (1992)	1.69×10^{-4}	10×10×10	Argon	1.93×10^{-4}	1.142
	Smith & Stabin (2012)	4.54×10^{-5}	10×10×10	Air	4.14×10^{-5}	0.912
^{131}I	Unger & Trubey (1982)	7.64×10^{-5}	6×6×6	Argon	8.91×10^{-5}	1.166
	Tschurlovits et al. (1992)	5.93×10^{-5}	6×6×6	Argon	8.91×10^{-5}	1.503
	Smith & Stabin (2012)	5.65×10^{-5}	6×6×6	Argon	8.91×10^{-5}	1.577
^{99m}Tc	Unger & Trubey (1982)	3.32×10^{-5}	9×9×9	Argon	3.39×10^{-5}	1.021
	Tschurlovits et al. (1992)	3.60×10^{-5}	6×6×6	Argon	3.66×10^{-5}	1.017
	Smith & Stabin (2012)	2.06×10^{-5}	4×4×4	Argon	2.36×10^{-5}	1.146

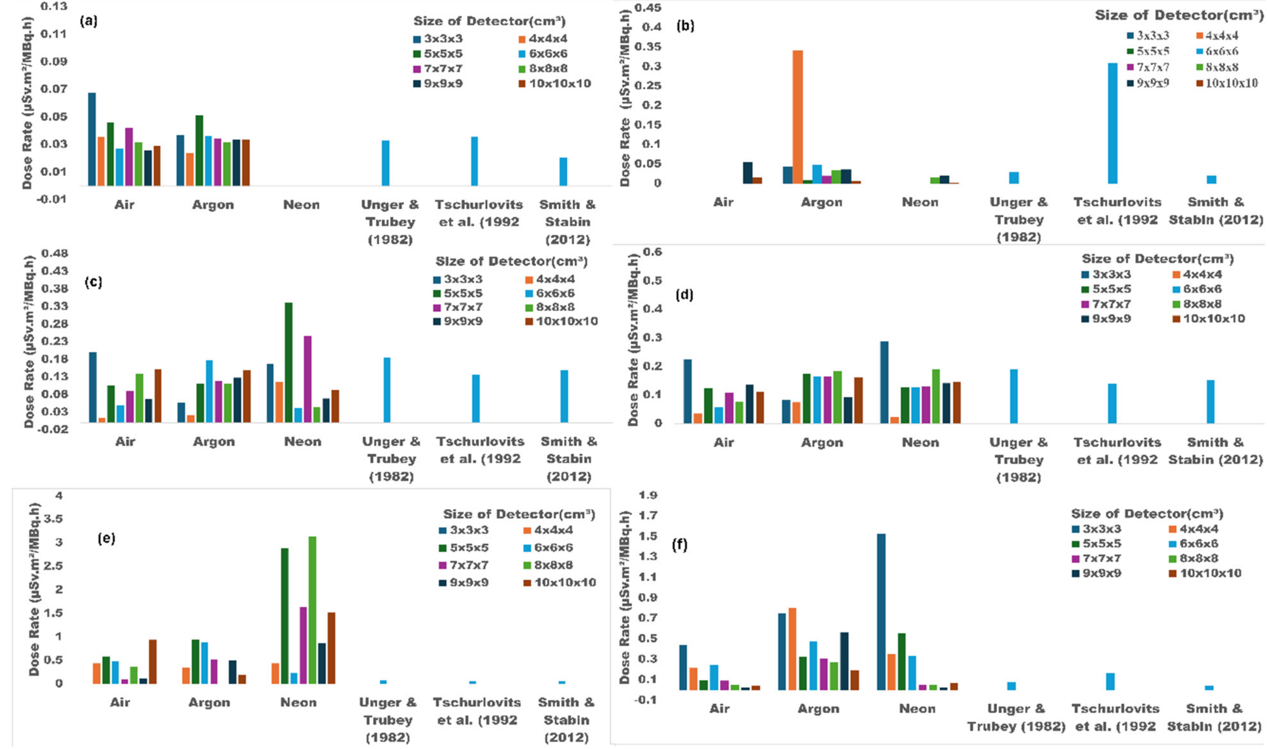

Figure 1. Simulation of external dose rate constants for (a) ^{99m}Tc, (b) ^{67}Ga, (c) ^{18}F, (d) ^{11}C, (e) ^{131}I, and (f) ^{123}I radionuclides in various detector media and different detector sizes, compared to previous studies at 1 m from an unshielded point source

The six nuclides used in the present work and investigated in different media (air, argon, and neon) are shown in Figure 2. The figure presents the mean external dose rate constant values for an unshielded point source isotropic emission, for detector sizes ranging from (8×8×8 to 10×10×10 cm^3). These values were compared with those from previous experimental studies that used an unshielded bare point source at 1m.

The results showed a dose rate constant of 0.0108 μSv·m^2·MBq^{-1}·h^{-1} in air detector media for ^{99m}Tc, a higher dose rate of 0.0418 μSv·m^2·MBq^{-1}·h^{-1} for argon detector media, the neon detector media failed to record a reading, unlike the air and argon detector media, which showed a perfect balance between the simulation results and previous reference studies.

In the ^{131}I, the highest reading was recorded in neon at 0.840 μSv.m^2. MBq^{-1}.h^{-1}, indicating the neon detector media high sensitivity to radionuclides that have multiple energies. ^{131}I recorded high values in the neon detector, exceeding those of the air and argon detectors. The ^{123}I nuclide in the argon detector media showed a higher response than in air and neon, consistent with the study conducted by Tschurlovits et al. in 1992 [23]. As for the ^{67}Ga nuclide, the study by Tschurlovits et al. 1992 [23] stands out as a high value compared to other studies of different detector media simulations.

Conversely, for ^{18}F and ^{11}C nuclides, there is significant agreement and stability in the different detector media with the results of previous studies. The ratio agreement between the simulation and experiment published data for ^{18}F showed the argon media 0.70,0.94, and 0.87 for Unger & Trubey (1982) [21], Tschurlovits et al. (1992) [23], and Smith & Stabin (2012) [24], respectively, and air media was 0.70,0.88, and 0.81 for Unger & Trubey (1982) [21], Tschurlovits et al. (1992) [23], and Smith & Stabin (2012) [24] , respectively, and neon media was 0.40,0.55, and 0.46.for Unger & Trubey (1982) [21], Tschurlovits et al. (1992) [23], and Smith & Stabin (2012) [24], respectively.

Followed by the ^{11}C nuclide, the argon media 0.77,1.06, and 0.96 for Unger & Trubey (1982) [21], Tschurlovits et al. (1992) [23], and Smith & Stabin (2012) [24], respectively. and the air media was 0.60,0.80, and 70 for Unger & Trubey (1982) [21], Tschurlovits et al. (1992) [23], and Smith & Stabin (2012) [24], respectively, while the neon media were 0.90,1.16, and for 0.84 Unger & Trubey (1982) [21], Tschurlovits et al. (1992) [23], and Smith & Stabin (2012) [24], respectively.

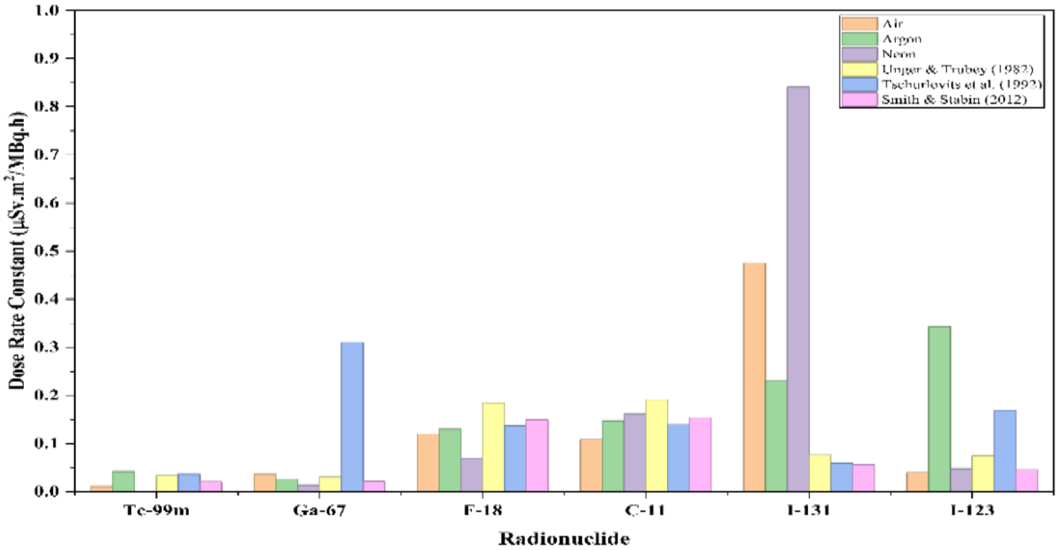

Figure 2. Mean dose rate constants for radionuclides in various detector media and different detector sizes (from 8×8×8 to 10×10×10 cm^3) at 1 m

3.2 Phantom Measurements (Shielded Source)

Figures (3, 4, 5) illustrate the effects of variations in phantom dimensions, detector size, and media (air, argon, and neon) on the dose rate constant. Variable phantoms measuring (25×15×20 cm^3, 30×20×25 cm^3, and 35×25×30 cm^3) were used, with detector sizes ranging from (3×3×3 cm^3 to 10×10×10 cm^3) at 1 m, compared with previous studies. Variations were measured from the initial valid readings to the 10×10×10 cm^3 detector size for each radionuclide.

Figure 3. (air detector media), ^{99m}Tc with variations of 78.3%, 94%, and 60% and ^{67}Ga recorded decreases of 69.4% and 47.7% and 81.9%, ^{18}F with variations of 35.1%, 47.1%, and 54.7%, ^{11}C and ^{131}I showed decreases for the small phantom (61.5% and 51.1%, respectively) but highly irregular increases for the larger phantoms, and ^{123}I with variations of 3.1%, 83.9%, and 99.8% for all the small, medium, and large phantoms, respectively.

Figure 4 (argon detector media) shows the same general pattern of decrease with phantom size, but with significantly higher dose rate values than the air media detector, with ^{99m}Tc 23.3% and 35% and 30.1%, ^{67}Ga with variations of 59.9%, 61.7%, and 60.3%, and ^{18}F showed variations of 10.9%, 90.5%, and 61.7%, ^{11}C recorded variations with decreases of 52.6%,5.3% and,12.1%and ^{131}I demonstrated variations of 142.0%, 151.8%, and 108.0%, and ^{123}I with variations 2.3%, 13.9%, and 17.3% for all the small, medium, and large phantoms, respectively.

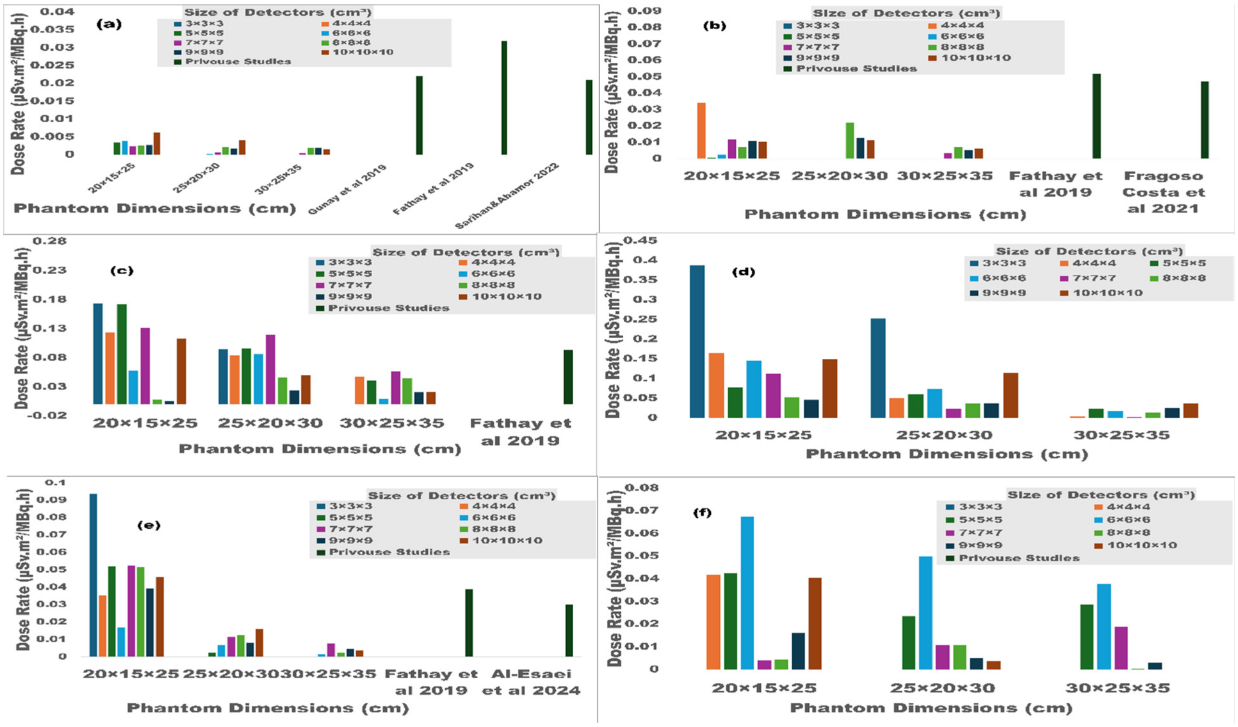

Figure 3. Simulation of external dose rate for (a)^{99m}Tc, (b) ^{67}Ga, (c) ^{18}F, (d) ^{11}C, (e) ^{131}I, and (f) ^{123}I radionuclides in air detector media and different phantom dimensions and detector sizes, compared to previous studies at 1 m.

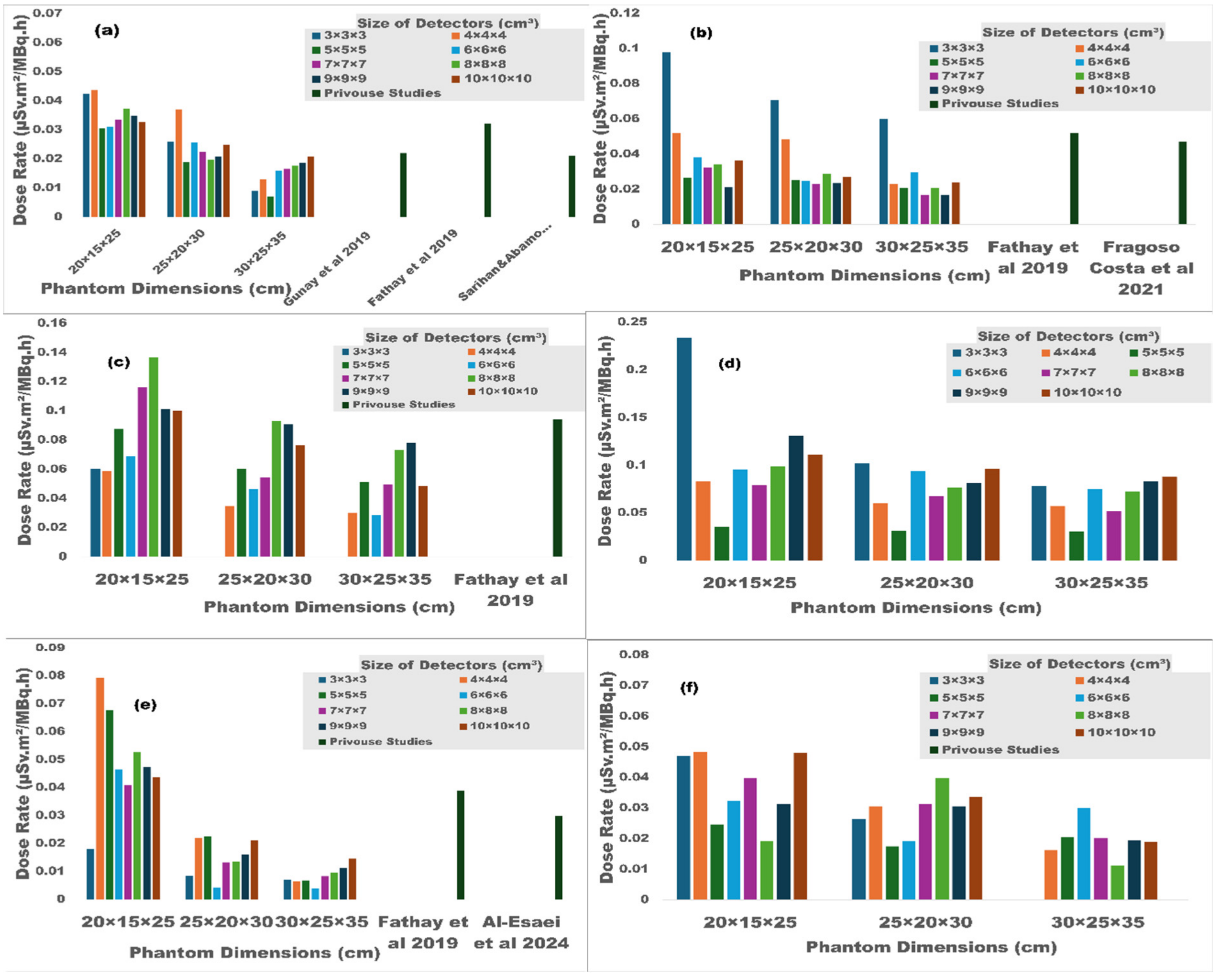

Figure 4. Simulation of external dose rate for (a)^{99m}Tc, (b) ^{67}Ga, (c) ^{18}F, (d) ^{11}C, (e) ^{131}I, and (f) ^{123}I radionuclides in argon detector media and different phantom dimensions and detector sizes, compared to previous studies at 1 m

Figure 5 (neon detector media) shows exhibited highly irregular behavior where ^{99m}Tc failed to register any measurable readings across all detector sizes and phantom dimensions, and ^{123}I failed to record large phantom(30×25×35 cm^3), ^{123}I recorded variations of 47.2% and 25.0% for the small and medium phantoms only, ^{67}Ga recorded with variations of 76.7%, 58.7%, and 92.3%, ^{131}I exhibited an increasing trend with variations of 73.4%, 50.5%, and 9.6%, and ^{11}C showed consistent decreasing trends of 41.5%, 34.6%, and 79.8%, ^{18}F showed variations of 31.7%, 91.2%, and 3.9%. for all the small, medium, and large phantoms, respectively,

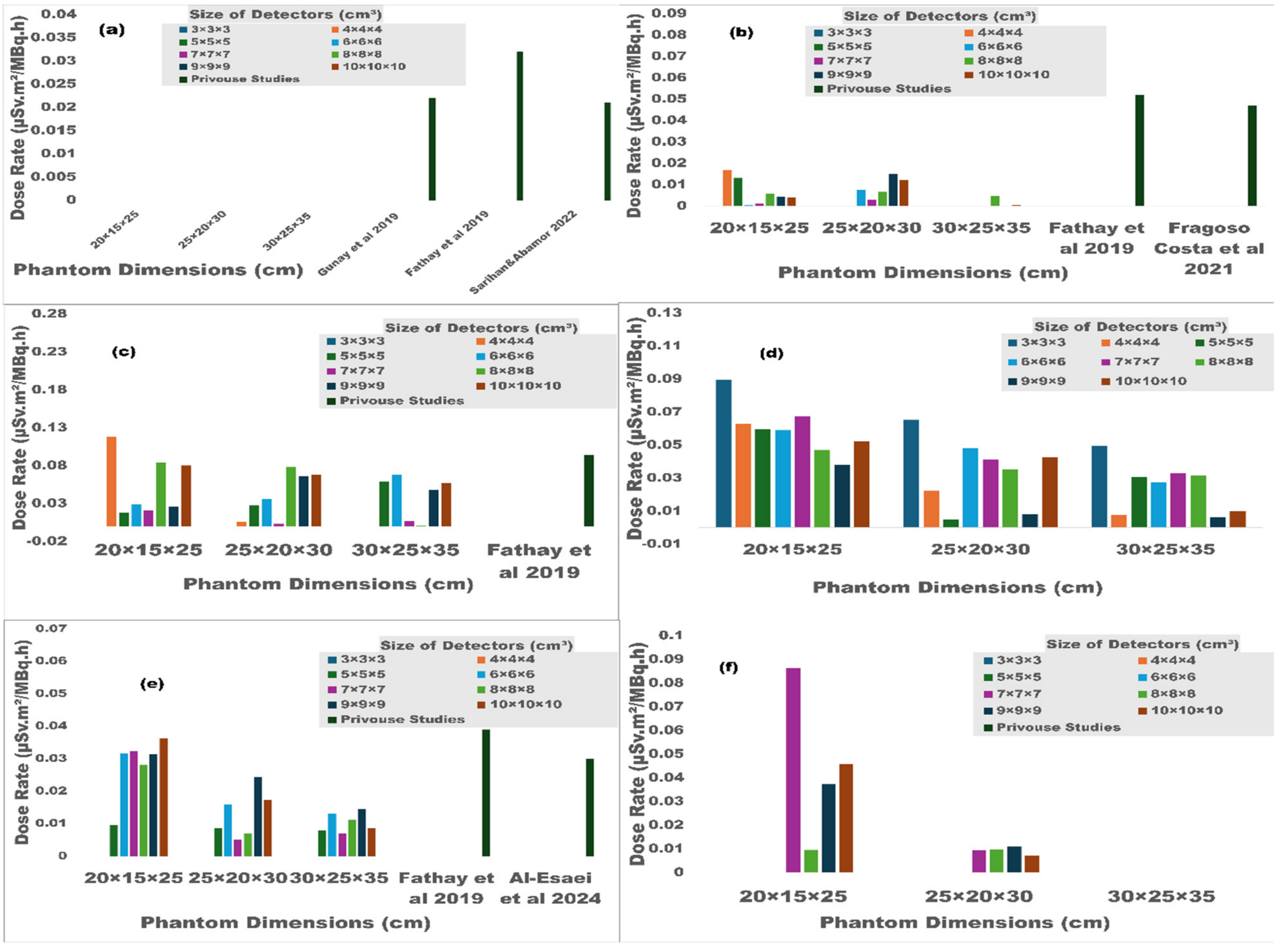

Figure 5. Simulation of external dose rate for (a)^{99m}Tc, (b) ^{67}Ga, (c) ^{18}F, (d) ^{11}C, (e) ^{131}I, and (f) ^{123}I radionuclides in Neon detector media and different phantom dimensions and detector sizes, compared to previous studies at 1 m.

Figure 6 presents three sets (a, b, c) showing the mean dose rates of the six radionuclides in the three-detector media (air, argon, and neon) across different phantom dimensions (25×15×20 cm^3, 30×20×25 cm^3, and 35×25×30 cm^3) and compares them with previous experimental studies.

In set (a) for the air detector media, ^{99m}Tc decreases from 0.0038 to 0.0019 µSv·m^2 (50% reduction), and ^{67}Ga decreases from 0.0125 to 0.0062 µSv·m^2·MBq^{-1}·h^{-1} (50% reduction), ^{18}F decreases from 0.0423 to 0.0211 µSv·m^2. MBq^{-1}·h^{-1} (50% reduction), and ^{11}C decreased from 0.0389 to 0.0254 µSv·m^2·MBq^{-1}·h^{-1} (35% reduction), ^{131}I decreased from 0.0318 to 0.0114 (64% reduction), and ^{123}I decreased from 0.0136 to 0.0011 µSv·m^2·MBq^{-1}·h^{-1} (92% reduction).

In set (b), the argon detector shows the same general pattern of decrease with phantom size, but with significantly higher dose rate values than the air media detector, with ^{99m}Tc increasing from 0.0349 µSv·m^2·MBq^{-1}·h^{-1} to 0.0218 µSv·m^2. MBq^{-1}·h^{-1} (37% reduction), ^{67}Ga increasing from 0.0420 to 0.0307 µSv·m^2 MBq^{-1}·h^{-1} (27% reduction), and ^{18}F rises from 0.0950 to 0.0760 µSv·m^2·MBq^{-1}·h^{-1} (20% reduction), ^{11}C rises from 0.0776 to 0.0564 µSv·m^2·MBq^{-1}·h^{-1} (27% reduction), ^{131}I decreases from 0.0478 to 0.0118 µSv·m^2·MBq^{-1}.h^{-1} (a 75% reductions), and ^{123}I decreases from 0.0362 to 0.0166 µSv·m^2·MBq^{-1}·h^{-1} (a 54% reductions).

In set (c), the neon media shows irregular, more complex, and inconsistent behavior where ^{99m}Tc and ^{123}I record very low or nearly zero values, and ^{123}I decreases from 0.0309 to 0.00 in the larger phantom, while ^{67}Ga rises to 0.0165 µSv.m^2. MBq^{-1}·h^{-1} and falls to 0.0017 µSv·m^2·MBq^{-1}·h^{-1} (90% reduction), and ^{131}I records the highest absolute value ever of 0.8407 µSv·m^2·MBq^{-1}·h^{-1} but drops sharply to 0.0035 (99% reductions), and ^{11}C rises to 0.1607 µSv·m^2·MBq^{-1}·h^{-1} and falls to 0.0293 µSv·m^2 (81% reductions). MBq^{-1}·h^{-1}, and ^{18}F rises to 0.0733 and falls to 0.0453 µSv·m^2·MBq^{-1}·h^{-1} (38.2% reductions).

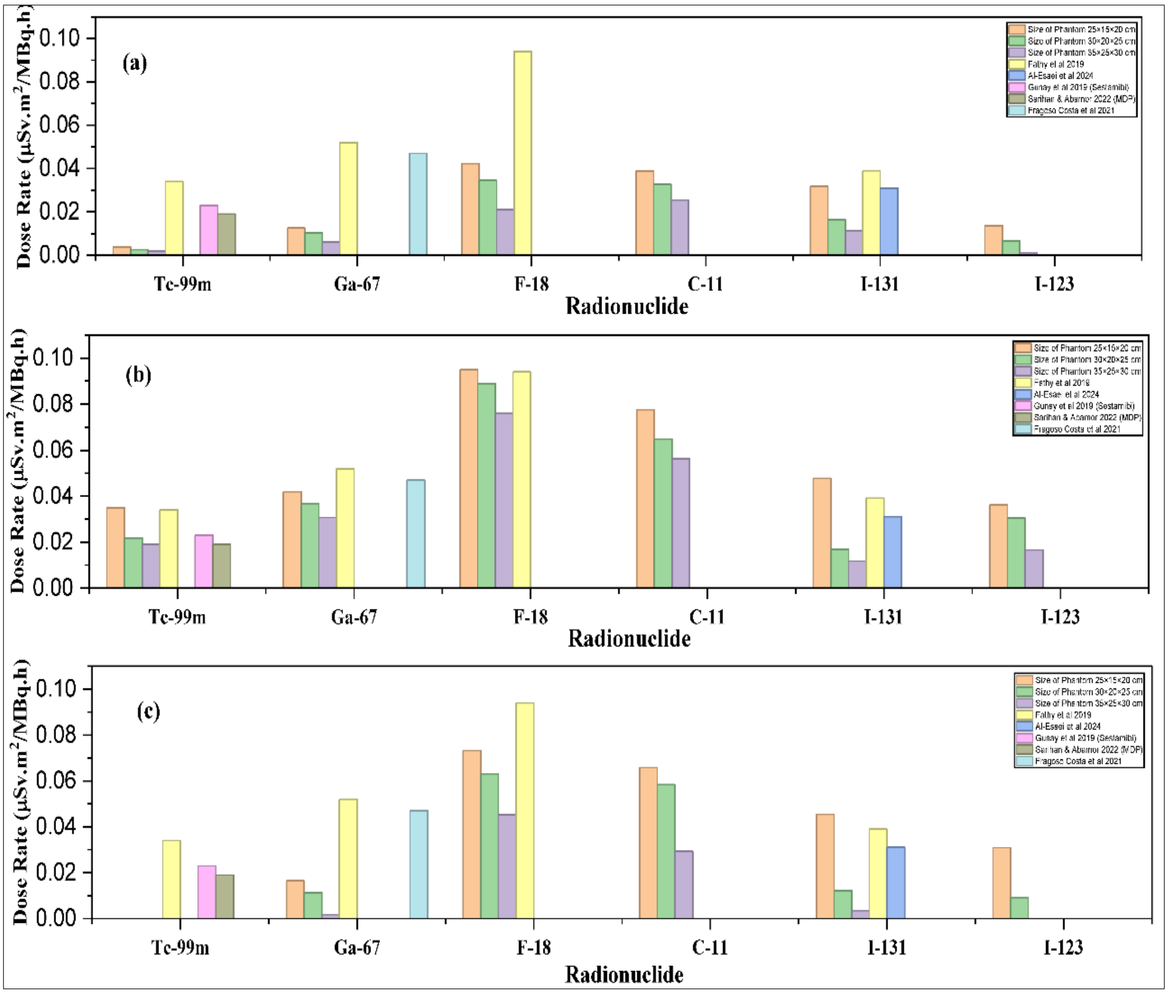

Figure 6. Mean dose rate constant for the radionuclides used, (a) air, (b) argon, and (c) neon detector media for detector size (from 8×8×8 to 10×10×10 cm^3) with different phantom dimensions, compared with previous studies at 1 m

Figure 7 (a and b) describes the ^{99m}Tc nuclide, comparing the dose rate across two different detector media (air and argon) and the two sets of phantoms. Where the dimensions were divided into small (170×15×20 and 25×15×20 cm^3), medium (170×20×25 and 30×20×25 cm^3), and large phantoms (170×25×30 and 35×25×30 cm^3) at 1 m compared with previous studies.

Figure (7a), which represents air detector media, the GATE simulation values are very low, starting at 0.0038 $\mu Sv \cdot m^2 \cdot MBq^{-1} \cdot h^{-1}$ for the small phantom and gradually decreasing to 0.0026 $\mu Sv \cdot m^2 \cdot MBq^{-1} \cdot h^{-1}$ for the medium phantom (a 31.6% reductions), then to 0.0019 $\mu Sv.m^2$. $MBq^{-1}.h^{-1}$ for the large phantom (50% reductions).

Figure (7b), which represents argon detector media, shows much better agreement, with GATE simulation values starting at 0.0349 $\mu Sv \cdot m^2 \cdot MBq^{-1} \cdot h^{-1}$ for the small phantom, but decreasing to 0.0218 $\mu Sv \cdot m^2 \cdot MBq^{-1} \cdot h^{-1}$ for the medium phantom (37.5% reductions), and then to 0.0191 $\mu Sv \cdot m^2 \cdot MBq^{-1} \cdot h^{-1}$ for the large phantom (12.4% reductions). (Supplement file shows the ^{99m}Tc nuclide used with an argon detector media for various phantoms and detector sizes at 1, 2, 3 m with previous studies in Figure S1 to Figure S3).

Table 2 presents the results for the ^{99m}Tc nuclide, demonstrating that the dose rates recorded conform to the inverse-square law across different phantom dimensions, and selected optimal detector sizes prove the inverse-square law.

The argon detector media maintained its ability to produce measurable readings at 1, 2, and 3 m, whilst the air and neon detectors failed. The power-law fitting function, whilst the exponential coefficient $1/r^2$ presents a range from −0.167 to −1.054 across all phantom dimensions, deviating from the ideal value -2 of the inverse-square law for an unshielded point source. (Supplement file shows Figure S4 to Figure S11)

Table 2. Analysis of the Inverse-Square Law distances of 1, 2, and 3 m from the source across various phantom dimensions and detector sizes for the ^{99m}Tc nuclide.

Phantom Dimension (cm^3)	Size of the Detector (cm^3)	Fitting Function	R^2	1/r^2
170×15×20	10×10×10	$y=0.0300x^{-0.258}$	0.9760	-0.258
	9×9×9	$y=0.0285x^{-0.293}$	0.8646	-0.293
	8×8×8	$y=0.0335x^{-0.483}$	0.9836	-0.483

Phantom Dimension (cm^3)	Size of the Detector (cm^3)	Fitting Function	R^2	1/r^2
170×20×25	9×9×9	$y=0.0243x^{-0.167}$	0.4924	-0.167
	8×8×8	$y=0.0301x^{-0.444}$	0.9983	-0.444
	7×7×7	$y=0.0220x^{-0.250}$	1	-0.250
170×25×30	9×9×9	$y=0.0232x^{-0.537}$	0.7758	-0.537
	8×8×8	$y=0.0279x^{-0.428}$	0.9926	-0.428
	7×7×7	$y=0.0214x^{-0.259}$	0.9979	-0.259
25×15×20	10×10×10	$y=0.0344x^{-0.963}$	0.9606	-0.963
	9×9×9	$y=0.0341x^{-1.054}$	0.9977	-1.054
	8×8×8	$y=0.0389x^{-0.845}$	0.9652	-0.845
30×20×25	10×10×10	$y=0.0260x^{-0.869}$	0.9664	-0.869
	9×9×9	$y=0.0212x^{-0.593}$	0.9939	-0.593
	8×8×8	$y=0.0198x^{-0.449}$	0.9993	-0.449
35×25×30	10×10×10	$y=0.022x^{-0.230}$	0.9515	-0.230
	9×9×9	$y=0.0199x^{-0.292}$	0.9082	-0.292
	8×8×8	$y=0.0129x^{-0.180}$	0.2028	-0.180

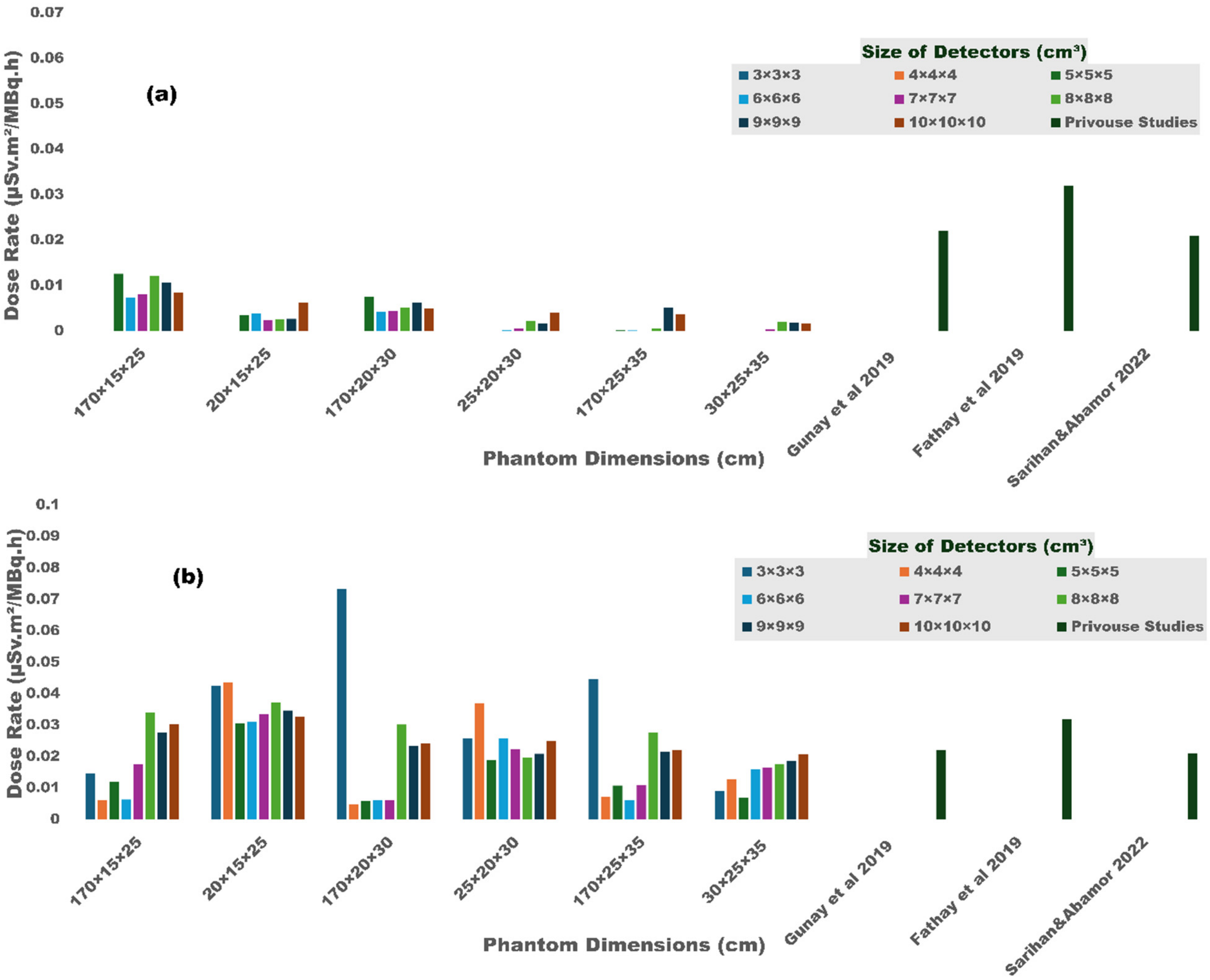

Figure 7. Comparison of Dose rate for the ^{99m}Tc nuclide using (a) Air, (b) Argon detector media for various phantom dimensions and detector sizes at 1 m with previous studies

4. DISCUSSION

This study used MC GATE/Geant4 simulations to calculate the external dose rate constants for six clinically important radionuclides, including ^{99m}Tc, ^{67}Ga, ^{18}F, ^{11}C, ^{131}I, and ^{123}I. The resulting simulated values were compared with three reliable and validated experimental references: Unger & Trubey (1982) [21], Tschurlovits et al. (1992) [23], and Smith & Stabin (2012) [24]. The comparison yielded agreement ratios of 1.089, 1.127, and 1.114, respectively, indicating that all simulation results fell within an acceptable ±10% deviation margin, confirming the accuracy and validity of the MC GATE computational model. This, in turn, indicated good agreement between the MC GATE simulation and experimentally measured values in radiation dose measurements, reinforcing confidence in computational methods as an effective tool in radiation protection research.

4.1 Influence of Detector Media

The results show a significant correlation between the effective atomic number of the detector media and the sensitivity of the recorded readings, as argon (Z=18) has a larger atomic number than neon (Z=10) and air (Z_{eff}=7.6). On this basis, the argon detector is more efficient than air and neon in absorbing low- and medium-energy photons. Therefore, due to the higher probability that the photoelectric absorption occurs with a higher atomic number, with photon interaction [25].

In contrast, the neon detector failed to record measurable readings, such as T-99m nuclide, and was very low for ^{67}Ga nuclide. As for ^{131}I, the neon detector recorded unexpected readings that were higher than those of the air and argon detectors media. This may be due to the multiple energies of photons. The remaining nuclides recorded readings lower than those of argon and air [26].

The calculated mean dose rate in the presence of the phantom yields the highest value at the argon detector media, followed by air and neon. The neon detector failed to provide any readings for the ^{99m}Tc and ^{123}I nuclides (specifically for the phantom dimension of 35×25×30 cm^3). This is due to the low emission energy of these radionuclides, combined with the low stopping power of neon, leading to insufficient energy deposition within the detector volume with absorption self-attenuation of the phantom [1].

The result shows excellent agreement with previous clinical studies, such as Fathy et al. 2019 [27], in the ^{18}F in an argon detector media; however, for the air detector media, the simulation results showed half the reference value. In the neon media, the reference studies showed higher values than the simulation results.

In contrast, the ^{131}I showed agreement with the reference studies by Fathy et al. 2019 [27] and Al-Esaei et al.2024 [28] across all detector media, particularly for the phantom dimension (25×15×20 cm^3), with perfect agreement. Followed by the ^{67}Ga, which is consistent with the simulation results in the argon media and with the reference studies by Fathy et al. 2019 [27], Fragoso Costa et al. 2021 [29].

Despite the ^{99m}Tc, the air detector media values are significantly lower than those in the reference studies by Fathy et al. 2019 [27], Gunay et al. 2019 [30], and Sarihan & Abamor 2022 [31]. In the argon detector media, however, excellent agreement was observed with the reference studies, in contrast to the neon detector media, which failed to register any readings.

4.2 Influence of Detector Size

The results shown demonstrate that the size of the detector is a decisive factor in measurement accuracy and reading stability, as it can be observed that the dose rate values decrease with an increase in detector size (from 3×3×3 to 10×10×10 cm^3). This phenomenon is physically attributed to the volume averaging effect. Although a larger detector absorbs more total energy, this energy is distributed over a larger mass. Because the regions of the large detector further from the source receive less radiation flux, this spatial averaging reduces the overall recorded dose rate compared to small detectors, which more closely approximate an ideal point-like measurement geometry [26].

In contrast, the simulation data indicates that the dose rate begins to reach a state of stability and convergence at a detector size of (8×8×8 to 10×10×10 cm^3), where it appears that large detectors have a higher stopping power for secondary particles and electrons resulting from the interaction of radiation with the detector media (whether air, argon or neon), as a large detector ensures that majority of secondary particle tracks remain within the volume active, facilitating the establishment of charge particle equilibrium.

4.3 Influence of Phantom Dimensions

The impact of phantom dimensions on the external dose rate was evaluated using different phantom dimensions (20×15×20, 25×20×30, and 30×20×35 cm^3) with detector sizes ranging from (3×3×3 to 10×10×10 cm^3) at 1 m. The results indicate. The increase in phantom dimensions correlates with a gradual decline in the recorded dose rate for all six radionuclides across the various detector media (air, argon, and neon).

Physically, this attenuation is primarily attributed to increased attenuation in tissue-equivalent phantom material. As the dimensions of the phantom increase, the absorption of photons by the phantom before they reach the detector increases, causing a decrease in the observed dose rate [18]. The decrease in the dose rate between the smallest phantom (20×15×25 cm^3) and the largest phantom (30×25×35 cm^3) was approximately 36.8%, indicating that self-attenuation and phantom dimensions reduce the external radiation dose.

The air detector showed lower values than the argon detector, with a total attenuation of 50% for the phantoms. In contrast, the 170 cm long phantoms showed a marked increase in photon attenuation.

Conversely, the results show more stable values for the argon detector, with the small phantoms showing a total attenuation of 37.5%, which is more consistent with previous studies. The large 170 cm phantom also showed a higher degree of photon attenuation compared to the shorter phantom.

These findings reveal that phantom dimensions have a direct effect on workers' radiation exposure. The data suggest that a patient's height, when injected with radioactive pharmaceuticals, is less important than the patient's body thickness, which is considered the most significant barrier to radiation, and that the patient's height does not affect radiation exposure. This was also confirmed by a Kinsara et al. 2014 study that used MCNP cylindrical phantom shapes of different diameters; it was observed that when the diameters changed, the amount of radiation exposure changed. This was also confirmed by a Kinsara et al. 2014 study that used MCNP cylindrical phantom shapes of different diameters; it was observed that when the diameters changed, the amount of radiation exposure changed [17].

In this context, the use of phantoms with dimensions that differ from the ICRP standard reference phantom, which is based on standardized geometries, is justified; the main reason is that the standard reference phantom is an idealized model, whereas the geometric shapes of patients in nuclear medicine vary and cannot be accurately reflected by the reference phantom. Consequently, the results of this study were designed to assess the extent of variation in phantom dimensions rather than to replace them, and it has been shown that using different phantom dimensions is a valid approach for assessing radiation exposure.

4.4 Influence of Source/Detector distance

As shown, the power-law exponents are highly significant and vary from -0.167 to -1.054 across all phantom configurations studied, in contrast to the theoretical exponent of -2.0 for the inverse-square law. This deviation is ascribed to several major causes, among which the most important that explain the difference in source size between the reconstructed and the real cases are photon attenuation and Compton scattering within the phantom, and effects of source geometry and detector size. The most striking observation is that the phantoms that produced the best values of the coefficient of determination R^2 had exponents that were no closer to the theoretical value of -2.0 for a point source in free space, These results finding the necessity of incorporating realistic phantom geometry and appropriate detector selection into occupational dose assessment for nuclear medicine personnel, rather than relying on simplified point source inverse-square law approximations that may yield inaccurate exposure estimates.. Lastly, these results indicate that argon media can give accurate measurements at 1, 2, and 3 meters.

5. CONCLUSION

This study demonstrated the effectiveness of the MC GATE simulation in calculating external dose rates for the six most important clinical radionuclides used in nuclear medicine: ^{99m}Tc, ^{67}Ga, ^{18}F, ^{11}C, ^{131}I, and ^{123}I. The results were compared with experimental references, and all fell within an acceptable 10± margin of error.

The results confirmed that the argon detector media proved to be the most sensitive and reliable, in contrast to air and neon media, which exhibited unexpected behavior and low sensitivity across the detector size.

Furthermore, detector size was shown to influence the measured response, with dose rate values remaining stable for detector sizes ranging from (8×8×8 to 10×10×10 cm^3), consistent with previous experimental studies.

The simulation results confirmed that phantom dimensions affect radiation exposure, with a mean overall reduction of 36.8% when phantom dimensions were increased from the smallest phantom (25×15×20 cm^3) to the largest phantom (35×25×30 cm^3). In contrast, through various detector media, the actual clinical exposure and how patient-induced exposure reduces occupational exposure for staff. The high-energy emitter radionuclides at 511 keV had the highest radiation exposure: ^{18}F and ^{11}C, followed by ^{67}Ga, ^{131}I, ^{123}I, and lastly ^{99m}Tc.

Conversely, the patient's height is less significant than body thickness, as phantom height does not reduce radiation exposure compared with body thickness, which acts as a physical barrier that reduces occupational exposure for staff. This was analyzed using the inverse-square law, which confirmed the effectiveness of the GATE/Geant4 simulation across various scenarios at different distances and the accuracy of the detector response, with the argon detector media standing out for maintaining readings even at 3 m. Finally, this study presents a reliable computational tool for optimizing external dose rates across various clinical scenarios, providing guidance for improving radiation protection protocols and assessing occupational exposure in nuclear medicine departments.

ORCID

Abdulkhaleq O. Jaralah, https://orcid.org/0009-0006-6399-4657; **Alaa M. Elgohary**, https://orcid.org/0000-0003-4600-6240
Monira M. Rageh, https://orcid.org/0000-0002-2350-6595; **Magdy M. Khalil**, https://orcid.org/0000-0003-2087-5229

REFERENCE

[1] M.M. Khalil, Basic *Sciences of Nuclear Medicine* (Springer International Publishing, Cham, 2021).
[2] M.M. Khalil, Basic *Science of PET Imaging* (Springer International Publishing, Cham, 2017).
[3] M.U. Khan, and M.S. Usmani, "Radionuclide Infection Imaging: Conventional to Hybrid," in: *12 Chapters on Nuclear Medicine*, (IntechOpen, 2011).
[4] R.J. Groper, D.K. Glover, and A.J. Sinusas, *Cardiovascular Molecular Imaging* (CRC Press, Boca Raton, 2007). https://doi.org/10.3109/9781420005097
[5] H.R. Maxon, and H.S. Smith, "Radioiodine-131 in the diagnosis and treatment of metastatic well differentiated thyroid cancer," *Endocrinol. Metab. Clin. North. Am.* **19**(3), 685–718 (1990).
[6] X. Deng, J. Rong, L. Wang, N. Vasdev, L. Zhang, L. Josephson, and S.H. Liang, "Chemistry for Positron Emission Tomography: Recent Advances in 11 C-, 18 F-, 13 N-, and 15 O-Labeling Reactions," *Angw. Chem.* **58**(9), 2580–2605 (2019). https://doi.org/10.1002/anie.201805501

[7] S.Y. Ho, and D.R. Shearer, "Radioactive contamination in hospitals from nuclear medicine patients," *Health Physics*, **62**(5), 462-466 (1992). https://doi.org/10.1097/00004032-199205000-00015

[8] F. Jafarian-Dehkordi, and C. Hoeschen, "Low-Dose radiation risk in medicine: a look at risk models, challenges, and future prospects," Z. Med. Phys. **35**(4), 393–400, (2025). https://doi.org/10.1016/j.zemedi.2025.07.002

[9] IAEA, *Occupational Radiation Protection: General Safety Guide*, (International Atomic Energy Agency, Vienna, 2018).

[10] IAEA, *ORPGUIDE: Occupational radiation protection; IAEA safety standards series*, (International Atomic Energy Agency, Vienna, 2000).

[11] ICRP. "The 2007 Recommendations of the International Commission on Radiological Protection. ICRP publication 103," Ann. ICRP **37**(2-4), 1–332 (2007). https://doi.org/10.1016/j.icrp.2007.10.003

[12] M. Abuqbeitah, M. Demir, I. Çavdar, H. Tanyildizi, N. Yeyin, L. Uslu-Beşli, L. Kabasakal, *et al.*, "Red bone marrow dose estimation using several internal dosimetry models for prospective dosimetry-oriented radioiodine therapy," Radiat. Environ. Biophys. **57**(4), 395–404 (2018). https://doi.org/10.1007/s00411-018-0757-2

[13] L.K. Harding, N.J. Harding, H. Warren, A. Mills, and W.H. Thomson, "The radiation dose to accompanying nurses, relatives and other patients in a nuclear medicine department waiting room," Nucl. Med. Commun. **11**(1), 17–22 (1990). https://doi.org/10.1097/00006231-199001000-00004

[14] N. Sirag, and A. Elrazek, "Design considerations to minimize staff doses in nuclear medicine units," Int. J. Eng. Tech. Res. **4**(1), 226–245 (2015).

[15] D. Visvikis, M. Bardies, S. Chiavassa, C. Danford, A. Kirov, F. Lamare, L. Maigne, *et al.*, "Use of the GATE Monte Carlo package for dosimetry applications," Nucl. Instrum. Methods Phys. Res., Sect. A, **569**(2), 335–340 (2006). https://doi.org/10.1016/j.nima.2006.08.049

[16] J. Ierace, P. Rowshanfarzad, C. Sinnott, R. Nezich, P. Brayshaw, and M. Djukelic, "From Point Sources to Phantoms: Refining Dose Rate Models in Nuclear Medicine with Tc-99m, F-18, I-131 and Lu- 177," Physical and Engineering Sciences in Medicine, preprint (2025). https://doi.org/10.21203/rs.3.rs-7707816/v1

[17] A. Kinsara, S. Abdul-Majid, W. El-gammal, T. Albaghdadi, A. Maimani, and W. Abulfaraj, "External radiation doses from patients administered with radiopharmaceuticals measurements and Monte Carlo simulation," Nucl. Technol. Radiat. Prot. **29**, 199–206 (2014). https://doi.org/10.2298/NTRP1403199K

[18] A. D. Soares, L. Paixão, and A. Facure, "Determination of the dose rate constant through Monte Carlo simulations with voxel phantoms," Med. Phys. **45**(11), 5283–5292 (2018). https://doi.org/10.1002/mp.13181

[19] J. Allison, *et al.*, "Recent developments in Geant4," Nucl. Instrum. Methods Phys. Res., Sect. A, **835**, 186–225 (2016). https://doi.org/10.1016/j.nima.2016.06.125

[20] E. N. Obikili, and A. B. Okesina, "Transverse thoracic diameter in frontal chest radiographs of an adult Nigerian population," West Afr. J. Med. **25**(3), 186–189 (2007). https://doi.org/10.4314/wajm.v25i3.28275

[21] L. M.Unger, and D. K. Trubey, *Specific gamma-ray dose constants for nuclides important to dosimetry and radiological assessment*, (Oak Ridge Nat. Lab. Radiat. Shielding Inform. Cent., Oak Ridge, TN, 1982).

[22] OpenGATE Collaboration, Tools to Interact with the Simulation: Actors (GATE Documentation, 2026).

[23] M. Tschurlovits, A. Leitner, and G. Daverda, "Dose Rate Constants for New Dose Quantities," Radiat. Prot. Dosim. **42**(2), 77–82 (1992). https://doi.org/10.1093/oxfordjournals.rpd.a081281

[24] D. S.Smith, and M. G. Stabin, "Exposure rate constants and lead shielding values for over 1,100 radionuclides," Health Phys. **102**(3), 271–291 (2012). https://doi.org/10.1097/HP.0b013e318235153a

[25] D.W.O. Rogers, "Introduction to Radiological Physics and Radiation Dosimetry by F. H. Attix," Med. Phys. **14**(4), 692 (1987). https://doi.org/10.1118/1.596041

[26] G. F. Knoll, *Radiation detection and measurement*, (John Wiley & Sons, 2010).

[27] M. Fathy, M. M. Khalil, W. M. Elshemey, and H. S. Mohamed, "Occupational radiation dose to nuclear medicine staff due to Tc99m, F18-FDG PET and therapeutic I-131 based examinations,"" Radiat. Prot. Dosim. **186**(4), 443–451 (2019). https://doi.org/10.1093/rpd/ncz046

[28] A. Al-Esaei, E. Saleh, S. Maghraby, T. Elsayed, and T. Kany, "Evaluation of Radiation Safety Parameters from Patients Receiving I-131 Therapy for Thyroid Carcinoma," J. Med. Phys. Appl. Sci. **9**(1), 52 (2024). https://doi.org/10.36648/2574-285x.9.1.52

[29] P. F. Costa, *et al.*, "Radiation Protection and Occupational Exposure on 68Ga-PSMA-11–Based Cerenkov Luminescence Imaging Procedures in Robot-Assisted Prostatectomy," J. Nucl. Med. **63**(9), 1349–1356 (2022). https://doi.org/10.2967/jnumed.121.263175

[30] O. Günay, M. Sarıhan, O. Yarar, *et al.*, "Determination of radiation dose from patients undergoing Tc-99m Sestamibi nuclear cardiac imaging," Int. J. Environ. Sci. Technol. **16**, 5251–5258 (2019). https://doi.org/10.1007/s13762-019-02262-1

[31] M. Sarihan, and E. Abamor, "Radiation dose measurement on bone scintigraphy and planning clinical management," Open Phys. **20**(1), 1176–1184 (2022). https://doi.org/10.1515/phys-2022-0211

ОЦІНКА ПОТУЖНОСТІ ГАММА-ОПРОМІНЮВАННЯ ДЛЯ КЛІНІЧНО ЗНАЧНИХ РАДІОНУКЛІДІВ У ЯДЕРНІЙ МЕДИЦИНІ З ВИКОРИСТАННЯМ МОДЕЛЮВАННЯ МОНТЕ-КАРЛО GATE/GEANT4

Абдулхалек О. Джаралах[1], Алаа М. Елгохарі[1], Моніра М. Рагех[1], Магді М. Халіл[2,3]
[1]*Кафедра біофізики, факультет природничих наук, Каїрський університет, Єгипет*
[2]*Медична біофізика, кафедра фізики, факультет природничих наук, Хелуанський університет*
[3]*Школа прикладних медичних наук, Університет Бадр у Каїрі (BUC), Каїр, Єгипет*

Мета. Розробити надійний обчислювальний метод для розрахунку потужності дози зовнішнього опромінення пацієнтів ядерної медицини за допомогою моделювання методом Монте-Карло та систематично оцінити вплив геометрії фантома й характеристик детектора на професійне опромінення. **Методи:** Моделювання MC GATE версії 9.1 (Geant4 10.7) розрахувало константи потужності зовнішньої дози для більшості клінічних радіонуклідів: ^{99m}Tc, ^{67}Ga, ^{18}F, ^{11}C, ^{131}I та ^{123}I. Було використано два фантоми: один із розмірами (25×15×20, 30×20×25 та 35×25×30 см^3), а інший — з фіксованою довжиною 170 см та змінною шириною (15×20, 20×25 та 25×30 см^3), специфічними для нукліда ^{99m}Tc. Розміри детекторів (від 3×3×3 до 10×10×10 см^3) оцінювалися на відстанях 1, 2 та 3 м. Різні середовища детектора (повітря, аргон та неон) оцінювалися на чутливість до фотонів. Результати порівнювали з експериментальними даними. **Результати:** Результати моделювання узгоджувалися з експериментальними даними в межах ±10%. Аргон продемонстрував вищу чутливість порівняно з повітряними і неоновими середовищами детектора. Розміри фантома загалом збільшилися, що призвело до зменшення самозатухання на 36,8%. Радіонукліди ^{18}F та ^{11}C, а також ^{67}Ga, ^{131}I, ^{123}I та ^{99m}Tc, становили найбільшу небезпеку професійного опромінення. Товщина тіла пацієнта була більш значним фактором ослаблення, ніж його зріст. **Висновок:** Моделювання GATE/Geant4 забезпечує надійний і точний інструмент для оцінки потужності зовнішньої дози у відділеннях ядерної медицини. Ці результати підкреслюють важливість використання відповідних розмірів детекторів і середовищ, а також реалістичної геометрії пацієнта в оцінці професійної дози та надають важливі дані для вдосконалення протоколів радіаційного захисту.

Ключові слова: *потужність зовнішньої дози; ядерна медицина; радіаційний захист; моделювання методом Монте-Карло; константа швидкості гамма-випромінювання*

East European Journal of Physics. **2.** 554-562 (2026)
DOI:10.26565/2312-4334-2026-2-62 ISSN 2312-4334

RADIOBIOLOGICAL EFFECTS FOR PROSTATE CANCER HIGH-DOSE-RATE BRACHYTHERAPY

Alaa A. Abou Khadra[1]*, Intesar A. El-Mesady[2], Ehab M. Attalla[3], Mohamed A. Shehata[4]
[1]Clinical Oncology and Nuclear Medicine Department, Faculty of Medicine, Menoufia University, Shebin Elkom, Egypt
[2]Department of Physics, Faculty of Science, Menoufia University, Shebin Elkom, Egypt
[3]Medical Physics Department, National Cancer Institute, Cairo University, Cairo, Egypt
[4]Clinical Oncology and Nuclear Medicine Department, Faculty of Medicine, Menoufia University, Shebin Elkom, Egypt
**Corresponding Author email: alaa.ahmed.h2018@gmail.com, phone: +201060517706*

Received February 26, 2026, revised May 19, 2026; accepted May 21, 2026

Background: HDR brachytherapy represents a cornerstone in prostate cancer management by enabling high tumor doses while sparing surrounding normal tissues. Radiobiological modelling allows quantitative assessment of tumour control and normal tissue complication probability for optimization of fractionation schedules. **Objective:** The purpose of this study is to comparatively appraise the radiobiological outcome of two HDR brachytherapy regimens, 13.5 Gy × 2 fractions versus 15 Gy × 1 fraction, regarding tumor control probability, normal tissue complication probability, and dose-effect metrics in patients presenting with intermediate- to high-risk prostate cancer. **Materials and Methods**: A retrospective analysis of 20 patients treated by Co-60 HDR brachytherapy was performed. The treatment planning was image-based, in which, target and organ-at-risk delineation was followed standard guidelines. BED, EQD2, and Deff were computed using the linear-quadratic model. TCP and NTCP modeling utilized Poisson-based and Lyman–Kutcher–Burman methods, respectively. Correlations between radiobiological parameters and TCP/NTCP were analyzed. **Results**: The single 15 Gy fraction regimen resulted in significantly higher BED, EQD2, Deff, and modeled TCP compared with 13.5 Gy×2 fractions ($p \leq 0.031$). However, NTCP for urethra at 10% volume was higher in the 15 Gy group (8.42% ± 1.58 vs. 6.86% ± 1.24; $p = 0.006$). Strong positive correlations were observed between BED, EQD2, Deff and TCP ($\rho = 0.984$–1.000; $p < 0.001$). NTCP at 30% urethral volume negatively correlated with BED, EQD2, and Deff ($\rho \approx -0.52$; $p = 0.003$). **Conclusions:** Higher radiobiological doses (BED, EQD2, Deff) in prostate HDR brachytherapy are strongly associated with improved tumor control, with Deff showing perfect correlation with TCP. A single 15 Gy fraction yields greater radiobiological effectiveness than 13.5 Gy × 2. Urethral toxicity shows no clear correlation at 10% volume but a strong negative correlation at 30%, indicating that higher doses may reduce toxicity at this level. Radiobiological modeling is thus valuable for optimizing HDR planning, enhancing tumor control prediction, and balancing urethral toxicity.

Keywords: *Prostate cancer; HDR brachytherapy; Biologically Effective Dose; Equivalent Dose; Tumor Control Probability; Normal Tissue Complication Probability; Radiobiological modeling; Fractionation*
PACS: 87.53.Jw, 87.55.D-, 87.55.de, 87.55.dk

1.1. INTRODUCTION

Brachytherapy is one internal radiation therapy technique whereby a high dosage of radiation can be delivered directly to the tumor while exposing the normal tissues surrounding it to minimal radiation. This technique has grown to become an important modality in the treatment of a number of malignancies, especially those of the prostate [1]. High-dose-rate brachytherapy, facilitated by advanced remote afterloading technology, has significantly transformed clinical practice by providing superior dose optimization, reduced treatment duration, and enhanced patient comfort compared with conventional low-dose-rate (LDR) techniques [2].

The basic principle of HDR brachytherapy is to utilize steep dose gradients developed by the temporary placement of radioactive sources within or in proximity to the tumor volume [3]. State-of-the-art HDR treatment planning encompasses, the highly conformal dose distributions accounted for the unique geometry and radiobiological features of prostate tumors. A thorough understanding of the radiobiological influence of HDR fractionation schemes is thus crucial for delivering maximum therapeutic benefit with minimal complications to OARs. [4]

Prostate cancer remains one of the most studied indications for HDR brachytherapy, and a wide range of HDR fractionation schedules including single- and multifraction (each with distinct radiobiological implications) [5]. The main parameters-the biologically effective dose, the equivalent dose in 2-Gy fractions, and the effective dose-play a fundamental role in tumor control probability and normal tissue complication probability calculations [6]. There have been several comparative studies, such as 13.5 Gy×2 versus 15 Gy×1, aimed at offering some balance between tumor sterilization and the risk of toxicity [7].

Radiobiological modeling has enabled further refinement of the assessment of HDR brachytherapy beyond the use of conventional dosimetry [8]. Inclusion of α/β ratios, DNA repair kinetics, and fractionation sensitivity in models allows quantitative predictions of both TCP and NTCP, thus addressing individualized clinical decision-making. These models facilitate systematic comparisons across treatment schedules, enabling more personalized and biologically adaptive dose prescriptions [9, 10].

Prostate tumors are slow-growing tumors with a relatively low α/β ratio, which contributes to their significant sensitivity to hypofractionation, making HDR brachytherapy particularly effective for this kind of tumor **[11]**. Biological

Cite as: A.A.A. Khadra, I.A. El-Mesady, E.M. Attalla, M.A. Shehata, East Eur. J. Phys. 2, 554 (2026), https://doi.org/10.26565/2312-4334-2026-2-62

behavior is important in understanding and optimizing dose-delivery strategies and supports the rationale for high-dose-per-fraction treatments [12].

Simultaneous evaluation of TCP and NTCP yields a more complete characterization of therapeutic effectiveness [13]. The difference between the two probabilities, which describes the margin between TCP and NTCP, is an increasingly useful surrogate for therapeutic gain. The wider the margin, the greater the treatment selectivity; further dose escalation is thus possible, with less risk of significant increased toxicity [14].

Recent advances in imaging and 3D planning have also enhanced HDR brachytherapy precision in prostate cases. The integration of CT and MRI further enhances target volume and OAR delineation to improve dosimetric parameter correlations and clinical outcomes [15]. The technological evolution has heightened interest in performing systematic comparisons of BED, EQD2, Deff, and modeled TCP/NTCP across different HDR regimens in order to better understand their radiobiological equivalence and its clinical implications [16, 17].

Therefore, the objective of this study is to investigate the radiobiological benefits of HDR brachytherapy for prostate cancer quantitatively by considering the most relevant parameters: BED, EQD2, Deff, TCP, and NTCP. This study explores the variation in these parameters with the most common HDR fractionation schedules applied to clarify issues concerning the relative therapeutic benefit of various HDR approaches and aid in dose prescription optimization in order to achieve maximum tumor control with minimum normal tissue toxicity.

1.2. PATIENTS AND METHODS

1.2.1. Study Design

This was a retrospective quantitative study designed to evaluate the radiobiological and dosimetric effect resulting from Co-60 source-based high-dose-rate brachytherapy among patients with prostate cancer falling into the intermediate and high-risk categories. The study received approval from the Institutional Review Board of Menoufia University, and all patient information was treated with confidence.

1.2.2. Study Population

The patient group consisted of 20 male subjects diagnosed with adenocarcinoma of the prostate from January 2024 to December 2024. The stages were all T2b-T3a according to AJCC 8th edition. HDR brachytherapy was administered either as monotherapy, given as 13.5 Gy in two fractions or a single fraction of 15 Gy, or as a boost after EBRT at 9.5 Gy in two fractions. Exclusion criteria included incomplete or corrupted CT datasets, prior pelvic irradiation, anatomical or medical contraindications to transperineal needle placement, and poor performance status (ECOG > 2).

1.2.3. Implant Procedure and Imaging

CT was performed immediately after needle implantation for all patients with a SIEMENS Somatom Definition AS scanner with 2-mm slice thickness in the supine position. Interstitial implantation was carried out transperineally under spinal or general anesthesia with a template-guided technique. Real-time transrectal ultrasound ensured the geometric accuracy of needles. The timing of the CT images, within one hour of implantation, ensured that there was no movement of the needles and thus provided anatomically correct information before treatment planning.

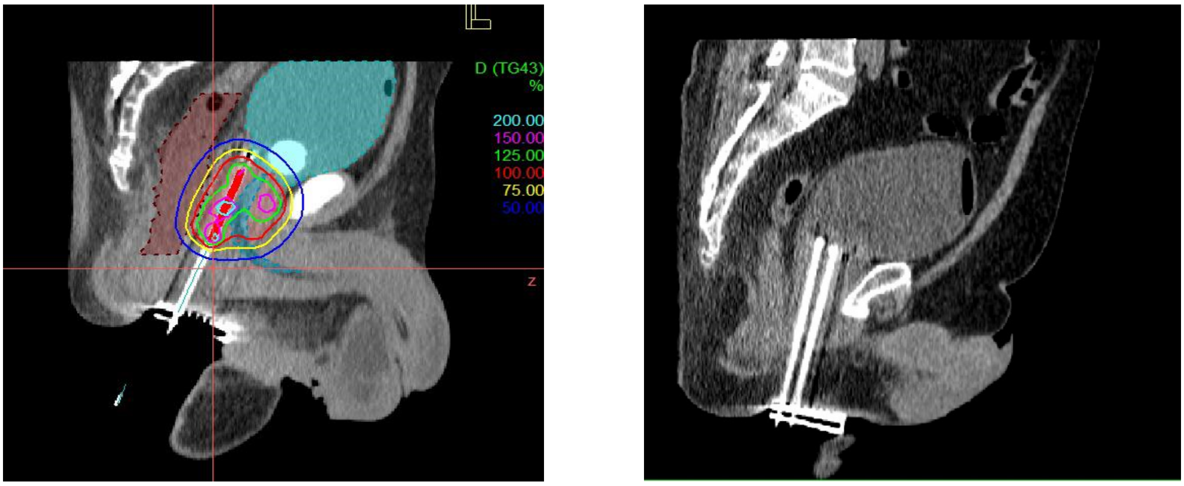

Figure A1. Sagittal CT confirms the intracavitary–interstitial brachytherapy implant geometry, showing multiple interstitial needles traversing the pelvis and their depth relative to pelvic anatomy. Sagittal CT complements this by verifying applicator/needle trajectory and insertion depth, ensuring correct positioning before (and during) treatment planning

1.2.4. Contouring of Target Volumes and OARs

Target and organ-at-risk delineation was performed in accordance with guideline-based standards. The clinical target volume included the whole prostate gland and the proximal 1-1.5 cm of seminal vesicles based on risk category. The urethra was outlined with a contrast-filled Foley catheter, while the rectum was contoured from the rectosigmoid junction to the anal canal. All contours were then reviewed by two experienced radiation oncologists. All volumetric definitions presented conformed to ICRU Report 50, including gross tumor volume, clinical target volume, planning target volume, and the treated and irradiated volumes.

1.2.5. Dose Prescription and Constraints

Dose prescriptions are chosen according to the treatment modality. Monotherapy regimens consisted of two fractions of 13.5 Gy or a single fraction of 15 Gy, whereas HDR boost regimens delivered two fractions of 9.5 Gy following EBRT. Dose constraints included urethral limits of D10% < 125% and D30% < 105% of the prescription dose, and a rectal constraint of D2cc < 75% of prescription.

Treatment Planning and Optimization Treatment planning was executed with a three-dimensional image-based brachytherapy planning system such as BrachyVision or Oncentra Brachy. First, 3D Conformal planning algorithms were applied in order to achieve an optimum target coverage; then, this was supplemented by manual refinement of dwell times and dwell positions in order to further improve normal tissue sparing. Dosimetric and Radiobiological Evaluation The dose-volume histogram parameters extracted for all patients included D90, D98, and D100 for the target and D2cc for the rectum and urethra. Additionally, Coverage Index, Dose Homogeneity Index, Overdose Index, and Dose Non-Uniformity Ratio were calculated to determine the quality of implant dose uniformity and overall adequacy of the plan. Collectively, these parameters allowed for an assessment of the dosimetric and radiobiological characteristics of HDR brachytherapy in intermediate- to high-risk prostate cancer.

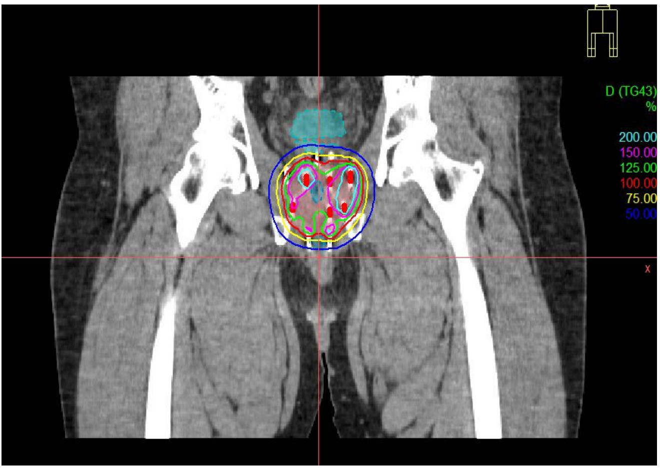

Figure A2. Coronal CT treatment planning slice showing representative isodose distribution (color wash/isodose lines) around the prostate target, illustrating high-dose coverage centered on the implant with rapid dose fall-off to spare surrounding tissues.

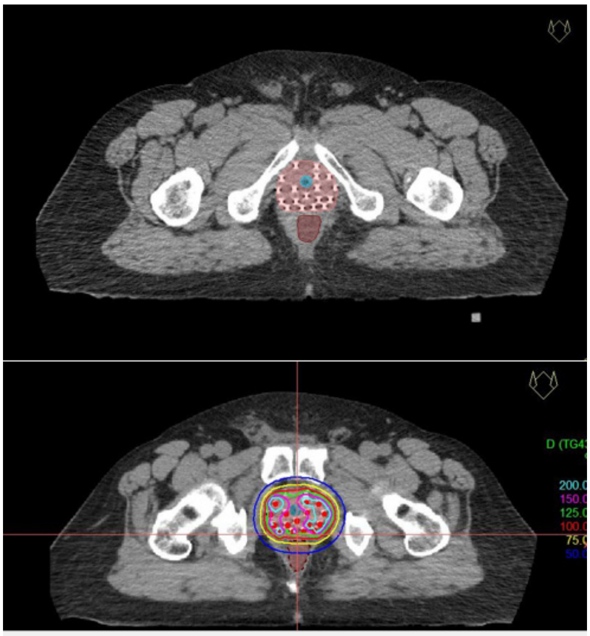

Figure A3. Axial CT-based brachytherapy plan demonstrating contoured target volume and organs at risk (e.g., urethra and rectum) together with catheter/needle trajectories, dwell positions, and isodose contours illustrating how dwell time/position optimization achieves target coverage while limiting hotspots and sparing OARs for DVH-based dosimetric and radiobiological evaluation.

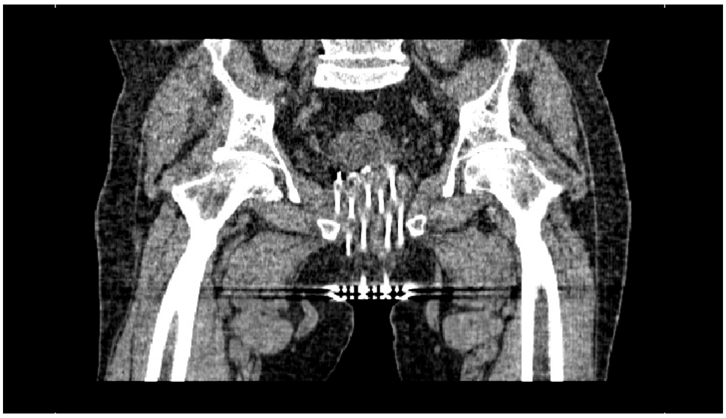

Figure A4. Coronal CT view showing the implant in profile with representative dose distribution, highlighting the anterior-posterior dose gradient and proximity of high-dose regions to nearby organs at risk**.**

Radiobiological Analysis

Radiobiological modeling was conducted based on the Linear–Quadratic (LQ) model for the computation of the Biologically Effective Dose (BED) and the Equivalent Dose in 2 Gy fractions (EQD2).

The **BED** was calculated as:

$$\mathrm{BED}=\mathrm{n}\times\mathrm{d}\times\left(1+\frac{\mathrm{d}}{\alpha/\beta}\right)$$

where *n* is the number of fractions, *d* is the dose per fraction, and *α/β* represents the tissue-specific ratio (10 Gy for tumor tissue and 3 Gy for organs at risk).

The **EQD2** was then derived from the BED using the following relationship:

$$\mathrm{EQD2}=\frac{\mathrm{BED}}{1+\frac{2}{\alpha/\beta}}$$

This conversion normalizes doses of differing fractionation schedules to an equivalent dose delivered in 2 Gy fractions, facilitating inter-patient comparison.

The **effective dose (Deff)** representing the equivalent uniform dose to a given organ or target volume was calculated using Niemierko's model as:

Deff = EQD2 brachytherapy + EQD2 external beam

The **Tumor Control Probability (TCP)** was calculated using Niemierko's Poisson-based model, describing the probability of eradicating all clonogenic tumor cells as:

$$\mathrm{TCP}=\frac{1}{1+\left(\frac{\mathrm{TCD}_{50}}{\mathrm{D}_{\mathrm{eff}}}\right)^{4\gamma_{50}}}$$

where TCD_{50} is the dose required to achieve 50% tumor control and γ_{50} is the slope of the dose–response curve at 50% control probability.

The **Normal Tissue Complication Probability (NTCP)** for organs at risk, particularly the urethra, rectum, and bladder, was calculated using the Lyman–Kutcher–Burman (LKB) model, defined as:

$$\mathrm{NTCP}=\Phi\left(\frac{\mathrm{D}_{\mathrm{eff}}\text{-}\mathrm{TD}_{50}}{\mathrm{m}\times\mathrm{TD}_{50}}\right)$$

where TD_{50} is the uniform dose causing a 50% complication rate, *m* is the slope parameter representing the steepness of the dose–response curve, and *Φ* is the cumulative normal distribution function.

The model parameters used in the computation included the dose required to produce a 50% response (D_{50}), the slope of the response curve (γ), and the volume-effect parameter (*n*). All radiobiological parameters were extracted from the dose–volume histogram (DVH) using dedicated analytical tools within the treatment planning system.

1.2.6. Data Collection and Statistical Analysis

All statistical analyses were performed to evaluate the relationship between radiobiological parameters (BED, EQD2, Deff) and tumor control probability (TCP) and normal tissue complication probability (NTCP) in prostate HDR brachytherapy patient groups. Data normality was established prior to inferential testing, and appropriate parametric (independent t-test, Pearson correlation) or nonparametric (Mann–Whitney U test, Spearman's ρ) tests were employed for analyzing differences. Statistical significance was established at $p < 0.05$.

1.3. RESULTS

Compared with the 13.5 Gy × 2 regimen, the single-fraction 15 Gy regimen yielded significantly higher BED, EQD2, DEFF and modelled TCP (all $p \le 0.031$), indicating a greater predicted tumoricidal effect for the 15 Gy single fraction. However, the 15 Gy arm also showed a statistically significant increase in predicted urethral toxicity for the NTCP Urethra 10 % metric (8.42% ± 1.58 vs 6.86% ± 1.24; $p = 0.006$). NTCP Urethra 30% did not differ between groups ($p = 0.517$). Clinically this suggests that while a single 15 Gy fraction may improve predicted tumor control, it may increase the risk of urethral complications; careful urethral dose-sparing, close follow-up, and correlation with observed toxicity are therefore recommended **(Table A1).**

Table A.1. Patient Demographics and Baseline Clinical Characteristics

Characteristic	Overall (N = 20)	13.5 Gy × 2 (n = 10)	15 Gy × 1 (n = 10)	P value
Age (years)	68.43 ± 4.96	67.85 ± 5.03	69.60 ± 4.84	0.371
Initial PSA (ng/mL)	11.44 ± 6.08	11.17 ± 6.52	11.98 ± 5.23	0.737
Gleason Grade Group	2 (2–3.25)	2 (2–3)	3.5 (3–4)	**0.041**
EBRT dose (Gy)	46 (45–50.4)	48.2 (45–50.4)	46 (45–50.4)	0.642
EBRT fractions	26 (25–28)	27 (25–28)	26 (25–28)	0.642
ECOG	0 (0–1)	0 (0–1)	0.5 (0–2)	0.056
Risk group				0.439
High-risk	15 (50%)	9 (45%)	6 (60%)	
Intermediate	15 (50%)	11 (55%)	4 (40%)	
Clinical T stage				0.555
T2b	13 (43.3%)	10 (50%)	3 (30%)	
T2c	8 (26.7%)	5 (25%)	3 (30%)	
T3a	9 (30.0%)	5 (25%)	4 (40%)	
ADT use				0.297
No	13 (43.3%)	10 (50%)	3 (30%)	
Yes	17 (56.7%)	10 (50%)	7 (70%)	
Treatment approach				0.605
HDR boost	16 (53.3%)	10 (50%)	6 (60%)	
HDR monotherapy	14 (46.7%)	10 (50%)	4 (40%)	

Data are presented as mean ± SD or median (IQR) for continuous variables and n (%) for categorical variables. Comparisons were performed using t-test, Mann–Whitney U test, Chi-square, or Fisher's exact test as appropriate. Two-sided $p < 0.05$ was considered significant. Abbreviations: PSA, prostate-specific antigen; EBRT, external beam radiotherapy; ECOG, Eastern Cooperative Oncology Group; ADT, androgen deprivation therapy; HDR, high-dose-rate.

In the 13.5 Gy×2 group, tumor control probability (TCP) showed a perfect positive correlation with all evaluated radiobiological parameters (BED, EQD2, and Deff), reflecting that increases in these parameters were consistently associated with increases in TCP. The correlations were statistically significant ($p < 0.01$) **(Table A2)**

Table A.2. Radiobiological Parameters for Prostate HDR Brachytherapy

Parameter	13.5 Gy × 2 (n = 10)	15 Gy × 1 (n = 10)	P value
BED (Gy) Median (IQR)	125.0 (121.65 – 136.50)	140.91 (132.44 – 148.83)	0.004
EQD2 (Gy) Median (IQR)	53.57 (52.14 – 58.50)	60.39 (56.76 – 63.78)	0.004
Deff (Gy) Median (IQR)	103.17 (101.74 – 108.10)	107.91 (104.28 – 111.30)	0.031
TCP (%) Median (IQR)	92.00 (91.16 – 94.36)	94.29 (92.63 – 95.49)	0.031
NTCP Urethra 10 (%) Mean ± SD	6.86 ± 1.24	8.42 ± 1.58	0.006
NTCP Urethra 30 (%) Mean ± SD	9.02 ± 1.24	8.71 ± 1.28	0.517

BED = biologically effective dose; EQD2 = equivalent dose in 2-Gy fractions; Deff = dose-effect metric; TCP = tumor control probability; NTCP = normal tissue complication probability; IQR = interquartile range; SD = standard deviation. BED and EQD2 were derived using the linear-quadratic model ($\alpha/\beta = 1.5$ Gy for prostate). Data are median (IQR) or mean ± SD; p-values from Mann–Whitney U or t-test as appropriate ($p < 0.05$ significant).

In the 13.5 Gy×2 group (n = 10), NTCP for the urethra at 10% volume (NTCP.URETHRA.10) showed no significant correlation with BED, EQD, or DEFF (ρ = 0.087, p = 0.714). However, NTCP at 30% volume (NTCP.URETHRA.30) demonstrated a moderate negative correlation with BED, EQD, and DEFF (ρ = -0.479, p = 0.033), indicating that higher radiobiological doses are associated with lower predicted urethral complications at this volume threshold **(Table 3).**

Table A.3. Correlation Between Radiobiological Parameters and Tumor Control Probability (TCP) in the 13.5 Gy×2 Group (n = 10)

Parameter	Spearman's ρ	p-value
BED	1.000	<0.01
EQD2	1.000	<0.01
Deff	1.000	<0.01

TCP = Tumor Control Probability; BED = Biologically Effective Dose; EQD2 = Equivalent Dose in 2 Gy fractions; Deff = Effective Dose. Spearman's rho (ρ) indicates the strength and direction of a monotonic relationship.

TCP is very strongly and significantly positively correlated with BED, EQD, and DEFF in the 15 Gy × 1 group, indicating that higher radiobiological doses are associated with higher tumor control probability **(Table 4)**

Table A.4. Correlation Between Radiobiological Parameters and NTCP Urethra in the 13.5 Gy×2 Group (n = 10)

Parameter (Gy)	NTCP.URETHRA.10 (ρ, p)	NTCP.URETHRA.30 (ρ, p)
BED	0.087, 0.714	-0.479*, 0.033
EQD	0.087, 0.714	-0.479*, 0.033
DEFF	0.087, 0.714	-0.479*, 0.033

*ρ = Spearman's correlation coefficient; p = two-tailed significance. BED = Biologically Effective Dose; EQD = Equivalent Dose in 2 Gy fractions; DEFF = Effective Dose; NTCP = Normal Tissue Complication Probability. *p < 0.05 indicates statistical significance.

There is a moderate negative correlation between BED/EQD/DEFF and NTCP.URETHRA.10 and NTCP.URETHRA.30, but none are statistically significant (p > 0.05). This suggests that in this small sample, urethral toxicity is not strongly dependent on radiobiological dose parameters **(Table A5).**

Table A.5. Correlation Between Radiobiological Parameters and Tumor Control Probability (TCP) in the 15 Gy × 1 (n = 10)

Parameter	Spearman's ρ	p-value
BED	0.996	0.000
EQD	0.996	0.000
DEFF	0.996	0.000

Spearman's ρ = Spearman's rank correlation coefficient; NTCP = Normal Tissue Complication Probability; N = 10.

Table B. 5. Correlation Between Radiobiological Parameters and NTCP Urethra in the 15 Gy × 1 (n = 10)

Parameter (Gy)	NTCP.URETHRA.10 (ρ, p)	NTCP.URETHRA.30 (ρ, p)
BED	-0.419, 0.229	-0.542, 0.106
EQD	-0.419, 0.229	-0.542, 0.106
DEFF	-0.419, 0.229	-0.542, 0.106

1.4. DISCUSSION

Radiobiological doses measured as a result of the single-fraction 15 Gy HDR brachytherapy regimen were significantly higher compared with the 13.5 Gy × 2 regimen: BED, 140.91 Gy versus 125.0 Gy; EQD2, 60.39 Gy versus 53.57 Gy; Deff, 107.91 Gy versus 103.17 Gy; and TCP, 94.29% versus 92.00%. These data depict a higher predicted tumoricidal effect for the single-fraction 15 Gy HDR protocol.

This finding is consistent with previously reported evidence highlighting the radiobiological benefits associated with HDR brachytherapy. Dutta et al. [18] described that HDR allows for higher conformality than EBRT, enabling higher doses per fraction to be delivered with consistent dosimetry. Similarly, Yoshioka et al. [19] assured that BEDs of 208–299 Gy could be achieved with single-fraction HDR monotherapy, which offers a convenience and potential radiobiological benefit. Morton and Hoskin [20] mentioned that HDR, used either as a boost or as monotherapy combined with EBRT, exploits the low α/β ratio of prostate cancer to achieve that BEDs is higher than EBRT alone. Patel et al. [21] and Strouthos et al. [22] also emphasized the precision and dose-escalation capability of HDR, achieving BEDs comparable to or exceeding LDR while respecting normal tissue constraints. Hauswald et al. [23] and De Bari et al. [24] confirmed that HDR monotherapy alone provides an adequate BED to ensure excellent biochemical and local control. Chapman et al. [25] demonstrated that focal dose escalation to dominant intraprostatic lesions is feasible, delivering up to 150% of the prescription dose without compromising normal tissue constraints.

Nevertheless, several reports have demonstrated limited survival differences despite differences in BED. For instance, Barnes et al. **[26]** reported that although HDR brachytherapy enables highly precise dose modulation, overall survival outcomes remained comparable to those achieved with LDR in a large patient cohort.

Skowronek **[27]** similarly noted, while HDR afforded dosimetric advantages that the tumor control rates were comparable to LDR and that both approaches can be clinically effective.

Our findings are in agreement with the majority of published studies supporting single-fraction HDR brachytherapy due to its enhanced radiobiological efficacy, while also indicating that its impact on long-term clinical survival outcomes may remain limited.

Analysis of the urethral NTCP demonstrated that the 15 Gy single-fraction cohort had significantly higher NTCP at 10% volume (8.42% vs 6.86%, $p = 0.006$) but not at 30% volume ($p = 0.517$). This may indicate that higher single-fraction doses increase the risk of urethral complications for small volumes but not for larger volumes.

This finding is consistent with previous studies emphasizing the importance of meticulous treatment planning to optimize urethral dose sparing. Dutta et al. **[18]** and Yoshioka et al. **[19]** referred to the HDR's ability to sculpt the dose distribution to spare the urethra. Morton and Hoskin **[20]** and Yamada et al. **[27]** demonstrated a low incidence of severe urethral toxicity with accurate HDR treatment planning. Patel et al. **[21]**, Strouthos et al. **[22]**, and De Bari et al. **[24]** showed favorable urethral sparing with HDR compared with LDR, while Hauswald et al. **[23]** reported only 4.9% late grade 3–4 genitourinary toxicity. Chapman et al. **[25]** similarly demonstrated low toxicity with focal dose escalation.

Conversely, Barnes et al. **[26]** observed no significant difference in urethral toxicity between HDR and LDR brachytherapy, underscoring the critical role of appropriate patient selection and meticulous treatment planning.

In summary, these reports suggest that single-fraction HDR treatment can maintain acceptable urethral safety provided dose constraints are carefully applied.

All the radiobiological parameters in our study had strong positive correlations with TCP: BED $\rho = 0.984$; EQD2 $\rho = 0.984$; Deff $\rho = 1.000$, $p < 0.001$, thus confirming their reliability in predicting tumor control. Of note, Deff had a perfect correlation with TCP, underlining its potential as a robust predictor.

These findings are consistent with those in previous literature. Dutta et al. **[18]** and Yoshioka et al. **[19]** reported improved biochemical control at higher BED and EQD2 in particular for intermediate- and high-risk disease. Morton and Hoskin **[20]** and Yamada et al. **[29]** also confirmed that higher HDR are associated with reduced recurrence and excellent biochemical control. Patel et al. **[21]** and Strouthos et al. **[22]** highlighted that HDR can facilitate dose escalation to improve biochemical control and recurrence-free survival. Hauswald et al. **[23]** reported that 6- and 10-year PSA progression-free survival rates exceeding 97%, further supporting the relationship between HDR dose escalation and improved tumor control. Chapman et al. **[25]** reported no biochemical failures following focal dose escalation to DIL over median 4.9-year follow-up.

Although Barnes et al. **[26]** and Skowronek **[27]** previously suggested that overall survival outcomes may not differ significantly between HDR and LDR brachytherapy, the association between higher radiobiological dose delivery and improved tumor control has been consistently demonstrated in the literature.

This study revealed that no significant correlation of the radiobiological parameters with NTCP for 10% urethral volume and a strong negative correlation for NTCP at 30% volume ($\rho \approx -0.52$, $p = 0.003$). These findings indicate that higher BED, EQD2, or Deff values do not necessarily translate into increased urethral toxicity across larger treatment volumes, thereby highlighting the critical importance of optimized dose distribution and meticulous treatment planning.

This is in line with prior publications that showed HDR planning can deliver high BEDs while minimizing urethral exposure. Dutta et al. **[18],** and Yoshioka et al. **[19]** confirmed that precise HDR planning can safely escalate tumor dose. Morton and Hoskin **[20]**, Patel et al. **[21]**, and Strouthos et al. **[22]** further emphasized that precise HDR dosimetry reduces urethral toxicity even at higher doses. Hauswald et al. **[23]**, De Bari et al. **[24]**, and Chapman et al. **[25]** have reported low genitourinary toxicity despite high radiobiological doses, while Yamada et al. **[29]**, on their part, observed a very low incidence of severe urethral complications. Collectively, they support the results that HDR can increase tumoricidal doses without compromising urethral safety.

This study has several limitations, including the relatively small sample size, particularly within the single-fraction 15 Gy cohort, which may restrict the generalizability of the findings. The analysis was based on radiobiological modeling instead of long-term clinical outcomes; actual toxicity and tumor control may differ in larger prospective cohorts. Patient-specific anatomical variations and uncertainties in urethral contouring could influence NTCP estimates. Finally, our follow-up period may not fully capture late genitourinary or gastrointestinal toxicity, which can manifest years after single-fraction HDR. Future studies with larger patient cohorts and long-term follow-up are needed to validate these findings and refine optimal fractionation strategies.

CONCLUSIONS

Single-fraction 15 Gy HDR prostate brachytherapy demonstrated superior predicted tumor control compared with the 13.5 Gy × 2 regimen, although with a modest increase in the potential risk of urethral toxicity. While the 13.5 Gy × 2 schedule showed a more consistent balance between tumor control probability and urethral dose tolerance, the 15 Gy regimen maintained high tumor control efficacy with less predictable urethral response patterns. These findings support the clinical feasibility of single-fraction HDR brachytherapy, provided that meticulous urethral dose optimization and careful post-treatment monitoring are implemented to maximize therapeutic benefit while minimizing toxicity.

Declarations

Funding: This case report received no specific grant from any funding agency in the public, commercial, or not-for-profit sectors.

Conflicts of Interest/Competing Interests: The authors declare that they have no conflicts of interest related to this case report.

Consent to Participate: Written informed consent was obtained from the patient for participation in this case report.

Consent for Publication: Written informed consent was obtained from the patient for publication of this case report and any accompanying images. A copy of the written consent is available for review by the Editor-in-Chief of this journal upon request.
Availability of Data and Materials: All data generated or analyzed during this case report are included in this published article.
Code Availability: Not applicable.
Author Contributions
Writing, review, and editing; visualization; validation; methodology; investigation; data curation; and supervision; and conceptualization are among the skills **Alaa A. Abou Khadra**; **Intesar A. El-Mesady**; **Ehab M. Attalla**; **Mohamed A. Shehata,** possesses. **Alaa A. Abou Khadra**: Writing: reviewing and revising, writing: initial draft, data curation, supervision, investigation, methodology. **Intesar A. El-Mesady & Ehab M. Attalla**: review, and editing; writing, original draft; visualisation; validation; conceptualisation; methodology; investigation. The published version of the manuscript has been read and approved by all authors.
Acknowledgment: Not applicable

ORCID

Alaa A. Abou Khadra, https://orcid.org/0009-0001-1798-1816; **Ehab M. Attalla,** https://orcid.org/0000-0003-4779-4445;
Mohamed A. Shehata, https://orcid.org/0000-0003-1526-0019

REFERENCES

[1] S.R. Nurkic, A.I. Ocampo, M.J.P. Gadea, J. Greenwalt, M.J. Vicente, A.L. Velasquez, L.C.L. Peralta, *et al*., "Implementation of High Dose-rate Brachytherapy for Cervix Cancer in a Low-income Country," Ann. Glob Health. **84**(4), 679-682 (2018). https://doi.org/10.29024/aogh.2377
[2] C.D. Lee, "Recent developments and best practice in brachytherapy treatment planning," Br. J. Radiol. **87**(1041), 20140146 (2014). https://doi.org/10.1259/bjr.20140146
[3] H. Samlalil, N. Assaid, Y. Khobbaizi, O. Hanicha, M. Abou El Houda, S. Nabil, *et al.* "High-dose-rate brachytherapy boost for prostate cancer: A retrospective observational study in low- and middle-income countries," Adv. Radiat. Oncol. 101861 (2025). https://doi.org/10.1016/j.adro.2025.101861
[4] L.C. Mendez, and G.C. Morton, "High dose-rate brachytherapy in the treatment of prostate cancer," Transl. Androl. Urol. **7**(3), 357-370 (2018). https://doi.org/10.21037/tau.2017.12.08
[5] J.M. Hannoun-Levi, M.E. Chand-Fouche, T. Pace-Loscos, M. Gautier, J. Gal, R. Schiappa, and N. Pujol, "Single fraction of HDR brachytherapy for prostate cancer: Results of the SiFEPI phase II prospective trial," Clin. Transl. Radiat. Oncol. **18**(37), 64-70 (2022). https://doi.org/10.1016/j.ctro.2022.08.007
[6] W. Luo, and W.St. Clair, "Replacing 2 Gy Per Fraction Equivalent Dose with Fractionation-Specific Biological Equivalent Dose for Normal Tissues," International Journal of Molecular Sciences, **25**(23), 12891 (2024). https://doi.org/10.3390/ijms252312891
[7] S.R. Villalba, D.G. Barrera, L. Suso-Martí, E. Sanchis-Sánchez, J. Pérez-Calatayud, J.D.L. Martín, F.B. Molina, *et al*., "High-dose-rate (2 fractions of 13.5 Gy) and low-dose-rate brachytherapy as monotherapy in prostate cancer. Long term outcomes and predictive value of nadir prostate-specific antigen," Brachytherapy, **24**(2), 310-317 (2025). https://doi.org/10.1016/j.brachy.2024.10.014
[8] A.J. Stewart, C. Chargari, A. Chyrek, F. Eckert, J.L. Guinot, T.P. Hellebust, *et al*., "Radiobiology and modelling in brachytherapy: A review inspired by the ESTRO Brachytherapy pre-meeting course," Clin. Transl. Radiat. Oncol. **50**, 100885 (2025). https://doi.org/10.1016/j.ctro.2024.100885
[9] D. Zheng, K. Preuss, M.T. Milano, X. He, L. Gou, Y. Shi, B. Marples, *et al*., "Mathematical modeling in radiotherapy for cancer: a comprehensive narrative review," Radiat. Oncol. **20**, 49 (2025). https://doi.org/10.1186/s13014-025-02626-7
[10] J. O'Donoghue, P. Zanzonico, J. Humm, and A. Kesner, "Dosimetry in radiopharmaceutical therapy," J. Nucl. Med. **63**(10), 1467–1474 (2022). https://doi.org/10.2967/jnumed.121.262305
[11] Wang J.Z., Li X.A., Yu C.X., DiBiase S.J. The low alpha/beta ratio for prostate cancer: what does the clinical outcome of HDR brachytherapy tell us? Int J Radiat Oncol Biol Phys. 2003 Nov 15;57(4):1101-8.
[12] Yang Y., Xing L. Optimization of radiotherapy dose-time fractionation with consideration of tumor specific biology. Med Phys. 2005 Dec;32(12):3666-77.
[13] Yorke E. Modeling clinical outcomes in radiotherapy: NTCP, TCP and the "TECs". Med Phys. 2023 Jun;50 Suppl 1:122-124.
[14] L.B. Marks, E.D. Yorke, A. Jackson, R.K.T. Haken, L.S. Constine, A. Eisbruch, S.M. Bentzen, *et al*., "Use of normal tissue complication probability models in the clinic," Int. J. Radiat. Oncol. Biol. Phys. **76**(3 Suppl), S10-9 (2010). https://doi.org/10.1016/j.ijrobp.2009.07.1754
[15] P. Pathak, J.J. Thomas, A. Baghwala, C. Li, B.S. Teh, E.B. Butler, and A.M. Farach, "Personalized Brachytherapy: Applications and Future Directions," Cancers, **16**(19), 3424 (2024). https://doi.org/10.3390/cancers16193424
[16] A. Mesbahi, N. Rasouli, M. Mohammadzadeh, B.N. Motlagh, and H.O. Tekin, "Comparison of Radiobiological Models for Radiation Therapy Plans of Prostate Cancer: Three-dimensional Conformal versus Intensity Modulated Radiation Therapy," J. Biomed Phys. Eng. **9**(3), 267-278 (2019). https://doi.org/10.31661/jbpe.v9i3jun.655
[17] D. Karia, Radiobiological optimization of lung and prostate radiotherapy treatments—a macroscopic approach [dissertation]. Liverpool (UK): University of Liverpool; 2018.
[18] S.W. Dutta, C.E. Alonso, B. Libby, and T.N. Showalter, "Prostate cancer high dose-rate brachytherapy: review of evidence and current perspectives," Expert Rev Med Devices, **15**(1), 71–79 (2018). https://doi.org/10.1080/17434440.2018.1419058
[19] Y. Yoshioka, O. Suzuki, Y. Otani, K. Yoshida, T. Nose, and K. Ogawa, "High-dose-rate brachytherapy as monotherapy for prostate cancer: technique, rationale and perspective," J. Contemp. Brachytherapy, **6**(1), 91–98 (2014). https://doi.org/10.5114/jcb.2014.42026
[20] G.C. Morton, and P.J. Hoskin, "Brachytherapy: current status and future strategies—can high dose rate replace low dose rate and external beam radiotherapy?" Clin. Oncol. (R. Coll. Radiol.), **25**(8), 474–482 (2013). https://doi.org/10.1016/j.clon.2013.04.009
[21] S.A. Patel, M. Kollmeier, J. Crook, D. Krauss, G. Morton, A.J. Chang, *et al*., "High-dose-rate (HDR) brachytherapy boost in combination with external beam radiotherapy for localized prostate cancer: an evidence-based consensus statement," Brachytherapy, (2025). https://doi.org/10.1016/j.brachy.2025.06.005

[22] I. Strouthos, E. Karagiannis, N. Zamboglou, and K. Ferentinos, "High-dose-rate brachytherapy for prostate cancer: rationale, current applications, and clinical outcome," Cancer Rep (Hoboken), **5**(1), e1450 (2022).
[23] H. Hauswald, M.R. Kamrava, J.M. Fallon, P.C. Wang, S.J. Park, T. Van, *et al.*, "High-dose-rate monotherapy for localized prostate cancer: 10-year results," Int. J. Radiat. Oncol. Biol. Phys. **94**(4), 667–674 (2016). https://doi.org/10.1016/j.ijrobp.2015.07.2290
[24] B. De Bari, A. Daidone, F. Alongi, "Is high dose rate brachytherapy reliable and effective treatment for prostate cancer patients? A review of the literature," Crit. Rev. Oncol. Hematol. **94**(3), 360–370 (2015). https://doi.org/10.1016/j.critrevonc.2015.02.003
[25] C.H. Chapman, S.E. Braunstein, J. Pouliot, S.M. Noworolski, V. Weinberg, A. Cunha, *et al.*, "Phase I study of dose escalation to dominant intraprostatic lesions using high-dose-rate brachytherapy," J. Contemp. Brachytherapy, **10**(3), 193–201 (2018). https://doi.org/10.5114/jcb.2018.76881
[26] J. Barnes, W. Kennedy, B. Fischer-Valuck, B. Baumann, J. Michalski, and H. Gay, "Treatment patterns of high-dose-rate and low-dose-rate brachytherapy as monotherapy for prostate cancer," J. Contemp. Brachytherapy, **11**(4), 320–328 (2019). https://doi.org/10.5114/jcb.2019.86974
[27] J. Skowronek, "Low-dose-rate or high-dose-rate brachytherapy in treatment of prostate cancer–between options," J. Contemp. Brachytherapy, **5**(1), 33–41 (2013). https://doi.org/10.5114/jcb.2013.34342
[28] H. Hauswald, C. Kirisits, R. Pötter, *et al.* "Long-term outcomes of HDR monotherapy for localized prostate cancer," Radiother. Oncol. **115**(2), 236–242 (2015).
[29] Y. Yamada, L. Rogers, D.J. Demanes, G. Morton, B.R. Prestidge, J. Pouliot, *et al.*, "HDR brachytherapy dose response and tumor control in prostate cancer," Int. J. Radiat. Oncol. Biol. Phys. **81**(4), e487–e493 (2011).

РАДІОБІОЛОГІЧНІ ЕФЕКТИ ПРИ ВИСОКОДОЗОВІЙ БРАХІТЕРАПІЇ РАКУ ПРОСТАТИ

Алаа А. Абу Хадра[1], Інтесар А. Ель-Месаді[2], Ехаб М. Атталла[3], Мохамед А. Шехата[4]
[1]Кафедра клінічної онкології та ядерної медицини, медичний факультет, Університет Менуфії, Шебін-Ельком, Єгипет
[2]Кафедра фізики, факультет природничих наук, Університет Менуфії, Шебін-Ельком, Єгипет
[3]Кафедра медичної фізики, Національний інститут раку, Каїрський університет, Каїр, Єгипет
[4]Кафедра клінічної онкології та ядерної медицини, медичний факультет, Університет Менуфії, Шебін-Ельком, Єгипет

Передумови: Брахітерапія HDR є наріжним каменем у лікуванні раку передміхурової залози, дозволяючи отримувати високі дози опромінення пухлини, не впливаючи при цьому на навколишні нормальні тканини. Радіобіологічне моделювання дозволяє кількісно оцінити контроль пухлини та ймовірність ускладнень у нормальних тканинах для оптимізації графіків фракціонування. **Мета:** Метою цього дослідження є порівняльна оцінка радіобіологічного результату двох режимів брахітерапії HDR, фракції 13,5 Гр × 2 проти фракції 15 Гр × 1, щодо ймовірності контролю пухлини, ймовірності ускладнень у нормальних тканинах та показників доза-ефект у пацієнтів з раком передміхурової залози середнього та високого ризику. **Матеріали та методи:** Було проведено ретроспективний аналіз 20 пацієнтів, які отримували брахітерапію Co-60 HDR. Планування лікування базувалося на візуалізації, при цьому визначення мішеней та органів ризику проводилося згідно зі стандартними рекомендаціями. BED, EQD2 та Deff були розраховані за допомогою лінійно-квадратичної моделі. Моделювання TCP та NTCP використовувало методи Пуассона та Лаймана–Кутчера–Бурмана відповідно. Було проаналізовано кореляцію між радіобіологічними параметрами та TCP/NTCP. **Результати:** Режим одноразового фракційного опромінення 15 Гр призвів до значно вищих BED, EQD2, Deff та змодельованого TCP порівняно з фракціями 13,5 Гр×2 ($p \leq 0{,}031$). Однак, NTCP для уретри при 10% об'ємі був вищим у групі 15 Гр (8,42% ± 1,58 проти 6,86% ± 1,24; $p = 0{,}006$). Сильні позитивні кореляції спостерігалися між BED, EQD2, Deff та TCP ($\rho = 0{,}984$–$1{,}000$; $p < 0{,}001$). NTCP за 30% об'єму уретри негативно корелював із BED, EQD2 та Deff ($\rho \approx -0{,}52$; $p = 0{,}003$). **Висновки:** Вищі радіобіологічні дози (BED, EQD2, Deff) при брахітерапії простати HDR тісно пов'язані з покращеним контролем пухлини, причому Deff демонструє ідеальну кореляцію з TCP. Одноразова фракція 15 Гр дає більшу радіобіологічну ефективність, ніж 13,5 Гр × 2. Уретральна токсичність не показує чіткої кореляції при 10% об'ємі, але сильну негативну кореляцію при 30%, що вказує на те, що вищі дози можуть знизити токсичність на цьому рівні. Таким чином, радіобіологічне моделювання є цінним для оптимізації планування HDR, покращення прогнозування контролю пухлини та балансування уретральної токсичності.

Ключові слова: *рак простати; HDR брахітерапія; біологічно ефективна доза; еквівалентна доза; ймовірність контролю пухлини; ймовірність ускладнень у нормальних тканинах; радіобіологічне моделювання; фракціонування*